Retrieval of CO_2 and collisional parameters from the MIPAS spectra in the Earth atmosphere

Tesis doctoral realizada por:

Ángel Aythami Jurado Navarro

Granada, 2015

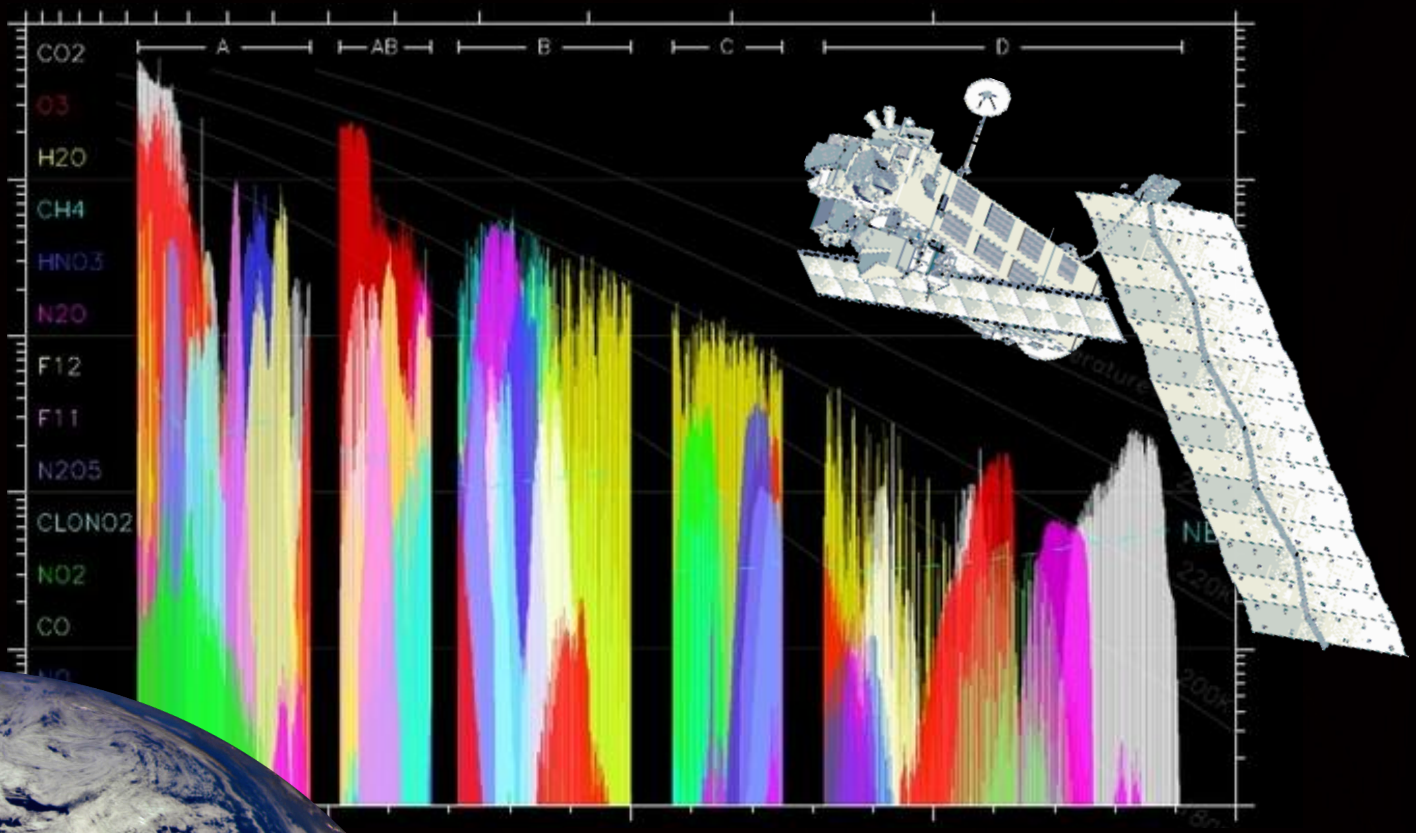

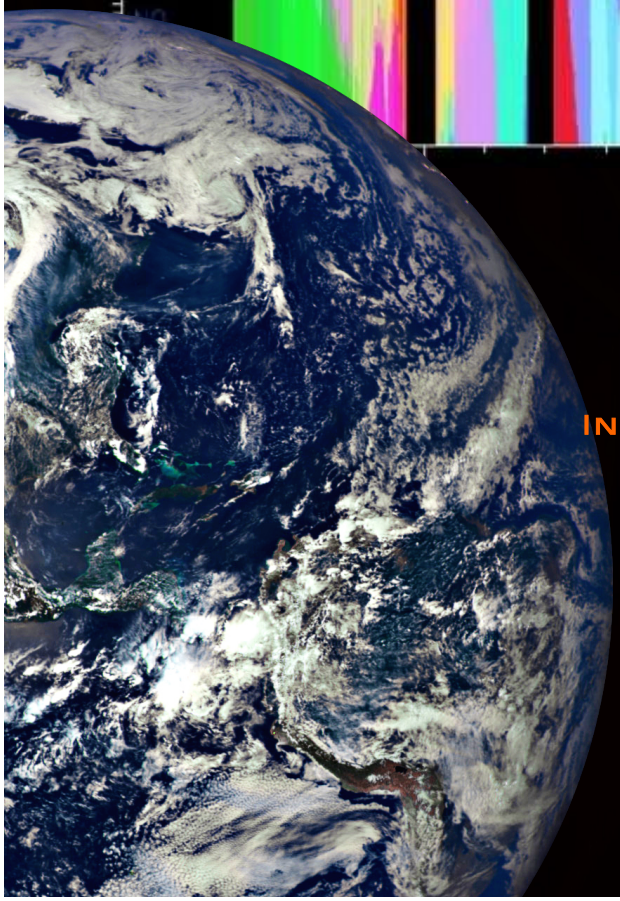

Instituto de Astrofísica de Andalucía, CSIC

Universidad de Granada

II

Universidad de Granada

DEPARTAMENTO DE FÍSICA APLICADA

INSTITUTO DE ASTROFÍSICA DE ANDALUCÍA

CONSEJO SUPERIOR DE INVESTIGACIONES CIENTÍFICAS

Inversión del CO_2 y de parámetros colisionales de los espectros de MIPAS en la atmósfera terrestre

Ángel Aythami Jurado Navarro

Memoria de Tesis

presentada para optar al grado de

Doctor en Ciencias Físicas por la Universidad de Granada

Dirigida por:

Manuel López Puertas
Prof. Investigación del CSIC

Bernd Funke
Científico Titular del CSIC

Granada, a 19 de octubre de 2015

A mi mujer y a mi hijo.

Examina tus sentimientos, sabes que es verdad.
DARTH VADER (EPISODIO V)

Yo he visto cosas que vosotros no creeríais.
Atacar naves en llamas más allá de Orión.
He visto Rayos-C brillar en la oscuridad cerca de la puerta de Tannhäuser.
Todos esos momentos se perderán en el tiempo... como lágrimas en la lluvia.
Es hora de morir.
ROY BATTY (BLADE RUNNER)

... Para ir audazmente donde ningún hombre ha ido antes
CAPITÁN JAMES T. KIRK (STAR TREK TOS INTRO)

Agradecimientos

En primer lugar quiero dar las gracias a mis co-directores de tesis, Manuel López Puertas y Bernd Funke. Sin su apoyo, esfuerzo y dedicación este complicado trabajo jamás se habría realizado. No sólo han aguantado con eterna paciencia mis continuos despistes y meteduras de pata, sino que me han animado en los momentos claves. Me gustaría también extender estos agradecimientos al resto del Grupo de Atmósferas Planetarias Terrestres (GAPT). Gracias a Maya por su preocupación y sus consejos (no sé cómo pero siempre daba en el clavo) y a Ángela por su indispensable trabajo y apoyo. Gracias también a la gente de Marte: Francisco González Galindo y Miguel Ángel López Valverde.

También agradezco al Instituto de Astrofísica de Andalucía en general por darme cobijo y hacerme sentir un auténtico científico todo este tiempo. Gracias a todos, desde la gente de mantenimiento hasta del centro de cálculo (me han sacado las castañas del fuego unas cuantas veces), pasando por el personal de la biblioteca, el científico, el administrativo y el personal de seguridad. Mención especial a los cafés de Paco, que me mantenían despierto todas las mañanas. Otro especial agradecimiento va para Karlsruhe, Alemania, a toda la gente del IMK que tan bien me trataron y me ayudaron, en especial a Gabriele y a Thomas.

Por supuesto también agradecer a mis grandes amigos del Metal: el Dr. don Francisco "Batallas" Parra Rojas y el futuro Dr. don Jorge "Purple Lips" Abreu Vicente. Enormes esos Sonisphere, Wacken (embarrado), Guns 'N Roses, W.A.S.P., Mamá Ladilla... Y esas birras moviendo la melena y tocando la guitarra invisible en el Rainbow. También al resto de componentes del núcleo duro: Toño, Sergio, Jonathan... Unos cracks. A mis compañeras de despacho, Sara Esteban y Clara Cortijo, me gustaría agradecer su apoyo y de paso darles ánimo para el final de sus tesis. No me puedo olvidar de aquellos con los que compartí momentos musicales: los ex-miembros de Chasing Simon (Carl, Migue, Víctor, Juanan y Fran) y el señor Guillermo Carbajosa, con el que he disfrutado muchos buenos momentos tocando los clásicos, improvisando o simplemente hablando de música con unas birras. Con cariño, me gustaría agradecer a la tripulación principal del U.S.S. Enterprise por ayudarme cada noche con el inglés (James T. Kirk, Mr. Spock, Leonard McCoy, Nyota Uhura, Hikaru Sulu y Montgomery Scott). Afortunadamente tengo otros muchos amigos (reales y ficticios) de los que acordarme: Gabriella, Pío, Luis, Antonio, los Pablos (Santos y Ramírez), Dominika, Sol, Zaira, Yoli, Javi (Pascual), Javi (Antequera), Alba, Darío, Eduardo, Gonza, Migue... Si nombrara a todos tendría que hacer otra tesis... Gracias a todos.

Finalmente, doy las gracias a mi familia. A mi mujer, Marien, por su continuo apoyo y cariño (en lo bueno y en lo malo) y por su puesto a mi "cabezón", el pequeño y simpático Aythami Jr. (a ver cuando tu madre nos deja ir a algún conciertazo). Con estas dos prendas tengo la sensación de que me he llevado lo mejor de Granada. No me gustaría olvidarme de Lola que tanto nos ha ayudado en estos últimos tiempos. Y sin ser menos, millones de gracias a mis grandes patrocinadores y fans, mis padres

Antonio Jurado Torres y Alicia Navarro Alonso y a mi hermano y amigo, Tony.

Resumen

El CO_2 es un gas de efecto invernadero importante y es una de las piezas fundamentales en el balance energético de la atmósfera terrestre Tierra y, en consecuencia, en su estructura térmica. Su emisión en 15 μm representa el mecanismo más importante de enfriamiento de la estratosfera, mesosfera y baja termosfera. La absorción de la luz del sol en las bandas del CO_2 cercanas al infrarrojo (2.7 y 4.3 μm) contribuyen significativamente al calentamiento atmosférico. Las transiciones ro-vibracionales de la molécula implicadas en estos procesos están en no equilibrio termodinámico local (no-ETL) en la media y alta atmósfera.

Desde el siglo pasado hasta el presente, se han realizado un gran número de estudios que muestran cómo la concentración del CO_2 está aumentando continuamente. El impacto de este incremento en el enfriamiento y el calentamiento de las distintas capas atmosféricas es evidente. Por ejemplo, la tendencia de la temperatura en la troposfera ha sido positiva mientras, en la mesosfera, ha sido negativa. Desde el principio de la industrialización, la humanidad ha ido emitiendo cada vez más cantidad de sustancias volátiles a la atmósfera cambiando su composición pero, todavía no tenemos respuestas claras sobre cuáles son sus efectos sobre los distintos cambios atmosféricos observados. Desde las primeras medidas de cohetes *in situ* en los setenta hasta las más recientes medidas de satélites de ocultación solar como ACE, o instrumentos de emisión en limbo como SABER, hemos aumentado considerablemente nuestro conocimiento sobre la abundancia del CO_2. Todos estos estudios indican que un conocimiento más preciso de la distribución espacio-temporal del CO_2 en la mesosfera y la termosfera es crucial para conocer mejor el balance energético de esta región, de su dinámica (que acopla ésta con las regiones inferiores), y la respuesta de la atmósfera a los cambios antropogénicos.

Vale la pena mencionar la gran dificultad de analizar las emisiones de las distintas bandas del CO_2 en el infrarrojo y de invertir su abundancia a partir de las medidas de dichas emisiones (principalmente provenientes de los complejos procesos del no-ETL). El conocimiento preciso de las poblaciones en no-ETL de los estados del CO_2 que emiten cerca de 4.3 μm ha limitado la precisión de las abundancias del CO_2 derivadas de medidas de emisión en limbo. Los espectros de MIPAS, con su resolución espectral sin precedentes, nos permiten conocer mucho mejor los distintos procesos de no-ETL del CO_2 y, por lo tanto, mejorar la inversión del CO_2 a partir de medidas de emisión tomadas en 4.3 μm.

Así, el **principal objetivo** de este trabajo es invertir las distribuciones globales

de la abundancia del CO_2 (razón de mezcla en volumen o vmr) a partir de los espectros infrarrojos de alta resolución de MIPAS en la mesosfera y termosfera con alta precisión. Esto requiere primero invertir los principales parámetros colisionales de no-ETL (incluyendo su dependencia con la temperatura) que afectan a las poblaciones de los niveles del CO_2 a partir de espectros de MIPAS en las regiones de 4.3 y 10 μm, lo que constituye el **segundo objetivo principal** de esta tesis. Dado que estos parámetros se necesitan en la inversión del CO_2, este objetivo se realizará en primer lugar y, después, invertimos la concentración relativa (razón de mezcla) del CO_2. Una vez que las abundancias del CO_2 están invertidas, analizamos la calidad de los datos y realizamos un minucioso análisis de errores, tanto de los parámetros colisionales como de las concentraciones de CO_2. Además, realizamos un estudio de validación comparando los datos del CO_2 de MIPAS con medidas independientes previas de ACE y SABER. Por otra parte, también analizamos las principales características de las distribuciones globales de CO_2 obtenidas en base a los procesos químicos y dinámicos reinantes en la alta atmósfera con la ayuda del modelo 3D 'Whole Atmosphere Community Climate Model' (WACCM).

En lo concerniente a la inversión de los principales parámetros colisionales, hemos desarrollado un esquema de inversión en no-ETL y lo hemos aplicado a los espectros de MIPAS en 10 y 4.3 μm. Los extensos intervalos, tanto en altura como en latitud, han permitido también obtener la dependencia con la temperatura de los parámetros colisionales en el rango de 130 a 250 K. Todos los parámetros se han invertido con una precisión mucho mejor que la obtenida hasta ahora. Los resultados más notables son:

- El $k_{vv,2}$ derivado aquí tiene una dependencia con la temperatura mayor que la utilizada hasta ahora, y es considerablemente mayor que valores previos por debajo de 300 K, abarcando factores entre 1 y 1.5 desde 300 K a 130 K. Este resultado es de suma importancia debido a que este parámetro controla las poblaciones de los niveles del CO_2 (10011) y (10012), y por consiguiente también controla la radiación atmosférica cerca de 4.3 y 2.7 μm de la alta mesosfera y baja termosfera.

- Los parámetros colisionales que controlan la transferencia V-V de niveles de alta energía, $k_{vv,3}$ y $k_{vv,4}$, han sido invertidos por primera vez. Hemos invertido una dependencia con la temperatura de $1/T^{0.6}$, un poco más fuerte que $1/\sqrt{T}$, con valores mayores que parámetros previos cerca en un 20% a temperaturas mesosféricas. No hemos encontrado diferencias significativas entre $k_{vv,3}$ y $k_{vv,4}$.

- Hemos invertido valores de k_{F1} y k_{F2} muy distintos a los utilizados anteriormente. k_{F1} es de 5 a 43 veces menor que lo usado hasta ahora. El rango de error de k_{F2} es considerablemente menor que los valores usados hasta ahora, que diferían en más de un factor 10. Esto conduce a cambios considerables en la radiación atmosférica de las dos principales bandas calientes que emiten en 4.3 μm, disminuyéndo su contribución en un 20-30% para condiciones de latitudes medias.

- El parámetro colisional k_{vt} derivado es un factor 0.4–0.7 menor que los utilizados

anteriormente. El parámetro colisional $k_{O(^1D)}$ derivado junto con k_{vt}, es muy similar a los valores publicados en la literatura reciente.

- Los nuevos parámetros tienen efectos muy importantes en las radiancias atmosféricas en las regiones espectrales de 10, 4.3 y 2.7 μm cuando se comparan con las obtenidos usando los parámetros colisionales típicos utilizados en trabajos previos. Su efecto es principalmente notorio en medidas efectuadas en el limbo (geometría tangencial), aunque también importante en medidas en nadir.

Hemos invertido las concentraciones del CO_2 a partir de los espectros de emisión de MIPAS en la región de 4.3 μm obtenidos en su modo de observación de alta atmósfera (UA) en condiciones diurnas (versión de los datos CO2_620.0). El CO_2 invertido cubre desde los 70 km hasta los 140 km. La inversión se ha realizado utilizando un esquema de inversión para no-ETL desarrollado en IAA/IMK. Esta inversión del CO_2 tiene la ventaja de usar otras medidas simultáneas de parámetros atmosféricos proporcionadas por MIPAS, como la temperatura cinética (hasta los $\sim$100 km) de la región del CO_2 de 15 μm, la temperatura termosférica del NO en 5.3 μm, las medidas de O_3 (hasta $\sim$100 km, que permiten una fuerte restricción en la concentración de $O(^1D)$ por debajo de $\sim$100 km), y un cálculo preciso del $O(^1D)$ por encima de $\sim$100 km. El modelo de no-ETL incorpora los parámetros colisionales vibración-vibración y vibración-traslación derivados de los espectros de MIPAS antes descritos.

La precisión de los perfiles de vmr del CO_2 varían con la altura abarcando desde un $\sim$1% por debajo de 90 km, hasta un 5% sobre los 120 km, siendo mayor que el 10% por encima de los 130 km. Los valores mayores a alturas más elevadas se deben a la menor relación señal/ruido del instrumento. La precisión varía muy poco con la latitud y la estación, con pequeños cambios debidos a las condiciones de iluminación solar.

Los perfiles de CO_2 invertidos tienen una resolución vertical de unos 5–7 km debajo de 120 km, y entre 10 y 20 km en 120-140 km.

Las características más importantes observadas en el CO_2 invertido se pueden resumir en:

- El CO_2 invertido muestra las características principales que se esperan y predicen por los modelos: la abrupta caída del vmr del CO_2 por encima de 80-90 km, causada por la predominancia de la difusión molecular, y el cambio estacional de la distribución latitudinal. Esta última se ve reflejada en mayores abundancias de CO_2 en el verano polar entre 70 km y $\sim$95 km, y menores en el invierno polar, ambas inducidas por las ramas ascendentes y descendentes de la circulación meridional, respectivamente. Por encima de $\sim$95 km, el CO_2 es más abundante en el invierno polar que en latitudes medias y que en el verano polar, debido a la inversión de la circulación meridional en esa región.

- Las distribuciones latitudinales típicas del solsticio y equinoccio se encuentran en los datos muy frecuentemente, durante casi 2.5 meses en cada estación, y la transición solsticio/equinoccio ocurre generalmente de manera rápida, tardando alrededor de un mes.

- Hemos encontrado un pequeño descenso en el vmr del CO_2 de MIPAS alrededor de los 80 km en el invierno polar. No estamos seguros de si es real, debido, por ejemplo, a un CO_2 remanente de la estación previa, o si se debe a un comportamiento inadecuado del esquema de inversión causado por una combinación de la elevada iluminación solar y las bajas temperaturas de la mesopausa polar.

Con el objetivo de validar el vmr del CO_2 de MIPAS, hemos realizado una comparación detallada con las medidas más recientes tomadas por los instrumentos ACE y SABER a bordo de satélites. Los resultados principales se pueden resumir en:

- En equinoccio, MIPAS muestra un buen acuerdo general con ACE. Las medidas del CO_2 de MIPAS son un poco mayores que las de ACE a 80-100 km. A mayores altitudes, las diferencias varían con la latitud, estando siempre dentro de un $\pm$20%.
- En equinoccio, el acuerdo de MIPAS con SABER es incluso mejor que con ACE, estando dentro de un 5% por debajo de 100 km. En la región de 100-120 km, MIPAS tiende a ser un $\sim$20% mayor en regiones polares y un $\sim$10-20% menor cerca de los trópicos.
- Durante el solsticio hay, en general, un muy buen acuerdo entre las medidas del CO_2 de los tres instrumentos. El acuerdo entre MIPAS y ACE es similar al de condiciones de equinoccio, pero hay una clara distinción en el verano polar, donde la caída del vmr del CO_2 con la altitud por encima de $\sim$100 km es más pronunciada en MIPAS que en ACE. Este comportamiento está también presente en los datos de SABER (en un acuerdo excelente con MIPAS) y es incluso más prominente (probablemente demasiado pronunciado) en las simulaciones de WACCM (ver debajo).
- El acuerdo de MIPAS con SABER es, en general, muy bueno. El CO_2 de MIPAS es, sin embargo, menor (un $\sim$5%, y probablemente demasiado bajo) sobre los 80 km en el verano polar. Por otro lado, SABER parece ser demasiado bajo en 60–80 km en el invierno polar en enero, y demasiado alto en 65-95 km en el invierno polar en febrero.
- WACCM sobreestima generalmente el CO_2 de los tres instrumentos por encima de $\sim$90 km en latitudes medias y en los trópicos durante el equinoccio. Aún así, lo contrario ocurre en el solsticio en latitudes medias y altas para el hemisferio de verano, cuando el CO_2 de WACCM disminuye más pronunciadamente que el CO_2 de los tres instrumentos a dichas altitudes.

Con objeto de obtener conclusiones a escala global también hemos comparado los promedios zonales y perfiles en bandas latitudinales para el promedio **anual** de 2010. Los resultados muestran que:

- Las medidas de MIPAS son generalmente mayores (un $\sim$5%) que las de ACE a 80-100 km y un 20-30% menores a 100-120 km.

- MIPAS y SABER concuerdan muy bien hasta los 100 km. En 100-120 km, también concuerdan bien cuando se promedia sobre todas latitudes, pero MIPAS es generalmente mayor que SABER excepto cerca del ecuador, donde MIPAS es menor. Esto es, en la región de 100-120 km y globalmente, el CO_2 de ACE es el mayor, SABER el menor y el de MIPAS está entre ambos.

- Las medidas de CO_2 de SABER entre 100 y 120 km son globalmente menores que los valores de MIPAS, ACE y WACCM.

De la comparación detallada del CO_2 de MIPAS con las simulaciones de WACCM extraemos las siguientes conclusiones:

- En términos generales WACCM reproduce los principales patrones de la distribución vertical del CO_2 y las variaciones estacionales y latitudinales observadas en los datos de MIPAS.

- Por debajo de aproximadamente 100 km la concordancia es muy buena, con diferencias menores que $\pm$10% (para $P_r = 2$) excepto para las condiciones de solsticio cerca de 90-100 km, donde pueden llegar hasta el 20%, siendo WACCM menor. En el polo de verano, cerca de 80 km, MIPAS es menor hasta un 5%, que podría señalar un problema en la inversión del CO_2 de MIPAS.

- A alturas de 100-140 km, el CO_2 de WACCM es generalmente mayor que el de MIPAS en equinoccio y a casi todas las latitudes con diferencias de 20-100%. En los hemisferios de verano, sin embargo, el CO_2 de WACCM es generalmente menor en 20-70%. En los hemisferios de invierno, el CO_2 de WACCM es también generalmente mayor que MIPAS aunque no tan grande como en equinoccio.

- In general, MIPAS sugiere un valor del número de Prandtl bajo, $P_r = 2$, esto es, una mayor difusión turbulenta, sobre todo por debajo de los 100 km. En la región de 100 a 120 km, sin embargo, las simulaciones de WACCM con P_r=4 contrarrestan las sobre-estimaciones de WACCM con P_r=2 y arrojan, globalmente, un mejor acuerdo con MIPAS.

- Las diferencias entre las distribuciones del CO_2 de MIPAS y WACCM nos plantean nuevas cuestiones aún por resolver. Así, por ejemplo, ¿pueden las distintas distribuciones latitudinales/estacionales del CO_2 de MIPAS/WACCM ser debidas a una variación latitudinal/estacional de la difusión turbulenta?; ¿es la circulación residual de la baja termosfera demasiado fuerte en WACCM?; ¿se deben dichas diferencias a una subestimación en WACCM de las pérdidas fotoquímicas del CO_2?

Finalmente, la concentración del CO_2 de MIPAS promediada entre 60°S y 60°N muestra por encima de $\sim$100 km una disminución de 2010 a 2011, que es consistente con la mayor actividad solar en 2011. Este resultado es también consistente con las medidas de SABER y las predicciones de WACCM. Las medidas de ACE muestran una disminución entre 95 y 110 km pero no entre 110 y 120 km.

En un futuro cercano, el trabajo más urgente sería completar la inversión del CO_2 para todo el periodo de medidas de MIPAS en el modo de atmósfera alta (UA): desde el 2005 hasta el final de la misión Envisat en 2012. Esta base de datos del CO_2 cubriría casi un ciclo solar completo y, por lo tanto, podría ser utilizado para estudiar la tendencia del CO_2. De particular importancia es comprobar si el CO_2 muestra una tendencia en la media y alta atmósfera mayor que la esperada del aumento antropogénico del CO_2 en la baja termosfera, como se ha observado recientemente en las medidas de ACE y SABER.

MIPAS tiene la ventaja de proveer simultáneamente y globalmente, además del CO_2, la abundancia del CO, y cubrir mayores alturas (hasta 140 km) que otros instrumentos anteriores. Este hecho permite estudiar en detalle la química del CO_x (CO y CO_2) y la dinámica de la termosfera media, una región prácticamente inexplorada.

Otro trabajo potencial de gran interés para llevarse a cabo en el futuro es el estudio del enfriamiento infrarrojo de la alta atmósfera. La comparación de las tasas de enfriamiento del CO_2 y del NO calculadas con datos de MIPAS y aquellas medidas por SABER serían de mucho valor. También, la comparación con simulaciones de WACCM serían de mucha utilidad, ya que MIPAS ofrece importantes restricciones con las medidas de la temperatura y las concentraciones (razón de mezcla) del CO, CO_2 y NO.

En la parte de desarrollo de algoritmos, sería muy útil adaptar este esquema de inversión para las inversiones del CO_2 a partir de los modos de observación de MIPAS de media atmósfera (MA, 20–100 km) y de 'noctilucent cloud' (NLC, 42-100 km).

Abstract

CO_2 is an important greenhouse gas and is is one of the master pieces in the energy balance of the Earth and, therefore, in its thermal structure. Its 15 μm emission represents the most important cooling mechanism of the stratosphere, mesosphere and lower thermosphere. Absorption of sunlight in the near-infrared CO_2 bands (2.7 and 4.3 μm) contribute significantly to the atmospheric heating. The involved ro-vibrational transitions of the molecule are in a non local thermodynamic equilibrium (non-LTE) in the middle and upper atmosphere.

There are a large number of studies performed from the last century to the present day, showing how the CO_2 concentration is being continually increased. The impact of this increase in the cooling and heating of the different atmospheric layers is clear. For instance, the trend of the temperature in the troposphere has been positive meanwhile, in the mesosphere, has been negative. Since the beginning of industrialization, mankind has been emitting increasing mounts of harmful volatile substances into the atmosphere changing its composition but, we still have to answer what are the effects of these emissions on the different observed atmospheric changes. From the first *in situ* rocket measurements in the seventies until the most recent satellite measurements from solar occultation instruments like ACE or limb emission instruments like SABER, we have significantly gained knowledge about the CO_2 abundance. All these studies indicate that a more precise knowledge of the spatial-temporal distribution of CO_2 in the mesosphere and thermosphere is crucial for a better understanding of the energy balance of this important region, of its dynamical coupling to the regions below, and for understanding its response to anthropogenic changes.

It is worth to mention the great difficulty of analyzing the infrared emissions from the different CO_2 bands and to derive its abundance from these emissions, primary coming from the complex non-LTE processes. The accurate knowledge of the non-LTE populations of the CO_2 states emitting near 4.3 μm has limited the accuracy of the CO_2 abundances derived from limb emission measurements. The MIPAS spectra, with its unprecedented high spectral resolution, allow to make significant advances in the knowledge of the different CO_2 non-LTE processes and hence, to improve the CO_2 retrieval from the emission measurements taken at 4.3 μm.

Thus, **the major aim of this work** is to retrieve global distributions of the CO_2 abundance (volume mixing ratio or vmr) from the MIPAS high resolution infrared spectra in the mesosphere and thermosphere with high accuracy. This requires first to retrieve the main non-LTE parameters (including their temperature dependence)

affecting the population of the CO_2 levels from the MIPAS spectra in the 4.3 and 10 μm regions, and constitutes the **second major objective** of this thesis. Because the collisional rates are required in the inversion of the non-LTE model, this objective is tackled first and later we perform the retrieval of the CO_2 vmr. Once the CO_2 abundances are retrieved, we analyze the quality of the data and perform a thorough error analysis. In addition, we perform a validation study by comparing the MIPAS CO_2 data with the previous independent measurements of ACE and SABER. Furthermore the main physical features of the retrieved global distribution of CO_2 are analyzed with the help of the 3D Whole Atmosphere Community Climate Model (WACCM).

Regarding the retrieval of the main collisional parameters, a non-LTE retrieval scheme, used in the previous analysis of the MIPAS non-LTE emission, has been applied to the MIPAS 10 and 4.3 μm spectra. The wide altitude and latitude ranges have allowed to retrieve also the temperature dependence of the rates in the range of 130 to 250 K. All of them were retrieved with a much better accuracy that known before. The most salient results are:

- The $k_{vv,2}$ derived here has a stronger temperature dependence than that used before. Also, it is significantly larger than previous values at temperatures below 300 K, ranging from a factor of 1 to 1.5 from 300 K to 130 K. This is a result of major importance since this rate controls the populations of the $CO_2(10011)$ and (10012) levels, and therefore the atmospheric radiation near 4.3 μm and 2.7 μm at upper mesospheric and lower thermospheric limb paths.

- The collisional rates for the V-V transfer from high energy levels, $k_{vv,3}$ and $k_{vv,4}$, have been retrieved here for the first time. We have retrieved a temperature dependence of $1/T^{0.6}$, slightly stronger than $1/\sqrt{T}$, with values larger than previous rates by about 20% at mesospheric temperatures. We have not found any significant difference between $k_{vv,3}$ and $k_{vv,4}$.

- We have retrieved values for the k_{F1} and k_{F2} rates very different from those previously used. k_{F1} is about 5 to 43 times smaller than reported before. The results for k_{F2} narrow significantly the uncertainty of previous estimates which show a spread of more than a magnitude. This leads to significant changes in the modeled atmospheric radiation of the two stronger 4.3 μm second hot bands, decreasing them by 20-30% for mid-latitude conditions.

- The derived k_{vt} collisional rate is smaller (factor of 0.4 – 0.7) than the values used before. The $k_{O(^1D)}$ collisional rate derived here jointly with k_{vt}, is very similar to the values published in recent literature.

- The new rates have very important effects on the atmospheric limb spectral radiances in the 10, 4.3 and 2.7 μm spectral regions when compared to typical collisional rates used in previous works.

The CO_2 vmrs have been retrieved using MIPAS daytime limb emission spectra from the 4.3 μm region in its upper atmosphere (UA) mode (data version CO2_-620.0). The retrieved CO_2 covers from 70 km up to about 140 km. The inversion

has been performed by using a non-LTE retrieval scheme developed at IAA/IMK. It takes the advantage of other (simultaneous) MIPAS measurements of atmospheric parameters, as the kinetic temperature (up to ∼100 km) from the CO_2 15 μm region, the thermospheric temperature from the NO 5.3 μm, the O_3 measurements (up to ∼100 km), which allows a strong constrain of the $O(^1D)$ concentration below ∼100 km, and an accurate calculation of $O(^1D)$ above ∼100 km. The non-LTE model incorporates the accurate vibrational-vibrational and vibrational-translational collisional rates derived from the MIPAS spectra and described above.

The accuracy of the retrieved CO_2 vmr profiles varies with altitude ranging from ∼1% below 90 km, to 5% around 120 km and larger than 10% above 130 km. The larger values at higher altitudes are due to the lower signal-to-noise ratio. There are very little latitudinal and seasonal variations, which are driven by the solar illumination conditions.

The retrieved CO_2 profiles have a vertical resolution of about 5–7 km below 120 km and between 10 and 20 km at 120-140 km.

The most important features observed on the retrieved CO_2 can be summarized in:

- The retrieved CO_2 shows the major general features expected and predicted by models: the abrupt decline of the CO_2 vmr above 80-90 km, caused by the predominance of the molecular diffusion, and the seasonal change of the latitudinal distribution. The latter is reflected by higher CO_2 abundances in polar summer from 70 km up to ∼95 km, and lower CO_2 vmr in the polar winter, both induced by the ascending and descending branches of the meridional circulation, respectively. Above ∼95 km, CO_2 is more abundant in the polar winter than at mid-latitudes and polar summer regions, caused by the reversal of the meridional circulation in that altitude region.

- The typical solstice and equinox latitudinal distributions are found in the data periods of about 2.5 months in each hemisphere, and the solstice/equinox seasonal transition usually takes place rather quickly, in about one month.

- We have found a small decrease in MIPAS CO_2 vmr at ∼80 km at polar summer latitudes. We are not sure if this is real, e.g., remnant CO_2 air from previous season, or a retrieval artifact caused by a combination of high solar zenith angles and low temperatures.

With the aim of validating the retrieved MIPAS CO_2 vmr, a detailed comparison has been performed with the most recent satellite measurements taken by ACE and SABER. The major results can be summarized in:

- In equinox, MIPAS shows an overall good agreement with ACE. MIPAS CO_2 measurements are slightly larger than those of ACE at 80-100 km. At higher altitudes, the differences varies with latitude, being comprised always within ±20%.

- Also in equinox, the agreement of MIPAS with SABER is even better than with ACE, being within 5% below 100 km. In the 100-120 km region, MIPAS tends to be a ∼20% larger in polar regions and a ∼10-20% smaller near the tropics.

- During solstice there is, in general, a very good agreement between the CO_2 measurements of the three instruments. The agreement of MIPAS with ACE is similar as for equinox conditions, but there is a clear distinction in the polar summer, where the decay of the CO_2 vmr with altitude above ∼100 km is steeper in MIPAS than in ACE. This behavior is also present in SABER data (in excellent agreement with MIPAS) and is it is even more prominent (probably too steep) in WACCM simulations (see below).

- The agreement of MIPAS with SABER is in general very good. MIPAS CO_2 is, however, smaller (∼5%, and probably too low) around 80 km in the polar summer. SABER, on the other hand, seems to be too low at 60–80 km in the polar winter in January, and too high at 65-95 km in the polar winter in February.

- WACCM generally overestimates the CO_2 of the three instruments above ∼90 km at mid- and tropical latitudes during equinox. However, the opposite occurs during solstice at mid and high latitudes of the summer hemisphere, when WACCM CO_2 decreases more pronouncedly than the CO_2 of the three instruments at those altitudes.

In order to draw more general conclusions we have also compared zonal mean cross-section and latitudinal band profiles for the annual mean of 2010. The results showed that:

- MIPAS measurements are generally larger (∼5%) than ACE ones at 80-100 km and 20-30% smaller at 100-120 km.

- MIPAS and SABER agree very well up to 100 km. At 100-120 km, they also agree very well when averaging over all latitudes, but MIPAS is generally larger than SABER except near the equator where MIPAS is lower. That is, in the 100-120 km region, globally, ACE is the largest, SABER the smallest and MIPAS is in between.

- SABER CO_2 measurements between 100 and 120 km are globally smaller than MIPAS, ACE and WACCM.

From the detailed comparison of WACCM simulations with MIPAS observations we draw the following conclusions:

- Overall, WACCM reproduces the major CO_2 vertical distribution patterns and the seasonal and latitudinal variations observed in MIPAS data.

- Below about 100 km the agreement is very good, with differences smaller than $\pm$10% (for $P_r = 2$) except for solstice conditions near 90-100 km where they can be as large as 20%, being WACCM smaller. In the polar summer, near 80 km, MIPAS is smaller by up to 5%, which might point to a problem in the MIPAS CO_2 retrieval.

- At 100-140 km altitudes, WACCM CO_2 is generally larger than MIPAS at equinox at almost all latitudes with differences of 20-100%. In the summer hemispheres, however, WACCM CO_2 is generally lower in 20-70%. In the winter hemispheres WACCM CO_2 is also generally larger than MIPAS although not as large as in equinox.

- In general, MIPAS favors more a value of $P_r = 2$ (larger eddy diffusion), principally below around 100 km. In the 100-120 km region and above, however, WACCM simulations with P_r=4 somehow mitigates the WACCM P_r=2 overestimations and give an overall better agreement with MIPAS.

- The WACCM/MIPAS comparison give rise to new questions. For example, can the different MIPAS/WACCM CO_2 seasonal/latitudinal distributions be explained by a seasonal/latitudinal dependence of the eddy diffusion?; or is the lower thermosphere residual circulation in WACCM too strong?; or are they caused by an underestimation of the photochemical losses of CO_2 in WACCM?

Finally, the MIPAS global (60°S–60°N) CO_2 vmr above $\sim$100 km showed a decrease in 2011 with respect to 2010, which is consistent with the larger solar activity of 2011. This result is also consistent with SABER measurements and WACCM predictions. ACE measurements show also a decrease from 95 km up to 110 km but not between 110 and 120 km.

In a near future, the most urgent work will be to complete the CO_2 retrieval from the whole MIPAS optimized resolution upper atmosphere (UA) mode data set, from 2005 to the end of the Envisat mission in 2012. This CO_2 database will then cover nearly a complete solar cycle and, therefore, could be used to perform an inter-annual variability study. Of particular importance is to check if it shows also a trend of CO_2 in the middle and upper atmosphere larger than that expected from the CO_2 anthropogenic increase in the lower thermosphere, as has been recently reported from the ACE and SABER measurements.

The MIPAS CO_2 measurements have the advantages of providing simultaneously and globally, besides CO_2, the CO abundance, and covering higher altitudes, up to 140 km. These would allow to study in detail the CO_x chemistry and the dynamics of the middle thermosphere, practically an unexplored region.

Other potential work to be carried out in the future is the study of the upper atmosphere infrared cooling. Comparison of the CO_2 and NO cooling rates calculated with the MIPAS products and those measured by SABER would be very valuable. Also, comparison with WACCM simulations would be very useful, since MIPAS offers important constraints as the temperature, and the CO, CO_2 and NO relative concentrations.

On the algorithm development side, it would be very useful to develop the “setups" for the retrievals of CO_2 from the middle atmosphere (MA) and Noctilucent Cloud (NLC) MIPAS observations modes.

Contents

List of Figures

List of Tables

Chapter 1

Introduction

Abstract

The purpose of this chapter is to give an overview of the basic facts about the Earth's atmosphere and the role played by CO_2. We begin presenting a glimpse of the history of the atmosphere and the effects of the CO_2 concentration in the evolution of global temperature along the 20^{th} century. Next we highlight the scientific interest in the atmosphere and the different sounding techniques. Following that we describe the basic features of the Earth's atmosphere: its vertical structure, composition and the energy balance. Regarding CO_2, first we give a general description of its spectra and energy levels. In the same section we explain the role of CO_2 in the cooling and heating of the mesosphere and lower thermosphere. Later we look back in order to summarize the CO_2 measurements taken during the last 40 years. Finally, we describe the motivation and objectives of this thesis.

1.1. Scope of this Work

The human being had lived without being aware of its impact on the Earth environment. This fact have become more evident with the development of industrial activities and the exponential growth of the population. Thus, we are now considering how human actions have gradually become the main driver of global environmental change[1]. Since the beginning of industrialization, mankind has been emitting increasing amounts of harmful volatile substances into the atmosphere changing its composition but we still have to answer what are the effects of these emissions on the different observed atmospheric changes.

Carbon dioxide, CO_2, one of the master pieces in this jigsaw, is a well known greenhouse gas[2]. There are also other greenhouse gases in the atmosphere like H_2O (water vapour) or CH_4 (methane). They warms the atmosphere by absorbing infrared emission critically affecting its energy balance. Thus the thermal structure and the atmospheric dynamics are shaped by them. The increasing release of this kind of

[1] Steffen et al. (2015) classifies the climate change as a planetary boundary of increasing risk for the Earth System.

[2] Those gases with infrared activity that warms the atmosphere contributing to the greenhouse effect.

gases along 20^{th} century is considered as one of the most important reasons of global warming (IPCC report, 2014). The Keeling curve, based on continuous measurements taken at the Mauna Loa Observatory in Hawaii, shows an increase in atmospheric CO_2 of ∼25% since 1958 (Figure 1.1 upper panel). NOAA report (2015) shows the increment on the temperature of the oceans and the surface in the last 130 years (Figure 1.1 lower panel). On the other hand, in the middle and upper atmosphere, the radiative effects of greenhouse gases generate a cooling effect (Rishbeth and Roble, 1992; Akmaev, 2002). Focusing on temperature trends at these altitudes, Beig et al. (2003) analysed data from several studies in the 50 to 100 km region. In the lower and middle mesosphere a negative trend of 2-3 K per decade was found. A slightly larger cooling trend appears at low and mid-latitudes. In summary, there are several studies that shows how the increase of greenhouse gases, as CO_2, changes the terrestrial thermal structure.

1.2. Earth's atmosphere basics

1.2.1. History

Let us start giving a brief review of the history of the Earth's atmosphere. It was originated about 4500 millions years ago from the outgassing of volcanism, principally hydrogen, water vapour, carbon dioxide and sulphur dioxide. About 4000 million years ago, the cooling of the planet led to the condensation of water vapour causing the origin of the oceans. Meanwhile the photodissociation of water molecules by solar UV radiation gave rise to hydrogen and oxygen. But the oxygen did not begin to rise significantly until about 3000 million years ago caused by photosynthesis of the first biological activities. This fact provoked a simultaneous decrease in CO_2 and, over a period of millions of years, the creation of the ozone layer. About 1500 million years ago the oxygen level in the atmosphere was stabilized and the atmosphere, roughly acquired the chemical composition of present day. Approximately, it is composed by 78% of N_2, 21% of O_2 and 1% of minor gases like CO_2, H_2O, O_3, CH_4, and Ar. The gravitational attraction concentrates about half of the whole atmospheric mass in the first 5.5 km. The 99% of its mass is located within the first 15 km.

The atmosphere is also being affected by natural phenomena like the 11 years solar activity cycle. The amount of radiation and energetic particles reaching the upper atmosphere are continuously changing. This upper region is heated and expanded at solar maximum and cooled and compressed at the solar minimum. In addition, changes of the solar wind and its interaction with the magnetosphere impact the state of the upper atmosphere.

1.2.2. Vertical Structure

Along the 20^{th} century different classifications of vertical layers of the atmosphere were proposed attending to different phenomena and/or concepts. The first were based on studies of the atmospheric conductivity by analyzing charged particles, the

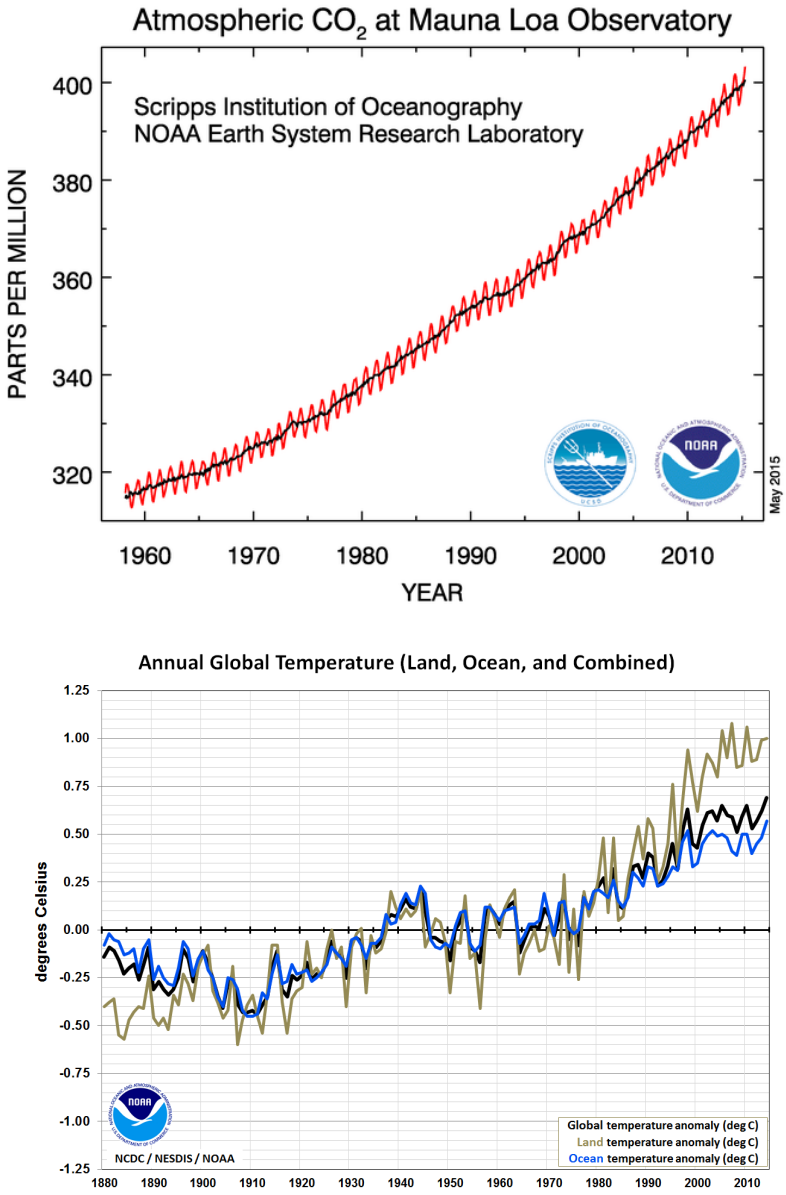

Figure 1.1: Upper panel: CO_2 concentration (ppmv) time series from 1958 to 2015 taken at Mauna Loa, Hawaii.(data website: http://www.esrl.noaa.gov/gmd/ccgg/trends/). Lower panel: Temperature time series for land-only (green), ocean-only (blue) and land-and-ocean (black) (data website: http://www.ncdc.noaa.gov/sotc/summary-info/global/201412).

electrons and ions. Using this criterium we find a non-conducting atmosphere called **neutral atmosphere** and a conducting atmosphere known as the **ionosphere**. The latter is subdivided in three main layers: i) the D layer from 50 km up to 90-100 km; ii) the E layer, located at 100-150 km and; iii) the F layer, situated at 150-300 km (divided again in F1 and F2 layers).

Another classification of the vertical structure attends to its composition and mixture. In this way the effect of molecular diffusion determines two regions: the **homosphere**, where the mean molecular weight varies little with altitude (from lower altitudes up to 90-100 km) and above, the **heterosphere**, where the mean molecular weight varies with altitude (Brasseur and Solomon, 2005). In the heterosphere, molecular diffusion dominates and the different constituents are layered depending on its molecular weight.

Since temperature is a key parameter to understand the major part of the physical processes in the Earth's atmosphere, the most interesting classification of the vertical structure is based on it (particularly on temperature inversions). Each inversion determines a transition layer between atmospheric regions of a well-defined temperature gradient (Figure 1.2). To better understand this vertical temperature structure, we need to briefly introduce some basic facts of atmospheric dynamics and energy balance.

Approximately 30% of the solar radiation flux is reflected into space, 21% is absorbed by the atmosphere and 49% is absorbed by the Earth's surface (Figure 1.3). The atmosphere is nearly transparent in the visible and hence the visible radiation reach the ground. This incoming energy heats the surface which re-emits it back to the atmosphere as infrared radiation or releases it as latent heat to the lower atmospheric layers. Thus, the lower atmosphere is warmer near the surface and cooler at higher altitudes. Hence there is a negative vertical temperature gradient. Taking into account the hydrostatic equilibrium, there is also a negative vertical pressure gradient. The gradients produce a convective motion with a constant decrease of temperature with altitude of $\sim$8 K/km (Houghton, 1986). This region dominated by convective motions is known as the **troposphere** and is where the weather phenomena take place. Because of its nature, the tropospheric extension vary depending on the incoming solar flux. In this way at lower latitudes, the tropospheric convective instability exist up to about 18 km due to the larger solar irradiation. At higher latitudes (polar region), with lower solar irradiance, the upper tropospheric limit extends up to about 8 km. This layer contains around 85% of the total atmospheric mass.

Above the troposphere we find a boundary layer where the first temperature inversion takes place. This layer is called the tropopause and is where the temperature gradient changes its sign from negative to positive. The layer above the tropopause is characterized by a positive temperature gradient due to the absorption of solar UV photons by O_3 in the Hartley ($\sim$200-300 nm) and Huggins ($\sim$310-340 nm) bands. This region is called the **stratosphere** and is where the air layers are quite stable. This fact inhibits the vertical convective motions favoring the horizontal ones. The stratosphere extends from about 10-15 km up to about 50 km. In this layer resides the ozone layer, where the UV radiation, harmful for life, is absorbed.

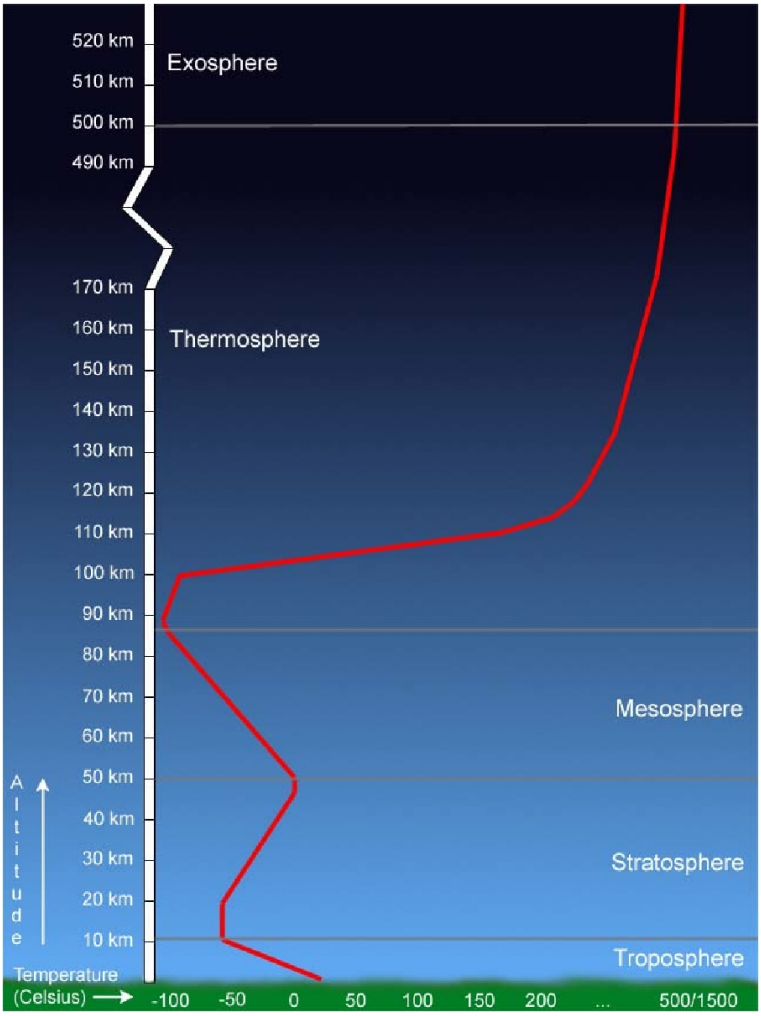

Figure 1.2: Vertical structure of atmosphere based on temperature inversions

At 50 km we find another transition layer, the stratopause. At these altitudes the temperature gradient become negative again (second inversion point). This occurs because the cooling is greater than the heating. The negative temperature gradient region, known as the **mesosphere**, extends from about 50 km up to about 87 km in the summer pole and up to approximately 100 km in the winter pole. The latter region is called the mesopause, the third inversion point and the coolest region of the atmosphere.

The next positive temperature gradient region is called the **thermosphere** and spans from 80-100 km up to 500-600 km. Here, the absorption of extreme UV solar photons and the interaction with energetic particles cause ionization and photodissociation of O, O_2 and N_2 (these effects are responsible of the temperature increase). During nighttime, the thermospheric temperature is about 400 K (Eddy, 2009). At daytime, the solar heating expands the thermosphere and, depending on the solar activity, the atmospheric temperature can reach values between 700 K to 2000 K (Eddy, 2009). In the region between 200 km to 500-600 km, the air density is so small that

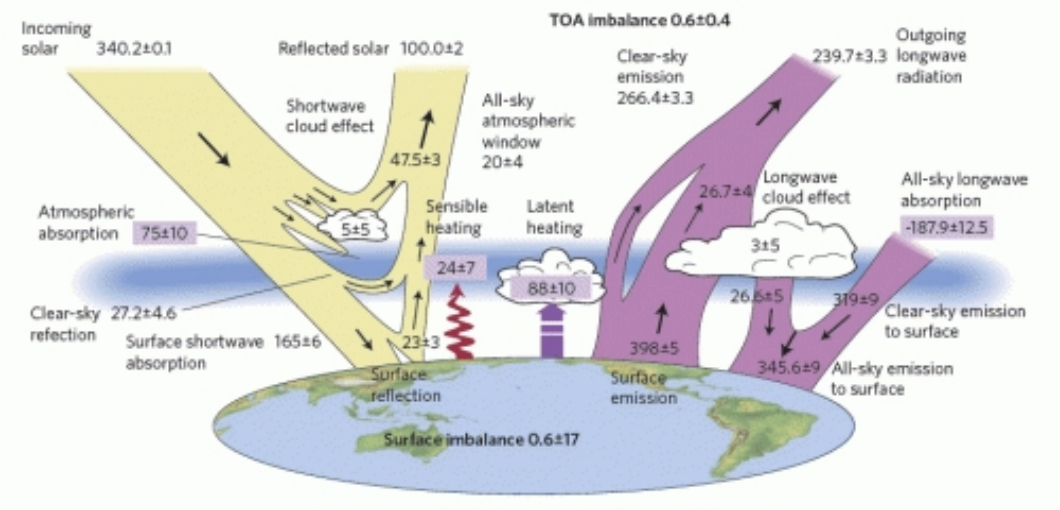

Figure 1.3: The global annual mean energy budget for approximately the 2000-2010 period (Stephens et al., 2012). The fluxes units are $W \cdot m^{-2}$. Solar fluxes are in yellow and infrared fluxes in pink.

there is a balance between the incoming solar radiation and the photons escaping to space. Thus the temperature becomes effectively constant.

The next boundary layer is the thermopause which defines the limit where the solar interaction with the atmosphere ends. Beyond this point, the particles (mostly H and He) move with large mean free paths. This last region is called the **exosphere** and conforms the Earth's last frontier to outer space.

It is also very frequent to find in the atmospheric research literature terms as low, middle and upper atmosphere. Although these terms are not clearly defined, they are often referred to the troposphere (low), to the stratosphere and sometimes to the stratosphere and mesosphere (middle) and to the mesosphere or mesosphere + thermosphere or thermosphere (upper).

1.2.3. Composition

The chemical composition of the atmosphere has been varying hand in hand with the evolution of the planet. Different factors, as geology or solar radiation, has been shaping the evolution of the atmosphere until today. Nowadays the two main compounds are molecular nitrogen and oxygen (N_2 and O_2) in a ratio of 78% and 21% respectively (Brasseur and Solomon, 2005). The remaining gases like CO_2, O_3 or CH_4 are below 1% (Figure 1.4). This composition is modeled mainly by the reaction between its compounds, by interaction with solar radiation (photoionization and photoabsorption) and by atmospheric dynamics.

The main gases (N_2 and O_2) have a relatively constant abundance until the photo-disassociation becomes important above approximately 90 km (Brasseur and Solomon,

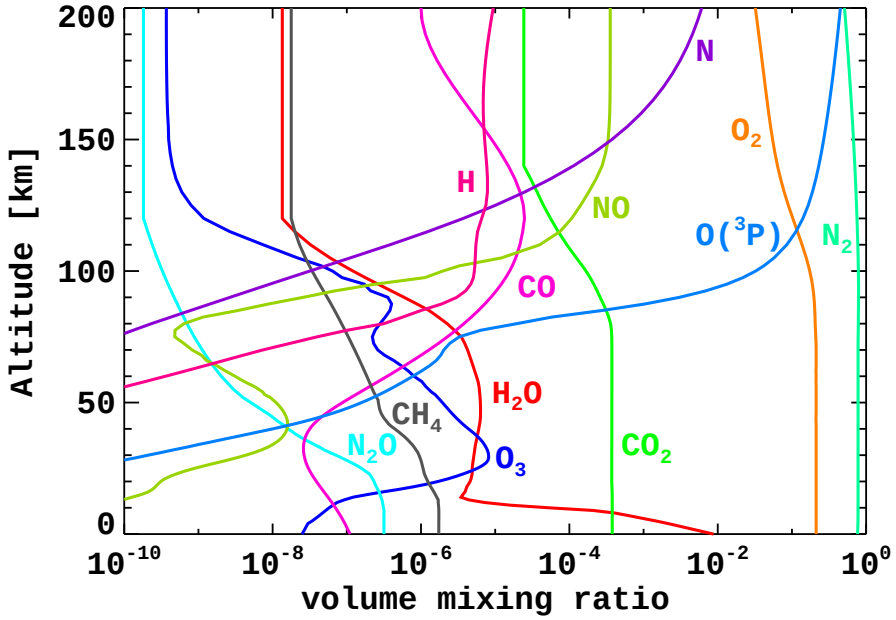

Figure 1.4: Volume mixing ratios of main components of Earth's atmosphere given for usual daytime and mid-latitude conditions from López-Puertas and Taylor (2001).

2005).

Water vapour (H_2O) concentrations are high near Earth's surface because of the proximity of the oceans. At higher altitudes, H_2O, decreases up to the hydropause (Milz et al., 2005). Above, it remains roughly constant up to 70-80 km, where the photodissociation induces another decrease (Brasseur and Solomon, 2005). Water vapour is very important for the study of the radiative balance of the atmosphere because of its strong infrared emissions.

Carbon dioxide (CO_2) has a constant volume mixing ratio up to 70-80 km where it begins to decrease because of molecular diffusion and photodissociation (Garcia et al., 2014). As mentioned before, it is a key gas for understanding the radiative balance and global warming due to its infrared emissions. Its spectroscopic molecular properties are described in detail in the next section.

Other gases like CH_4 and N_2O are abundant at the surface and their concentrations decrease with altitude due to oxidation and photodissociation. Carbon monoxide (CO) is an important molecule for the tropospheric chemistry. It is produced in the stratosphere and the mesosphere (by the oxidation of methane), and in the lower thermosphere (by CO_2 photolysis) (Brasseur and Solomon, 2005; Garcia et al., 2014).

Another important source of greenhouse gases are the human activities. As we commented earlier, the industrial development has been increasing their concentrations over the last century.

Although the percentage of atmospheric ozone (O_3) is less than 1%, it plays an important role in the energy budget, the chemistry and composition of the atmosphere,

particularly in the stratosphere and upper mesosphere (Brasseur and Solomon, 2005). The absorption of ultraviolet solar radiation by O_3 in the stratosphere acts as shield for life on the surface and produces the high temperatures of the stratosphere. Ozone also produces an important cooling that affects critically to the thermal structure and hence to the radiative balance. The ozone abundance below 30 km is variable due to atmospheric dynamics. In this region it is produced by photodissociation of O_2 and recombination with atomic oxygen (Chapman, 1930). The O_3 density maximum is located at approximately 25 km. At higher altitudes it decreases due to photodissociation. At 80 km, O_3 increases again because of the presence of atomic oxygen.

NO and NO_2 (known as NO_x) are very important constituents, contributing to ozone destruction due to their catalytic cycle (Brasseur and Solomon, 2005). Nitric oxide (NO) plays also an important role in the thermospheric cooling, particularly during auroral events (Kockarts, 1980). In addition, NO is an important source of ionization in the ionosphere, particularly in the D and E regions (Barth et al., 2009).

1.2.4. Energy Balance

The Earth's energy balance consists in the difference of the energy fluxes between the incoming solar radiation and the outgoing (mainly terrestrial) radiation. The atmosphere, the clouds or the surface reflects, absorbs or re-emits the energy incoming from the Sun or the Earth's atmosphere itself (see Fig. 1.3).

The incoming solar radiation (Figure 1.5a) has an approximate spectral shape of a black body at ∼6000 K. Its major spectral contribution extends from 200-250 nm to 1300-1700 nm and peaks at ∼500 nm. As mentioned earlier, the major part of the incoming radiation reaching the surface is within the visible part of the spectrum. On a global average, 30% of the incoming energy is reflected back to space (albedo). Another 21% is absorbed by the atmosphere and the Earth's surface absorbs the remaining 49% of the total solar radiation. The surface re-emits the absorbed solar radiation as infrared radiation and also by transferring latent heat to the atmosphere. A fraction of the infrared emission is radiated to outer space but the major part is absorbed in the atmosphere by molecules with strong vibration-rotational bands, the greenhouse gases (water vapour, CO_2, O_3, CH_4 and N_2O). The total outgoing infrared radiation (Fig. 1.5a) can be described as a black body at an approximate temperature of 250 K.

In the thermosphere, O, N_2 and O_2 absorb the photons with wavelengths shorter than 102.5 nm producing photodissociation and ionization. At larger wavelengths (UV), O_2 absorbs in the Schumann-Runge continuum (100-175 nm), in the Schumann-Runge bands (175-205 nm) and more weakly in the Herzberg continuum (Figs. 1.5b, and 1.5c) (Mlynczak and Marshall, 1996; López-Puertas and Taylor, 2001; Brasseur and Solomon, 2005).

The thermosphere can be also heated by quenching of $O(^1D)$ (through N_2) and O_2 and by collisions between ambient electrons and ions and neutrals. Regarding

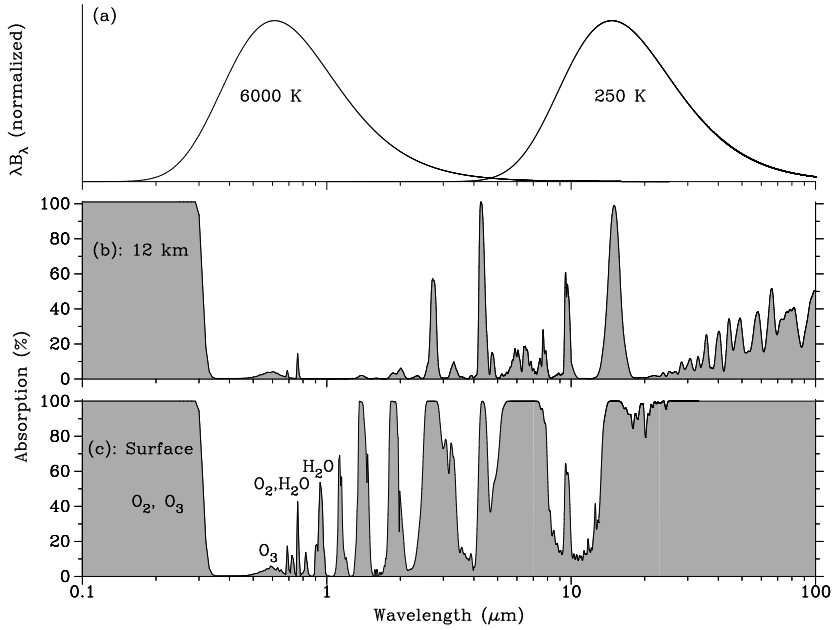

Figure 1.5: Atmospheric absorption: (a) The blackbody emission curves for 6000 K (symbolizing the Sun emission) and 250 K (symbolizing the terrestrial emission) normalized to the energy emitted. (b) Absorption spectra of the atmosphere for 12 km to its upper part. (c) Atmospheric absorption spectra at the surface. (López-Puertas and Taylor, 2001)

the mesospheric radiative heating, it is produced by the absorption in the O_3 Hartley bands (24.2-31.0 nm) and O(^{1}D) quenching following the O_3 and O_2 photolysis.

With respect to cooling mechanisms, emissions of NO at 5.3 μm (most important around 120-200 km), of CO_2 at 15 μm (further explained below), and of O at 6.3 μm are the most important in the thermosphere (López-Puertas and Taylor, 2001; Mlynczak et al., 2010, 2014). In the mesosphere, the 15 μm CO_2 emission is the most important and, to a lesser extend, 9.6 μm emissions from O_3 (López-Puertas and Taylor, 2001; Brasseur and Solomon, 2005). Above 140 km, it is important to take into account the cooling by downward molecular heat conduction.

There are other important heating mechanisms like that produced by the exothermic chemical reactions (chemical heating) (Mlynczak and Solomon, 1993; Smith et al., 2015) (see, also tables of neutral and ion-chemistry involving nitrogen and oxygen in Roble (1995)), and Joule dissipation[3] of ionospheric currents (upper atmosphere). Dynamic effects contribute also to the heating of the mesosphere and lower thermosphere by dissipation of tides, planetary and gravity waves originated in the lower atmosphere or by adiabatic compressions due to vertical motions. For example, the tides propagating from below generate pressure gradients that force the gas of the thermosphere into motion following negative temperature gradients (Fuller-Rowell, 1995). A very good overview of the energetics of the middle and upper atmosphere can be found in the book edited by Siskind et al. (2000).

[3] Joule heating is caused by frictions associated to collisions between neutral and ions due to the presence of electric fields (see Rees, 1989).

1.3. Carbon Dioxide

Historically, carbon dioxide was identified in 1757 by the Scottish physician and chemist Joseph Black (he called it *fixed air*). The molecule is formed by two carbon atoms and one oxygen atom linked by 116.3 pm symmetric covalent bonds (Figure 1.6). CO_2 is a colorless and odorless gas with a molar mass of 44.01 g mol^{-1}, a density of 1.977 kg m^{-3} (at 1 atm and 0°C), a melting point of 216.6 K, a sublimation point at 194.7K (at 1 atm) and with no permanent dipolar moment. At present, it forms the 0.0596%[4] of the total mass of atmospheric air.

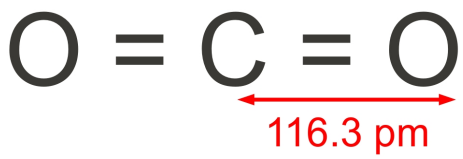

Figure 1.6: CO_2 structural formula showing the covalent bonds length.

The abundance of *natural* CO_2 is controlled by the carbon cycle: A biogeochemical cycle by which carbon is exchanged among the biosphere, pedosphere, geosphere, hydrosphere, and atmosphere of the Earth. The *anthropogenic* CO_2 comes mainly from the use of fossil fuels in transportations and from the activity of different industries like iron and steel production or cement manufacturing.

1.3.1. Spectroscopy and energy levels

There are three kinds of internal energy transitions: rotational, vibrational and electronic transitions. The ro-vibrational and pure rotational transitions establish the near and middle infrared spectrum. The electronic ones, with highest energy values, are located in the visible and in the ultraviolet. We consider here only the infrared emissions. The CO_2 does not have a pure rotational spectrum because it does not have a permanent dipolar moment.

Let us briefly summarize the theory of the rotational energy spectra. Since CO_2 is a linear molecule, it can be modeled using the *rigid rotator* model. This model assumes that the molecule is composed of two different masses linked by a rigid bond of distance r[5]. The moment of inertia is $I = mr^2$, where $m = m_1m_2/(m_1+m_2)$ is the *reduced mass*. Taking into account the solution for the time-independent Shrödinger equation for this system:

$$\Psi_{J,M} = \sqrt{\frac{(2J+1)(J-|M|)!}{4\pi(J+|M|)!}} e^{im\phi} P_J^{|M|}(cos\theta) \tag{1.1}$$

where θ and ϕ are the polar and azimuthal angles of the spherical coordinates,

[4] Source: NOAA Earth System Research Laboratory

[5] Since the coordinate r, is taken to be constant (r_0), the partial derivatives with respect to r are zero. Thus, r does not appear as a variable in the wave functions.

$P_J^{|M|}(cos\theta)$ are the associated Legendre polynomials, and J and M are quantum numbers representing the total angular momentum and its component along the polar axis, respectively. Thus, the energies of the different rotational transitions are:

$$E_J = BJ(J+1) \qquad J = 0, 1, 2, ... \tag{1.2}$$

where $B = \hbar/(2I)$ is the rotational constant ($\hbar$ is the reduced Planck constant). The symmetry of the wave functions $\Psi_{J,M}$ characterize the selection rule for transitions $J' - J''$ between two levels. Given the selection rule $\Delta J = J' - J'' = \pm 1$, the energy involved in a transition is:

$$E_{J+1} - E_J = 2B(J+1). \tag{1.3}$$

In the *non-rigid rotator* model the bond forces are assumed to depend linearly on the distance. The energy of the system is:

$$E_J = BJ(J+1) - DJ^2(J+1)^2, \tag{1.4}$$

where D is the *centrifugal distortion constant* ($\hbar^2/\sqrt{2k}mr_0^3$ with k as the force constant).

For the vibrational levels, to describe the lower excitation transitions, we can use the *Born-Oppenheimer approximation*[6]. The interaction energy, V(r), can be expressed in the form of a MacLauren series taking the zero of potential energy at $r = r_0$ (where $dV/dr = 0$ and V(0)=0), thus:

$$V(r - r_0) = \frac{1}{2}\left[\frac{d^2V}{dr^2}\right]_{r=r_0} (r - r_0)^2 + higher\ order\ terms. \tag{1.5}$$

For the transitions between lower energy states, higher order terms of the equation can be truncated. In this case, taking the first term of the equation, we are approximating the potential energy curve by a parabolic function. This is known as the *harmonic oscillator* approximation. With the Schrödinger equation we obtain the quantized energy expression by:

$$E = \left(v + \frac{1}{2}\right)\nu_v \tag{1.6}$$

where v is the quantum number associated with a given vibrational level and $\nu_v = \hbar\sqrt{\frac{k}{m}}$ is called the *fundamental frequency*. Since the selection rule is $\Delta v = \pm 1$, the energy involved in a transition is:

$$E' - E'' = \left[\left(v' + \frac{1}{2}\right) - \left(v'' + \frac{1}{2}\right)\right]\nu_v = \Delta v\,\nu_v = \nu_v \tag{1.7}$$

[6]The *Born-Oppenheimer approximation* allows the use of wave function of the molecule as two wave functions (electronic and molecular), $\Psi_{total} = \Psi_{electr} \times \Psi_{molec}$.

For higher excitation transitions, we cannot use neither the *harmonic oscillator* nor the *Born-Oppenheimer* approximations. Thus we will use the *anharmonic oscillator* model. The energy can be calculated with the (Equation 1.5), just taking the two first terms

$$E = \left(v + \frac{1}{2}\right)\nu_v - \left(v + \frac{1}{2}\right)^2 \chi\nu_v \tag{1.8}$$

where χ is the *anharmonicity constant*. The selection rule is $\Delta v = \pm 1, \pm 2$.

In the case of polyatomic molecules, the vibration modes can be treated as the sum of normal vibrations. For CO_2 there are three fundamental vibrational modes: v_1, v_2 and v_3 (Figure 1.7). The first is the symmetric stretch (v_1) and neither has absorption nor emission in infrared because there is no dipolar momentum variation associated with its motion. The other two are:

- *Bending stretch mode* v_2: Selection rule $\Delta J = 0, \pm 1$. It is degenerated twice because the movement can happen in the two perpendicular directions.
- *Asymmetric stretch mode* v_3: Selection rule $\Delta J = \pm 1$. Known as the parallel mode, its dipolar moment does vary along the internuclear axis.

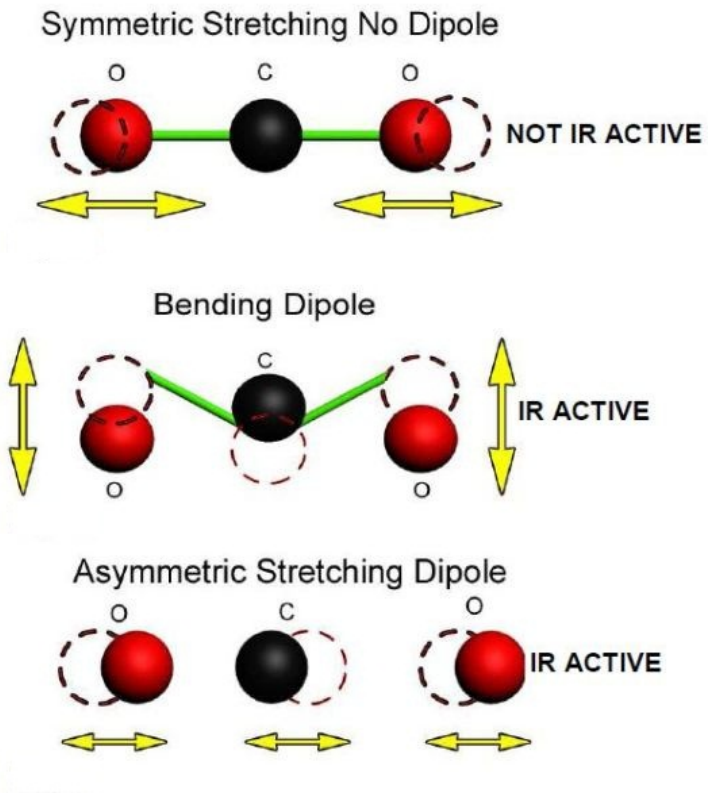

Figure 1.7: CO_2 fundamental vibrational levels.

The vibration-rotation transitions of these modes are the most important ones for the description of the CO_2 spectrum in the IR and NIR. For the asymmetric stretch mode (v_3), if v_2=0, due to the selection rule $\Delta J = \pm 1$, the v_3 spectra will show two branches with the following line center frequencies:

$$\text{R branch: } \nu(J) = \nu_0 + 2B(J+1) \quad \text{for } \Delta J = +1 \tag{1.9}$$

$$\text{P branch: } \nu(J) = \nu_0 - 2BJ \quad \text{for } \Delta J = -1. \tag{1.10}$$

On the other hand, the bands of the v_2 bending mode (selection rule $\Delta J = -1, 0, 1$) have P, Q, and R branches.

The transitions between the ground vibrational state and the first vibrationally excited modes ($v_i = 1$) are called *fundamental* transitions or bands and are, by far, the strongest. The bands with lower vibrational state different from the ground state are often known as *hot* bands. The reason is because they occur more profusely in hot gases. For CO_2, hot bands are of special significance in atmospheric regions where non-LTE processes populate the higher vibrational levels (see Fig.1.8). The transitions occurring between the excited vibrationally states with quantum number larger than one and the ground state are usually called *overtones*. Furthermore, the bands that take place between vibrational levels that differ in more than one vibrational quanta are called *combinational* bands.

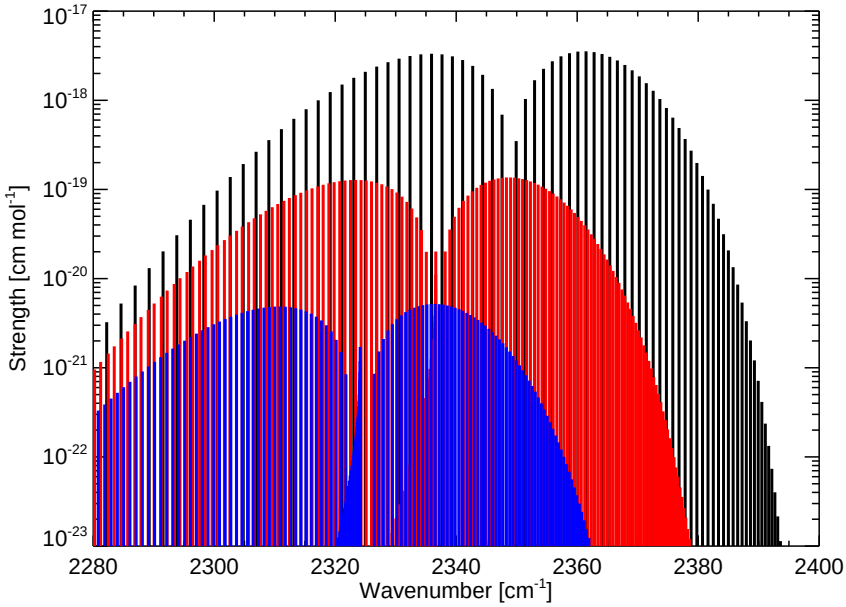

Figure 1.8: CO_2 transition lines from the fundamental $00^01 \rightarrow 00^00$ (black), first hot $01^11 \rightarrow 01^10$ (red) and second hot $02^21 \rightarrow 02^20$ (blue) bands in the 4.3 μm region. Data from HITRAN 2004 database (Rothman et al., 2005).

1.3.2. CO_2 Cooling and Heating

The most important cooling mechanism of the stratosphere, mesosphere and lower thermosphere is the CO_2 15 μm emission (López-Puertas and Taylor, 2001; López-Puertas and Funke, 2015). The respective cooling rate depends on two very variable parameters: the kinetic temperature and the CO_2 abundance. Hence, we must consider a range of global and seasonal conditions. In addition, it depends also on the rate coefficient for the collisional deactivation of $CO_2(0,1^1,0)$ by atomic oxygen (k_{CO_2-O}) and on the $O(^3P)$ number density.

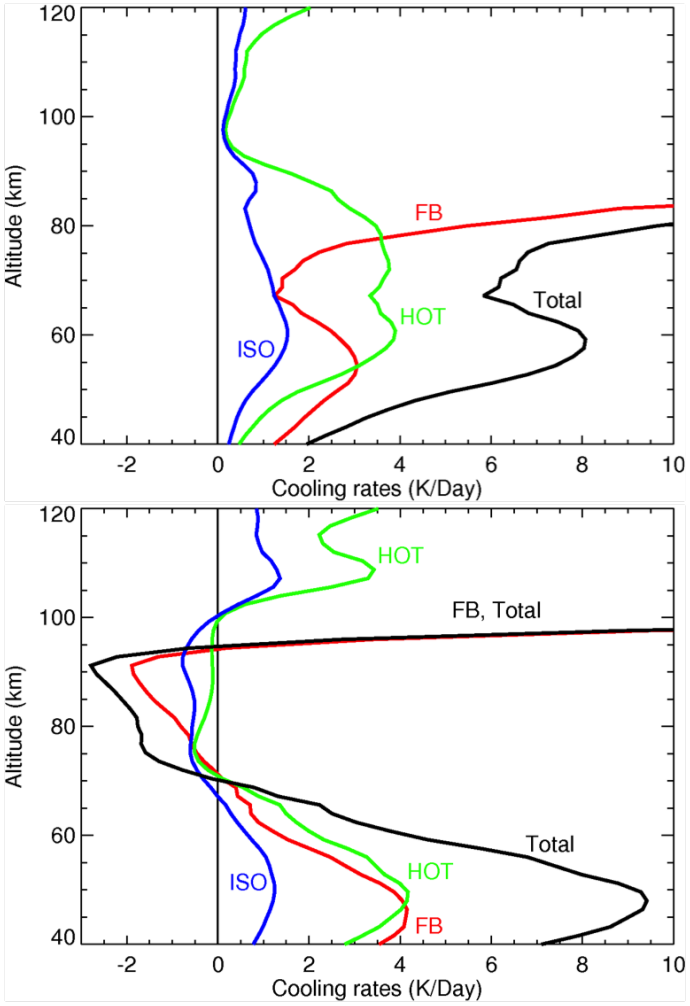

Figure 1.9: Upper panel: 15 μm bands cooling rate in polar winter. Lower panel: 15 μm bands cooling rate in polar summer. The profiles represent calculated cooling for the fundamental (red line), the 3 first hot bands and the 7 second hot bands for the 626 isotope (green line), and the fundamental bands of the minor isotopes 636, 628 and 627 (blue line) (López-Puertas and Taylor, 2001).

Analyzing the contributions of the CO_2 bands to the cooling in the stratosphere and the mesosphere, we find that it is driven by the optically thin isotopic and hot

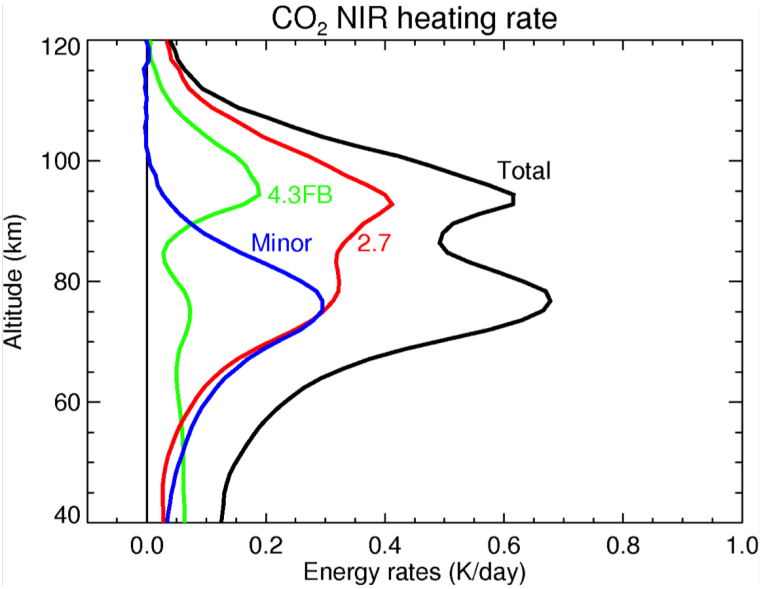

Figure 1.10: Heating rates profiles integrated over one day in winter conditions (30°N) for the energy initially absorbed in the CO_2 2.7 μm band (red line), 4.3 μm fundamental band of the 626 isotope (green line) and the 2.0 and 4.3 μm isotopic and hot bands (blue line) (López-Puertas and Taylor, 2001).

bands (principally the first hot) rather than the strong fundamental band. In these regions the maximum cooling ranges from –2 to 10 K/day and depends on temperature (López-Puertas and Taylor, 2001). In the lower thermosphere the cooling is driven by the fundamental band with a significant contribution from the first hot band. One of the most interesting feature is the large increase of the cooling rate in summer conditions compared to winter (Figure 1.9).

The near-infrared CO_2 bands contribute significantly to the atmospheric heating of the mesosphere. This heating is mainly induced by solar absorption in the bands around 2.7 and 4.3 μm during daytime (López-Puertas and Taylor, 2001; Fomichev et al., 2004). Most of the energy absorbed by the atmospheric CO_2 in these bands is re-emitted back to space and only a little fraction causes a net heating[7]. Even though it is still significant. The overall CO_2 heating averaged over a full day, adding the 2.0, 2.7 and 4.3 μm contributions, shows a double-peak structure with values close to 0.5 K/day (Figure 1.10). The upper one, around 90 km, is due to the 4.3 μm fundamental band and 2.7 μm bands and the lower one, around 80 km, is due to the 2.7 μm bands, the weaker 2.0 μm bands and the hot and isotopic 4.3 μm bands.

[7]Net heating: The difference between the amount of incoming solar radiation and the amount heat radiated by the Earth back to space.

1.3.3. Measurements of CO_2 Abundances in the Middle and Upper Atmosphere

CO_2 is well mixed in the atmosphere with an almost constant mixing ratio up to the upper mesosphere. As we mentioned before, this "constant" mixing ratio with altitude is being increased by anthropogenic emissions (Figure 1.1 upper panel). Above this region, i.e. above 80 km, it begins to decrease because of diffusive separation, UV photodissociation and by chemical reaction with O^+. In the following we review the CO_2 measurements in the middle and upper atmosphere.

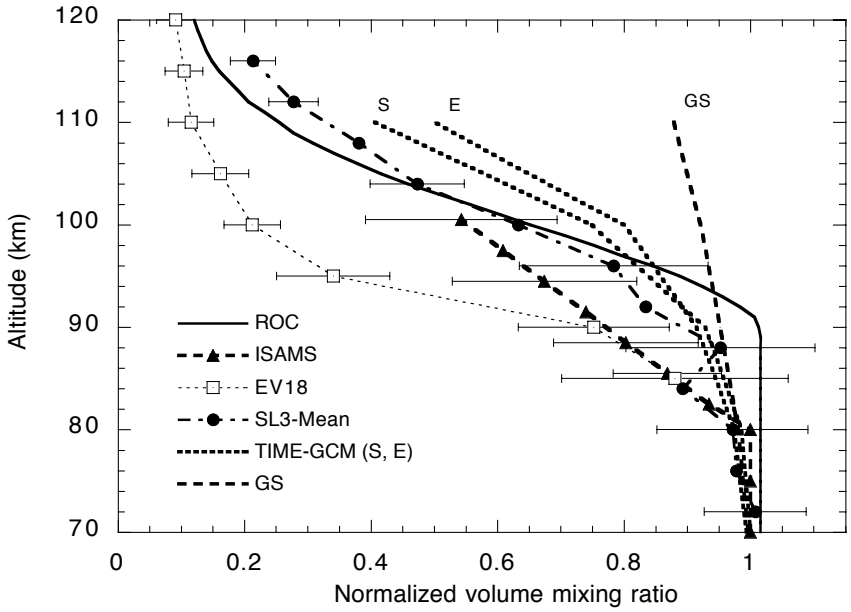

Figure 1.11: CO_2 vertical profiles comparison from different observations by rocket-borne mass spectometers (ROC), ISAMS, Grille (EV-18) and ATMOS (SL3-Mean). Vertical profiles from two models are shown: NCAR TIME-GCM (E for equinox and S for solstice conditions) and the Garcia-Solomon two-dimensional model (López-Puertas et al., 2000). The profiles are normalized to their respective values in the lower region.

Despite its importance in the middle atmospheric infrared energy balance, CO_2 has been scarcely measured, there. CO_2 was first measured in the upper atmosphere by *in situ* measurements carried out by rocket-borne mass spectrometers (Figure 1.11). The first time it was measured was at nighttime from 120 to 140 km (Offermann and Grossmann, 1973). Different *in situ* measurements were performed during the seventies and in the early eighties by Trinks and Fricke (1978) and Trinks et al. (1978) during the Aladdin 74 campaign and by Offermann et al. (1981). The CO_2 vmr profiles obtained at that time were approximately constant (335 ± 50 ppmv) up to about 90 km where it starts dropping rapidly with altitude. The errors of these measurements where of the order of 20-30% (López-Puertas et al., 2000). Beyond this epoch two different methods (techniques) were used to measure CO_2: solar occultation and infrared emission.

The Grille spectrometer aboard Spacelab 1 used solar occultation taking infrared limb spectra at sunrise and sunset in 1983. CO_2 abundances were measured in the mesosphere and lower thermosphere in four occultations. The results showed a lower CO_2 in the 90-110 km region (Figure 1.11) (Vercheval et al., 1994; Girard et al., 1988). The Atmospheric Trace Molecule Spectroscopy (ATMOS) on Spacelab 3 obtained IR occultation spectra in the troposphere-lower thermosphere region in 1985. In addition the kinetic temperature and pressure profiles were obtained. CO_2 mixing ratios were retrieved by Rinsland et al. (1992) from 70 km up to 116 km, with an average 320 ppmv in 70-90 km, and a decrease around 90 km in the southern hemisphere and around 100 km in the northern hemisphere (Figure 1.11) (López-Puertas et al., 2000).

Regarding CO_2 4.3 μm emissions it is worth mentioning some constrains affecting its measurements. There are uncertainties in the modelling of the non-LTE populations of the emitting levels. As explained in Chapter 5, for 4.3 μm it is important to take into account collisional processes like the $CO_2(\nu_3)$ with $N_2(1)$ or the excitation of N_2 through $O(^1D)$. The 15 μm emission is strongly affected by kinetic temperature, pressure, atomic oxygen and collisions of $CO_2(010)$ with $O(^3P)$ above 100 km. The Spectral Infrared Rocket Experiment (SPIRE) measured limb radiance from 15 and 4.3 μm bands at tangent heights from 50 up to 150 km. SPIRE had a radiometric calibration error of $\pm$ 25% (Stair et al., 1985). The CO_2 from SPIRE 15 μm measurements are consistent with other rocket experiments and with the lower CO_2 values encountered at 80-110 km. For example, Wintersteiner et al. (1992) analysed the 15 μm measurements using pressure, kinetic temperature and atomic oxygen from MSIS-86 and adjusting the collisional parameter k_{CO_2-O}. They find the best overall fit using a value for this rate of 5×10^{-12} cm^3 s^{-1} at 300 K and the CO_2 rocket measurements. The depletion of CO_2 vmr in the 80-110 km region fits the SPIRE observations for a k_{CO_2-O} value of 6×10^{-12} cm^3 s^{-1} at 300 K (20% higher).

Nebel et al. (1994) studied the SPIRE 4.3 μm daytime measurements that found that they are consistent with the CO_2 rocket measurements up to 110 km. Above this altitude up to 130 km, the measurements are clearly underestimated by a factor of 2. As we mentioned before, measurements are constrained by uncertainties in the non-LTE excitation processes.

The Spectroscopic Infrared Structure Signatures Investigation (SISSI), measured 15 and 4.3 μm zenith radiances in four rocket experiments (between 1990 and 1991) during twilight. This instrument measured simultaneously kinetic temperature, pressure and $O(^3P)$ number density although with considerable errors ($\pm$ 10% for kinetic temperature and $\pm$ 30% for atomic oxygen). The radiance measurements themselves presented errors of $\pm$ 30% (Vollmann and Grossmann, 1997). They fit the 4.3 μm radiance below 100 km according to previous rocket measurements by multiplying it by 2.5 and by 4 above 105 km. Regarding 15 μm, the radiance was also explained but have to decrease the k_{CO_2-O} rate to $\sim 1.5 \times 10^{-12}$ cm^3 s^{-1} at 300 K (notably lower than that required in SPIRE). The increase in the 4.3 μm radiances above 105 km[8] may be caused by an unidentified non-LTE source (e.g., $NO^+(\nu_3)$). The 15 μm band

[8] Nebel et al. (1994) and López-Puertas et al. (1998b) found similar increases in SPIRE and ISAMS measurements, respectively.

emission would also be consistent with rocket measurements if k_{CO_2-O} values are between $3-5\times10^{-12}$ cm^3 s^{-1} at 300 K (more consistent also with SPIRE results).

The first global measurements of CO_2 4.3 μm were performed by the Stratospheric and Mesospheric Sounder (SAMS) on Nimbus 7 between 1978 and 1981 by using the pressure modulation technique. López-Puertas and Taylor (1989) and López-Puertas et al. (1998b) analysed daytime data using simultaneous measurements of kinetic temperature and pressure up to 60 km and using he CIRA 72 climatology above that altitude. The best radiance agreement gave a CO_2 vmr profile notably lower than rocket measurements in the 80-95 km region (López-Puertas et al., 2000).

The Improved Stratospheric and Mesospheric Sounder (ISAMS) aboard Upper Atmosphere Research Satellite (UARS) carried out 4.6 μm global measurements from around 10 km up to 105 km during six months. The main ISAMS improvements with respect to SAMS are: i) more sensitivity to the second CO_2 isotope (636) emissions; ii) better signal to noise ratio ($\sim$ 1 up to 120 km) and; iii) simultaneous measurements of temperature and pressure up to 80 km. López-Puertas et al. (1998b) and Zaragoza et al. (2000) performed a detailed analysis of the 4.3 μm daytime emission. These studies showed that the CO_2 vmr profile does not change (within ISAMS uncertainties) with latitude or season up to 100 km during daytime (Figure 1.11).

The Cryogenic Infrared Spectrometers and Telescopes for the Atmosphere (CRISTA), a limb scanning instrument on board two space shuttle missions, measured the 4.3 μm emissions with global distribution in 1994 and 1997. Kaufmann et al. (2002) retrieved CO_2 number densities by analyzing daytime radiance from 60 km up to 130 km. Considering the optical thickness of 4.3 μm radiances between 75 km and 110 km and the excitation of N_2 through O(^{1}D) uncertainties, the systematic error of the retrieved CO_2 was within the range of 10-20%. The CO_2 falloff of CRISTA, where diffusive separation starts, is situated at 70-80 km, lower than from rocket measurements, ATMOS and ISAMS measurements (Figure 1.12). Above this altitude, the mean CRISTA CO_2 vmr results are lower than SAMS and ISAMS in the 80-100 km region and than ATMOS CO_2 between 80 km and 120 km.

The Fourier Transform Spectrometer on the Canadian Atmospheric Chemistry Experiment (ACE-FTS) aboard SCISAT-1 satellite measured by solar occultation the CO_2 in mesosphere and lower thermosphere. ACE CO_2 vmr shows the falloff at 70-80 km with higher values than CRISTA above 70 km, slightly higher values than those of ISAMS in 80-100 km and lower than rocket measurements (Beagley et al., 2010).

More recently, the Sounding of the Atmosphere using Broadband Emission Radiometry (SABER) on board the NASA Thermosphere Ionosphere Energetics and Dynamics (TIMED) satellite has been measuring CO_2 4.3 and 15 μm limb emission radiances in the mesosphere and lower mesosphere. Rezac et al. (2015) presented a simultaneous T_k/CO_2 non-LTE retrieval and its application to the whole "13-plus" years of SABER daytime measurements. The total uncertainty in the unconstrained CO_2 vmr retrieval takes the following values: 35% at 70 km, 12% at 90 km, 32% at 110 km (where the O(^1D) sensitivity maximum is) and 22% at 130 km. The global mean of the CO_2 vmr profiles seems to be well mixed up to 80-85 km. Considering equinox conditions, the CO_2 vmr depart from a well mixed value from 65 to 70 km at high and mid-latitudes.

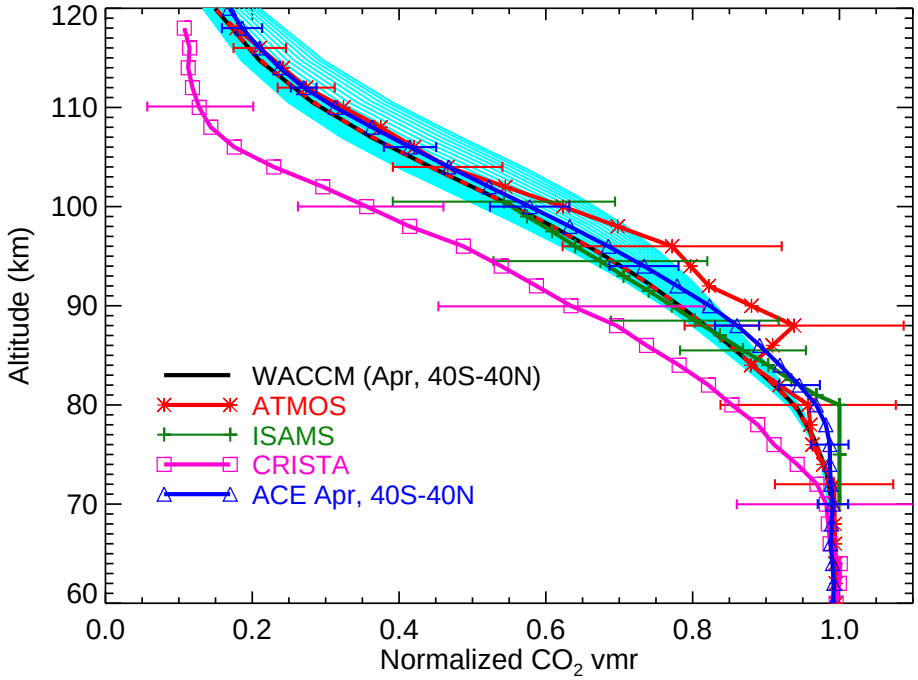

Figure 1.12: Comparison of observational vertical profiles from ATMOS, ISAMS, CRISTA and ACE and modeled vertical profiles from SD-WACCM (setting the Prandtl number in 4). SD-WACCM data is shown as a black line (mean of all models profiles) and as a blue shaded area (profiles in the latitude range of 40°S-40°N). The data have been normalized to the mixing ratio at 60 km (Garcia et al., 2014).

Regarding summer hemisphere solstice, the CO_2 vmr is well mixed up to 87-90 km. A detailed comparison of the ACE and SABER CO_2 measurements with those retrieved in this work are presented in Chapter6.

Although not studied in this work, we give, for completeness, a brief summary of the most recent measurements of CO_2 vmr in the lower atmosphere. Foucher et al. (2011) presented 5 years (2004-2008) of monthly mean CO_2 vertical profiles from ACE-FTS measurements in the 5-25 km altitude range. These vertical profiles are averaged over 10° latitude bands for Northern mid-latitudes. These measurements show a 'significant' variation with altitude ($\sim$0.1 ppmv/km) and a notable seasonal variability of 5 ppmv (1.2%)[9]. Comparisons with in-situ aircraft measurements from the CONTRAIL (Sawa et al., 2008), CARIBIC (Schuck et al., 2009) and SPURT (Gurk et al., 2008) campaigns show that ACE-FTS concentrations are consistent with them in the Northern Hemisphere mid-latitudes. However the stratospheric seasonal cycle amplitude seems to be slightly overestimated.

[9]Note these changes are much smaller than the variations at higher altitudes described above.

1.4. Motivation and Objectives

Let us begin describing the state of the art on our current understanding of the role of CO_2 in the middle atmosphere. As mentioned before, CO_2 is a key element for understanding the Earth's energy balance, playing an essential role in the cooling and heating of all atmospheric regions and therefore on its temperature structure. Another important fact is the anthropogenic increase of CO_2, registered by the Keeling curve, which has a major impact on the atmosphere, including the upper atmosphere. Thus, the CO_2 cooling fingerprint has been observed as a negative trend of mesospheric temperature affecting its thermal structure (Beig et al., 2003) and the drop of the ionospheric F2-layer (Rishbeth, 1990).

Along that line, Emmert et al. (2010) suggested that during the 2008 solar minimum, the increase of CO_2 may have partially produced a low thermospheric density peak, induced by a faster CO_2 cooling of the mesosphere and lower thermosphere (see Fig. 1.13).

Beagley et al. (2010) proposed a new CO_2 loss process (sequestration in dust) around the mesopause as a possible explanation for the overestimation of the CMAM 3D simulations of the ACE CO_2 measurements. However, Garcia et al. (2014) have shown more recently that the ACE CO_2 distributions can be explained by the WACCM model without the need of invoking a new CO_2 loss mechanism.

Emmert et al. (2012) have studied the trends of CO_x ($CO_x = CO + CO_2$) in the mesosphere and lower thermosphere in the ACE CO and CO_2 observations. They have found a notably large growth rate of CO_2 in this region, larger than expected from the CO_2 increase by human activities in the troposphere (Figure 1.14). In the altitude range of 90-105 km, the ACE-FTS trends are 5-10 ppm per decade larger than predicted by the NCAR global mean model (Figure 1.15).

Yue et al. (2015) have very recently analyzed the trends of CO_2 in the mesosphere and lower mesosphere using SABER measurements from 2002 to 2014. They have found a trend of $\sim$5% per decade at $\sim$80 km and below. Above 80 km the trend, larger in the northern hemisphere mesopause, can be as large a $\sim$12% per decade at 110 km, thus confirming the previous finding of Emmert et al. (2012).

These studies suggest that a more precise knowledge of the spatial-temporal distribution of CO_2 in the mesosphere and thermosphere is needed in order to understand better the energy balance of this region, its dynamical coupling to the regions below, and its response to anthropogenic changes.

Historically, global CO_2 measurements in the mesosphere and lower thermosphere have been limited. In the last few years, instruments like ACE (Beagley et al., 2010), SABER (Brown et al., 2006) and MIPAS (Fischer et al., 2008) have contributed to provide a global view of these regions. Compared to ACE, an occultation instrument, MIPAS has the advantage of providing global latitudinal (pole-to-pole) and seasonal measurements. Compared to SABER, a wide band limb emission radiometer, MIPAS measured high resolution limb emission spectra and in a wide spectral coverage. Thus, MIPAS is able to discriminate the contributions of the many CO_2 bands that

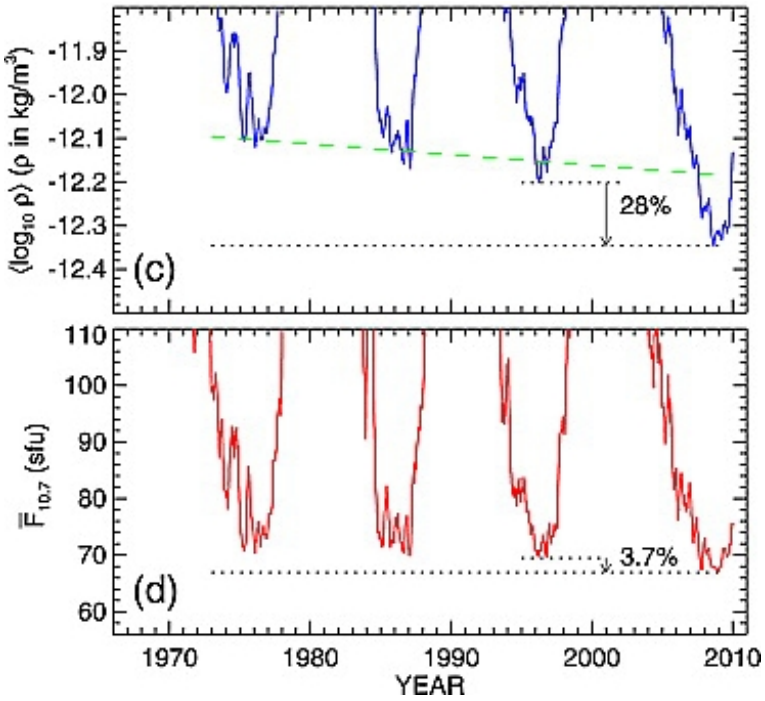

Figure 1.13: Upper panel: 81-day global average logarithmic densities at a fiducial altitude of 400 km. Green dashed line indicates the solar minimum. Black dotted represents the overall density minimum. Lower panel: 81-day global average solar flux at 10.7 cm normalized to 1 AU ($\bar{F}_{10.7}$). The units are 10^{-22} Wu m^{-2} Hz^{-1}. Dotted horizontal lines expresses the difference between the two last solar cycle minimums. The seasonal and geomagnetic activity effects are removed from the data (after Emmert et al., 2010).

gives rise to the 4.3 μm atmospheric emission; which results in achieving a more accurate knowledge of the CO_2 non-LTE processes (see below). Also, the wide spectral range of MIPAS allow us to have simultaneous measurements of other atmospheric parameters, as the kinetic temperature (up to ∼100 km) from the CO_2 15 μm region, the thermospheric temperature from the NO 5.3 μm, and the O_3 measurements (up to ∼100 km, that provides very accurate $O(^1D)$ concentrations). The latter two facts lead both to a very accurate retrieval of the CO_2 abundance from MIPAS spectra. Additionally, since MIPAS has a high sensitivity, it is able to measure the CO_2 atmospheric emission in a wide altitude range, up to ∼140 km.

Thus, the major aim of this work is to retrieve global distributions of CO_2 vmr profiles from MIPAS high resolution infrared spectra in the mesosphere and thermosphere (60-140 km).

The lack of knowledge of the non-LTE populations of the CO_2 states emitting near 4.3 μm is a limitation for the accurate retrieval of CO_2 abundances from this emission, particularly from limb measurements (López-Puertas and Taylor, 2001; Kaufmann et al., 2002; Rezac et al., 2015). Non-LTE emissions are also affecting the temperature sounding from nadir 4.3 μm spectral measurements. Thus, DeSouza-Machado et al. (2007) found a brightness temperature 10 K larger if they do not include non-LTE in the simulations of the Atmospheric InfraRed Sounder (AIRS) daytime radiances. Chen

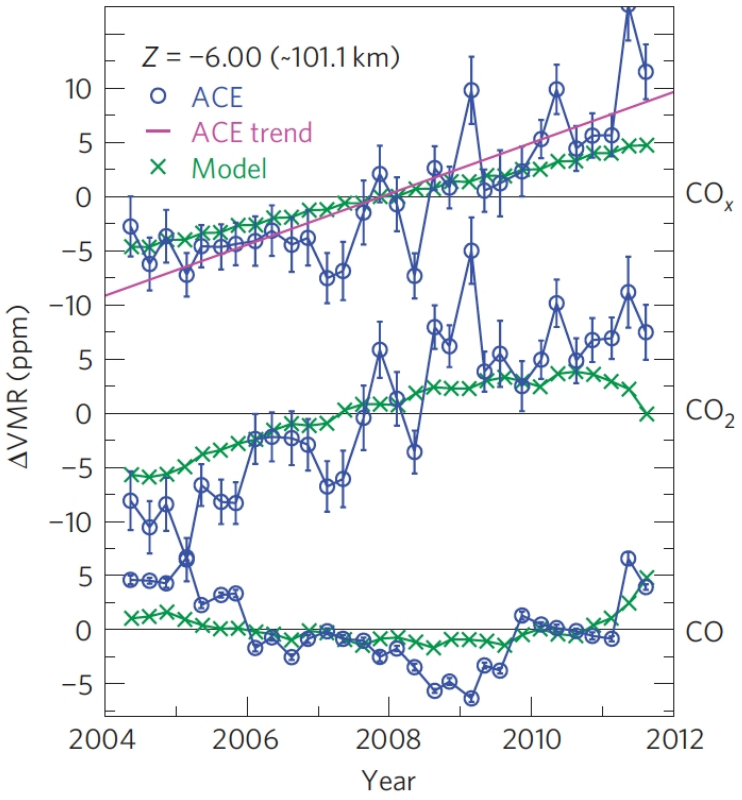

Figure 1.14: Residuals volume mixing ratios of CO_x (top), CO_2 (middle) and CO (bottom). Results are shown after removal of seasonal-latitudinal effects at ∼101 km. ACE-FTS measurements are represented by blue circles and NCAR global mean model by green crosses. The linear trend is calculated from a linear least-squares fit of the ACE-FTS CO_x residuals (pink line). Errors bars are the estimated 1σ uncertainty of the mean. (after Emmert et al., 2012)

et al. (2013) and Mengtao and Xiaolei (2015) have found similar results when analyzing the Infrared Atmospheric Sounding Interferometer (IASI) and the Cross-track Infrared Sounder (CrIS) measurements, respectively.

MIPAS spectra, however, with its high spectral resolution, offer an unprecedented information on the non-LTE emissions of the different CO_2 4.3 μm bands (fundamental, hot and isotopic) and on the processes populating its originating energy levels. Thus, the second major objective of this work is to derive new non-LTE collisional energy transfer rates between the different levels of CO_2 emitting near 10, 4.3 and 2.7 μm and with N_2. This information is necessary for performing the CO_2 retrieval, therefore this objective was tackled first in thesis. The first direct consequence of this objective is that MIPAS CO_2 abundances can be more accurate that those obtained before from previous limb emission instruments. Further, this non-LTE information is not only applicable to MIPAS but can also be used in other limb emission experiments like SABER, or the nadir emission instruments mentioned above.

The analysis of the 4.3 μm emission spectra is very difficult because of the many lines of the many bands with so different optical thicknesses that conforms them.

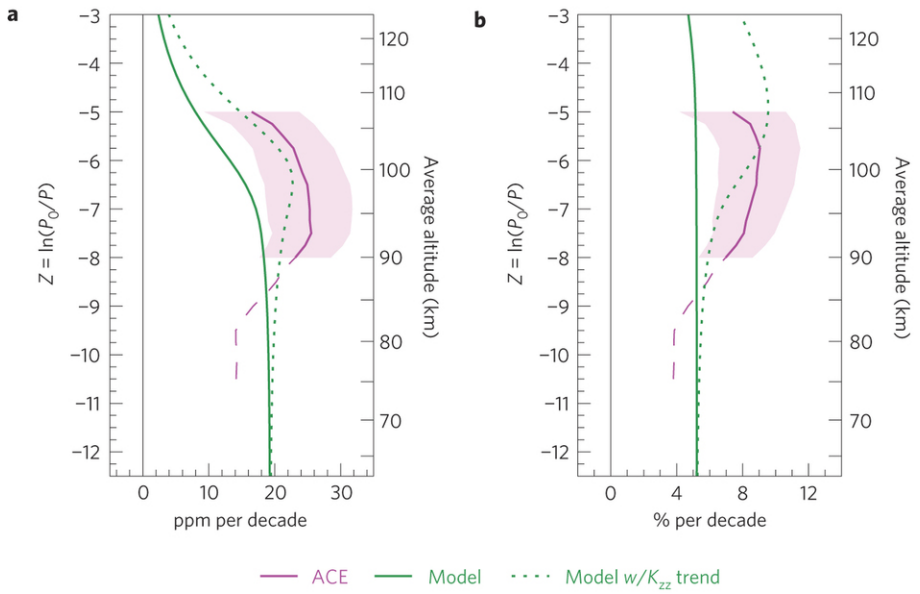

Figure 1.15: a) Absolute trends and b) relative trends of CO_x obtained by dividing the absolute trends by the profiles shown in Emmert et al. (2012) (Figure 4.1 therein). Pink lines represents ACE-FTS measurements, the solid green lines the NCAR global mean model and the dotted green, the global mean model with a 15% per decade eddy diffusion trend added.

Thus, to accomplish the second objective we have developed a non-LTE retrieval scheme that retrieve the main non-LTE collisional parameters (the rate coefficients and their temperature dependence) from the MIPAS spectra in the 10 and 4.3 μm regions. The CO_2 vmr is jointly retrieved in this case in order to minimize the systematic errors. This algorithm is applied to a subset of the data, large enough and covering different atmospheric conditions, to obtain accurate rate coefficients. Once this is done, the non-LTE model is updated with the obtained collisional rates and then the retrieval of the CO_2 vmr is performed. The inversion has been applied to two years of MIPAS data, 2010 and 2011.

As it is usual in these studies, the quality of the retrieved CO_2 has been assessed, providing key parameters such as its noise errors and vertical resolution. A thorough analysis of the systematic errors of both the collisional rates and the retrieved CO_2 vmr has also been performed.

In addition, we have carried out a validation study by comparing the MIPAS CO_2 data with the previous independent measurements of ACE and SABER.

Furthermore the main physical features of the retrieved global distribution of CO_2 have been analyzed with the help of the 3D Whole Atmosphere Community Climate Model (WACCM).

The CO_2 data obtained in this work have been added to the MIPAS IMK[10]-IAA[11] database, for its use by the scientific community.

[10]Institut für Meteorologie und Klimaforschung, Karlsruhe, Germany
[11]Instituto de Astrofísica de Andalucía, Granada, Spain

Chapter 2

The MIPAS instrument

Abstract

In this chapter we present a detailed description of the MIPAS instrument, its modes of operation, and the major characteristics of its measurements. First we explain the main characteristics of the ESA/Envisat mission and the importance of MIPAS measurements for the atmospheric science. Then, we described the scientific goals, from weather forecasting to upper atmospheric studies. Later, we describe the MIPAS design, its performance, and the different processing levels (0, 1b and 2) and the calibration of level 1b spectra. Then we outline the MIPAS spectral channels (A, AB, B, C and D) covering from 685 to 2410 cm^{-1}. MIPAS was designed and operated to have a global latitudinal, longitudinal and vertical coverage. Thus, we also describe the different MIPAS observation modes. MIPAS was launched in March 1 2002 and was working until March 2004 in its so-called full spectral resolution mode. After January 2005, it was working in the reduced (also called "optimized" resolution mode). The MIPAS measurements analyzed in this work were taken during the period of reduced resolution. We finalize the chapter we a detailed description of the MIPAS observation modes.

2.1. Major Features

The Michelson Interferometer for Passive Atmospheric Sounding (MIPAS) is a infrared Fourier transform spectrometer designed to measure limb atmospheric emission from the upper troposphere to the thermosphere in the mid-infrared (Fischer et al., 2008). MIPAS was part of Envisat (ENViromental SATellite, see Figure 2.1), successfully launched on March 1^{st}, 2002 aboard an Ariane 5 from the Guiana Space Center in Kourou, French Guiana. The spacecraft was placed into an helio-synchronous polar orbit with an inclination of 98.55° at a height of 860 km. Envisat, the largest Earth-Observation spacecraft ever built, was the first ESA (European Space Agency) satellite dedicated to the Earth's observation[1]. Its measurements comprises many different areas like the atmosphere, the oceans and its biology, or ice sheet.

Besides MIPAS there were another two instruments embarked on Envisat to study the Earth's atmosphere: the Global Ozone Monitoring by occultation of Stars (GO-

[1] https://earth.esa.int/web/guest/missions/esa-operational-eo-missions/Envisat

MOS) (Kyrölä et al., 2004) and the Scanning Imaging Absorption Spectrometer for Atmospheric Cartography (SCHIAMACHY) (Bovensmann et al., 1999). The three instruments were part of the Envisat Atmospheric-Chemistry section. The rest of the instruments on board Envisat were: An Advanced Synthetic Aperture Radar (ASAR), MEdium Resolution Imaging Spectrometer (MERIS), Advanced Along Track Scanning Radiometer (AATSR), Radar Altimeter 2 (RA-2), a microwave radiometer (MWR), Doppler Orbitography and Radio-positioning Integrated by Satellite (DORIS) and Laser Retro-Reflector (LRR) (see Figure 2.1).

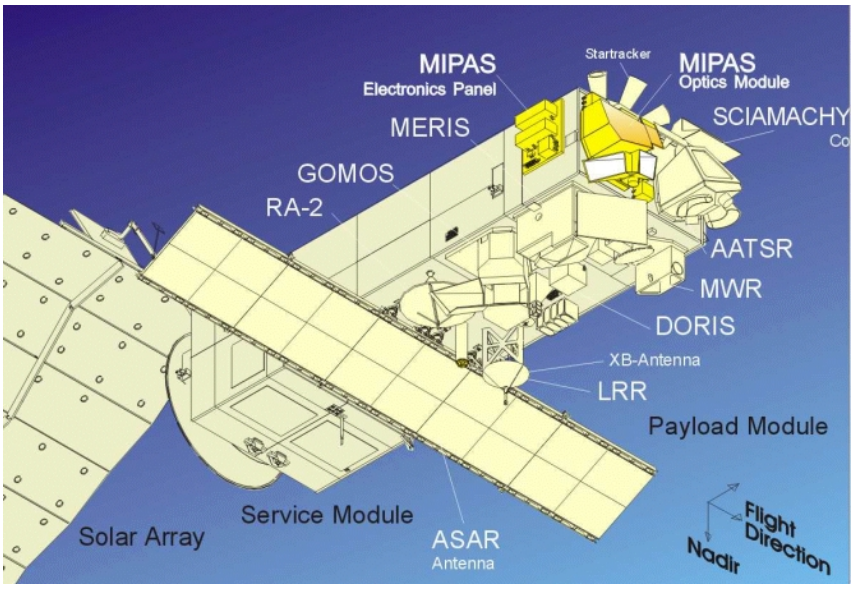

Figure 2.1: Envisat drawing showing its different parts. The ten instruments are pointed specifying their location on the satellite body. In the lower left corner nadir and flight direction are indicated. In yellow, MIPAS electronic panel and optics module are highlighted.

MIPAS has three main characteristics of special interest for non-LTE atmospheric radiance studies: i) a wide spectral coverage comprising the most important mid-IR atmospheric bands; ii) a high spectral resolution, able to resolve the ro-vibrational lines and; iii) its high sensitivity. In addition, MIPAS was operated at high spatial coverage and was measuring during 10 years, thus allowing to perform seasonal and mid-term studies. The instrument was designed using the knowledge gained by its predecessor, the MIPAS-b (atmospheric balloon).

2.2. Scientific Goals

MIPAS was conceived as an instrument able to study the dynamics and the chemistry of the upper troposphere, stratosphere, mesosphere and lower thermosphere. Furthermore the instrument should take measurements over a long period to address

climatological studies. The main scientific goals of the MIPAS project are:

- *The ozone chemistry and the stratospheric dynamics*. Including the ozone and CFC's monitoring, the Antarctic vortex, and the physical structure of the non-polar stratosphere.
- *The stratosphere-troposphere interaction*. Including the stratospheric waves propagation affecting the tropospheric weather, the tropical pipe and the tropospheric-stratospheric exchanges along the tropopause.
- *The physics and chemistry of the upper atmosphere*. Including the thermal structure, the energy balance, the chemistry and the dynamics. For that purpose parameters like temperature or trace gases concentrations such as H_2O, O_3, CO_2, CO, CH_4 and NO were measured.
- *Climate and weather forecast*. MIPAS contributed in this sense with a decade of measurements of temperature and water vapor in the upper troposphere and stratosphere.

2.3. Design

To achieve the above-mentioned scientific objectives requires an instrument with high spectral resolution in the mid-IR combined with a wide spectral coverage and high sensitivity. For this reason, ESA selected as the core instrument of the atmospheric package, an IR Fourier transform spectrometer (FTIR), i.e., MIPAS.

The main advantages of FTIR instruments for taking atmospheric measurements are:

- FTIR instruments are able to measure signal independently of sunlight conditions. This is because the Planck function peaks near 10 μm at typical atmospheric temperatures, i.e. atmospheric signal is higher in the infrared.
- The mid-infrared region allows smaller instruments than those measuring at longer wavelengths. This is determined by the diffraction limits and the higher spectral resolution.
- The instruments operating in the mid-infrared region can be calibrated by observing cold space and black bodies.

On the other hand, the FTIR mechanical complexity is the main disadvantage. A very high precision alignment is needed and the different optic elements should have space for motion and stability. Another problem is the optics cooling (down to 210 K) which is used to reduce its background thermal emission. Thus building an instrument with these special characteristics for space, has additional technical difficulties.

MIPAS was a complex instrument made of several sub-systems. Its optical module was located at the opposite part to the solar light of Envisat and consisted of three main parts: the Front-End optics, the interferometer and the focal planes subsystem (see Figure 2.2).

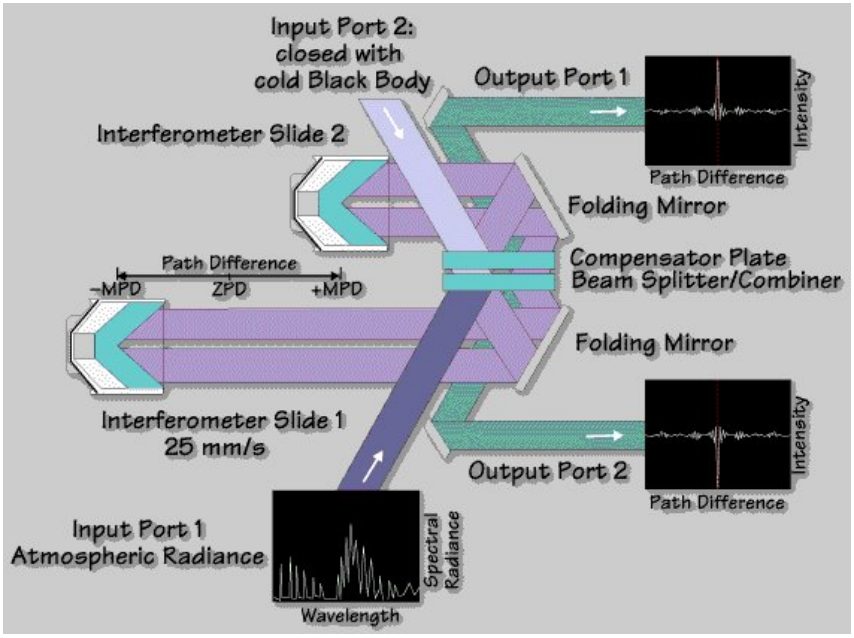

Figure 2.2: The MIPAS optical system formed by the Front-End optics (lower part), the interferometer (upper right) and the focal planes subsystem (upper right).

The limb atmospheric radiation entered through the frontal part. Then it was reflected in an azimuthal mirror first and then in an elevation mirror. MIPAS was able to select the orientation and the altitude of the target by using these two mirrors. Later, the radiation passed through a collimator telescope that fit the beam size in accordance to the size of the interferometer aperture. When the radiation entered into the Michelson interferometer, the beam was split in two. Then the beams were directed into two moving mirrors which redirected them into the beam recombiner. The recombined radiation emerging from the interferometer formed the interference pattern. At this point the beam was again split into two beams redirected into the two output ports. Finally the radiation beams passed through to the focal planes subsystem where each beam was separated in spectral channels by optical filters. In order to increase the sensitivity, the beams were directed onto CMT (Cadmium Mercuride Telluride) detectors. These detectors were cooled to 70 K in order to reduce the thermal emission and to minimize its own noise. As we will see later, MIPAS was designed to cover from 4.15 up to 14.6 μm (685 to 2410 cm^{-1}) using five spectral channels. The separation of the beam into five spectral regions was done in order to reduce the noise arising from detectors and to ease the temperature measurements.

As wee have seen above, the MIPAS output signal is an interferogram formed

from the two beams combined at the Michelson interferometer. In a interferogram we find a number of dark and bright lines composing the interference pattern. The dark lines, where the intensity is zero, derives from the *destructive interference* of the two beams. The bright ones or zones of maximum intensity, comes from the *constructive interference*. The aspect of the pattern is defined by the distance between the two mirrors, i.e. the optical path, and the wavelength of the incoming beam of light. The radiance information is given by the intensity of the output function. When a Fourier Transform is applied on a interferogram, the function is decomposed into the frequencies that make it up, thus obtaining the frequency spectrum.

The MIPAS spectral resolution is given by the optical path difference (OPD[2]) between the mirrors. As we will describe later in Section 2.5, a mechanical failure in March 2004 forced to reduce the OPD in about half of its length and thus decreasing the spectral resolution in the same quantity. Nevertheless, MIPAS spectral resolution was still very high and also allowed to gain in spatial resolution since the integration time of the interferometer sweep was reduced and allowed a better vertical and horizontal sampling.

2.4. Calibration and Characterization

The raw data (interferograms) obtained from MIPAS are not adequate to be directly used in scientific studies. Thus it is necessary to transform the interferograms into radiometrically and spectrally calibrated and geo-located spectra by applying a series of specific procedures (see Fig. 2.3).

In a first step, the interferogram was pre-processed aboard Envisat producing the *level 0* data. This procedure includes amplification, complex filtering, compression and digitalization[3] of the signal. The goal of all this processing was to reduce the instrument data rate to less than 550 kbits/s. Later, the data set, information about telemetry and auxiliary data for calibration was sent to ESA ground station. Then the data processing was divided into two phases: *level 1b* and *level 2*. In the *level 1b* processing, the Fast Fourier Transform (FFT) is applied and the raw interferogram is converted into a calibrated spectra. In the following, we describe the major steps of the *level 1b* data processing.

- *Radiometric calibration*. This is divided in two steps, offset and gain calibration. Regularly calibrations were carried out in order to assign absolute radiance units to the measured spectra. The offset calibration was taken from the thermal emission of the instrument obtained by pointing it to the deep space, where the 3 K background emission was measured (and actually considered negligible). The gain calibration was obtained from the spectra radiance from a black body at a known temperature (L_{BB}). From the difference of the measured spectra from the blackbody and from the deep space spectra, S_{BB} and S_{DS} respectively,

[2]The spectral resolution is about 0.6/OPD

[3]By the on board analogue-to-digital converter (ADC)

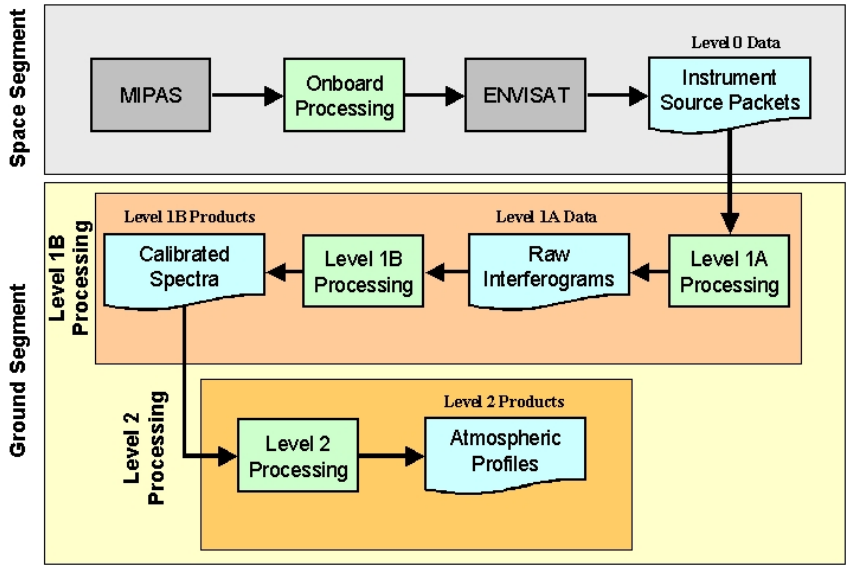

Figure 2.3: Scheme of the different parts of MIPAS data processing. The *level 0*, *level 1b* and *level 2* are briefly described.

the gain function is obtained as follows,

$$G = \frac{L_{BB}}{S_{BB} - S_{DS}}. \tag{2.1}$$

The calibration of the spectra is obtained by using the following equation,

$$L_{atm} = G\,(S_{atm} - S_{DS}), \tag{2.2}$$

where S_{atm} is the measured spectra and L_{atm} the calibrated spectra. The gain calibration could be affected by the ice formation on the cooled detector optical components. The stability of the gain calibration allowed to perform it once per week.

Regarding offset calibrations, much less stable, they were performed each $\sim$7 minutes. During these calibrations the interferogram was cleaned of spurious spikes due to cosmical rays. The difference of sampling between measured and calibrated interferograms were also corrected. The imaginary component of L_{atm}, which should only contain noise, was used for quality verification and for computing the noise equivalent spectral radiance of the measurement.

- *Noise Equivalent Spectral Radiance (NESR)*. The noise levels were obtained from the data. Depending on the spectral channel it ranges from 3 to 50 nW/(cm^2 sr cm^{-1}). The NESR within the 5 spectral channels did not show a significant systematic drift over the time. In addition, the ice accumulation on the detectors could degrade the NESR up to 20% with respect to regular ice free conditions.
- *Non-linearity of the detector*. The amount of incident photons could affect to

the linearity of channels A, AB and B. This fact could trigger important errors in radiometric calibration so it was previously corrected. The interferogram was scaled using the following polynomial function

$$k = 1 + d_0F + d_1F^2 + d_2F^3 + d_3F^4, \tag{2.3}$$

where k is the black body emission at a given temperature, F is the total flux incident on the detector and d_i are the non-linearity coefficients for each detector. The non-linear behavior of the detector was characterized on board, within the device, and in the ground station simultaneously.[4]

- *Spectral calibration*. The Doppler effect due to the orbital movement of the satellite with respect to the atmosphere was corrected. As usual, reference lines with well known frequencies were chosen. For MIPAS, one line per channel was chosen: two ozone lines (802.5074 cm^{-1} and 1125.2085 cm^{-1}) and three water vapor lines (1409.9686 cm^{-1}, 1672.4750 cm^{-1} and 1966.2615 cm^{-1}). In order to assure the stability of the calibration, it was performed every four limb scans.

- *Instrument line shape (ILS) calibration*. The output radiance measured by a given instrument is the response of the device to the input radiance coming from the atmosphere. The different elements of the instrument distort the incoming radiance. In an ideal case, the instrument response to a monochromatic source is a *sync* function (see Figure 2.4).

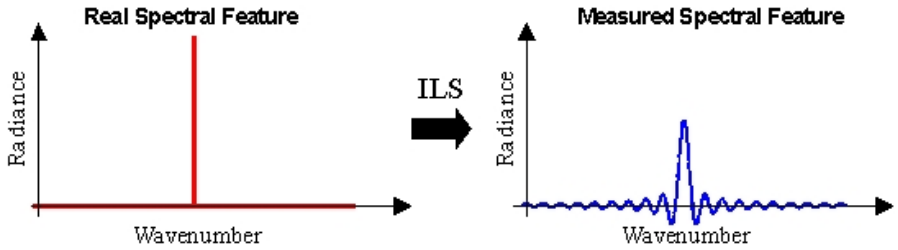

Figure 2.4: Interferometer's response to an ideal spectral line. Left panel (red line) shows an input monochromatic atmospheric radiance. Right panel (blue line) shows the response of the instrument, a *sync* function, i.e. the convolution of the input radiance with the instrument line shape (ILS).

Thus, the measured spectrum is the convolution of an atmospheric spectrum with the ILS. The full width at half maximum of the ILS main lobe gives the spectral resolution. The secondary minor lobes affect the measured spectrum in a broader spectral interval. They can be reduced by a smooth truncation of the interferogram close to the maximum OPD (apodization). In this way a convolution of the ILS with an apodization function (the AILS) is needed

[4] A new non-linearity correction has been recently derived (Manfred Birk and Georg Wagner, TN: Radiometric impact of new non-linearity analysis, 12 Nov. 2013). This has been applied to the newest V7 L1b data. However, this most recent version of L1B is not used in this work.

before convolving the measured spectrum. The adjustments of MIPAS ILS were performed using a physical model of the interferometer.

- *Line of sight calibration*. This is required to determine pointing biases and harmonic variations. It is based on observations of stars moving through the field of view of the instrument at the short wavelength channels. The calibration gives a pointing correction derived from variations between the Envisat pointing system and the line of sight of MIPAS.[5]
- *Field of View (FOV) modeling*. The characterization of the FOV was performed before and after the launch. Pre-launch FOV width was fixed in 52 mdeg (FWHM) in the elevation direction. After the launch, the FOV width was confirmed to be better than 1.3 mdeg in the elevation direction.

Level 2 MIPAS data are the retrievals of the geophysical parameters obtained from level 1b calibrated data. To perform retrievals is necessary to dispose of a forward radiative transfer code used for the simulations of the measured spectra. In the case of non-LTE conditions measurements, a modeling of the non-LTE populations is also needed.

2.5. Spectral Coverage and Resolution

MIPAS covers the spectral range from 4.15 up to 14.6 μm (685 to 2410 cm^{-1}) divided into five channels or bands: *A, AB, B, C and D*. This configuration optimized the sensitivity of each channel. As we show in Fig. 2.5, MIPAS is able to measure a large number of atmospheric constituents, including pressure (LOS) and temperature from the CO_2 15 μm bands, O_3, practically all species controlling the O_3 chemistry, water vapor, the six species comprising NO_y, several tracers (CH_4, N_2O and CO), the CO_X ($CO+CO_2$) budget, many tropospheric contaminants (PAN, HCN, etc.), bromine nitrate ($BrONO_2$), PSCs, aerosols, among others. In addition, MIPAS also measure the 4.3 μm emission from CO_2 in band D, not exploited operationally, but that allow to retrieve the CO_2 abundance in the middle and upper atmosphere, the subject of this work. We detail below the spectral channels of MIPAS and the main species that can be retrieved from them.

- *Channel A:* From 685 to 970 cm^{-1} with a NESR of 30 $nW/(cm^2\ sr\ cm^{-1})$. Measurable species: CO_2, O_3, CFC's, HNO_3, $ClONO_2$, HNO_4, C_2H_2, C_2H_6, CCl_4, OCS, SF_6 and aerosols.
- *Channel AB:* From 1020 to 1170 cm^{-1} with a NESR of 24 $nW/(cm^2\ sr\ cm^{-1})$. Measurable species: O_3, N_2O, CFC12 and aerosols.
- *Channel B:* From 1215 to 1500 cm^{-1} with a NESR of 12 $nW/(cm^2\ sr\ cm^{-1})$. Measurable species: N_2O, H_2O, CH_4, HNO_3, N_2O_5, $ClONO_2$, CF_4, COF_2 and HCN.

[5] We should mention that the LOS is more accurately retrieved later, in the processing of L2.

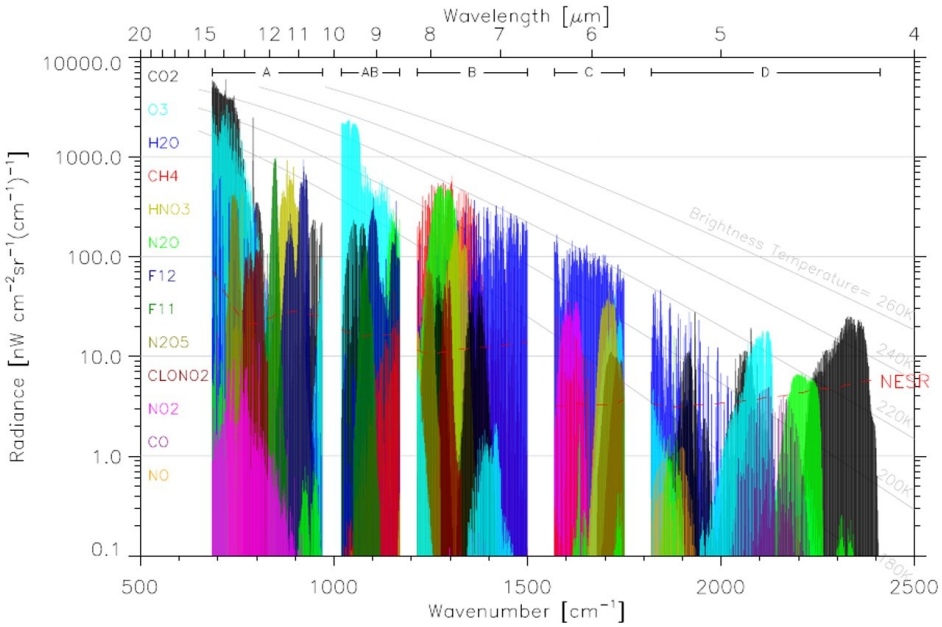

Figure 2.5: Simulations of the spectral contributions of different atmospheric gases at a tangent height of 12 km for the five MIPAS channels. The red dashed line represents the noise equivalent spectral radiance (NESR).

- *Channel C:* From 1570 to 1750 cm^{-1} with a NESR of 4 $nW/(cm^2\ sr\ cm^{-1})$. Measurable species: H_2O, NO_2, O_3, and HNO_3.
- *Channel D:* From 1820 to 2410 cm^{-1} with a NESR of 4 $nW/(cm^2\ sr\ cm^{-1})$. Measurable species: CO_2, CO, NO, O_3, N_2O, OH, NO^+, H_2O, OCS and COF_2.

The original spectral resolution of MIPAS, known as full resolution (FR), was of 0.025 cm^{-1} that was operating from September 2002 to March 2004. Due to a malfunction of the mirrors movements, the optical pathway was reduced from 20 to 8 cm, leading to a reduction in the spectral resolution of 41%, i.e. to 0.0625 cm^{-1} (optimized spectral resolution, OR). The OR was introduced in January 2005 and was operating until the end of Envisat mission in April, 2012. All the data used in this work were taken with the optimized spectral resolution.

2.6. Spatial and Temporal Coverage

The spatial and temporal coverage of MIPAS are defined by its instrumental characteristics, its mode of operation (Fig. 2.6) and the Envisat orbit. MIPAS was operated in various modes of limb measurements, sampling different tangent heights[6] intervals. The targeting of a given tangent height was carried out by using the elevation mirror. MIPAS kept the TH stable while the interferogram sweep was

[6]Tangent Height (TH): the lowest height pointed by the line of sight.

Table 2.1: MIPAS filters. The spectral range (in $cm^{-1}1$), the average noise (in $nW/(cm^2\,sr\,cm^{-1})$) and the most important absorbing or emitting species are specified for each filter.

Band	Spectral range	NESR	Species
A	685 – 970	30	CO_2, O_3 CFCs, HNO_3 $ClONO_2$, HNO_4, C_2H_2, C_2H_6 CCl_4, OCS, SF_6, aerosols
AB	1020 – 1170	24	O_3, N_2O, CFC12, aerosols
B	1215 – 1500	12	N_2O, H_2O, CH_4, HNO_3, N_2O_5 $ClONO_2$, CF_4, COF_2, HCN
C	1570 – 1750	4	H_2O, NO_2, O_3, HNO_3
D	1820 – 2410	4	CO_2, CO, NO, O_3 N_2O, OH, NO^+ H_2O, OCS, COF_2

acquired. This time was of 4.45 s for the full resolution spectral mode and 2.1 s for the optimized resolution spectra. Later, discrete jumps were performed pointing at different TH's to finally obtain a limb scan sequence. Each sequence of sweeps, i.e., the whole scan, was started always at the uppermost tangent height and moving downwards to maximize the horizontal resolution (see Table 2.2). MIPAS observed in rearward direction taking pole to pole measurements as Envisat moves in its polar orbit. MIPAS was also designed to take sidewards (cross track) scans. The original idea was to be used for monitoring volcanic eruptions, measure across the terminators and other scientific topics (Laurentis, 2005; Oelhaf, 2008). However, along the MIPAS lifetime, this mode was very scarcely used.

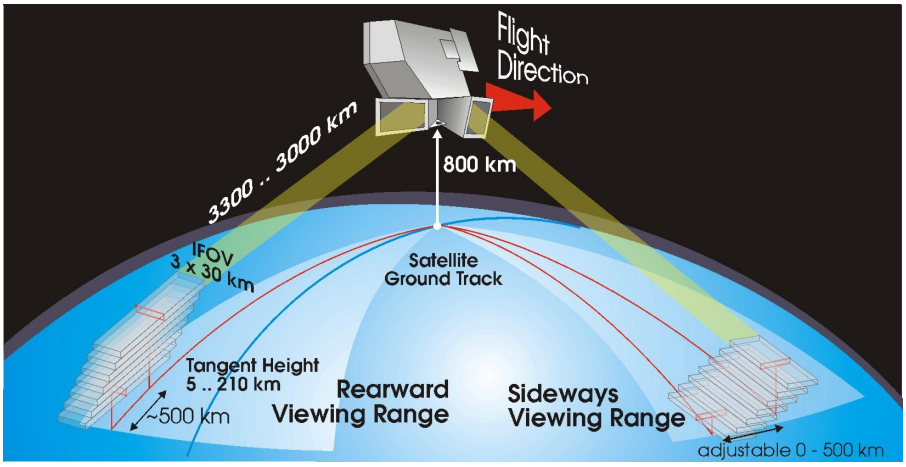

Figure 2.6: Observational strategy of MIPAS.

In general, MIPAS was designed to observe from 5 to 170 km in altitude (with

steps from 1 to 8 km). The field of view of MIPAS is 30 km in the horizontal direction and 0.9 mrad in the vertical. Thus, the spatial vertical sampling is ∼3 km in the TH point. The atmospheric path along the line of sight is typically 400 km and the horizontal spacing between profile single measurements depended on the observation mode (ranging from 200 to 500 km).

With its helio-synchronous orbit, Envisat spent 100.6 min per orbit, about 14 orbits per day (Fig. 2.7). As mentioned above, the time for taking an optimized resolution spectra is 2.1 s, this translates into more than 1000 scans per day in Upper Atmosphere mode. The near-polar orbit of Envisat and MIPAS lifetime of 10 years allowed to measure the temperature and species abundances for time scales of days, months, seasons and years. Times scales of hours, however, were hardly resolved since MIPAS took only 2 local time of measurements, 10 am and 10 pm.

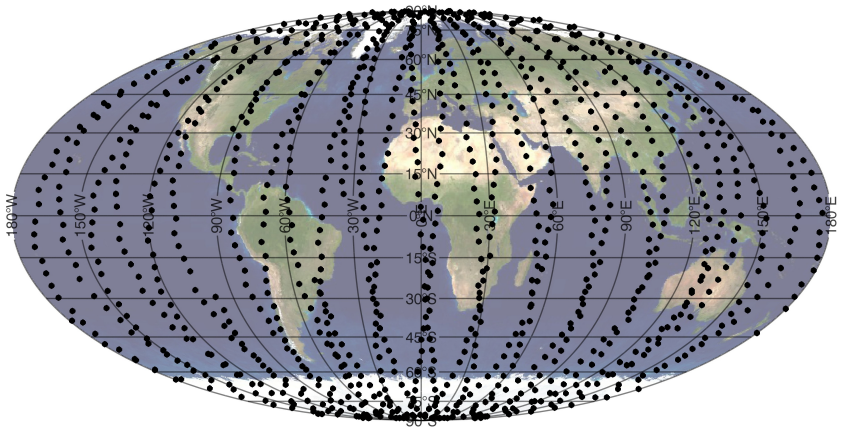

Figure 2.7: MIPAS Upper Atmosphere (UA) mode spatial coverage for a single day (January 17, 2010). Each dot stands for a single scan.

Driven by the scientific studies, different observations modes were devised attending to: i) its vertical coverage; ii) its vertical sampling, and iii) its horizontal resolution. Since degraded spectral resolution was implemented in 2005, new observation modes for faster soundings were defined. The data analyzed in this work corresponds to the OR (or phase 2) period. Hence we describe here only the observations modes of this period (see Table 2.2).

- *Nominal (NOM - RR Nominal Mode).* Designed to cover the upper troposphere, the stratosphere and the lower mesosphere. NOM was devised to study the stratospheric dynamics and (O_3) chemistry, to provide climatological data and to carry out trend analysis. The vertical coverage ranges from 7 to 72 km. MIPAS performs 27 sweeps, at tangent heights steps of 1.5 km in the upper troposphere/lower stratosphere (UTLS) to 4 km steps at the highest altitudes. The spatial displacement (horizontal sampling) of this mode is 410 km. The time to take the whole scan is of 56.7 s.

Table 2.2: MIPAS observations modes for the optimized resolution phase of operation. It lists the sweep number and the tangent heights of the limb scan sequence for each observation mode.

Sweep	Nominal	UTLS-1	UTLS-2	MA	UA	NLC	AE
#1	72	49	42	102	172	102	38
#2	67.5	44.5	37	99	167	99	35
#3	63	40	33	96	162	96	29
#4	59	35.5	29	93	157	93	24.5
#5	55	31	26	90	152	90	20
#6	51	28	23	87	147	87	17
#7	47	25	20	84	142	85.5	15
#8	44	23	18	81	137	84	13
#9	41	21	16	78	132	82.5	11.5
#10	38	19	14	75	127	81	10
#11	35	17.5	12	72	122	79.5	8.5
#12	32	16	–	69	117	78	7
#13	30	14.5	–	66	112	75	–
#14	28	13	–	63	107	72	–
#15	26	11.5	–	60	102	69	–
#16	24	10	–	57	99	66	–
#17	22	8.5	–	54	96	63	–
#18	20.5	7	–	51	93	60	–
#19	19	5.5	–	48	90	57	–
#20	17.5	–	–	45	87	54	–
#21	16	–	–	42	84	51	–
#22	14.5	–	–	39	81	48	–
#23	13	–	–	36	78	45	–
#24	11.5	–	–	33	75	42	–
#25	11.5	–	–	30	72	39	–
#26	8.5	–	–	27	69	–	–
#27	7	–	–	24	66	–	–
#28	–	–	–	21	63	–	–
#29	–	–	–	18	60	–	–
#30	–	–	–	–	57	–	–
#31	–	–	–	–	54	–	–
#32	–	–	–		51	–	–
#33	–	–	–	–	48	–	–
#34	–	–	–	–	45	–	–
#35	–	–	–	–	42	–	–
Total	**27**	**19**	**11**	**29**	**35**	**25**	**12**

- *Upper Troposphere Lower Stratosphere (UTLS)*. This mode covers tangent altitudes from 5.5 up to 49 km with an horizontal displacement of 290 km and

performing 19 sweeps. The vertical sampling is 1.5 km in the lowest region and 4 km in the upper region, similar to the nominal mode. There is a variant of the UTLS mode, the UTLS-2, designed to test bi-dimensional retrievals. ULTS-2 carried out 11 sweeps with a horizontal displacement of 180 km in a time of 23.1 s and with a vertical coverage from 12 up to 42 km.

- *Middle Atmosphere (MA)*. This mode covers part of the stratosphere, the mesosphere, and the lower thermosphere. This observation mode is used to study the middle atmosphere and its interaction with the lower atmosphere. The vertical coverage is from 18 up to 102 km with 29 sweeps (60.9 s) equally spaced by 3 km and with an horizontal displacement of 430 km.
- *Upper Atmosphere (UA)*. This mode is principally dedicated to study the thermosphere, mainly the temperature and the NO abundance. It covers from 42 to 172 km using 35 sweeps in 73.5 s. In the 42 to 102 km interval the vertical sampling is equally spaced at 3 km and in the upper region is 5 km. The horizontal displacement is of 515 km.
- *Noctilucent Clouds (NLC)*. This mode is similar to the UA mode but truncated at 102 km altitude. Additional heights are included at 79.5, 82.5 and 85.5 km, in order to get a better vertical resolution and easy the study of the noctilucent clouds. This mode is used regularly in the mentioned regions during polar summer conditions in both hemispheres. MIPAS takes the whole scan in 52.5 s.
- *Aircraft Emission (AE)*. This mode was designed to try to detect aircraft emission of gases and how can they affect the chemistry of the upper troposphere and the lower stratosphere. Using this mode MIPAS scan for 12 sweeps (25.2 s) with a vertical coverage from 7 to 38 km.

As we mentioned before, the first measurements of MIPAS were taken in March 2002. The instrument continued working almost uninterruptedly from September 2002 until April 2004 using the full resolution (FR) mode. Since January 2005 MIPAS was operated in the optimized resolution mode (OR). However MIPAS was not working on a 100% duty cycle until mid-2007. From this date until April 2012 the nominal mode were used a 80% of the total time; the middle atmosphere and upper atmosphere modes were used one day in ten; the NLC mode were used three days after each solstice in each hemisphere; and the remaining modes were used only occasionally. The MIPAS observations finished on 8 April 2012 when Envisat passed through a communications anomaly. The end of the Envisat mission was announced by ESA on 9 May 2012. Nowadays the satellite is drifting at an altitude of 790 km as a part of the space debris orbiting planet Earth.

2.7. MIPAS Data Used in this Work

In this work we analysed the MIPAS upper atmosphere (UA) observation mode. This mode has the most extended altitude coverage (50 to 172 km) allowing to retrieve

CO_2 in the highest possible altitude range. Also, MIPAS single spectra taken during daytime in the region of the CO_2 4.3 μm emission have a good signal to noise ratio up to about 140 km tangent height. Since several bands of CO_2 are optically thick in the limb up to tangent altitudes as high as 100-110 km, it was then very important to have measurements above that altitude, i.e. to use the UA instead of the MA mode, to constrain the upper atmospheric emissions in the retrieval of CO_2. As mentioned before, MIPAS took UA spectra in the period of mid-2007 until March 2012. The concrete days of measurements are listed in Table 2.3. For performing the retrieval we used the geo-located and calibrated MIPAS *level 1b* Version V5 (5.02/5.06) spectra provided by ESA (Perron et al., 2010; Raspollini et al., 2010).

The level 2 dataset is obtained by the IMK/IAA retrieval processor which includes the forward model Karlsruhe Optimized and Precise Radiative transfer Algorithm (KOPRA) and the non-LTE model Generic RAdiative traNsfer AnD non-LTE population Algorithm (GRANADA), both further explained in Chapter 4.

Table 2.3: MIPAS observations days in the upper atmosphere (UA) mode.

	2007	2008	2009	2010	2011	2012	**#Days**
January	–	9, 17, 27	2, 12, 19, 20	9, 17	4, 14, 24, 30, 31	9, 24, 26, 28, 30	*19*
February	–	6, 16, 26	6, 16, 26	18, 28	1, 13, 23	1, 3, 5, 7, 18, 28	*17*
March	22	7, 17	8, 18, 28	10, 30	5, 15, 25	9, 19, 29	*14*
April	–	6, 16, 26	7, 17	9	14, 24	8	*9*
May	–	16, 26, 31	7, 17, 27	19, 29	4, 14	–	*10*
June	–	9, 22	6, 16, 26	8, 18, 28	3, 13, 23	–	*11*
July	–	16, 26	16, 26	18, 28	3, 14, 27	–	*9*
August	–	5, 15, 25	2, 12, 22	7, 17, 27	4, 12, 22	–	*12*
September	21,22,23	4, 14, 24	1, 11, 21	6, 16, 26	1, 11, 21	–	*15*
October	–	4, 14, 24	1, 11, 21	6	1, 11, 21, 31	–	*11*
November	5, 15, 25	3, 13, 23	30	5, 15, 25	10, 20, 30	–	*13*
December	10, 20, 30	3, 13, 23	10, 20, 30	5, 15, 25	20, 30	–	*14*
#Days	*10*	*33*	*33*	*27*	*36*	*15*	**154**

Chapter 3

Basic Theory of Atmospheric Radiative Transfer and the Inversion Problem

Abstract

In this chapter we present the basic aspects of radiative transfer theory required for the understanding of this work. First we describe the basic steps to obtain the Radiative Transfer Equation (RTE), its formal solution, and its form for limb observations. In this part, the radiance (L_ν), the flux (F_ν), the heating rate (h_ν), the absorption/emission coefficients (k_ν and j_ν) and the optical thickness (τ_ν) are defined. Later we explain the main concept of Local Thermodynamic Equilibrium (LTE) which allows to express the source function $J_\nu(T)$ by the Planck's function $B_\nu(T)$. LTE breakdown conditions and main considerations to obtain the non-LTE source function are further explained. For this purpose it is necessary to know all the microscopic processes populating the different excited levels and gather them into the Statistical Equilibrium Equation (SEE). The radiance emitted by an air parcel is calculated from the resolution of the coupled system of RTE and SEE equations. Then we describe the inverse problem, i.e., how obtain information on the different atmospheric parameters starting from the measured emission. Besides, we describe the Jacobian matrix, the covariance matrix (S_y), the treatment of *a priori* information including the regularization, and the Levenberg-Marquardt damping. All this information is required in the inversion process in order to retrieve atmospheric parameters. Finally, we present a brief description of the diagnostics, including the averaging kernel, the residuals, and the retrieval errors.

3.1. Introduction

Energy transfer in Earth's atmosphere occurs mainly in form of electromagnetic radiation. This physical phenomenon is known as the radiative transfer. Accordingly, to know the basics of the interaction between radiation and matter is essential to perform an appropriate analysis in this area. The main processes that characterize the interaction of the radiation with a given medium like the terrestrial atmosphere are: absorption, emission and scattering.

- *Absorption*: in this process the incident radiant energy is retained by the atmosphere. Considering the molecular scale, we define the absorption as the phenomenon of acquiring photons from incident radiation in order to populate its excited levels. Since absorption depends directly on the molecular density of the medium, absorption becomes stronger at lower atmospheric layers.
- *Emission*: the emission of a photon in a de-excitation process of atmospheric molecules.
- *Scattering*: the general physical process where a photon changes the direction of its propagation trajectory ($\vec{s}$) by one or more non-uniformities located in the medium. In this way the light is deviated from its original optical path by the atmospheric molecules.

As we mention in the first chapter, CO_2 vibration-rotation transitions emit and absorb electromagnetic radiation principally in the infrared. Scattering has a strong dependence on the wavelength ($\sim \lambda^{-4}$) and, since we study here only infrared emissions, we can neglect this effect in our analysis. The presence of clouds could require to deal with scattering (specially at near-infrared wavelengths) but they are mostly restricted to the lower atmosphere and do not affect the altitudes where non-LTE emissions prevails. Under certain conditions, i.e, during the polar summer, there can be found clouds in the upper mesosphere. They are so thin, however, that their effects, compared to the CO_2 absorption/emission at the IR wavelengths studied here, are negligible.

The incoming energy comes from solar radiation from above, and upwelling flux reaching the higher atmospheric layers from below. These photons interacts with the different layers of the atmosphere and also with the terrestrial surface[1]. Thus the amount of solar energy in interaction with the the different atmospheric layers and with the surface, are important drivers for the atmospheric thermal structure.

It is worth to highlight that knowledge of radiative transfer under non-LTE conditions is necessary for understanding the role of CO_2 emissions in the mesosphere and lower thermosphere.

3.2. Radiative Transfer

First we present the radiative transfer theory. The photons of all wavelengths travelling in all directions define the radiative field (Figure 3.1) at a given point P and can be described with the concept of radiance or specific intensity. The radiance, L_ν, is related to the amount of energy, dE_ν, within the frequency interval $(\nu, \nu + d\nu)$, transported by the radiative field across an infinitesimal area, $d\sigma$ (centred at P), along a direction $\mathbf{s}$ (forming an angle θ with $\mathbf{n}$) and confined at a solid angle $d\omega$ during the

[1] In this work we approximate the surface Earth's radiation as a black body radiation.

time dt, by

$$dE_\nu = L_\nu(P, \mathbf{s}) \cos\theta \, d\sigma \, d\omega \, d\nu \, dt. \tag{3.1}$$

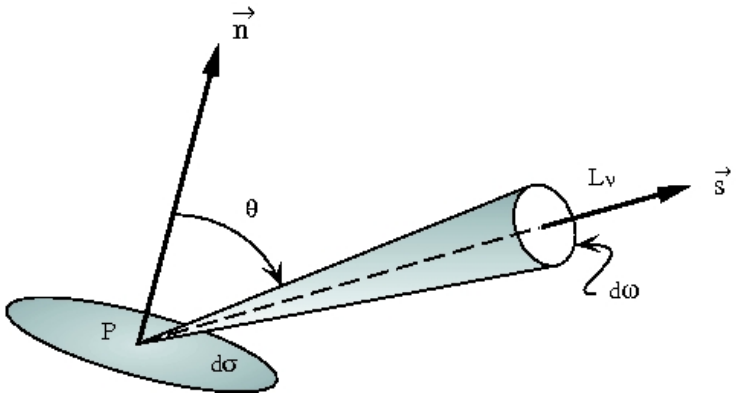

Figure 3.1: Basic radiance element and its elementary parts.

Integrating $L_\nu(P, \mathbf{s})$ over the frequency interval we obtain the spectrally-integrated radiance, $L(P, \mathbf{s})$, with dimensions of W m^{-2} sr^{-1}. Integrating again over solid angle we obtain the flux density. If we integrate over all $\mathbf{s}$ directions in $d\omega$, the radiative flux along the $\mathbf{n}$-direction is obtained:

$$F_{\nu,n}(P) = \int_\omega L_\nu(P, \mathbf{s}) \cos\theta \, d\omega. \tag{3.2}$$

For a three dimensional Cartesian coordinate system with the typical unit vectors ($\mathbf{i}$, $\mathbf{j}$, $\mathbf{k}$), we can express the radiative flux in the vector Cartesian form:

$$\cos\theta = \mathbf{n} \cdot \mathbf{s} = (\mathbf{n} \cdot \mathbf{i})(\mathbf{s} \cdot \mathbf{i}) + (\mathbf{n} \cdot \mathbf{j})(\mathbf{s} \cdot \mathbf{j}) + (\mathbf{n} \cdot \mathbf{k})(\mathbf{s} \cdot \mathbf{k}), \tag{3.3}$$

$$F_{\nu,n}(P) = \int_\omega L_\nu(P, \mathbf{s}) \, (\mathbf{n} \cdot \mathbf{s}) \, d\omega, \tag{3.4}$$

$$\mathbf{F}_\nu(P) = F_{\nu,x}(P) \, \mathbf{i} + F_{\nu,y}(P) \, \mathbf{j} + F_{\nu,z}(P) \, \mathbf{k}. \tag{3.5}$$

The divergence of the radiative flux expresses the net rate at which the energy per unit volume of the radiation field is increased or decreased. This magnitude is represented by the scalar quantity h_ν known as the heating/cooling rate (hereafter heating rate):

$$h_\nu = -\nabla \, \mathbf{F}_\nu(P) = \int_\omega \frac{dL_\nu}{ds} \, d\omega. \tag{3.6}$$

Once we have defined these basic quantities we can construct of the Radiative Transport Equation (RTE). First we express the variation of radiance traveling through a path ds. The form of the equation including only extinction, either absorption or scattering, is given by the Lambert's law:

$$dL_\nu = -e_\nu \, n_a \, L_\nu \, ds \Rightarrow dL_\nu = -k_\nu \, n_a \, L_\nu \, ds. \tag{3.7}$$

In this equation we include the number density[2], n_a, of the absorbing molecules, the atmospheric extinction coefficient, e_ν, for absorption and scattering; and the radiance, L_ν. Neglecting the scattering we consider the absorption coefficient, $e_\nu = k_\nu$.

Taking into account only the increase of the radiance when traveling along the path ds, i.e. atmospheric emission, the variation of radiance is expressed by

$$dL_\nu = j_\nu \, n_a \, ds \Rightarrow dL_\nu = k_\nu \, n_a \, J_\nu \, ds. \tag{3.8}$$

Here, j_ν is the emission coefficient. We define the source function as $J_\nu = j_\nu / k_\nu$. To complete the RTE we join the two parts, absorption and emission, along a optical path from s_0 to s (Figure 3.2) at a fixed point (P),

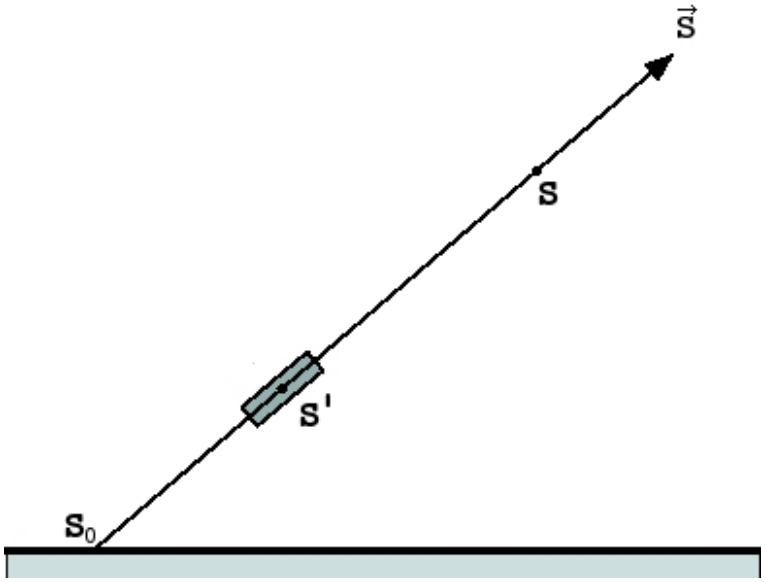

Figure 3.2: Graphical definition of optical path.

$$\frac{dL_\nu(P,\mathbf{s})}{ds} = -k_\nu n_a \Big[L_\nu(P,\mathbf{s}) - J_\nu(P,\mathbf{s}) \Big]. \tag{3.9}$$

This is the basic form of the Radiative Transfer Equation. We can also express it in terms of the heating rate (Eq. 3.6) and the definition of the radiative flux as a

[2]The intensive quantity used to describe the degree of concentration of countable objects. In this case the number of atmospheric molecules per volume.

function of radiance (Eq. 3.2). Thus the Equation 3.9 integrated over all solid angles can be written as follows:

$$h_\nu(P) = 4\pi k_\nu n_a \left(\bar{L}_\nu(P) - \bar{J}_\nu(P)\right), \tag{3.10}$$

where $\bar{L}_\nu(P)$ and $\bar{J}_\nu(P)$ are the incident radiance and the source function averaged over all solid angles:

$$\bar{L}_\nu(P) = \frac{1}{4\pi}\int_\omega L_\nu(P,\mathbf{s})\, d\omega, \tag{3.11}$$

$$\bar{J}_\nu(P) = \frac{1}{4\pi}\int_\omega J_\nu(P,\mathbf{s})\, d\omega. \tag{3.12}$$

At this point we introduce a parameter which controls the absorption of light between two points, s and s', along the optical path, the optical thickness, $\tau_\nu(s,s')$:

$$\tau_\nu(s,s') = \int_{s'}^{s} k_\nu(s'')\, n_a(s'')\, ds''. \tag{3.13}$$

It is important to remark some points: *a)* we take $s > s'$ so; *b)* $\tau_\nu(s,s')$ is a positive quantity and, as a consequence; *c)* the quantity $d\tau_\nu/ds$ is negative. Introducing this definition in the RTE we obtain:

$$\frac{dL_\nu}{d\tau_\nu} = L_\nu(s',s) - J_\nu(s',s). \tag{3.14}$$

Now the RTE is described as a first order ordinary differential equation with the formal solution:

$$L_\nu(s,\mathbf{s}) = L_\nu(s_0,\mathbf{s})\, e^{-\tau(s_0,s)} + \int_{s_0}^{s} k_\nu(s')\, n_a(s')\, J_\nu(s',s)\, e^{-\tau(s',s)}\, ds'. \tag{3.15}$$

This equation describes the radiance at s in the direction $\mathbf{s}$, $L_\nu(s,\mathbf{s})$, after passing through the optical path from s_0 to s in a given medium. In this case $k_\nu(s)$ and $n_a(s)$ are the absorption coefficient and the absorbing molecules' density along the optical path, respectively. The first term of the equation, $L_\nu(s_0,\mathbf{s})e^{-\tau(s_0,s)}$, expresses the initial radiance at s_0 (radiance from the Sun, the deep space or the Earth's surface) and its attenuation, the exponential part, between s_0 and the observation point s. The second term expresses the contributions (emissions) of all the volume elements at positions s' along the path reduced in their corresponding absorptions.

3.2.1. Radiative Transfer Equation for Limb Observations

MIPAS measures the radiance emitted by the atmosphere using the limb sensing technique (Figure 3.3). Hence we need to adapt the Radiative Transfer Equation (RTE) to limb observations. The limb radiance, with tangent point x_t, observed from direction $\vec{x}$ is obtained by convolution of the radiance emitted by the atmosphere at

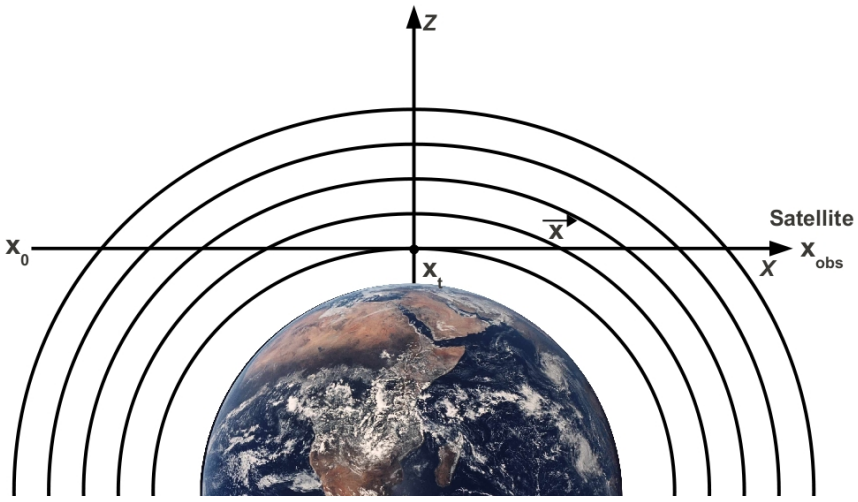

Figure 3.3: Earth limb observation geometry.

frequency ν with the instrumental response function $F(\nu)$ and over a finite range of frequency, $\Delta\nu$,

$$L_{instr}(x_{obs}, \mathbf{x}) = \int_{FOV} \int_{\Delta\nu} L_\nu(x_{obs}, \mathbf{x})\, F(\nu)\, d\nu\, d\omega, \tag{3.16}$$

where $L_\nu(x_{obs}, \mathbf{x})$ is the monochromatic limb radiance at a given observation point x_{obs} and in the direction of the line of sight vector $\mathbf{x}$. At this point we introduce the transmittance, the exponential part of the RTE:

$$\mathrm{T}_\nu(x, x_{obs}) = \exp[-\tau_\nu(x, x_{obs})] = \exp\Big(-\int_x^{x_{obs}} k_\nu(x')\, n_a(x')\, dx'\Big). \tag{3.17}$$

Considering this definition and assuming that the background radiation, $L_\nu(x_0)$ is zero, we can rewrite Eq. 3.15 as follows

$$L_\nu(x_{obs}, \mathbf{x}) = \int_{x_0}^{x_{obs}} J_\nu(x)\, \frac{d\mathrm{T}_\nu(x, x_{obs})}{dx}\, dx. \tag{3.18}$$

3.2.2. Discretization of the RTE

In this work we need to simulate the limb radiance in order to compare with the real measurements. This modeling using a numerical code is known as the forward problem. In our case we use a numerical solution of the RTE which divides the atmosphere in homogeneous layers. For that reason, it is useful to divide the whole atmosphere in concentric layers of constant temperature, pressure and density. We define the density of the absorbing gas, n_l, the absorption coefficient, $k_{\nu,l}$, and the source function, $J_{\nu,l}$, as constants within each atmospheric layer *l*, between, x_l and x_s. First, it is necessary to define the optical mass or absorbing amount, u_l in the

direction of $\mathbf{x}$, as the density between n_s and n_l times the distance, i.e.,

$$u_l(\mathbf{x})_l(x_s - x_l). \tag{3.19}$$

The optical thickness of the layer *l* in the direction of $\mathbf{x}$ can be expressed as:

$$\tau_{\nu,l}(\mathbf{x}) = \tau_{\nu,l}(x_s, x_s) = k_{\nu,l}u_l(\mathbf{x}). \tag{3.20}$$

Thus, once we have all the information to describe the RTE (Eq. 3.18) in a discrete form, we change the integration by a sum over all the layers involved as follows:

$$L_\nu(x_{obs}, \mathbf{x}) = \sum_{l=0}^{N} \Big[J_{\nu,l}(1 - \exp[-k_{\nu,l}u_l(\mathbf{x})]) \prod_{j>l} \exp(-k_{\nu,j}u_j(\mathbf{x})) \Big], \tag{3.21}$$

where the layer $l = 0$ is located at x_0. The next step is to determine the source function, J_ν, that depends on the interaction between the radiative field and matter.

3.3. Non-Local Thermodynamic Equilibrium (non-LTE)

3.3.1. Local Thermodynamic Equilibrium (LTE) and Breakdown Conditions

Schwarzschild introduced the concept of LTE in 1906 when studying stellar atmospheres. He was wondering about the possibility to assume equilibrium not in the whole atmosphere but in gas parcels as a close approximation to reality. These gas parcels are composed of atoms and molecules with excited electronic, vibrational and rotational energy levels which interact with a radiative field.

If we consider a gas parcel completely enclosed and isolated from the rest of the atmosphere, it will eventually becomes in thermodynamic equilibrium. This condition allow us to define a common macroscopic quantity within this region, the temperature of the gas parcel.

Under these conditions, the energy emitted by the components of this gas parcel in thermodynamic equilibrium at a certain frequency, ν, can be described by the Planck function. According to Planck's law, the electromagnetic radiation emitted by a black body in thermal equilibrium is given by

$$B_\nu(T) = \frac{2h\nu^3}{c^2} \frac{1}{\exp(\frac{h\nu}{kT}) - 1}, \tag{3.22}$$

where h is the Planck's constant, k is the Boltzmann's constant and c is the speed of light. The absorption at a given frequency also depends only on the particular gas and temperature.

The molecular and atomic velocities distribution is given by the Maxwellian distribution at that temperature:

$$n\,du = 4\pi N\Big(\frac{m}{2\pi kT}\Big)^{\frac{3}{2}} u^2 exp\Big(-\frac{mu^2}{2kT}\Big)du, \tag{3.23}$$

where $n\,dv$ is the number of particles with a velocity between u and $u+du$, N is the total number of particles and m is the mass of a single one. The kinetic energy is expressed as function of temperature:

$$E_k = \frac{3}{2}kT. \tag{3.24}$$

In a real atmosphere, thermodynamic equilibrium is not fulfilled. In this way, an accurate approximation is to take the neighboring parcel of gas described as if it were in thermodynamic equilibrium and ruled by a 'local' kinetic temperature T_k. This is the Local Thermodynamic Equilibrium (LTE) case. In this situation, the source function $J_\nu(T)$ can be approximated by $B_\nu(T_k)$. It is important to note, however that the radiance of the radiative field, L_ν, is not necessarily be given by the Planck function $B_\nu(T_k)$. The velocities distribution and the kinetic energy are given by the same expression above but at the local kinetic temperature T_k.

Then, in LTE, the redistribution of the kinetic energy of molecules occurs very quickly, much more quickly than the redistribution with other energy forms such as radiation or internal energy. The population distribution of the excited levels is given by the Boltzmann's law:

$$\frac{n_i}{n_j} = \frac{g_i}{g_j}\, exp\left(-\frac{E_i - E_j}{kT_k}\right), \tag{3.25}$$

where i and j indicates the two states involved in the transition; n_i and n_j their respective population; g_i and g_j their degeneracies and E_i and E_j their energies. Therefore we can describe the emission at a given wavelength and the populations of the excited levels involved by using the local kinetic temperature, T_k.

In a planetary atmosphere, where kinetic energy transfer prevails, the approximation of LTE provides an accurate representation of the realistic case. Of course we will find temperature gradients but they are caused by the different vicinities where thermodynamic equilibrium dominates, i.e., each gas parcel neighborhood defines different kinetic temperatures depending on altitude, $T_k(z)$.

The LTE treatment is, however, unable to describe the radiative properties of a gas parcel under many other physical conditions. For example, when thermal collisions are not fast enough to provide the energy lost by radiation (spontaneous emission), or when the energy levels are over-populated by an external (e.g. the solar) radiative field. An appropriate treatment of them requires the inclusion of non-LTE. The concept of non-LTE was introduced in the context of stellar atmospheres by Milne in 1930 (Milne, 1930). After this first treatment, this subject has been extensively studied in astrophysics, mainly to interpret stellar spectra and to study line formation

in hot stars. A detailed description of non-LTE applied to planetary atmospheres, and the Earth's atmosphere in particular, is given by (López-Puertas and Taylor, 2001) and a brief summary and a few examples in (López-Puertas and Funke, 2015).

In addition to the two general examples given above, LTE is not applicable when the following processes become important:

- *Collisional vibrational-vibrational processes (V-V)*: Involving energy exchange between two or more vibrational states. For example, the exchange of CO_2 v_3 quanta and $N_2(1)$, very important for the understanding of CO_2 radiation at 4.3 μm.
- *Electronic-vibrational processes (E-V)*: Involving electronic relaxation for one molecule and vibrational excitation of the partner. Like the excitation of N_2 by the electronically excited $O(^1D)$.
- *Chemical recombination*: The energy of a vibrational excited molecule comes from the chemical energy of a reaction. For example, the O_3 excitation from the recombination process $O_2 + O + M \rightarrow O_3(v) + M$, or the excitation of the hydroxyl radical (OH) from the Bates-Nicolet reaction, $O_3 + H \rightarrow O_2 + OH(v \leq 9)$.
- *Photochemical reactions*: From reactions induced by the solar radiance like the photolysis of the ozone in the Hartley band.
- *Dissociative recombination*: The most common is $O_2^+ + e^- \rightarrow O^* + O$.
- *Collisions with charged particles*: For example during auroras and proton events.

All these situations lead to non Local Thermodynamic Equilibrium (non-LTE) populations. The most common scenarios for non-LTE emissions occur at high altitudes, where pressure is low and collisions infrequent. As we mention before, pressure is not high enough to make thermal processes to compensate for the energy gained by other processes described above or lost by the radiative processes as spontaneous emission. For the vibrational transitions we can find non-LTE emissions above 60 km (CO_2 at 4.3 μm), 90 km (CO_2 at 15 μm) and others such as O_3 hot bands at 30-40 km or NO 5.3 μm fundamental band from 20 km.

To understand the radiative emission in non-LTE it is essential to know all the microscopic processes populating the different energy levels involved (Figure 3.4). The Statistical Equilibrium Equation (SEE), further explained below, expresses the balance between all these processes and provides the level populations.

The thermal collisions, ruled by the kinetic temperature and density (pressure), loose importance as the non-LTE conditions go on stage. Thus the energy transfer involving radiative transitions and vibrational-vibrational processes prevails. We can then introduce the quantity of vibrational or rotational temperature to describe the

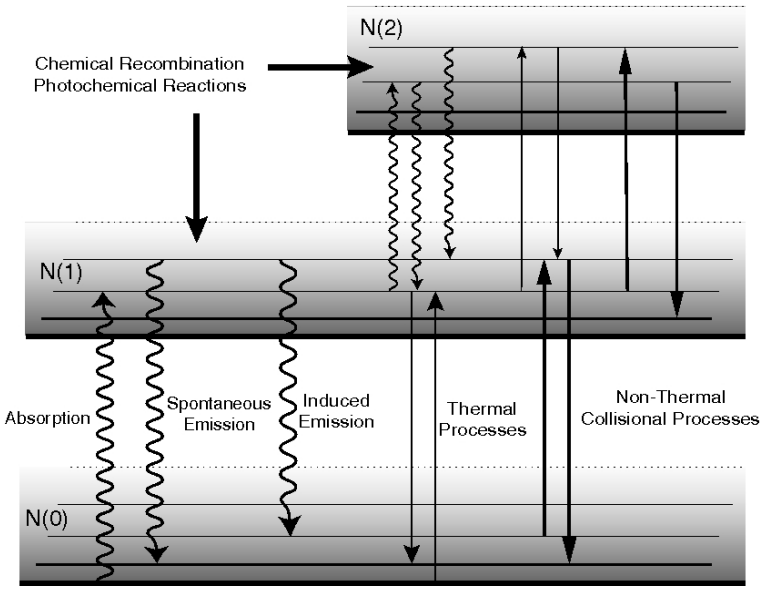

Figure 3.4: Microscopic processes affecting the populations of the vibrational states of molecule N.

population of the vibrational/rotational energy levels, e.g.,

$$\frac{n_{v,r}}{n_0} = \frac{g_{v,r}}{g_0}\, exp\left(-\frac{E_{v,r}}{kT_{v,r}}\right), \tag{3.26}$$

where lower-case expression *v,r* indicates a given vibrational or rotational state. Then $n_{v,r}$ is the number density of the upper state, $E_{v,r}$ its energy, $g_{v,r}$ its degeneracy, $T_{v,r}$ its vibrational/rotational temperature, n_0 is the number density of the lower state and g_0 its degeneracy. If the vibrational/rotational temperature differs from the kinetic temperature we have then non-LTE conditions.

3.3.2. The Source Function for Non-LTE

As we described above, in a gas parcel in non-LTE, the source function cannot be described by the Planck function. Hence, this function, $B_\nu(T)$, is not representative of the emissions from the different atoms and molecules. In order to characterize the emission we must find a form for the source function. For this purpose we need to solve the radiative transfer and statistical equilibrium equations, RTE and SEE, simultaneously.

Regarding SEE, firstly we consider a sample of gas interacting with the radiative field, L_ν. The spontaneous emissions and induced absorption and emission were described by Einstein by introducing the A and B coefficients. These coefficients depend only on the intrinsic quantum properties of the molecules and transitions so they are independent of the thermodynamic state of the gas and of the radiative field. Considering a lower level (1) and an upper level (2), the Einstein coefficients

are related by

$$\frac{A_{21}}{B_{21}} = \frac{2h\nu_0^3}{c^2} \quad \text{and} \quad \frac{B_{12}}{B_{21}} = \frac{g_2}{g_1}, \tag{3.27}$$

where ν_0 is the frequency of the vibrational transition or band centre, A_{21} is related to the spontaneous emission, B_{21} with the induced emission and B_{12} with absorption.

For the next step is necessary to establish the balance of absorbed and emitted photons when radiation interacts with matter. The change in the radiance along a path ds and over a solid angle $d\omega$ can be expressed as:

$$\frac{1}{h\nu}\frac{dL_\nu}{ds}d\omega = (n_2A_{21} + n_2B_{21}L_\nu - n_1B_{12}L_\nu)\frac{d\omega}{4\pi}. \tag{3.28}$$

The source function and the absorption coefficient can be expressed using the equation for the Einstein coefficients (Eq. 3.27) and the RTE (Eq. 3.9):

$$k_\nu = \frac{h\nu}{4\pi}\frac{n_1}{n_a}B_{12}\Big(1 - \frac{g_1n_2}{g_2n_1}\Big), \tag{3.29}$$

$$J_\nu = \frac{2h\nu^3}{c^2}\Big(\frac{g_2n_1}{g_1n_2} - 1\Big)^{-1}. \tag{3.30}$$

It is necessary to take into account the case when the width of the band is not negligible ($\nu - \nu_0 \neq 0$). With this assumption the absorption coefficient is considered over an interval of frequency $\Delta\nu$.

Regarding the population ratio, n_2/n_1, appearing in the equations above, if we consider non-LTE emissions, we need to take into account all populating and depopulating processes affecting the different vibrational levels involved. There are radiative processes, thermal collisions and non-thermal collisions (see Fig. 3.4):

- *Radiative processes*: they include the spontaneous and induced emission and absorption. The number of molecules radiatively absorbed per unit of volume is $B_{12}\,n_1\bar{L}_\nu$, where $\bar{L}_\nu$ is the radiance averaged over all solid angles. The number of emitted molecules is $A_{21}n_2 + B_{21}n_2\bar{L}_\nu$.
- *Thermal collisions*: constituted by the before-mentioned vibrational-translational collisions (V-T):

  $$k_t : n_2 + M \rightleftharpoons n_1 + M + \Delta E, \tag{3.31}$$

  where *M* is any air molecule, k_t is the collisional thermal rate and $\Delta E = E_2 - E_1 = h\nu_0$ is the energy difference of the upper and lower levels. The number of molecules de-excited from level 2 to level 1 by thermal collisions is $l_t = k_t[M]$ and the excited ones is $p_t = k_t'[M]$. Where k_t' is the inverse

collisional rate related to k_t by a detailed balance:

$$k'_t = k_t \frac{g_2}{g_1} exp\Big(- \frac{\Delta E}{kT} \Big). \tag{3.32}$$

- *Non-thermal collisional processes*:

$$k_{vv}: \quad n_1 + C(\nu) \rightleftharpoons n_2 + C(\nu') + \Delta E_\nu, \tag{3.33}$$
$$k_{ev}: \quad N^* + n_1 \rightarrow n_2 + N + \Delta E_{ev}, \tag{3.34}$$
$$k_c: \quad A + B + M \rightarrow n_2 + M, \tag{3.35}$$

  at rates k_{vv}, k_{ev} and k_c. $C(\nu)$ is an atmospheric molecule excited in vibrational level ν before, and ν' after, the collision; and N^* is an excited atom or a molecule electronically or vibrationally excited. $\Delta E_\nu = E_\nu - E_{\nu'} - h\nu_0$ and $E_{ev} = E^* - h\nu_0$ are the energy excesses, with E^* being the energy of N^*. $p_{nt} = k_{vv}[C(\nu)] + k_{ev}[N^*] + k_c[A][B]/n_1$ is the specific production rate of n_2 molecules due to the non-thermal processes (Eqs. 3.33, 3.34 and 3.35), and the specific loss rate of n_2 in non-thermal processes (Eq. 3.33) is $l_{nt} = k'_{vv}[C(\nu')]$.

In order to balance the excitation and de-excitation processes we set the conservative principle of steady state and define the Statistical Equilibrium Equation (SEE):

$$n_1(B_{12}\bar{L}_\nu + p_t + p_{nt}) = n_2(B_{21}\bar{L}_\nu + A_{21} + l_t + l_{nt}), \tag{3.36}$$

where all the processes described above are included. The lefthand side of the equation express the productions and the righthand side the losses of level n_2. In this way we can describe the population ratio as follows:

$$\frac{n_2}{n_1} = \frac{B_{12}\bar{L}_\nu + p_t + p_{nt}}{A_{21} + B_{21}\bar{L}_\nu + l_t + l_{nt}}. \tag{3.37}$$

Using this form of the SEE, the Einstein relations (3.27) and the source function (3.30) we can write the source function centered at ν_0 for the two levels approach as follows:

$$J_{\nu_0} = \frac{\bar{L}_{\Delta\nu} + \epsilon_1 B_{\nu_0}}{1 + \epsilon_2}, \tag{3.38}$$

where ϵ_1 and ϵ_2 are

$$\epsilon_1 = \frac{p_t + p_{nt}}{A_{21}} \frac{g_1}{g_2} \left[exp\left(\frac{h\nu}{kT_k} \right) - 1 \right]; \quad \text{and} \quad \epsilon_2 = \frac{l_t + l_{nt}}{A_{21}} \left(1 - \frac{p_t + p_{nt}}{l_t + l_{nt}} \frac{g_1}{g_2} \right). \tag{3.39}$$

This form of the source function is called the integral equation and depends on the unknown mean radiance over a spectral band, $\bar{L}_{\Delta\nu}$, and other known parameters such as the Planck function, the Einstein coefficients, and the collisional rates.

3.4. Solving the Non-LTE Problem

At this point the RTE (3.15) and the SEE (3.36) are expressed in forms which are interdependent. Both equations form a system of coupled equations. Thus obtaining of an analytical solution is not possible and the system must be resolved using a numerical method. To resolve the general case we must consider: i) the energy transfer between atmospheric layers; ii) external radiation fields (such as solar or Earth's surface radiations); iii) the strong dependence of the absorption coefficient on frequency; iv) all the processes described before affecting the vibrational-rotational states of the molecules and; v) the V-V collisional coupling between some vibrational levels. There are different techniques to resolve the integrations over frequency, solid angle and altitude of the system RTE and SEE equations.

A commonly used approach is the Curtis matrix method (Curtis, 1956; López-Puertas and Taylor, 2001) which algebraically solves a combination of SEE and linearized RTE for two levels systems connected by particular radiative transitions, sequentially for all the considered levels. Since the SEE and RTE are solved simultaneously, this method is computationally less expensive. However, it includes approximations related to linearized radiative transfer, and requires iterations between the two-levels systems of energy levels that are strongly coupled by V-V collisions.

This method uses the RTE in the form of the heating rate for the two-levels approach (levels 2 and 1), which, using the definition of the ro-vibrational band strength, S,

$$S = \int_{\Delta\nu} k_\nu d\nu, \tag{3.40}$$

takes the form:

$$h_{12} = 4\pi S n_a [\bar{L}_{\Delta\nu} - J_{\nu_0}]. \tag{3.41}$$

Introducing this equation into the equation for the source function, (3.38), we obtain the source function at each layer i:

$$J_{\nu_0,i} = \frac{\epsilon_{1,i}}{\epsilon_{2,i}} B_{\nu_0,i} + \frac{1}{4\pi S_i n_{a,i} \epsilon_{2,i}} \, h_{12,i}. \tag{3.42}$$

The Curtis matrix has an order of $N \times N$, where N is the number of atmospheric layers. Each matrix element, C_{ij}, represents the radiative transfer between all atmospheric layers and boundaries. The diagonal elements represent the cooling to space of the ith layer and the non-diagonal elements of the radiative contribution represent the layer jth to the ith net heating rate. With C_{ij} we can re-write the heating rate as:

$$h_i = \sum_j C_{ij} J_{\nu_0,j} + h_{l,i} + h_{u,i}, \tag{3.43}$$

where the heating rates from the lower and upper boundaries layer are $h_{l,i}$ and $h_{u,i}$ respectively. At the lower boundary of the atmosphere, the Earth's surface

emission is usually taken by a Planck function at surface's kinetic temperature. Since radiation coming from space is negligible, we take into account solely the incoming solar radiation for the upper boundary.

The last two equations, (3.42) and (3.43), form a linear system for all atmospheric layers. The heating rates and the source function are the unknown quantities. In matrix form, we can write:

$$\mathbf{h} = \mathcal{C}\mathbf{J} + \mathbf{h}_b \quad ; \quad \mathbf{J} = \mathcal{E}B + \mathcal{D}\mathbf{h}, \tag{3.44}$$

where $\mathbf{h}_b$ is the sum $\mathbf{h}_l + \mathbf{h}_u$, $\mathcal{C}$ is the Curtis matrix, $\mathcal{D}$ and $\mathcal{E}$ are both diagonal matrices given by:

$$\mathcal{E} = \frac{\epsilon_{1,i}}{\epsilon_{2,i}} \quad ; \quad \mathcal{D} = \frac{1}{4\pi S_i n_{a,i} \epsilon_{2,i}}. \tag{3.45}$$

If the radiative coupling between layers is important, the Curtis matrix method allows for an accurate solution without the need of iterations.

A different method for solving the combined SEE+RTE is by iterating between the statistical equilibrium and transfer equations. Commonly referred as Lambda iteration, it alternates SEE calculations involving all the energy levels with RTE calculations involving all atmospheric layers. The main disadvantage of Lambda iteration is the slow convergence in optically thick conditions. Therefore, different acceleration strategies, like the Accelerated Lambda Iteration (ALI) techniques (Kutepov et al., 1991; Rybicki and Hummer, 1991), have been employed in practical applications.

The advantages of both methods can be combined by optionally including Curtis matrix-type algebraical solutions of the RTE into the Lambda iteration in order to speed up the convergence.

3.5. The Inverse Problem

In order to derive atmospheric quantities from remotely sensed atmospheric radiances, we have to invert the forward problem, i.e., to solve the inverse problem. In this way we can retrieve pressure, temperature, density or gases abundances from measured atmospheric radiances. There are two main difficulties regarding the inverse problem: i) to go from discrete measurements to the retrieval of continuous profiles; and ii) the non-linearities of the retrieval equations. A theory of the inversion problem applied to atmospheric measurements is presented by Rodgers (2000).

Let us begin considering a certain vector of measurements, $\vec{y}$, typically a set of observed spectra, with m dimensions and a vector of retrieval parameters, $\vec{x}$, with n dimensions. The forward problem can be expressed as

$$\vec{y} = \mathbf{F}(\vec{x}), \tag{3.46}$$

where $\mathbf{F}(\vec{x})$ is a non-linear function representing the radiative transfer equation de-

pending on the retrieval parameter. When resolving the inverse problem we aim to calculate $\vec{x} = \mathbf{f}(\vec{y})$.

If we include random errors $\vec{\epsilon}$ due to the instrumentation, the forward problem can be written as

$$\vec{y} = \mathbf{F}(\vec{x}) + \vec{\epsilon}. \tag{3.47}$$

The radiative transfer problem (3.47) can be linearised with respect to a reference state, $\vec{x_0}$, as

$$\vec{y} = \mathbf{F}(\vec{x_0}) + \mathbf{K}(\vec{x} - \vec{x_0}) + \vec{\epsilon}, \tag{3.48}$$

where $\mathbf{K}$ is the Jacobian, a matrix of $m \times n$ dimensions:

$$\mathbf{K} = \frac{\delta \mathbf{F}(\vec{x})}{\delta \vec{x}}. \tag{3.49}$$

Physically, the Jacobian expresses the sensitivity of the measurement with respect to a given parameter. The rank of $\mathbf{K}$ is p and denotes the number of linearly independent rows which form a subspace within the state space. If this subspace is lower than the state space, $p < n$, there is a null space where the solution can take any value because it is not determined by the measurements. For instance, this can occur when the profile to be retrieved covers a vertical range not of sounded by the instrument. The characterization of the null space is essential for the resolution of the inverse problem. This space identifies how many measures are necessary to provide information of the retrieval parameter.

The measurement errors are represented by the covariance matrix, $\mathbf{S}_y$. The elements of the covariance matrix are given by

$$S_{ij} = \langle (\epsilon_i - \langle \epsilon_i \rangle)(\epsilon_j - \langle \epsilon_j \rangle) \rangle, \tag{3.50}$$

where $\epsilon_{i,j}$ are the errors of the measurements i and j.

An usual form of resolving the inverse problem (3.47) is by minimizing the quadratic sum of the difference of the measure vector and the forward problem, $[\vec{y} - \mathbf{F}(\vec{x})]^2$, weighted with $\mathbf{S}_y$:

$$\frac{\delta}{\delta \vec{x}} ([\vec{y} - \mathbf{F}(\vec{x})]^T \mathbf{S}_y^{-1} [\vec{y} - \mathbf{F}(\vec{x})]) = 0 \tag{3.51}$$

that, because of its non-linearity, have to be solved iteratively, i.e.,

$$\vec{x}_{i+1} = \vec{x}_i + \left[\mathbf{K}^T \mathbf{S}_y^{-1} \mathbf{K}\right]^{-1} \times \left[\mathbf{K}^T \mathbf{S}_y^{-1} (\vec{y} - \mathbf{F}(\vec{x}))\right]. \tag{3.52}$$

At this point we need *a priori* information to characterize the components of the state vector belonging to the null space, $\vec{x}_a$. The process of introducing additional information in order to resolve an ill-posed problem is called regularization. This is done by including the regularization matrix $\mathbf{R}$. We can think about it as a func-

tion that fills the gaps of information and provides a character of continuity to the measurements. The retrieval equation is then written as

$$\vec{x}_{i+1} = \vec{x}_i + \left[\mathbf{K}^T\mathbf{S}_y^{-1}\mathbf{K} + \mathbf{R}\right]^{-1} \times \left[\mathbf{K}^T\mathbf{S}_y^{-1}(\vec{y} - \mathbf{F}(\vec{x})) - \mathbf{R}(\vec{x}_i - \vec{x}_a)\right]. \quad (3.53)$$

The selection of a certain regularization depends on how accurate the *a priori* information is. Rodgers (2000) propose the "optimal estimation" or "maximum *a posteriori*" methods when a certain knowledge on the *a priori* information is given. In these cases the regularization matrix is equal to the covariance matrix of the *a priori* information, S_a. The information is generally obtained from climatological data known beforehand. This method provide the best trade-off between the retrieval random errors and the degrees of freedom, i.e. the number of independent pieces of information contained in the measurements.

Another option to define the regularization matrix is the Tikhonov formalism (Tikhonov, 1963). In this method the regularization matrix, $\mathbf{R}$, is given by $\gamma\mathbf{B}^T\mathbf{B}$, where γ represents the weight of the measurements versus the *a priori* information and $\mathbf{B}$ the matrix that defines the order of the regularization. The main advantage of the Tikhonov regularization of orders greater than zero is the independence of the results on the absolute value of the a priori. Zero-order Tikhonov regularization, that is $\mathbf{B} = \mathbf{I}$, is equivalent to optimal estimation with a diagonal covariance matrix. It minimizes the mean differences $\vec{x} - \vec{x}_a$. This method is useful if the retrieval parameter is known to be close to the *a priori* values. The first-order Tikhonov regularization minimizes the derivative of the mean differences $\vec{x} - \vec{x}_a$, in this case:

$$\mathbf{B} = \begin{pmatrix} -1 & 1 & 0 & 0 & \dots \\ 0 & -1 & 1 & 0 & \dots \\ 0 & 0 & -1 & 1 & \dots \\ \dots & \dots & \dots & \dots & \dots \end{pmatrix}. \quad (3.54)$$

This order is useful when the profile shape of the solution and of the *a priori* are expected to be close. Regarding the second-order regularization, it minimizes the second derivative of $\vec{x} - \vec{x}_a$ avoiding, strong oscillations. The form of $\mathbf{B}$ in this case is written as:

$$\mathbf{B} = \begin{pmatrix} -1 & 2 & 1 & \dots & \dots & \dots \\ 0 & -1 & 2 & 1 & \dots & \dots \\ 0 & 0 & -1 & 2 & 1 & \dots \\ \dots & \dots & \dots & \dots & \dots & \dots \end{pmatrix}. \quad (3.55)$$

As we mentioned above, the inverse problem is non-linear so the linear approximation of $\vec{x}$ described must be forced within a given iteration. The Levenberg-Marquardt damping is used to avoid problems with strong non-linearities (Levenberg, 1944; Marquardt, 1963). In this way we include a damping term, $\lambda\mathbf{I}$, into Eq. (3.53) to give:

$$\vec{x}_{i+1} = \vec{x}_i + \left[\mathbf{K}^T\mathbf{S}_y^{-1}\mathbf{K} + \mathbf{R} + \lambda\mathbf{I}\right]^{-1} \times \left[\mathbf{K}^T\mathbf{S}_y^{-1}(\vec{y} - \mathbf{F}(\vec{x})) - \mathbf{R}(\vec{x}_i - \vec{x}_a)\right]. \quad (3.56)$$

Within a given iteration the λ parameter is chosen depending on the value of χ^2 (this is described below). There are two options: i) if the χ^2 decreases in the iteration, a new $\vec{x}_i$ is calculated and λ is decreased before proceeding to the next iteration; and ii) if χ^2 increases, $\vec{x}_i$ is kept constant, λ is increased and starts a new iteration. This process if repeated until λ decreases.

Rodgers (2000) defines the gain matrix, $\mathbf{G}$, to express how the measurements, $\vec{y}$, maps into the retrieved parameters, $\vec{x}$. Hence it is the transformation of the measure space into the parameters space. $\mathbf{G}$ is given by:

$$\mathbf{G} = \left(\mathbf{K}^T\mathbf{S}_y^{-1}\mathbf{K} + \mathbf{R}\right)^{-1}\mathbf{K}^T\mathbf{S}_y^{-1}. \tag{3.57}$$

The gain matrix performs the inverse transformation of the Jacobian. The averaging kernel matrix, $\mathbf{A} = \mathbf{GK}$, describes how the true profile maps into the parameter space. In practice, particularly when the retrieval grid is finer than the measurement grid, the averaging kernel shows a broad diagonal structure with maximum values lower than 1. In an ideal case, if the retrieved values coincide with the true one, $\mathbf{A}$ would be equal to the identity matrix. The full width at half maximum of either the columns or rows of $\mathbf{A}$ provide the vertical resolution (Fig. 3.5). The $\mathbf{A}$ columns describes the sensitivity of the retrieval to a given perturbation of $\vec{x}$. In addition, the trace of the averaging kernel matrix gives the number of independent pieces of information, i.e. the degrees of freedom. Because of all these properties, the averaging kernel matrix, $\mathbf{A}$, is often used as a diagnostics tool to characterize the quality of the retrievals.

The χ^2 of the retrieval is calculated by

$$\chi^2 = [\vec{y} - \mathbf{F}(\vec{x})]^T\mathbf{S}_y^{-1}[\vec{y} - \mathbf{F}(\vec{x})] + (\vec{x} - \vec{x}_a)^T\mathbf{R}(\vec{x} - \vec{x}_a), \tag{3.58}$$

which give us a measure of the goodness of the retrieval. The smaller (close to unity) the better.

Regarding the error analysis, let us start using the gain matrix to express the random error covariance matrix. It provides the retrieval errors due to the instrumental noise:

$$\mathbf{S}_x = \mathbf{G}\mathbf{S}_y\mathbf{G}^T. \tag{3.59}$$

The retrieval error due to systematic error, ϵ_s, in the parameter a_j are

$$\Delta\vec{x}_j = G \cdot [\mathbf{F}(\vec{x}, a_j + \epsilon_s) - \mathbf{F}(\vec{x}, a_j)]\,. \tag{3.60}$$

For retrieving vertical profiles, Rodgers (2000) describe two main methods: i) global fitting, which consists of a simultaneous retrieval of the whole set of atmospheric layers; and ii) the onion peeling method, that consists in performing the retrieval from the higher layers to the lower ones sequentially.

In the next chapter we describe the radiative transfer code, Karlsruhe Optimized and Precise Radiative transfer Algorithm (KOPRA), the non-LTE code, Generic RAdiative traNsfer AnD non-LTE population Algorithm (GRANADA) and the retrieval

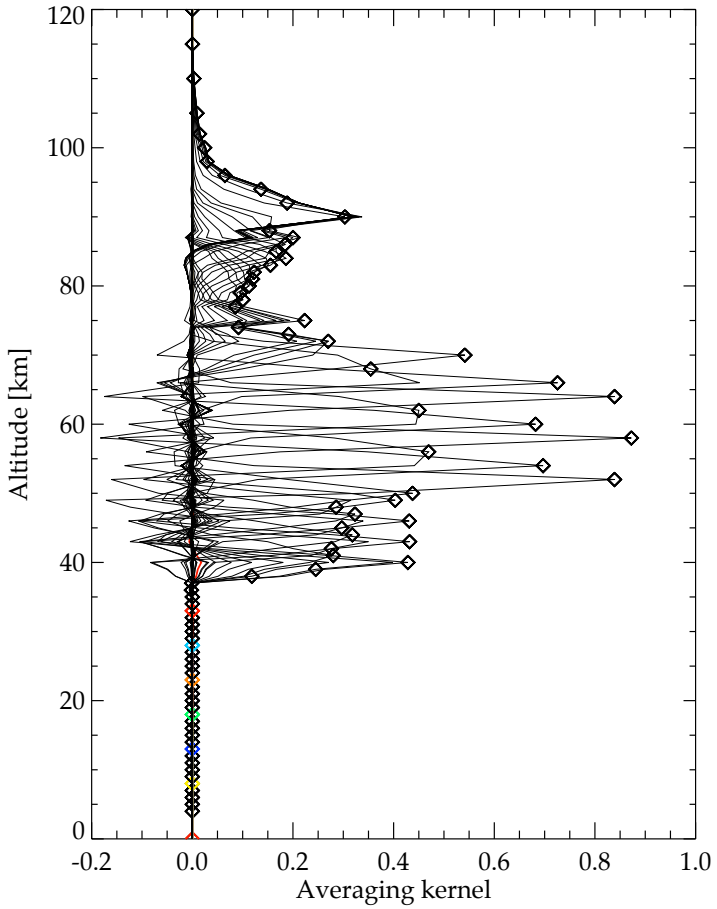

Figure 3.5: Normalized averaging kernel graphical representation of rows for the example of an O_3 retrieval from MIPAS spectra taken in the NLC observation mode. Each line represents the information profile from each tangent altitude.

code, Retrieval Control Program (RCP) used in this work. These codes are used for solving the RTE for limb observations, the calculation of the non-LTE populations used in the RTE, and the retrieval of non-LTE parameters (collisional rate coefficients) and of CO_2 abundance profiles.

Chapter 4

Models and Algorithms

Abstract

In this chapter we describe the three major models/computer codes used in the IAA-IMK retrieval scheme, that is: i) the Karlsruhe Optimized and Precise Radiative transfer Algorithm (KOPRA), used for modelling the atmospheric radiative transfer; ii) the Generic RAdiative traNsfer AnD non-LTE population Algorithm (GRANADA) that calculates the non-LTE populations of the different energy levels; and iii) the Retrieval Control Program (RCP), a constrained least squares algorithm for retrieving atmospheric profile parameters. In addition, within the GRANADA section, a more detailed description of the CO_2 non-LTE model is presented, where the main collisional and radiative processes that control the non-LTE populations of the CO_2 energy levels are discussed. Finally, we describe the setup of the IAA-IMK retrieval scheme.

4.1. KOPRA

The Karlsruhe Optimized and Precise Radiative transfer Algorithm, KOPRA, models the mid-infrared radiative transfer through the atmosphere. This code was devised at the Institut für Meteorologie und Klimaforschung, IMK (Karlsruhe, Germany) as a tool to simulate the atmospheric infrared ro-vibrational emission measured by the MIPAS instrument (Stiller et al., 2002, http://www.imk-asf.kit.edu/english/312.php). For this purpose, KOPRA uses the integrated radiative transfer Eq. 3.15 assuming the Curtis-Godson approximation. KOPRA calculates the infrared monochromatic radiance, $L_\nu(x_{obs})$, by using the line-by-line technique. It also provides Jacobians calculated in a quasi-analytical mode. Regarding the atmosphere, the radiative transfer modelling is based on a layer-by-layer approach, i.e., the partial gas columns and the Curtis-Godson means[1] are calculated for each path segment of the line of sight.

KOPRA takes into account the oblateness of the Earth for the calculation of the line of sight, and includes the refraction in a non-spherical atmosphere with horizontally inhomogeneous densities. Thus, the calculation of the ray tracing along the line of

[1]The Curtis-Godson means are calculated for temperature, pressure and non-LTE/LTE population ratios.

sight is performed by using changes in the refractive index and in the terrestrial geometry. If cirrus clouds in the upper troposphere or polar stratospheric clouds cross the line of sight, KOPRA models the continuum extinction in the mid-infrared spectrum caused by particles. As mentioned before, KOPRA is specifically suited for the analysis of the MIPAS data but it is able to handle many other observational geometries from satellite or balloon observations, taking into account the field-of-view and the spectral response (AILS) of the given instrument.

In the middle and upper atmosphere, KOPRA is able to handle the non-LTE effects in the radiance signal of the atmosphere. The information on the non-LTE populations of the molecular states is provided by the code GRANADA (see next section).

The spectral lines are modeled using a Voigt profile, i.e., convolving the Lorentz and Doppler line shapes. Spectroscopic information is usually taken from the HITRAN database (Rothman et al., 2013) although it can also handle other spectroscopic databases.

An additive low-frequency contribution to the absorption coefficient takes into account effects such as the contribution of heavy molecules; the absorption bands induced by collisions of the pairs N_2-N_2 and O_2-O_2, and overlapping of line wings from absorption bands like CO_2 4.3 μm or H_2O 6.3 μm. Also, other features can be handled like the line-mixing effect in the CO_2 bands, and the horizontal inhomogeneities in temperature or gas abundances. The vibrational bands and isotopes of the gases to be included, the atmosphere parameter profiles, the spectral resolution or the altitude grid can be specified by the user. In this way, KOPRA can be used also as a tool to perform sensitivity tests of simulated radiances in dependence of reference atmosphere by using its numerous possibilities.

The validation of KOPRA with respect to GENLN2, Reference Forward Model (RFM) and Simulation Program for Infrared Radiative Transfer (SPIRT) was performed by von Clarmann et al. (2002). For all these reasons it can be concluded that KOPRA fulfills the requirements and accuracy to be included in any automated retrieval system. The implementation of the non-LTE in KOPRA was performed by the Instituto de Astrofísica de Andalucía, IAA.

4.2. GRANADA

The Generic RAdiative traNsfer AnD non-LTE population Algorithm, GRANADA, calculates the non-LTE state populations of molecular rotational, vibrational spin and electronic levels (Funke et al., 2012). GRANADA, written in Fortran 95, expresses the non-LTE populations as population ratios with respect to those in LTE, $n_{\nu j}^{non-LTE}/n_{\nu j}^{LTE}$, or as vibrational/rotational temperatures (see Eq. 3.26). Furthermore, GRANADA is also able to compute the heating/cooling rates of the involved vibrational bands. This information is used by KOPRA to calculate the infrared radiance from non-LTE emissions. GRANADA uses many inputs including, among others, the gas abundances, the temperature profiles, the considered states and transitions and the non-LTE processes (radiative and collisional) to be included.

The model solves the locally defined statistical equilibrium equations (SEE) (Eq. 3.36) for all the energy levels considered and the radiative transfer equations (RTE) (Eq. 3.15) for all the bands connecting these levels in a discrete atmosphere prescribed at given altitude levels. The processes taken into account into the SEE are the radiative, collisional and chemical productions and losses.

As we described in the previous chapter, the RTE+SEE system cannot be solved analytically and hence a numerical method must be employed. In this way, GRANADA uses the Curtis matrix and the Lambda iteration methods (or a combination of both) to reach a solution iteratively. More details on the specific way we use it for calculating the CO_2 populations in this work are given below in Sec. 4.3.

The statistical equilibrium calculations are carried out by solving, at a given altitude, the linear equation system resulting for the state vectors $\mathbf{n}$ (population density) of all the energy levels considered by the inversion of the matrix equation $\mathbf{Wn} = \mathbf{p}$. $\mathbf{W}$ is a matrix with $n \times n$ dimensions which diagonal elements represent the radiative, collisional and chemical losses of state i, meanwhile the off-diagonal elements corresponds to the radiative and collisional productions from state j. The $\mathbf{p}$ vector represents the chemical productions of state i.

Three options are available for the radiative transfer calculations: (i) the standard line-by-line radiative transfer in Lambda iteration; (ii) the modified Curtis matrix method with line-by-line radiative transfer; and (iii) the modified Curtis matrix method with the equivalent line approach (see more detailed description in Funke et al. (2012)). The latter allows for a significant acceleration of radiative transfer calculations by histograming of ro-vibrational lines in bins of the logarithm of the line strength.

GRANADA also provides non-LTE corrections of the Jacobians calculated by KOPRA by taking into account the dependency of the non-LTE populations, n, on the retrieved parameter $\vec{x}$ (e.g., temperature, gas concentrations or collisional rates). . The correction of the KOPRA Jacobians is done as follows:

$$\mathbf{K} = \left.\frac{\partial \mathbf{F}(\vec{x})}{\partial \vec{x}}\right|_{n=cte} + \frac{\partial \mathbf{F}(\vec{x})}{\partial n} \times \frac{\partial n}{\partial \vec{x}}, \tag{4.1}$$

where $\mathbf{F}(\vec{x})$ is the modelled radiance. The terms $\left.\frac{\partial \mathbf{F}(\vec{x})}{\partial \vec{x}}\right|_{n=cte}$ and $\frac{\partial \mathbf{F}(\vec{x})}{\partial n}$, provided by KOPRA, express the sensitivity of the modelled radiance to the retrieved parameter and to the non-LTE populations, respectively. The derivatives $\partial n/\partial \vec{x}$ are provided by GRANADA. Therefore, GRANADA can also be used to perform sensitivity tests of the vibrational temperatures to, for instance, changes in the rates of the collisional processes or in the reference atmosphere (temperature and gas concentrations).

4.3. The CO_2 non-LTE model

The setup of GRANADA applied to CO_2 populations presented by Funke et al. (2012) takes into account 134 vibrational levels. At this point we should make a

note on notation. There are usually two ways for expressing the vibrationally excited states of CO_2, the old Herzberg notation (v_1,$v_2{}^l$,v_3), more physically intuitive, and the most modern HITRAN notation (v_1,v_2,l,v_3,r), adopted in the HITRAN database and easier to use in computer codes. In those notations v_j is the quantum number associated with the normal mode of vibration j, l is the vibrational angular momentum quantum number associated with the degenerate bending mode 2, and r is the ranking index, which is unity for the highest vibrational level of a Fermi resonating group (Rothman and Young, 1981; Rothman et al., 2005). In this work we use both notations indistinctly. Table A.1 might be useful in this respect, since it shows the correspondence between the two notations for most of the levels studied here. Additionally, to simplify the notation for the collisional processes (some of which are common to several levels), we also use a "compressed" notation, (v_d,v_3), where v_d=$2v_1$+v_2, independently of the values of l and r.

Thus, the GRANADA model version used here includes the $^{16}O^{12}C^{16}O$ (isotopologue 1) levels up to (7,0), (6,1), (3,2) and (1,3); $^{16}O^{13}C^{16}O$ (isotopologue 2) levels up to (4,0) and (4,1); $^{16}O^{12}C^{18}O$ and $^{16}O^{12}C^{17}O$ (isotopologues 3 and 4) levels up to (3,0) and (1,1); and $^{16}O^{13}C^{18}O$ and $^{16}O^{13}C^{17}O$ (isotopologues 5 and 6) levels up to (1,0) and (1,1).

Due to the strong collisional coupling of CO_2 with $N_2(v = 1)$ via V-V energy transfer, vibrational populations of $N_2(v \leq 1)$ are also included in the non-LTE model calculations. The SEE for $N_2(1)$ is coupled into the SEE for the main CO_2 isotope (626). The CO_2 levels are connected by 695 radiative transitions, 39 of them considering full radiative transfer in the atmosphere. These transitions involve vibrational states up to (4,1) for the main isotopologue, (3,0) and (2,1) for the isotopologue 636, and (1,1) for the isotopologues 628 and 627. Below 20 km, the upwelling component from the troposphere is approximated by a Planck function with a temperature from an estimated emission altitude located between 7 and 20 km. Above 20 km, radiative transfer is calculated in this case using the Curtis matrix formalism. The SEE for $N_2(1)$ is coupled into the 00011 $\rightarrow$ 00001 band RTE calculation. The spectroscopic data for CO_2 bands used by Funke et al. (2012) has been updated here with the most recent HITRAN database of 2012 Rothman et al. (2013).

The collisional scheme of the CO_2 levels is described in detail in Funke et al. (2012), which is adapted here in Table 4.1. This GRANADA setup for CO_2 has been significantly updated, benefiting from several analysis of SABER and MIPAS. Thus, López-Puertas et al. (2004) studied the SABER CO_2 4.3 μm nighttime radiance and found a larger excitation of N_2 by $OH(\nu)$ than assumed in previous works; and López-Puertas et al. (2005) analysed MIPAS data of the CO_2 4.3 μm emissions, as well as from other studies described below. Here we include a brief discussion of the major collisional processes. We should mention that this Table is not updated with the new collisional rates retrieved in this work, which are described in the next chapter (see Table 5.1).

The collisional deactivation of CO_2 by O,

$$k_O: \; CO_2^i(v_d) + O \rightleftharpoons CO_2^i(v_d - 1) + O, \tag{4.2}$$

Table 4.1: Collisional rates that influences the CO_2 and N_2 vibrational levels (adapted from Funke et al., 2012).

No.	Rate	Process	Rate coefficient†
1a	k_{vt,v_2,N_2}	$CO_2^i(v_d) + N_2 \rightleftharpoons CO_2^i(v_d-1) + N_2$	$k\times7\times10^{-17}\ \sqrt{T} + 6.7\times10^{-10}\ \exp(-83.8/T^{1/3})$‡
1b	k_{vt,v_2,O_2}	$CO_2^i(v_d) + O_2 \rightleftharpoons CO_2^i(v_d-1) + O_2$	$k\times7\times10^{-17}\ \sqrt{T} + 1.0\times10^{-9}\ \exp(-83.8/T^{1/3})$‡ ($k$=1, 3, 4.5, 6.75, 9, 12 for v_d = 1, ..., 6)
1c	k_O	$CO_2^i(v_d) + O \rightleftharpoons CO_2^i(v_d-1) + O$	$3.5\times10^{-13}\ \sqrt{T}+2.32\times10^{-9}\ \exp(-76.75/T^{1/3})$
2a	$k_{vt,a}$	$CO_2^i(v_d,v_3) + N_2 \rightleftharpoons CO_2^i(v'_d,v_3-1)+N_2$, Δv_d=2-4	$1.10\times10^{-15}+1.14\times10^{-10}\ \exp(-72.3/\sqrt[3]{T})+2.3\times10^{-40}\,T^9$
2b	$k_{vt,b}$	$CO_2^i(v_d,v_3) + O_2 \rightleftharpoons CO_2^i(v'_d,v_3-1)+O_2$, Δv_d=2-4	$1.82\times10^{-15}+3.10\times10^{-11}\ \exp(-63.3/\sqrt[3]{T})+2.0\times10^{-31}\,T^6$
2c	$k_{vt,c}$	$CO_2^i(v_d,v_3) + O \rightleftharpoons CO_2^i(v'_d,v_3-1) + O$, Δv_d=2-4	$2\times10^{-13}\ (T/300)^{1/2}$
3	k_{vt,CO_2}	$CO_2^i(v_d,v_3) + CO_2^i \rightleftharpoons CO_2^i(v_d+1,v_3-1)+CO_2^i(v_d=1)$	$3.6\times10^{-13}\ \exp(-1660\,T+176948/T^2)$
4	$k_{vv,O2}$	$CO_2^i(v_d,v_3) + O_2 \rightleftharpoons CO_2^i(v_d+1,v_3-1) + O_2(1)$	3×10^{-15}
5a	k_{vv,v_2}	$CO_2^i(v_d) + CO_2^i \rightleftharpoons CO_2^i(v_d-1) + CO_2^i(v_d=1)$	$v_d\times2.394\times10^{-11}\ \exp(-14.085\,\Delta E/T)$
5b	$k_{vv,v_2,iso}$	$CO_2^i(v_d) + CO_2^j(v'_d) \rightleftharpoons CO_2^i(v_d-1) + CO_2^j(v'_d+1)$	i = 1; j = 2-4; 2.35×10^{-11}
6	k_{vv}	$CO_2(v_d,v_3)+N_2 \rightleftharpoons CO_2(v_d,v_3-1)+N_2(1)$	$5.0\times10^{-13}\ (300/T)^{0.5}$ for v_d = 0, 1, 3, 5, 7 $7.0\times10^{-13}\ (300/T)^{0.5}$ for v_d = 2, 4, 6
7a	k_{F1}	$CO_2(v_1,v_2^l,v_3) + N_2 \rightleftharpoons CO_2(v'_1,v'^{l'}_2,v_3) + N_2$	5.4×10^{-13} for $v_2 = v'_2 = 0$ or v_2 and $v'_2 \neq 0$
7b	k_{F2}	$CO_2(v_1,v_2^l,v_3) + N_2 \rightleftharpoons CO_2(v'_1,v'^{l'}_2,v_3) + N_2$	8.1×10^{-13} for all other cases
8	$k_{vv,iso}$	$CO_2^i(v_3) + CO_2^i(v'_3) \rightleftharpoons CO_2^i(v_3-1) + CO_2^i(v'_3+1)$	i = 1; $6.8\times10^{-12}\ v_3\ \sqrt{T}$ for j = 1, 3-6 i = 1; $2.8\times10^{-12}\ v_3\ \sqrt{T}$ for j = 2
9	$k_{O(^1D)}$	$N_2 + O(^1D) \rightarrow N_2(1) + O(^3P)$	$\epsilon\times2.1\times10^{-11}\ \exp(115/T)$ ϵ = 0.2×6.8 ($N_2(1)$ per $O(^1D)$ molecule)
10	k_{OH}	$N_2 + OH^*(v \leq 10) \rightarrow N_2(1) + OH^*(v-1)$	$\epsilon\times(0.06,0.1,0.17,0.3,0.52,0.91,1.6,11,4.8,6)\times10^{-13}$ for v = 1-10: ϵ = 3.92 ($N_2(1)$ per $OH(v)$ molecule)
11	k_{N_2,O_2}	$N_2(1) + O_2 \rightleftharpoons N_2 + O_2$	$2.6\times10^{-19} + 5\times10^{-13}\ \exp(-73.9/T^{1/3})$
12	$k_{N_2,O}$	$N_2(1) + O \rightleftharpoons N_2 + O$	$3.2\times10^{-15}\ (T/300)^{2.9}$

†Rate coefficient for the forward sense of the process in cm^3s^{-1}. ‡This rate is taken as $10^{-15}\,cm^3s^{-1}$ for temperatures lower than 150 K (see text). T is temperature in K. i and j are different CO_2 isotopologues. i=1–6 except as noted. v_d=$2v_1$+v_2, e.g., v_d=2 is for the states (10002, 02201, 10001).

particularly for the CO_2(01101) level, is still a major uncertainty in the calculation of its populations in the upper atmosphere and lower thermosphere. García-Comas et al. (2008) show a discrepancy of about a factor 4 between the rates measured in the laboratory and those deduced from atmospheric measurements. In this model, the value of 6×10^{-12} cm^3 s^{-1} at 300 K (Sharma and Wintersteiner, 1990; López-Puertas et al., 1992) is adopted maintaining its temperature dependency:

$$k_{O,v_2=1\rightarrow 0} = 3.5 \times 10^{-13}\sqrt{T} + 2.32 \times 10^{-9} \exp\left(\frac{-76.75}{T^{1/3}}\right). \tag{4.3}$$

The vibrational-vibrational (V-V) energy transfer of v_2 quanta among the different CO_2 isotopologues has the following scheme:

$$\begin{aligned} k_{vv,v_2} &: CO_2^i(v_d) + CO_2^i \rightleftharpoons CO_2^i(v_d - 1) + CO_2^i(v_d = 1) \text{ and} \\ k_{vv,v_2,iso} &: CO_2^i(v_d) + CO_2^j(v'_d) \rightleftharpoons CO_2^i(v_d - 1) + CO_2^j(v'_d + 1), \end{aligned} \tag{4.4}$$

where k_{vv,v_2} represents the V-V exchange for levels within a given isotope, and $k_{vv,v_2,iso}$, the exchange between two different isotopes.

The exchange rate of v_2 quanta in CO_2-CO_2 V-V collisions has been updated by increasing it in a factor of two (López-Puertas et al., 2009). In addition, a new V-V v_2 collisional scheme has been included based on the rate constants measured by Dang et al. (1983). The expressions for k_{vv,v_2} and $k_{vv,v_2,iso}$ are

$$k_{vv,v_2} = v_d \times 2.394 \times 10^{-11} \exp\left(\frac{-9.788\, c_2\, \Delta E}{T}\right) \tag{4.5}$$

$$k_{vv,v_2,iso} = 2.35 \times 10^{-11}, \tag{4.6}$$

where c_2 is the second radiative constant, 1.438777.

The processes of V-T collisional relaxation of CO_2(v_d,0) with N_2 and O_2 drives the populations of the v_d levels below and around the mesopause:

$$k_{vt,v_d,N_2} : CO_2^i(v_2) + N_2 \rightleftharpoons CO_2^i(v_2 - 1) + N_2 \text{ and} \tag{4.7}$$

$$k_{vt,v_d,O_2} : CO_2^i(v_2) + O_2 \rightleftharpoons CO_2^i(v_2 - 1) + O_2, \tag{4.8}$$

where the rates values are

$$k_{vt,v_d,N_2} = k \times 7 \times 10^{-17}\sqrt{T} + 6.7 \times 10^{-10} \exp\left(\frac{-83.8}{T^{1/3}}\right) \tag{4.9}$$

$$k_{vt,v_d,O_2} = k \times 7 \times 10^{-17}\sqrt{T} + 1.0 \times 10^{-9} \exp\left(\frac{-83.8}{T^{1/3}}\right), \tag{4.10}$$

with k = 1, 3, 4.5, 6.75, 9, 12 for v_2 = 1, ..., 6 (García-Comas et al., 2008). Below 150 K no measurements were reported for these rates, and the extrapolated values from the fit of the measurements at higher temperatures resulted in very cold retrieved temperatures around the polar summer mesopause (García-Comas et al., 2011). For this reason, below 150 K, a constant value of 10^{-15} cm^3 s^{-1} is assumed.

The scheme for the V-T relaxation of $CO_2(0,0^0,1)$ in collisions with N_2 and O_2 is given by

$$k_{vt,a} : CO_2^i(v_d, v_3) + N_2 \rightleftharpoons CO_2^i(v'_d, v_3 - 1) + N_2, \text{with } \Delta v_d\text{=2-4, and} \quad (4.11)$$

$$k_{vt,b} : CO_2^i(v_d, v_3) + O_2 \rightleftharpoons CO_2^i(v'_d, v_3 - 1) + O_2, \text{with } \Delta v_d\text{=2-4,} \quad (4.12)$$

based on Taine and Lepoutre (1980) measurements. These processes have very important consequences for the population of $CO_2(0,0^0,1)$ in the mesosphere. The rate values (Inoue and Tsuchiya, 1975; Rosser et al., 1969; Rosser and Gerry, 1969; Siddles et al., 1994) are given by

$$k_{vt,a} = 1.10 \times 10^{-15} + 1.14 \times 10^{-10} \exp\left(-72.3/\sqrt[3]{T}\right) + 2.3 \times 10^{-40} T^9 \text{ and} \quad (4.13)$$

$$k_{vt,b} = 1.82 \times 10^{-15} + 3.10 \times 10^{-11} \exp\left(-63.3/\sqrt[3]{T}\right) + 2.0 \times 10^{-31} T^6. \quad (4.14)$$

Regarding the relaxation by O, the rate coefficient takes a value of $k_{vt,c} = 2 \times 10^{-13}(T/300)^{0.5}$ (López-Puertas et al., 1986b,a).

The collisional process of the relaxation of CO_2 v_3 to v_2 quanta during collision with a ground state CO_2 molecule is of little importance in the Earth's atmosphere, although it is crucial for Mars and Venus. Regarding the relaxation of v_3 to v_2 by collisions with O_2, it is not a significant producer of the CO_2 fundamental bending mode, but it is a significant loss mechanism for $CO_2(0,0^0,1)$, and is important also for determining the populations of $O_2(1)$ and $H_2O(0,1^1,0)$.

$$k_{vv,iso} : CO_2^i(v_d, v_3) + CO_2^i \rightleftharpoons CO_2^i(v_d + 1, v_3 - 1) + CO_2^i(v_d = 1) \text{ and} \quad (4.15)$$

$$k_{vv,O2} : CO_2^i(v_d, v_3) + O_2 \rightleftharpoons CO_2^i(v_d + 1, v_3 - 1) + O_2(1). \quad (4.16)$$

In the first case, the temperature dependency is given by (Lepoutre et al., 1977)

$$k_{vv,iso} = 3.6 \times 10^{-13} \exp(-1660\,T + 176948/T^2), \quad (4.17)$$

and in the second case it takes the constant value of $k_{vv,O2} = 3 \times 10^{15}$ (Alexander et al., 1968).

The V-V coupling of $CO_2(v_3)$ with N_2 has the form of

$$k_{vv} : CO_2^i(v_d, v_3) + N_2 \rightleftharpoons CO_2^i(v_d, v_3 - 1) + N_2(1). \quad (4.18)$$

These processes are of special interest in determining the populations of CO_2 isotopes, which significantly affected by the population of $N_2(1)$. Because of the infrared inactivity of $N_2(1)$, the energy absorbed from solar radiation by CO_2 in the near infrared (4.3 and 2.7 μm) is redistributed by these collisional processes among the $(v_d,1)$ states of all CO_2 isotopes. In addition, it also takes into account the excitation of these levels from other non-LTE sources such as $O(^1D)$ and OH(v $\leq$ 10), which previously excite $N_2(1)$. The temperature dependency is given by (Inoue and Tsuchiya,

1975; López-Puertas et al., 2005)

$$k_{vv} = 5.0 \times 10^{-13}(300/T)^{0.5} \text{ for } v_d = 0, 1, 3, 5, 7 \tag{4.19}$$

$$k_{vv} = 7.0 \times 10^{-13}(300/T)^{0.5} \text{ for } v_d = 2, 4, 6. \tag{4.20}$$

The relaxations within the CO_2 equivalent groups, i.e., all those levels having the same v_d, e.g. (10011, 10012, and 02211), sometimes called the Fermi coupled levels, are discussed in López-Puertas et al. (2005) and in more detail in Chapter 5. The solar pumping occurs only in allowed bands, but the exchange of energy between near-resonant high energy levels allows this energy to be re-emitted in other hot bands. These processes, k_{F1} and k_{F2} in Table 4.1, have rate coefficients of:

$$k_{F1} = 5.4 \times 10^{-13} \text{ for } v_2 = v_2' = 0 \text{ or } v_2 \text{ and } v_2' \neq 0; \tag{4.21}$$

$$k_{F2} = 8.1 \times 10^{-13} \text{ for all other cases.} \tag{4.22}$$

As we described before, the excitation of N_2 is very important due to the rapid V-V energy exchange between $N_2(1)$ and the $CO_2(v_3)$ levels. During daytime, the N_2 is excited from the collisions with electronically excited atomic oxygen, $O(^1D)$, and, at night, from the $OH(v \leq 10)$ vibrationally excited levels:

$$k_{O(^1D)} : N_2 + O(^1D) \rightarrow N_2(1) + O(^3P) \text{ and} \tag{4.23}$$

$$k_{OH} : N_2 + OH^*(v \leq 10) \rightarrow N_2(1) + OH^*(v-1). \tag{4.24}$$

The value for the rate corresponding to $O(^1D)$ collisions is taken from Ravishankara et al. (2002),

$$k_{O(^1D)} = \epsilon \times 2.1 \times 10^{-11} \exp\left(\frac{115}{T}\right), \tag{4.25}$$

where $\epsilon = 0.2 \times 6.8$ ($N_2(1)$ per $O(^1D)$ molecule). The rate coefficients for k_{OH} are $k_{OH} = \epsilon \times (0.06, 0.1, 0.17, 0.3, 0.52, 0.91, 1.6, 11, 4.8, 6) \times 10^{-13}$ for $v = 1$–10 (Adler-Golden, 1997); with $\epsilon = 3.92$ ($N_2(1)$ molecules per $OH(v)$ molecule) (López-Puertas et al., 2004).

The quenching of $N_2(1)$ is mainly due to collisions with molecular and atomic oxygen. In the collisional process

$$k_{N_2,O_2} : N_2(1) + O_2 \rightleftharpoons N_2 + O_2, \tag{4.26}$$

part of the vibrational energy of N_2 is transferred to the O_2 molecule (being an important excitation mechanism of O_2). The temperature dependency is given by (Gregory et al., 1983; Maricq et al., 1985)

$$k_{N_2,O_2} = 2.6 \times 10^{-19} + 5 \times 10^{-13} \exp\left(-\frac{73.9}{T^{1/3}}\right). \tag{4.27}$$

Regarding the N_2 quenching process by collisions with atomic oxygen,

$$k_{N_2,O} : N_2(1) + O \rightleftharpoons N_2 + O, \tag{4.28}$$

where the rate value is $k_{N_2,O} = 3.2 \times 10^{-15} \exp(T/300)^{2.9}$ (Whitson and McNeal, 1977).

4.4. The Retrieval Control Program

The Retrieval Control Program, RCP, is a constrained least squares algorithm for retrieving the atmospheric parameters. RCP was conceived and developed at IMK with the non-LTE section implemented by the IAA team. The inputs to RCP are the initial guess and *a priori* information of the quantities to be retrieved, as well as the MIPAS level 1b measured spectra or, alternatively, spectra generated by KOPRA (or other similar forward model) when performing retrievals from synthetic spectra. These can be either calculated for LTE or for NLTE conditions with non-LTE populations calculated, e.g. by the GRANADA model.

Basically RCP solves iteratively the retrieval equation 3.53. The calculation of the model spectra and Jacobians is performed with KOPRA, being called in each step of the iteration. The measurement covariance matrix is calculated from the noise-equivalent spectral radiance provided with the L1b data. The regularization matrix is build from Tikhonov-type terms of different orders which can be combined to obtain a custom-tailored regularization for any particular retrieval problem. Alternatively, an externally generated regularization matrix can be read in. The RCP code uses, for stability, a Levenberg-Marquardt damping, λI, (see Chapter 3, Sec. 3.5) which is forced to be zero in the last iteration. Convergence is reached when the change of the retrieval parameters with respect to the previous iteration is smaller than a certain fraction ϵ of the expected noise retrieval error. All required control parameters such as the start value of λI, or the convergence parameter ϵ can be specified by the user in order to optimize the retrieval performance.

The principal output are the retrieved parameters but RCP can also provides diagnostics of the retrieval such as the averaging kernels, the noise error covariance matrix or the vertical resolution (see Section 3.5).

4.5. IMK-IAA non-LTE Retrieval Scheme

The combination of the three previously described codes, their interactions and the whole set of their respective inputs and outputs conform the IMK-IAA non-LTE retrieval scheme (see Fig.4.1).

This system was planned to improve the operational near-real time data processing developed by the European Space Agency (ESA) to process the MIPAS nominal mode data. The operational ESA retrieval scheme was designed to provide pressure,

temperature and volume mixing ratios of H_2O, O_3, HNO_3, CH_4, N_2O, and NO_2 within the first 3 hours after MIPAS spectra were taken (Ridolfi et al., 2000). The IMK-IAA retrieval scheme, in turn, is an offline scheme which can handle a larger number of species and in an extended altitude range, can be applied to all the MIPAS observational modes (including the middle and upper atmosphere modes), can handle non-LTE, and does not make a number of approximations which, in principle, make the retrievals more accurate.

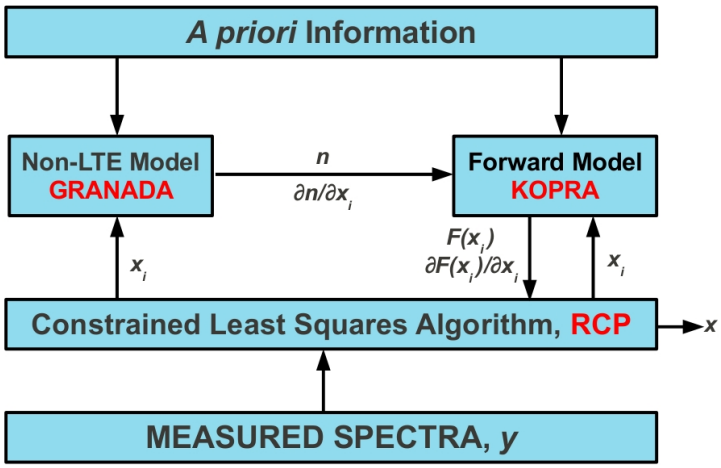

Figure 4.1: The IMK-IAA non-LTE retrieval scheme. The term x_i refers to the vector of the retrieval parameters within each iteration step, x to the output vector of retrieval parameter, and n to the non-LTE populations from GRANADA. KOPRA calculates the simulated spectra, $F(x_i)$, and the Jacobians, $\partial F(x_i)/\partial x_i$ at each iteration.

In summary, the retrieval scheme works following these basic steps: i) the *a priori*[2] information is introduced in KOPRA and GRANADA; (ii) the latter performs the calculation of the non-LTE populations; iii) KOPRA then takes the outputs from GRANADA for the calculation of the radiances and the Jacobians; iv) the simulated spectra from KOPRA and the measured L1b MIPAS spectra (or synthetic spectra) are introduced in the constrained least squares algorithm, RCP, for iteration; v) if the result does not satisfy the convergence criterion, the result is sent back to KOPRA and GRANADA for recalculation. Once the criterion is satisfied, the retrieved L2 data are finally obtained.

[2]In some cases the initial guess is used as *a priori*.

Chapter 5

Non-LTE Collisional Rates from MIPAS Data

Abstract

In this chapter we present the retrieval of several vibrational-vibrational (V-V) and vibrational-thermal (V-T) collisional rate coefficients affecting the populations of the CO_2 levels emitting at 10, 4.3 and 2.7μm from high resolution limb atmospheric spectra taken by MIPAS. The special characteristics of the MIPAS instrument (see Chapter 2) allows measuring the atmospheric limb emission in a wide altitude range, from 20 to 170 km in its middle and upper atmosphere modes, and hence obtain information on the temperature dependence of the collisional rates. In particular, the coefficients and their temperature dependence in the 130-250 K range of the following processes are retrieved: $CO_2(v_d, v_3)+N_2 \rightleftharpoons CO_2(v_d, v_3–1)+N_2(1)$ with $v_d = 2v_1 + v_2$=2, 3 and 4; $CO_2(v_1, v_2, l, 1, r)+M \rightleftharpoons CO_2(v'_1, v'_2, l', 1, r')+M$ with $\Delta v_d = v'_d - v_d = 0$ and Δl=0; and with Δv_d=0 and $\Delta l \neq 0$. In addition, we have also retrieved the thermal relaxation of $CO_2(v_3)$ into the v_1 and v_2 modes, e.g., $CO_2(v_d, v_3) + M \rightleftharpoons CO_2(v'_d, v_3–1) + M$ with Δv_d=2-4 and Δv_3=–1; and the efficiency of the excitation of $N_2(1)$ by $O(^1D)$. All of them were retrieved with a much better accuracy than were known before. The new rates have very important effects on the atmospheric limb radiance in the 10, 4.3 and 2.7 μm spectral regions (5-8% at 4.3 μm) and allow a more accurate inversion of the CO_2 volume mixing ratio in the mesosphere and lower thermosphere from measurements taken in those spectral regions. This work has been published in Jurado-Navarro et al. (2015c).

5.1. Introduction

As explained in Chapter 1, carbon dioxide, is an important greenhouse gas playing an essential role in the energy budget of the Earth's atmosphere. CO_2 originates strong atmospheric non-LTE (non Local Thermodynamic Equilibrium) infrared emission which is frequently use to infer its abundance in the middle/upper atmosphere.

The inversion of CO_2 abundances from atmospheric limb *emission* spectra requires, however, accurate and sophisticated modelling of the non-LTE populations of the states emitting at 10, 4.3 and 2.7 μm. These states are pumped by absorption of solar radiation, and are largely controlled by collisional vibrational-vibrational and

vibrational-thermal energy transfers to/from N_2 (see Chapter 4 Section 4.3).

The rates of these V-V and V-T processes are, however, poorly known. Only a few of them have been measured in the laboratory and when so, measurements were done long time ago as, e.g. the V-V transfer rate between $CO_2(00^01)$ and $N_2(1)$ (Inoue and Tsuchiya, 1975). Sometimes they were also derived from atmospheric emission observations (Nebel et al., 1994) but with large uncertainties and assuming a reference background atmosphere because the atmospheric state was not measured simultaneously.

Thus one of the aims of this work is, by taking the advantage of MIPAS high spectral resolution, its high sensitivity and its wide spectral range, to improve our knowledge of the collisional processes governing the non-LTE populations of the CO_2 levels emitting at 10, 4.3 and 2.7 μm. To reach that objective we have retrieved rate coefficients for a number of collisional processes affecting to the CO_2 states from MIPAS spectra. We describe in this chapter the methodology used and the results and conclusions obtained.

5.2. Retrieval Setup

As mentioned in Chapter 3, we have to make some a priori assumptions in order to stabilize the retrieval. The collisional rates are constrained to these a priori assumptions using a diagonal regularization matrix containing the related a priori variances, in the sense of maximum a posteriori (Rodgers, 2000). For the jointly fitted CO_2 profile, a Tikhonov-type smoothing constraint (Tikhonov, 1963) is used together with a strong diagonal constraint below 70 km. The latter forces the retrieved CO_2 in the stratosphere and lower mesosphere to be close to the well-known CO_2 mixing ratio in the homosphere. CO_2 a priori profiles have been taken from the Whole Atmosphere Community Climate Model with specified dynamics (SD-WACCM) simulations (Garcia et al., 2014) which is constrained with output from NASA's Modern-Era Retrospective Analysis (MERRA) (Rienecker et al., 2011) below approximately 1 hPa. Garcia et al. (2014) showed SD-WACCM simulations for Prandtl numbers (P_r) of 4 (standard) and 2, corresponding to lower and higher eddy diffusion coefficients respectively. Here we used the simulations for P_r=2, which gives an overall better agreement with ACE CO and CO_2, with MIPAS CO (Garcia et al., 2014), as well as with the MIPAS CO_2, as shown in Chapter 6.

The retrievals are performed using selected spectral regions (micro-windows) in the 4.3 and 10 μm regions which vary with tangent altitude in order to optimize computation time and minimize systematic errors (von Clarmann and Echle, 1998). In particular, error propagation due to horizontal inhomogeneities have been minimized by excluding opaque spectral lines which are insensitive to tangent point conditions.

In addition to the target retrieval variables, a height- and wavenumber-independent radiance offset and a continuum-like optical depth profile (below 60 km) are fitted jointly for each micro-window in order to compensate for offset calibration errors and spectrally smooth atmospheric contributions not reproduced by the radiative transfer

forward model.

To obtain the L2 data (retrieved quantities) from the L1b spectra, a sequence of preprocessing steps are required: i) Correction of the spectral shift, followed by the retrieval of temperature, horizontal temperature gradients, and elevation pointing from the 15 μm spectral region (García-Comas et al., 2014); ii) extension of the retrieved temperature profile above 100 km with those retrieved from the spectrally resolved NO 5.3 μm band (Bermejo-Pantaleón et al., 2011) and NRLMSIS-00 (Picone et al., 2002) above 170 km; iii) implicit determination of pressure by means of hydrostatic equilibrium (total density is obtained from pressure and temperature and using the ideal gas law); iv) retrieval of O_3 vmr (volume mixing ratio) from the 10 μm spectral region (Gil-López et al., 2005); and v) generation of atomic oxygen O(^3P) and O(^1D) profiles below 100 km with a photochemical model (Funke et al., 2012) constrained by the O_3 and pressure/temperature data obtained in the previous steps. Above 100 km, we took the O_2 and the atomic oxygen concentrations from the NRLMSIS-00 model, and also use the same photochemical model for the calculation of O(^1D) from the O_2 photodissociation (O_3 is not required in this region).

5.3. Microwindow Selection

The retrievals are performed from selected spectral regions which vary with tangent altitudes in order to optimize computation time, minimize systematic errors, and to avoid saturated spectral lines. The information coming from the CO_2 fundamental, first, second, third and fourth hot band emissions is mainly measured by the MIPAS channel D (1820-2410 cm^{-1}) near the 4.3 μm region. Additional information about the non-LTE population of the (00011) state, responsible for the 4.3 μm fundamental band, comes from the CO_2 laser bands measured by the MIPAS channels A (685-970 cm^{-1}) and AB (1020-1170 cm^{-1}) respectively near 10 μm (Jurado-Navarro et al., 2012, 2013). In order to obtain the information from all of these CO_2 bands, we used an extended set of 24 microwindows (MWs) covering these three channels. Considered spectral points within these MWs, vary with tangent height. That is, within each MW, a height-dependent mask of "sub-microwindows" is defined.

In this work we use the MIPAS spectra taken in its upper atmosphere observation mode (UA) from 40 km to 172 km (from high stratosphere to lower thermosphere including the mesosphere). Within these altitudes the non-LTE unsaturated lines gives an optimal sensitivity to the collisional rates involved in the retrieval with a good signal-to-noise ratio up to about 142 km.

The set of sub-microwindows was selected by analyzing the information in the calculated CO_2 vmr Jacobians, i.e. testing the sensitivity of the radiance to CO_2 vmr changes ($\partial \mathbf{F}(C\vec{O}_2)/\partial C\vec{O}_2$). This useful tool allows us to discriminate the lines with a local response from those opaque and saturated at any given tangent height. The Jacobians were computed using the GRANADA model (Sec. 4.2) and the KOPRA code (Sec. 4.1) for a typical mid-latitude reference atmosphere (April, 45°N) (see Funke et al., 2012).

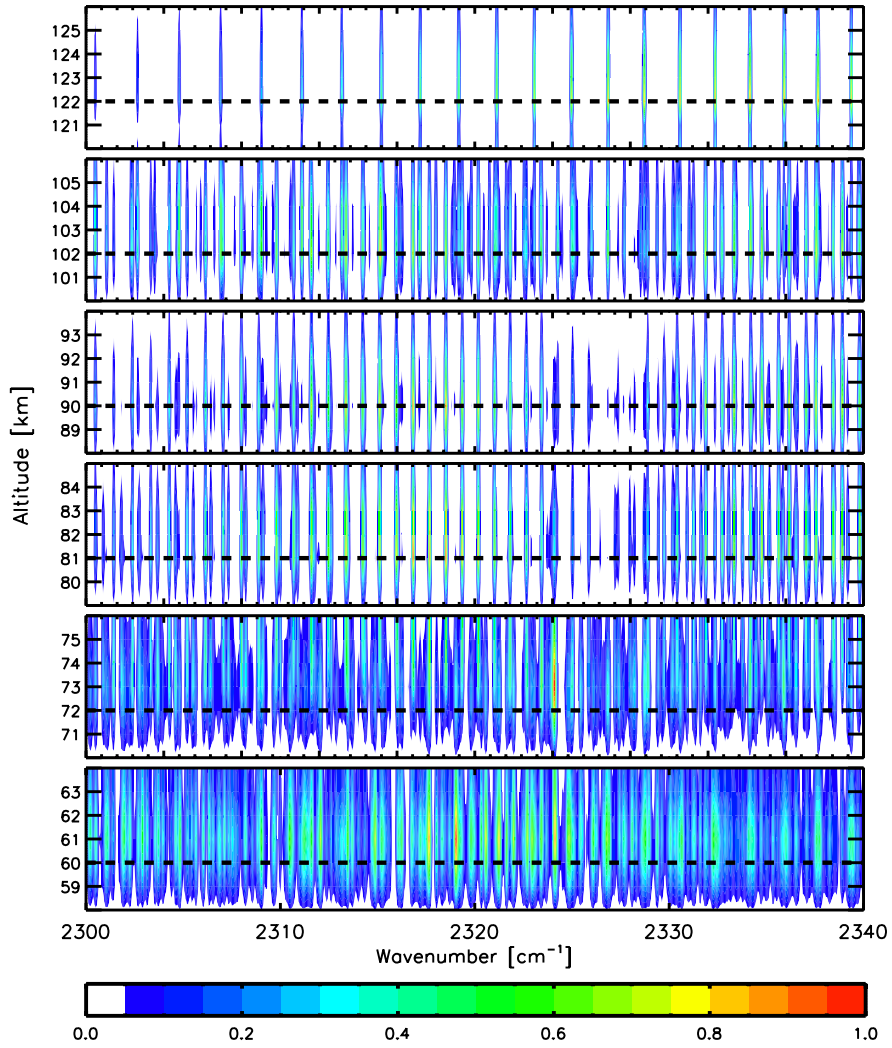

Figure 5.1: CO_2 Jacobians in the range 2300-2340 cm^{-1} for 5 tangent heights (60, 72, 81, 90 and 102 km). The Jacobians are normalized to the tangent height maximum value. The coolest colours indicates poor sensitivity and the warmest ones high sensitivity, white regions shows no sensitivity. Black dashed lines indicate the tangent height for each case.

Analysing the Jacobians in the 4.3 μm region (Figs. 5.1 and 5.2), we find that tangent heights from 60 to 81 km and above 102 km are mainly sensitive to the fundamental band lines while the second hot band contributes most in the altitude region from 84 to 102 km. The 2300-2340 cm^{-1} range (Fig. 5.1) includes the P branch of the fundamental band and the 2340 to 2380 cm^{-1} region (Fig. 5.2) includes its R branch. The P 16e (2335.9194 cm^{-1}) and the R 16e (2361.4660 cm^{-1}) are the strongest fundamental band lines in the 4.3 μm region. On the other hand, the second hot band has its P branch located from 2300 to 2325 cm^{-1} and the R branch in the 2330-2355 cm^{-1} range. As we know, the second hot band is constituted by 3 vibrational transitions, the most intense is $10^01 \rightarrow 10^00$, having its strongest lines at

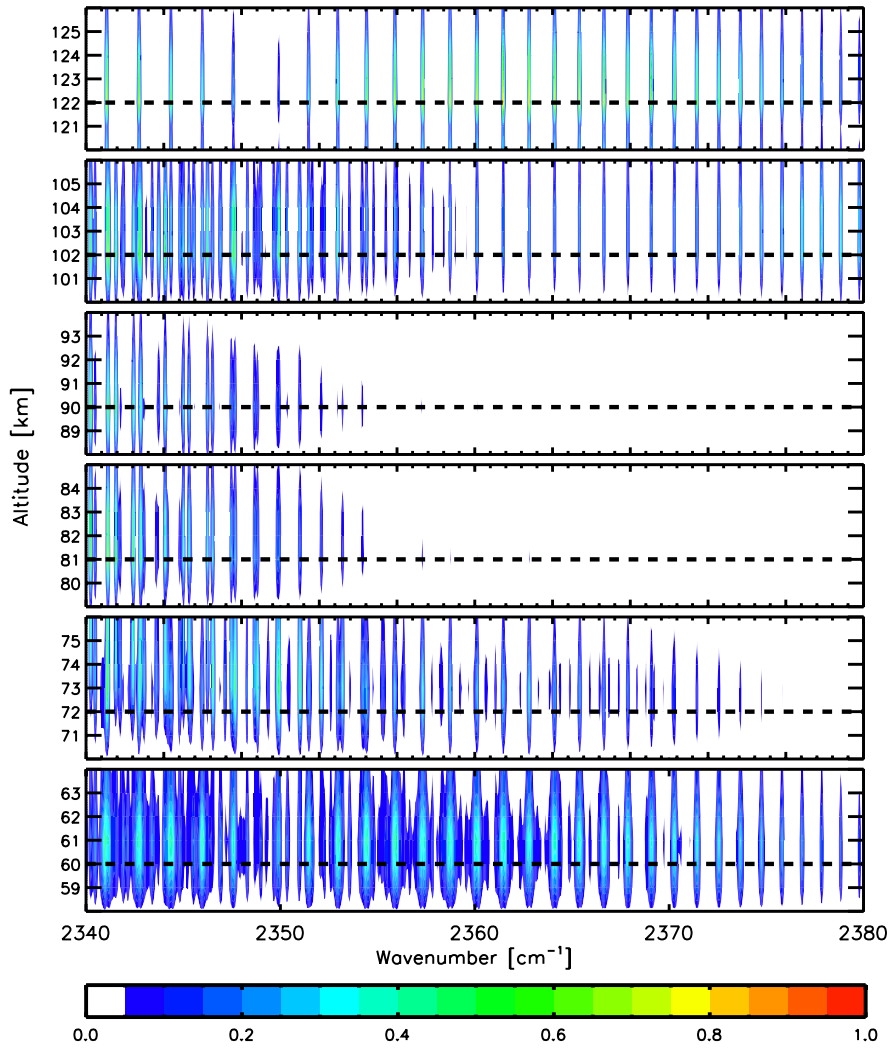

Figure 5.2: As Figure 5.1 but for the Jacobians in the range of 2340-2380 cm^{-1}.

2314.2246 cm^{-1} (P 16e) and at 2339.7941 cm^{-1} (R 16e).

Regarding the Jacobians in the 10 μm, sensitive lines of the transition $00^01 \rightarrow 10^00$ are found at 925-970 cm^{-1} (see Fig. 5.3) with the P16e and R16e lines at 947.7420 cm^{-1} and 973.2885 cm^{-1}, respectively, being the strongest ones. Those of the $00^01 \rightarrow 02^00$ band are located at 1020-1080 cm^{-1} (see Fig. 5.4) with the most intense lines P16e and R16e at 1050.4413 cm^{-1} and 1075.9878 cm^{-1}, respectively.

Spectral lines with strong non-local responses are mainly found in the fundamental and second hot bands at 4.3 μm. These lines are excluded from the MW selection at a given tangent height whenever the value of the Jacobian 5 km above this tangent height exceeds 40% of the value at the tangent height, or if its value 15 km above the tangent height is higher than 5%. This selection criterium warranties that we obtain information close to the tangent height at work, i.e. avoiding Jacobians with high values at altitudes well above the tangent height (long tails).

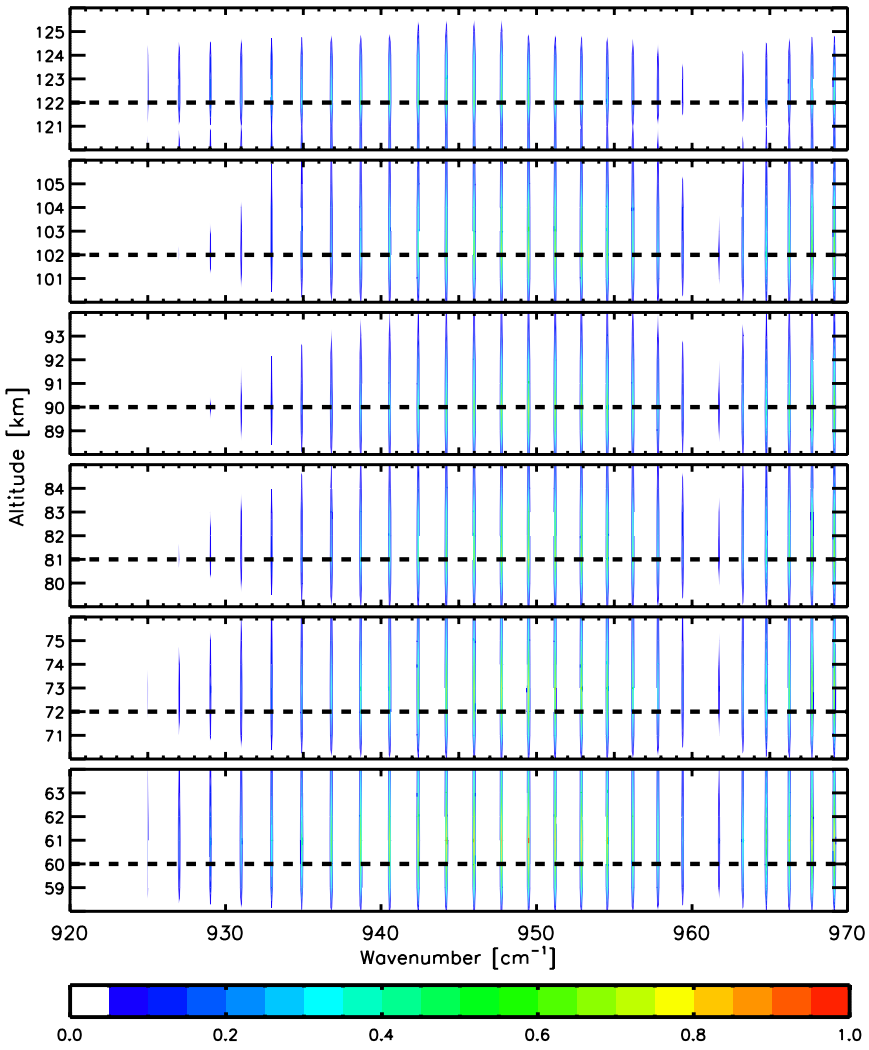

Figure 5.3: As Figure 5.1 but for the Jacobians in the range of 920-970 cm^{-1}.

In principle, only the stronger lines with high sensitivity should be considered in the MWs in order to optimize computation time. However, the Jacobians used in the MW selection were calculated only for the CO_2 vmr while our retrieval requires independent information on both CO_2 and collisional parameters. Therefore, broad sub-microwindows, including unsaturated spectral lines of a large variety of vibrational bands, have been added above 66 km in the 4.3 μm region in order to ensure independent information on both, the non-LTE collisional rates and the CO_2 abundance. The resulting height-dependent mask of sub-microwindows (also called occupation matrix) is shown in Figs 5.5 and 5.6.

Due to the need to consider broad sub-microwindows in the 4.3 μm region, the processor had to handle with heavy calculations. For this reason, the collisional rate retrieval had to be restricted to only for 4 representative days in 2010, 2 in solstice (17 January and 8 June) and 2 in equinox (30 March and 26 September).

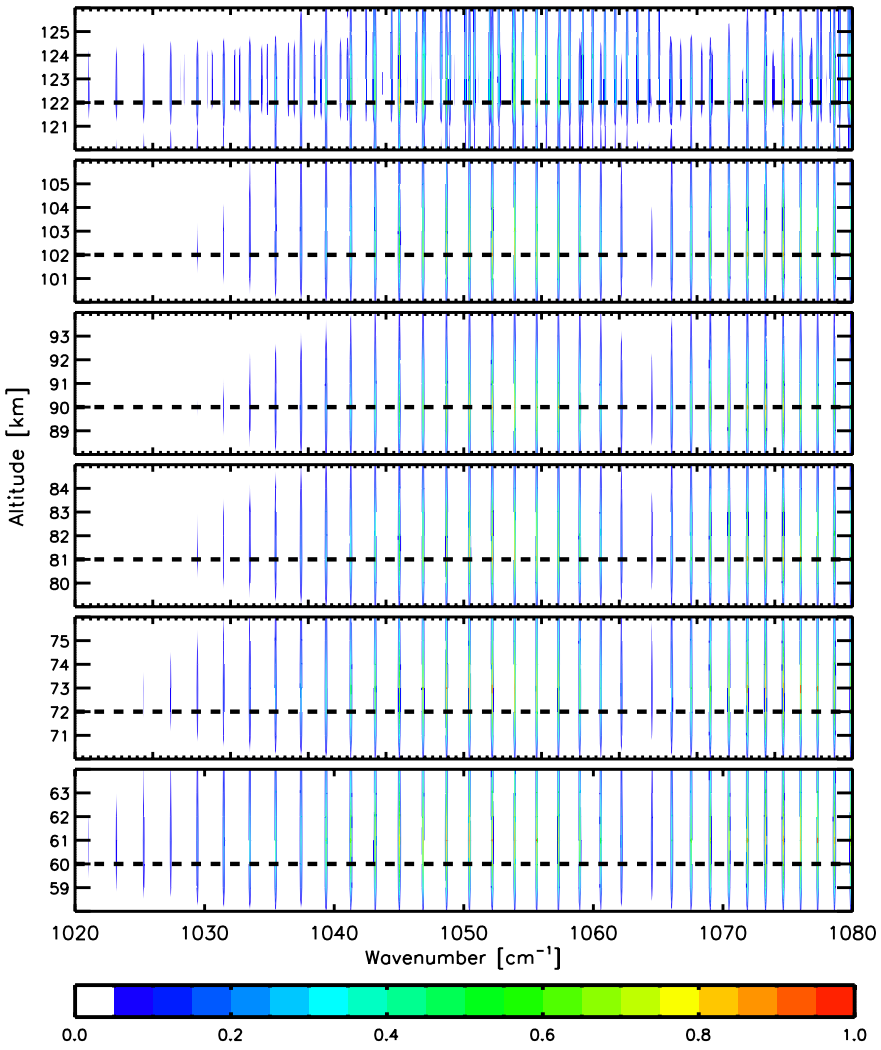

Figure 5.4: As Figure 5.1 but for the Jacobians in the range of 1020-1080 cm^{-1}.

5.4. Sensitivity of Non-LTE Populations and 4.3 μm Radiance to Collisional Rates

In Chapter 4, Sec 4.2, we described the non-LTE modelling of GRANADA including all collisional processes that control the populations of the CO_2 vibrational levels. Here, we have carried out sensitivity studies for the most important rate coefficients that control their populations in order to find out which of them will be retrievable from MIPAS spectra.

Table 5.1 is an extract of Table 4.1 showing the processes we have analyzed in detail, or that we have retrieved. Also, Figs. 5.7a-c show diagrams where we visualized the vibrational states connected by those collisional processes. We refer here to Sec. 4.3, where we explain the different notations used for the CO_2 vibrational states. Table A.1 is useful in this respect, since it shows the correspondence between

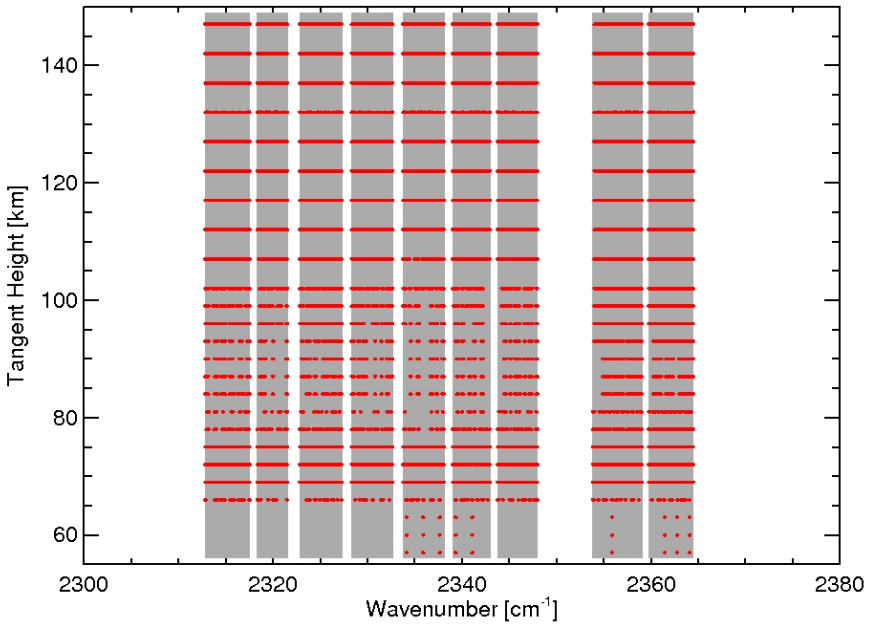

Figure 5.5: Occupation matrix of the joint retrieval of the rate coefficients and CO_2 vmr in 4.3 μm region. Shaded regions represent the micro-windows selected and red dots the sub micro-window masks at each tangent height.

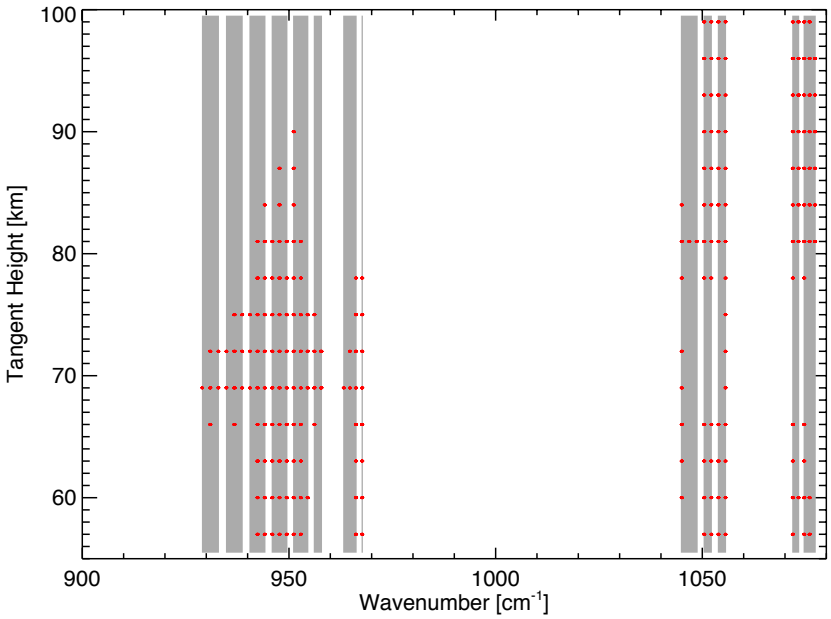

Figure 5.6: As Figure 5.5 but for the 10 μm region.

the two notations for most of the levels studied here.

Figures 5.8 and 5.9 show the vibrational temperature response of the main vibrational levels emitting at 4.3 μm (00011, 01111, 10011, 10012, and 02211 of the major

Table 5.1: Energy transfer processes studied in this work.

No.	Rate	Process	Rate coefficient (cm^3s^{-1}) (previous works)	Rate (this work) $k_0{}^{\ddagger}$	$\alpha^{\ddagger}$
1	k_{vv0}	$CO_2(v_d, v_3)^{\dagger}+N_2 \rightleftharpoons CO_2(v_d, v_3-1)+N_2(1)$, v_d=0	$5.0{\cdot}10^{-13}\sqrt{300/T}$	4.64*	0.64*
2	k_{vv1}	$CO_2(v_d, v_3)+N_2 \rightleftharpoons CO_2(v_d, v_3-1)+N_2(1)$, v_d=1	$5.0{\cdot}10^{-13}\sqrt{300/T}$	4.64*	0.64*
3	k_{vv2}	$CO_2(v_d, v_3)+N_2 \rightleftharpoons CO_2(v_d, v_3-1)+N_2(1)$, v_d=2	$5.0{\cdot}10^{-13}\sqrt{300/T}$	5.02±0.22	1.0
4	k_{vv3}	$CO_2(v_d, v_3)+N_2 \rightleftharpoons CO_2(v_d, v_3-1)+N_2(1)$, v_d=3	$5.0{\cdot}10^{-13}\sqrt{300/T}$	5.61±0.22	0.6
5	k_{vv4}	$CO_2(v_d, v_3)+N_2 \rightleftharpoons CO_2(v_d, v_3-1)+N_2(1)$, v_d=4	$5.0{\cdot}10^{-13}\sqrt{300/T}$	5.64±0.09	0.6
6	k_{F1}	$CO_2(v_1, v_2^l, 1)+M \rightleftharpoons CO_2(v_1', v_2'^{l'}, 1)+M$ Δv_d=0, Δl=0 e.g., $CO_2(1, 0^0, 1)+M \rightleftharpoons CO_2(0, 2^0, 1)+M$	$1.5{\cdot}10^{-13}$–$3{\cdot}10^{-11}$	7.04±0.33	0.0
7	k_{F2}	$CO_2(v_1, v_2^l, 1)+M \rightleftharpoons CO_2(v_1', v_2'^{l'}, 1)+M$ Δv_d=0, $\Delta l\neq$0 e.g., $CO_2(0, 2^2, 1) + M \rightleftharpoons CO_2(0, 2^0, 1) + M$, or	$1.5{\cdot}10^{-13}$–$2.4{\cdot}10^{-12}$	5.57±0.20	1.2
	$k_{F2'}$	$CO_2(1, 0^0, 1) + M \rightleftharpoons CO_2(0, 2^2, 1) + M$	$3{\cdot}10^{-13}$–$4.8{\cdot}10^{-12}$	5.57±0.20	1.2
8a	$k_{vt,a}$	$CO_2(v_d, v_3)+N_2 \rightleftharpoons CO_2(v_d', v_3-1)+N_2$ Δv_d=2-4	$f \cdot [1.10{\cdot}10^{-15} + 1.14{\cdot}10^{-10}\exp(-72.3/\sqrt[3]{T})]^{\star}$	f=0.7±0.13	
8b	$k_{vt,b}$	$CO_2(v_d, v_3)+O_2 \rightleftharpoons CO_2(v_d', v_3-1)+O_2$ Δv_d=2-4	$f{\cdot}[1.82{\cdot}10^{-15} + 3.10{\cdot}10^{-11}\exp(-63.3/\sqrt[3]{T})]^{\star}$	f=0.7±0.13	
9	$k_{O(^1D)}$	$N_2 + O(^1D) \rightarrow N_2(1) + O$	$f \cdot \epsilon \cdot 2.1{\cdot}10^{-11}\exp(115/T)^{\star}$ ϵ=0.2×6.8	f=1±0.15	
10	$k_{N_2,O}$	$N_2(1) + O(^3P) \rightarrow N_2 + O$	$4.5{\cdot}10^{-15}\,(T/300)^{1.5}$		

(†) $v_d = 2v_1 + v_2$. (‡) k_0 with estimated total errors (in units of $10^{-13}\,cm^3s^{-1}$) (see Table 5.2) and α as in $k = k_0\,(300/T)^{\alpha}$. *Used (not retrieved) in this work. $^{\star}f$ is equal to 1 in previous works.

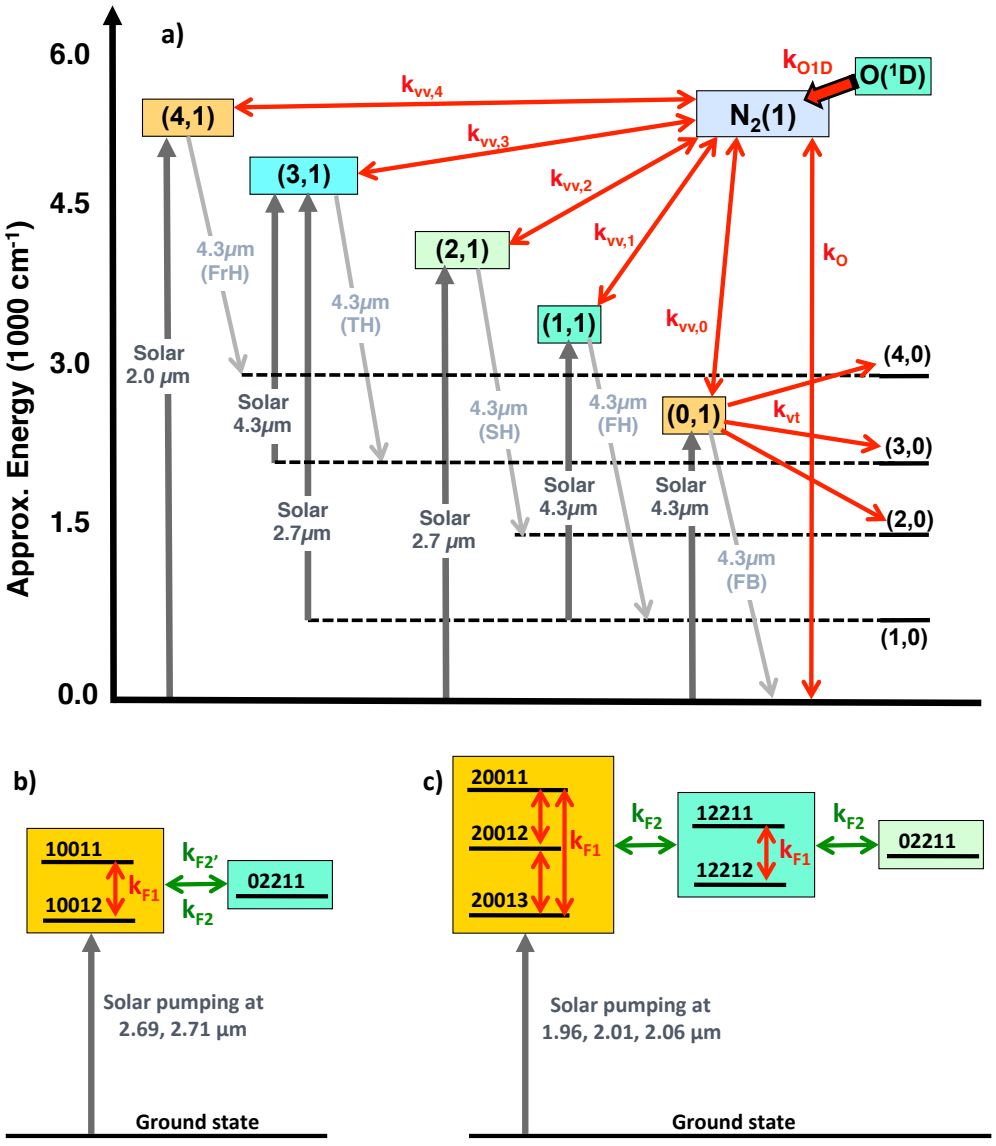

Figure 5.7: Schematic diagram showing the collisional rates k_{vv} considered in this work (see Table 5.1). Panel a) shows (in red) the processes $k_{vv,0}$, $k_{vv,1}$, $k_{vv,2}$, $k_{vv,3}$, $k_{vv,4}$, k_{vt}, and $k_{O(^1D)}$ of the major CO_2 isotopologue. The deactivation of $N_2(1)$ by $O(^3P)$, $k_{N_2,O}$, is also shown. The energy levels follow the (v_d, v_3) notation with $v_d = 2v_1 + v_2$. $N_2(1)$ and $O(^1D)$ energy levels are not at scale. Panels b) and c) show the k_{F1} (in red) and k_{F2} (in green) processes for the (v_d=2,v_3=1) and (v_d=4,v_3=1) levels, respectively. $k_{F2'}$ and k_{F2} in panel b) correspond to the processes between (10011–02211) and (10012–02211), respectively.

isotopologue, and 00011 of the second one) to 10% changes in the collisional rates $k_{vv,0}$, $k_{vv,1}$, $k_{vv,2}$, k_{F1}, k_{F2}, and k_{vt} (see Table 5.1 and Fig. 5.7a). The responses of these populations to 10% changes in the $k_{vv,3}$ and $k_{vv,4}$ rates are very small and are not shown. As we expect the response to be dependent on the temperature profile,

the sensitivity has been performed for typical, i.e., mid-latitudes, as well as extreme, polar summer- and polar winter-like, temperature profiles.

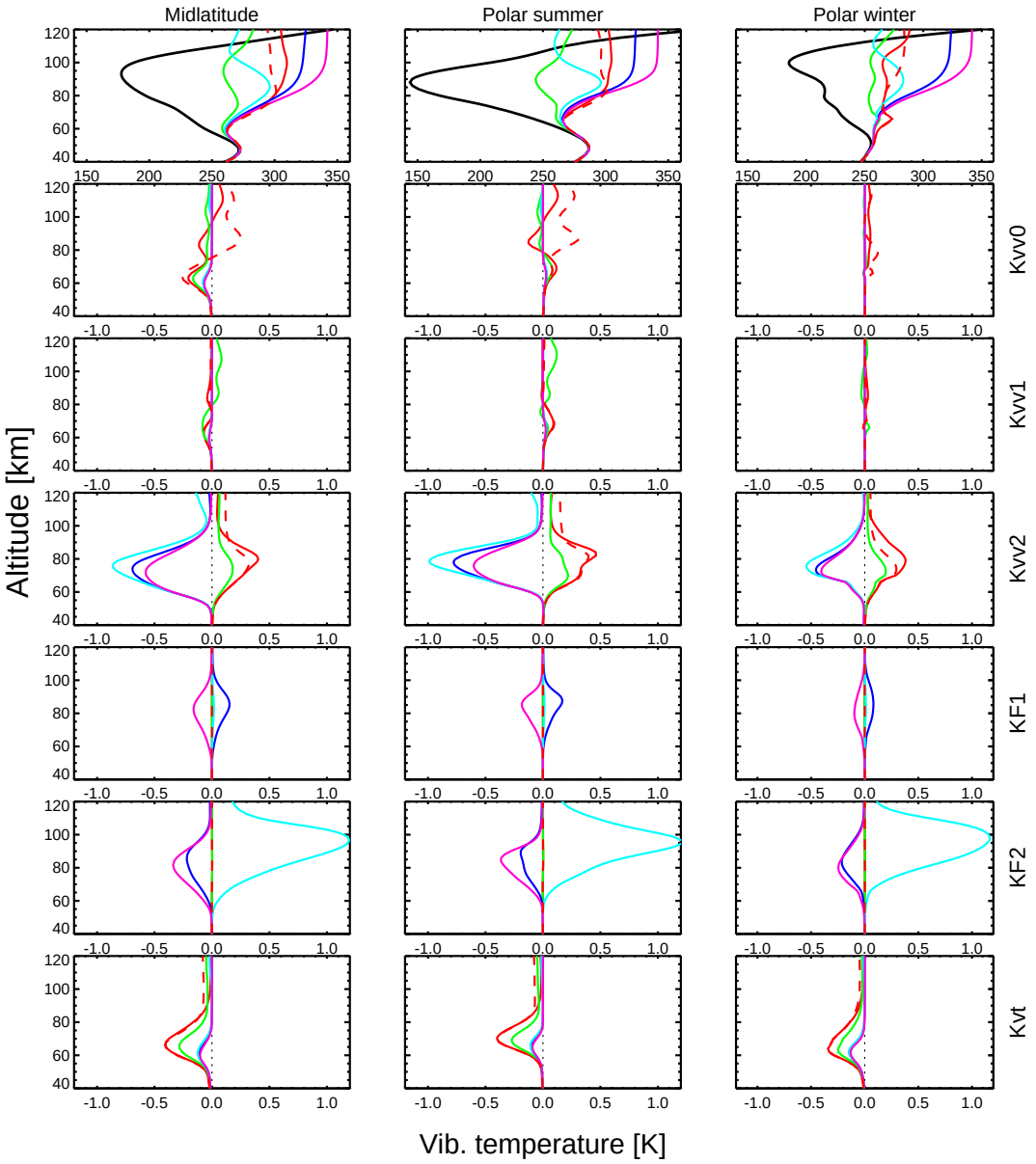

Figure 5.8: Sensitivity of the populations of the CO_2 levels 00011 (red solid: isotopologue 626, red dashed: isotopologue 636), 01111 (green), 10012 (dark blue), 02211 (light blue), and 10011 (magenta) to a 10% increase of the collisional rate constants for mid-latitude (left), polar summer (middle) and polar winter (right) conditions. From top to bottom: nominal vibrational temperatures; vibrational temperature changes due to an increase of k_{vv0}, k_{vv1}, k_{vv2}, k_{F1}, k_{F2}, and k_{vt} (see Table 5.1). The temperature profiles and reference atmospheres were taken from the case of April at 45°N (solar zenith angle of 44.5°) of Funke et al. (2012).

We see that there is a weak sensitivity to changes in $k_{vv,0}$ and particularly in $k_{vv,1}$

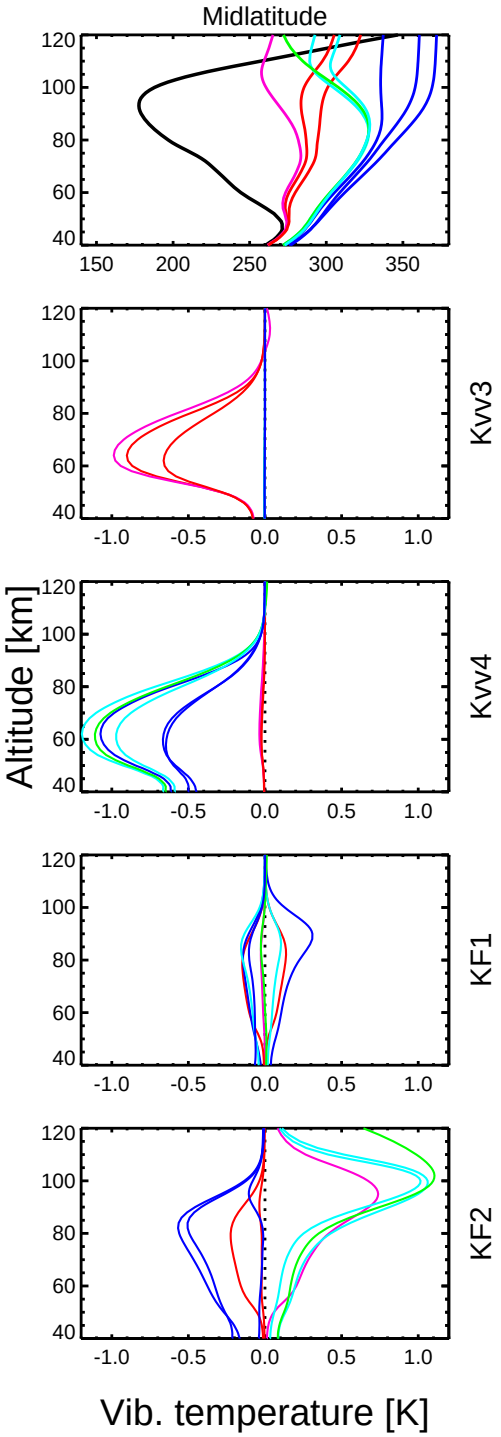

Figure 5.9: Sensitivity of the populations of the CO_2 levels 03311 (magenta), 1111f (red), 04411 (green), 1221f (light blue), and 2001f (dark blue) to a 10% increase of the collisional rate constants for midlatitude conditions. From top to bottom: nominal vibrational temperatures; vibrational temperature changes to due increases of k_{vv3}, k_{vv4}, k_{F1}, and k_{F2}.

(lower than 0.2 K) but a significant response to changes of $k_{vv,2}$, k_{F1}, k_{F2}, and k_{vt}. The response to $k_{vv,2}$ is particularly significant. The increase of this rate by 10% leads to a significant depletion of the populations of the 2.7 μm levels (10012, 02211 and 10011) and a simultaneous enhancement in the populations of the 00011 level of the two major isotopologues as well as that of 01111. Further, the response is found over a large altitude region, covering 50 to 95 km. As expected, the response is smaller for polar winter conditions when the mesospheric temperature is larger and more isothermal.

This large and altitude-extended response is very important since it would allow us to derive this rate accurately for different atmospheric conditions and therefore to gain information about its temperature dependence (Jurado-Navarro et al., 2015a, 2013). The response to the changes of the rates in the CO_2 limb spectral radiance as would be measured by MIPAS are shown in Figures 5.10 and 5.11 for tangent heights of 60 and 80 km, respectively. The effect of perturbing $k_{vv,0}$ and $k_{vv,1}$ is very small, $\leq$0.2 $\mathrm{nW/(cm^2\,sr\,cm^{-1})}$. This is about a factor of 15 smaller than the NESR (Noise Equivalent Spectral Radiance) of MIPAS in band D (1820-2410 $\mathrm{cm^{-1}}$) of 3 $\mathrm{nW/(cm^2\,sr\,cm^{-1})}$. Hence, the retrieval of these rates from single MIPAS spectra (as we have performed for the other rates) would be very difficult and unstable. Therefore we have not attempted to retrieve them.

On the other hand, the spectra clearly show the decrease of the emission from the 4.3 μm second hot bands when perturbing $k_{vv,2}$ for both tangent heights. These changes amount up to 3 $\mathrm{nW/(cm^2\,sr\,cm^{-1})}$ at 60 km and 4.5 $\mathrm{nW/(cm^2\,sr\,cm^{-1})}$ at 80 km.

The effects of perturbing $k_{vv,2}$ on the emission of the 4.3 μm fundamental is much smaller ($\sim$0.5 $\mathrm{nW/(cm^2\,sr\,cm^{-1})}$), and of opposite sign, but perceptible at a tangent height of 60 km (see the fourth panel of Figure 5.10).

The effects of perturbing the rates affecting the redistribution of energy among the solar pumped levels (k_{F1}) and between these and the adjacent non-pumped levels (k_{F2}) (see Table 5.1 and Figs. 5.7b and 5.7c) are shown in Figure 5.8 (5th and 6th rows) for the levels pumped by solar radiation in the 2.7 μm fundamental bands and in Figure 5.9 (4th and 5th panels) for the higher levels pumped by solar radiation in the 2.7 μm first hot bands and in the 2.0 μm bands. As expected, k_{F1} perturbs only the solar-pumped levels, increasing the population of the more weakly pumped level, 10012, at the expense of the more excited 10011 state. Vibrational populations are affected by these processes between 60 km and 100 km. Similarly, increasing the rate of the collisional coupling of the solar-pumped to the non-excited levels, depletes the populations of the former in favor of the latter. The enhancement of the non-pumped level is very large, extending to higher altitudes due to the absorption of upwelling radiation in the 4.3 μm hot band. We see similar effects in the higher energy levels in Fig. 5.9 (4th and 5th panels). All of these levels emit in the 4.3 μm region, generating the second (SH), third (TH) and fourth (FrH) hot bands (see Table A.1). The effects of the perturbations of these rates on the spectra as measured by MIPAS are shown in Figs. 5.10 and 5.11 (two bottom panels). We see that there is a significant change in the spectral radiance at both tangent altitudes, between about

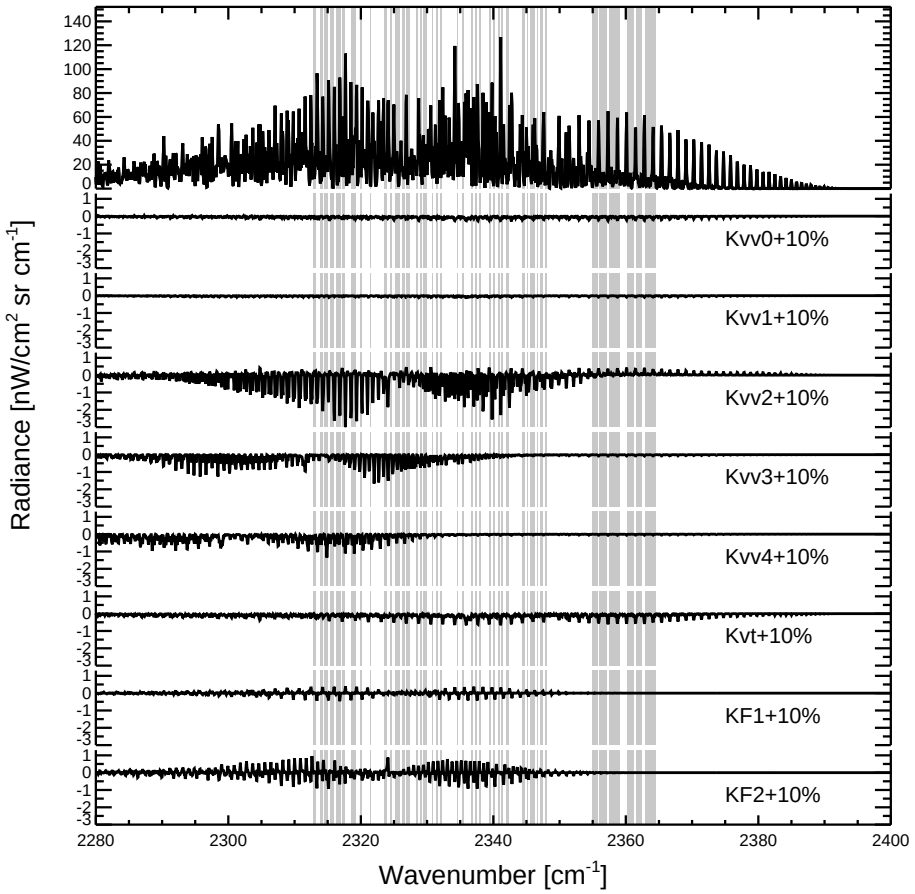

Figure 5.10: Sensitivity of CO_2 limb spectral radiances (tangent height of 60 km) as would be measured by MIPAS to a 10% increase of the collisional rate constants for midlatitude conditions (see Figs. 5.8 and 5.9). From top to bottom: simulated radiances; radiances changes to due an increase of k_{vv0}, k_{vv1}, k_{vv2}, k_{vv3}, k_{vv4}, k_{vt}, k_{F1}, and k_{F2}. Grey shaded regions indicate the spectral regions (micro-windows) used in the retrieval of the rates.

1.5 and 3.5 $\mathrm{nW/(cm^2\,sr\,cm^{-1})}$. The perturbations are more important at 80 km and k_{F2} shows a larger response.

The response of the population of the levels to the collisional rates $k_{vv,3}$ and $k_{vv,4}$ (see Table 5.1) are shown in Fig. 5.9 (2nd and 3rd panels). We see that only the more energetic levels directly affected by these rates are significantly perturbed while the populations of 00011, of the 2.7 μm levels, and of $N_2(1)$ (not shown) are hardly modified. That is important since the spectral lines of the bands originating from these levels will give us information on these rates, with no significant cross-talk to other rate coefficients. It is also noticeable that the sensitivity region is lower that for other rates, with a peak at around 60 km and significant down to as far as 40 km. The levels directly affected by these rates generate the third and fourth hot bands near 4.3 μm (see Table A.1). The mapping of the changes in their populations into the spectra are shown in Figs. 5.10 and 5.11 (5th and 6th panels) for 60 km and 80 km, respectively. They are significant, particularly at the 60 km tangent height.

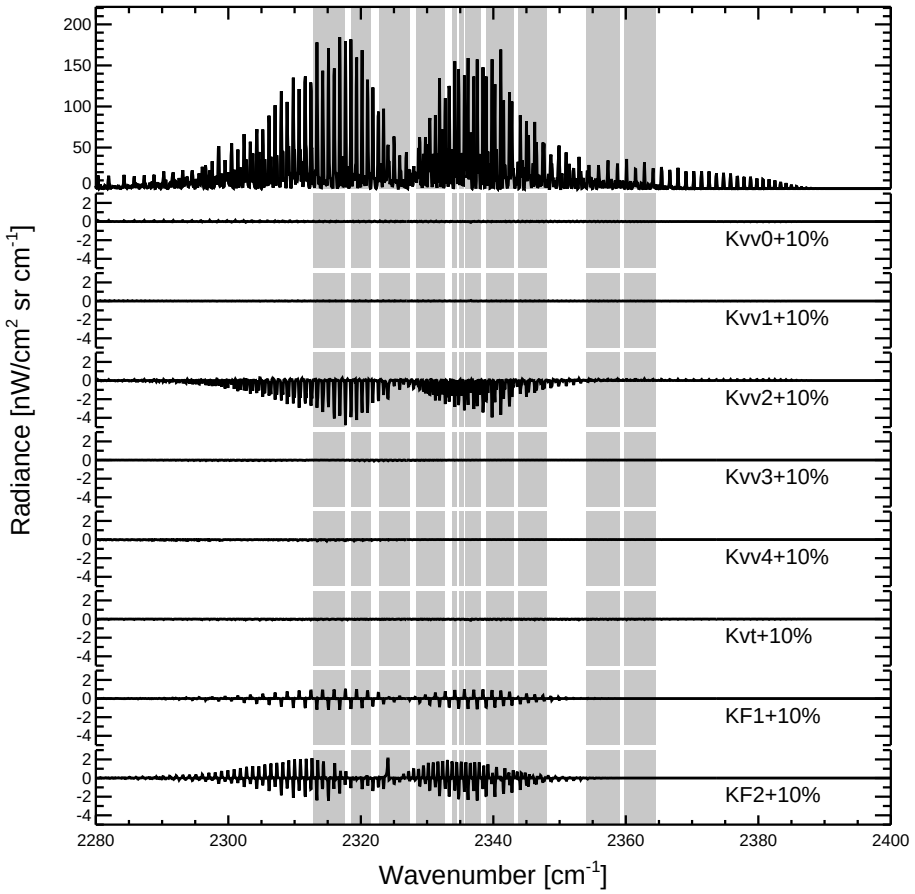

Figure 5.11: As Fig. 5.10, but for a tangent height of 80 km.

The sensitivity of the levels populations to k_{vt} is shown in Fig. 5.8, bottom row. As expected, when the rate increases, the population of 00011 significantly decreases. All other energy levels hardly change, except 01111, which is also significantly depopulated. Although the region of the change of the population of 00011 to this rate is slightly overlapping with that of $k_{vv,2}$ (4th row), they are very clearly distinguishable and hence, the emission from this energy level will provide independent information on the two parameters. The effects on simulated MIPAS spectra are shown in Figs. 5.10 and 5.11 (7th panel). We observe here that the major information comes from tangent heights closer to 60 km rather than 80 km.

In summary, we have demonstrated that MIPAS spectra in the altitude range from 40 to 100 km are very sensitive to the collisional rates $k_{vv,2}$, $k_{vv,3}$, $k_{vv,4}$, k_{F1}, k_{F2}, and k_{vt} (see Table 5.1). Furthermore, the different spectral responses and vertical structures of the perturbations of the rates provide independent information on each of the collisional parameters, and hence allows their joint retrieval and to gain information on their temperature dependencies. In the next section we further verify these results by applying the retrieval scheme to synthetic spectra.

5.5. Retrievals from synthetic spectra and error estimations

In this section we present the results of the joint inversion of the collisional rate coefficients and CO_2 vmr from synthetic spectra. The aim is to verify that the inversion scheme works as expected, to quantify how much information can be gained on each of the collisional rates, and to use this method to evaluate some systematic errors.

Synthetic spectra according to the MIPAS spectral specifications, including artificial NESR of 3 $\mathrm{nW/(cm^2\,sr\,cm^{-1})}$, have been computed for the mid-latitude, April 45°N reference atmosphere, SZA=44.5° (Funke et al., 2012) using the non-LTE populations shown in Figs. 5.8 and 5.9. Examples are shown in the top panels of Figures 5.10 and 5.11. We have performed retrievals of the state vector composed of the collisional rates $k_{vv,2}$, $k_{vv,3}$, $k_{vv,4}$, k_{F1}, k_{F2}, and k_{vt}, as well as the CO_2 abundance. The microwindows used in the joint retrieval are shown in Fig. 5.5, and by the grey shaded regions in Figs. 5.10 and 5.11, for the 4.3 μm region. Note that they change with the tangent height and they cover emissions from all the 4.3 μm bands sensitive to these parameters (see Table A.1). Additional micro-windows in the 10 μm region in the lines arising from the 00011→10002 band have also been included (see Fig. 5.6).

In the inversion of MIPAS spectra we have also derived the temperature dependencies of these rates, i.e., we have retrieved α in $k = k_0\,(300/T)^{\alpha}$. This has been carried out in an iterative way by varying the parameter α and minimizing the χ^2 of the residuals. In these simulations, however, we assumed that this dependence, i.e., α, was known.

The joint retrieval of the collisional rates and CO_2 was performed with initial guess rates equal to the true values perturbed by 20%. The CO_2 profile was systematically perturbed by a 5% increase at 60-90 km and by a 20% increase above 90 km.

The results showed that all inverted parameters were retrieved within ±1% of their true values, and thus that the retrieval was not over-regularized by the applied constraint. The CO_2 profile was also retrieved simultaneously with maximum deviations from the true profile smaller than 1% below 95 km, 1% at 100 km and 3% at 110 km.

Given the moderate vertical resolution of the retrieved CO_2 vmr profile (∼4 km), we have also estimated the impact of a possible systematic bias in the a priori CO_2 profile, particularly around the homopause, where CO_2 abruptly decreases with altitude (see Figure 5.13). This has been done by performing the retrieval with a different a priori CO_2 profile taken from SD-WACCM simulations for Prandtl numbers of P_r=4 (instead of P_r=2 used in the standard case). Garcia et al. (2014) have shown that the change in this parameter, equivalent to change the eddy diffusion parameter, significantly changes the altitude where CO_2 starts declining. The impact on the retrieved rates is negligibly small with deviations from the true values smaller than 0.1%. Hence, these results demonstrate the ability of the retrieval scheme to simultaneously retrieved those rates and the CO_2 profile with a high precision and a reasonably weak dependence on the a priori assumptions.

We have used this method to perform sensitivity studies in order estimate some of the known parameter errors in the retrieval of these parameters. Among those, we know that the abundances of atomic oxygen, O(^3P), and O(^1D), not measured simultaneously with MIPAS spectra, significantly affect to the population of the CO_2 levels (López-Puertas and Taylor, 2001; Kaufmann et al., 2002). The emission at 4.3 μm also depends very much on the solar flux, mainly at 4.3 and 2.7 μm.

O(^3P) and O(^1D) abundances, below about 95 km, are photochemically constrained by the retrieved O_3 from the same MIPAS spectra. Above 95 km, however, simultaneous O_3 observations are not available. O(^3P) has a large variability and it is not well known in the mesosphere and lower thermosphere (Kaufmann et al., 2014). Following previous studies (García-Comas et al., 2012; García-Comas et al., 2014) we have considered a 50% uncertainty in the O(^3P) concentration. O(^1D) has different major sources in the stratosphere/lower mesosphere and in the upper mesosphere/lower thermosphere. In the lower region it is mainly produced by O_3 photodissociation in the Hartley band (200-310 nm) (Brasseur and Solomon, 2005). Since the uncertainty in the solar flux in this spectral region is not very large, the O(^1D) uncertainty is dominated by the O_3 retrieval accuracy, estimated to be within 10% below 80 km. In the upper mesosphere/lower thermosphere O(^1D) is mainly produced from the photodissociation of O_2 in the Lyman$-\alpha$ and Schumann-Runge bands and continuum. The solar radiance at these wavelengths is rather uncertain (Ermolli et al., 2013) and the computation of the photo-absorption coefficient requires high spectral resolution. Overall we have considered an uncertainty of 30% in the abundance of O(^1D) above 80 km.

Solar fluxes near 4.3, 2.7, and 2.0 μm are calculated in the GRANADA model considering the time-dependent Sun-Earth distance. Attenuation by solar Fraunhofer lines is taken into account (Hase et al., 2006). The solar background radiance is expressed as a blackbody with an effective temperature T_e=$5450 + 0.25 \cdot (\tilde{\nu} - 2000)$, being $\tilde{\nu}$ wavenumber in cm^{-1}. This parametrization is similar to that developed by Platnick and Fontenla (2008) for 3.7 μm, and they agree within 0.5-1% at that wavelength. On the other hand, the calculated solar flux agrees within 0.1% with that of Kurucz (1995) in the 4.3, 2.7, and 2.0 μm spectral regions. Based on these results we have assumed an error of 1% in the solar fluxes. The mapping of these errors on the retrieved collisional rates is listed in Table 5.2. This table also includes other sources of errors as the gain calibration uncertainty of MIPAS, and the systematic error of temperature. The first was estimated to be in 1% in band D (Kaufmann et al. (2006), http://www.atm.ox.ac.uk/group/mipas/err/). However, more recent estimates suggest that this error is slightly larger, i.e., 1.25% [G. Perron, priv. comm.]. The temperature errors were taken as 1 K from 50 to 70 km, 2 K between 70 and 80 km and 5 K above (García-Comas et al., 2014).

We also included the error introduced by the uncertainty in the elevation pointing (tangent altitude). This is retrieved jointly with temperature from the 15 μm spectral region (García-Comas et al., 2014). However, there is little information on it above ~60 km. von Clarmann et al. (2003) estimated the total systematic error in the retrieved absolute pointing from 15 μm to be less than 200 m. Kiefer et al. (2007)

Table 5.2: Errors of the rate coefficients retrieved in this work (see Table 5.1).

Rate	Errors (%)							
	Random	Gain (1.25%)	Temp.†	Tangent altitude	[O(^3P)] (50%)	[O(^1D)]‡	Solar flux(1%)	Total
k_{vv2}	0.16	4.0	0.6	0.81	0.05	1.4	2.6	5.1
k_{vv3}	0.09	1.9	3.5	0.30	0.06	0.8	0.18	4.1
k_{vv4}	0.08	1.8	0.6	0.08	0.38	0.07	2.7	3.3
k_{F1}	0.09	0.8	4.6	1.2	0.22	0.11	0.33	4.8
k_{F2}	0.09	1.5	3.1	2.2	0.11	0.23	0.61	4.1
f_{vt}	0.19	9.2	2.9	0.47	3.1	11	4.3	15

†1 K at 50-70 km, 2 K at 70-80 km; 5 K above 80 km. ‡10% below 80 km and 30% above.

characterized the accuracy of the engineering information of the MIPAS elevation pointing and found that the relative pointing errors, i.e. uncertainties in the altitude differences between adjacent tangent altitudes, are on average about 200 m. Hence, in order to estimate the total systematic pointing error, both components (absolute and relative) have to be taken into account. Combining them quadratically leads to an uncertainty of 283 m, that constitute the pointing error included in the retrieved rates (see Table 5.2). Given the high spectral resolution of MIPAS, propagated errors arising from interfering species in this spectral region are negligible.

Table 5.2 shows that the major uncertainties in the $k_{vv,2}$ rate originate from the gain and solar flux uncertainties, with a non-negligible contribution from O(^1D). Adding all the sources quadratically they amount to a total error of 5.1%. The rate $k_{vv,4}$, affecting also solar-pumped levels, has similar error sources but the uncertainties induced by the gain and O(^1D) are smaller. The uncertainty of the $k_{vv,3}$ rate coefficient, affecting to the deactivation of levels not directly excited by solar radiation, is mainly driven by the temperature error. The same occurs to the k_{F1} and k_{F2} rate coefficients with overall errors of 4.8% and 4.1%, respectively. The error in the vibrational-thermal k_{vt} rate is, however, larger. Several sources contribute significantly: the gain, the kinetic temperature, atomic oxygen, the solar flux and, principally, the uncertainty in the concentration of O(^1D).

5.6. Results

The results of the retrieved collisional rates for all of the daytime scans of the four days of MIPAS UA measurements are shown in Figure 5.12 as a function of latitude. The mean values are listed in Table 5.1. As discussed above we have retrieved the rates as well as its temperature dependence in the form of $k = k_0\,(300/T)^{\alpha}$ through an iterative process. The mesospheric temperature changes significantly with latitude and season. However, Figure 5.12 shows that the retrieved k_0 values are essentially independent of latitude. This demonstrates that the retrieved temperature dependence, in the range of mesospheric temperatures, is very accurate. We estimated the error of α following the same procedure as we did for its derivation. We found that a perturbation of 10% introduces an appreciable increase in the χ^2; so this can be

considered as an upper limit of its error.

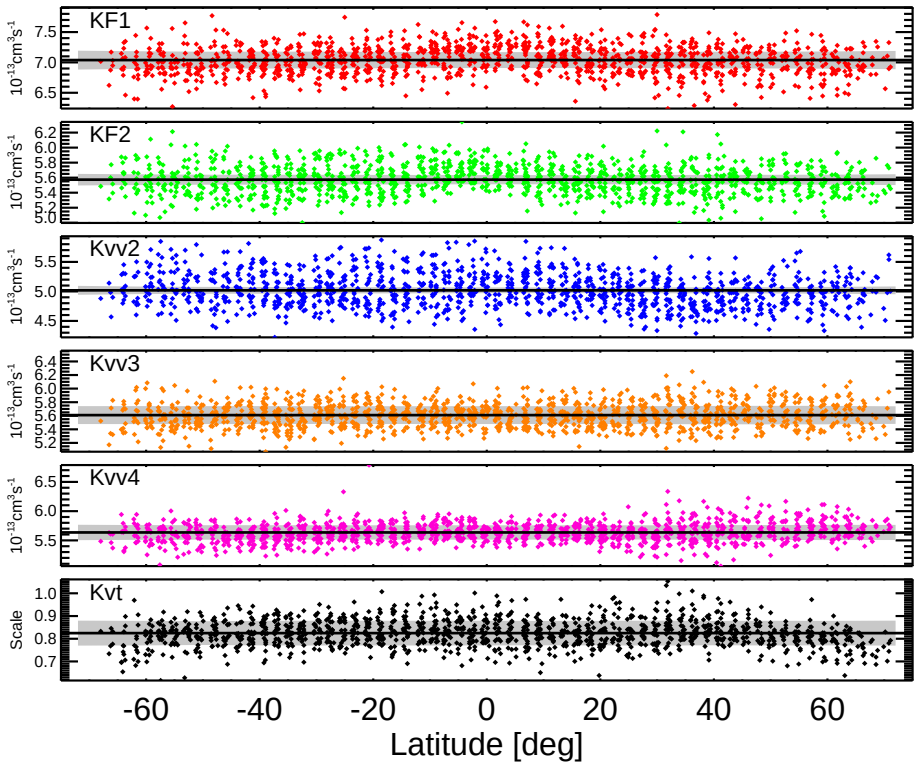

Figure 5.12: Retrieved collisional rates at 300 K, k_0, as function of scan latitude for all of the daytime scans of MIPAS spectra taken in the UA mode during 17 January, 30 March, 8 June and 26 September of 2010. The mean value from all latitudes is represented by solid lines. The grey shaded areas represent the noise error in the individual retrieved rates.

In Table 5.1 we also list the factor retrieved for the rate $k_{O(^1D)}$. This process enhances the population of $N_2(1)$ and because of its strong $k_{vv,0}$ coupling with CO_2 also largely controls the population of 00011 in the mesosphere. This process has, however, the opposite effect of the thermal relaxation of 00011 by air molecules, k_{vt} (process 8 in Table 5.1), and hence could not be jointly retrieved with k_{vt} in the inversion. We then followed a similar strategy as for determining the rate temperature dependence. That is, we retrieve k_{vt} assuming different values for $k_{O(^1D)}$. The retrievals showed that for changes $<$50% around the a priori values of the rates, we obtained a near one-to-one response. We then assumed as the best retrieved (k_{vt}, $k_{O(^1D)}$) pair the one that minimizes the χ^2 of the retrieval.

The retrieval noise, i.e. the mapping of the MIPAS NESR of 3 $\mathrm{nW/(cm^2\,sr\,cm^{-1})}$ into the rates, is generally very small (see grey shaded areas in Figure 5.12). However, the dispersion of the retrieved values is much larger than the noise error for all the rates. This suggests that the dispersion is caused by the random variability (stochastic errors) of the atmospheric parameters. Hence we have estimated the random error of the retrieved collisional rates (see Table 5.2), including the propagated uncertainties of not accurately known parameters, as the standard error of the retrieved values derived

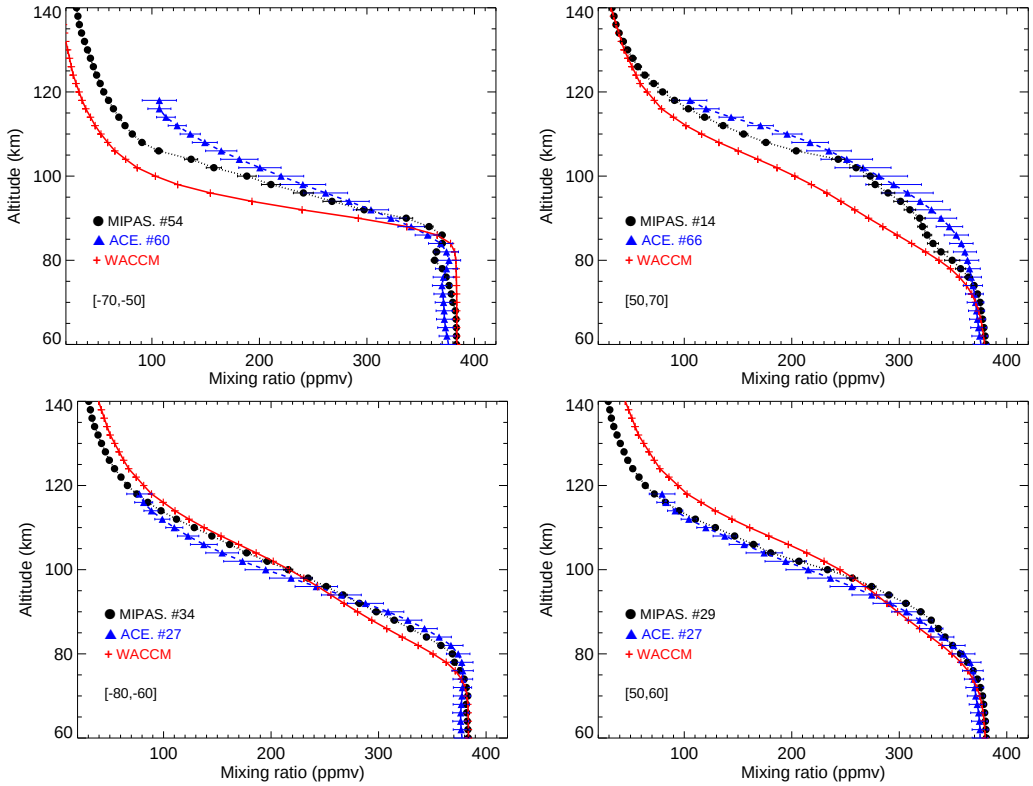

Figure 5.13: CO_2 vmrs retrieved jointly with the collisional rates and compared with co-located ACE measurements and the *a priori* SD-WACCM (P_r=2) CO_2 profiles. Top: solstice conditions (17 Jan 2010) for southern (polar summer) and northern (polar winter) conditions (left and right panels, respectively); and bottom: equinox conditions (30 March 2010) (left and right, respectively). The error bars in the ACE profiles are the total (random and systematic errors) (Beagley et al., 2010; Garcia et al., 2014). The small error bars of MIPAS represent only the noise error.

from all scans (see Figure 5.12).

As mentioned above, we have retrieved the CO_2 vmr jointly with the collisional rates. Although we have found (see Section 5.5) that there is only little dependence of the retrieved collisional rates on the CO_2 a priori profile, one may ask if the retrieved CO_2 is plausible, or if it is unrealistically biased. The latter could hint at a not yet identified systematic error source. Figure 5.13 shows the retrieved CO_2 profiles compared with co-located ACE measurements. There are very few contemporary measurements of CO_2 in the middle and upper atmosphere, only from ACE (Beagley et al., 2010) and SABER (Mertens et al., 2009; Rezac et al., 2015; Yue et al., 2015). SABER uses also the limb emission technique while ACE, using the solar occultation approach, is not affected by non-LTE. Hence ACE observations were taken here for comparison. The CO_2 from SD-WACCM simulations (P_r=2), which is used as a priori in the retrieval, is also shown for comparison. Due to the absorption technique used by ACE, there are very few profiles available for comparison (and located essentially only

at two different latitudes). In order to get a meaningful statistic we then considered the ACE measurements taken with ±3 days of the MIPAS measurements. We see that overall there is a very good agreement between the CO_2 of ACE and MIPAS. During solstice conditions (upper panels), the agreement is not as good but still within the error bars below ∼100 km. Only during polar summer at altitudes above ∼100 km, ACE and MIPAS profiles diverge, with MIPAS lying between the profile predicted by SD-WACCM and that measured by ACE. At northern latitudes the agreement is better. For equinox conditions, when the temperature and CO_2 gradients in the upper mesosphere/lower thermosphere are generally less pronounced, the agreement between ACE and MIPAS is excellent. In conclusion, the comparison of the jointly retrieved CO_2 vmr profiles to independent observations provides no hint at a systematic bias of the retrieved rates.

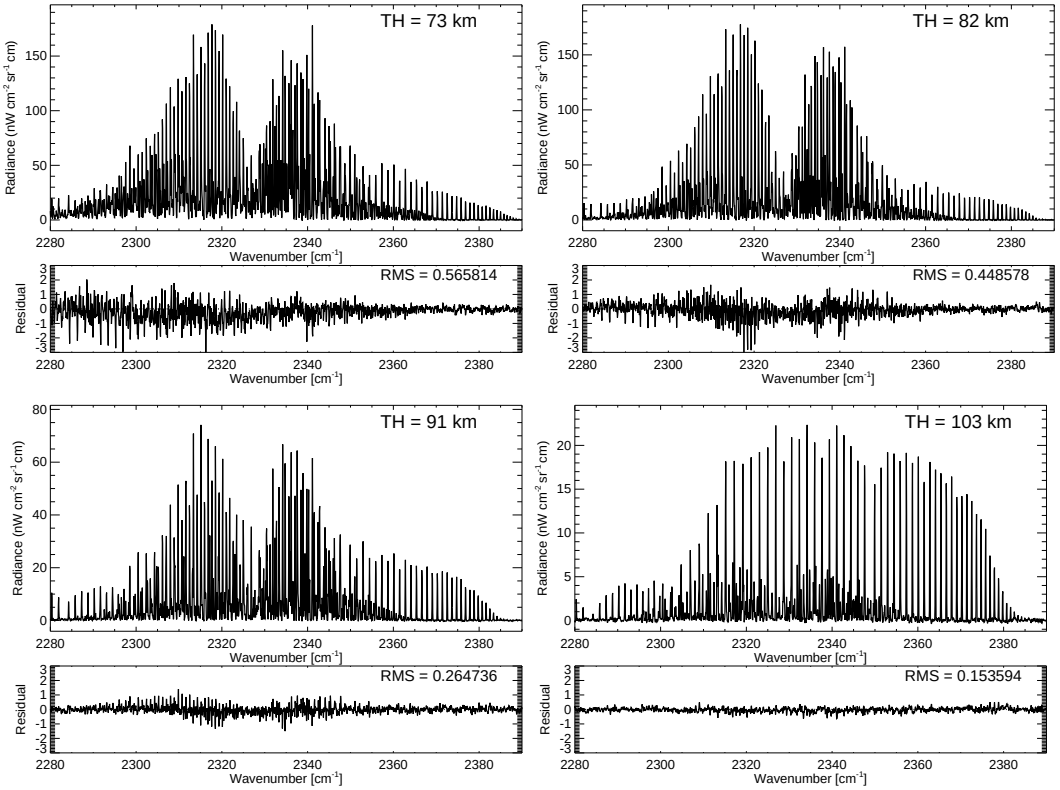

Figure 5.14: Co-added measured spectra (upper panels) and residuals, simulated−measured, (lower panels) at tangent heights of 73, 82, 91, and 103 km obtained from the retrievals for the four analysed days. The residuals are in the same radiance units of $\mathrm{nW/(cm^2\,sr\,cm^{-1})}$.

For a further check of the quality of the retrievals we looked at the spectral residuals at several tangent heights (see Figure 5.14). The residuals still show some systematic differences at lower tangent heights (73 km), but they are very small, in the order of ±1-2 $\mathrm{nW/(cm^2\,sr\,cm^{-1})}$, which is only ∼1% of the signal. At smaller wavenumbers (2280–2320 $\mathrm{cm^{-1}}$), a large fraction of these differences can be attributed

to the 4.3 μm fundamental band of second isotopologue, whose collisional rate with $N_2(1)$ was not retrieved here. This suggests that it is slightly different from the value for the most abundant isotopologue. Since ro-vibrational lines of the second isotopologue's fundamental band have been excluded from the micro-window selection, no impact on the retrieved rates is expected.

At 82 km the signal is very similar to that at 73 km but the root mean square (RMS) has decreased by a factor of 1.3, leading to an even better simulation of the measurements. The major reason is the better simulation of the mentioned isotopic band. At 91 km, the residuals are smaller, even in relative terms. We still appreciate some systematic residuals coming mainly from the second hot bands. However, given the excellent agreement of the observed and modelled band-averaged radiances (see below), these residuals are most likely introduced by a systematic error in the kinetic temperature distorting the rotational distribution. At higher altitudes, we observe that the measured spectra are very well reproduced. Overall, we have not found any significant feature (i.e. larger than $\simeq$1-2% of the signal) in the residuals, which provides confidence on the retrieved collisional rates.

To show more clearly the residuals in the different CO_2 4.3 μm bands (see Table A.1), we calculated the band-averaged radiance contributions in the measured and simulated spectra (see Figure 5.15). These were computed by weighting the total spectra by the line intensities of the corresponding band and normalizing it. Hence, they do not strictly represent the band contributions, since overlap and non-linearity in the radiative transfer are not properly taken into account, but are a good estimate of their contributions. Thus, some bands with strong overlap, as FrH2 and FrH3 (see Table A.1), were not shown. The very good agreement between measurements and simulations in all the bands and at all tangent heights is remarkable. The deviations are generally within $\pm$2-3%, and only at the uppermost tangent heights (above 115 km), where the signal-to-noise is smaller, the percentage deviations are slightly larger.

5.7. Discussion

In this section we discuss the retrieved collisional rates in the light of the values used in previous works and their effects on the CO_2 4.3 μm atmospheric emission. The rate $k_{vv,0}$ has not been retrieved here but it is discussed for completeness. This rate was measured by Inoue and Tsuchiya (1975) in the 150-300 K temperature range and it has been used as $k_{vv,0}$=5$\cdot 10^{-13}\sqrt{300/T}$ (see Table 5.1 and Figure 5.16a) in practically all the studies of the CO_2 atmospheric emission at 4.3 μm carried out so far. Thus, it was used in the analysis of SAMS measurements (López-Puertas and Taylor, 1989), of SPIRE observations (Nebel et al., 1994), and also introduced in the model of Shved et al. (1998) that was used in the retrieval of CO_2 from CRISTA spectra (Kaufmann et al., 2002) and more recently from SABER measurements (Rezac et al., 2015). By the way, we noted a typographical error in process 7 of Shved et al. (1998), where it should be $1/\sqrt{T}$ instead of $\sqrt{T}$. The same rate was used by Funke et al. (2012). Only the analysis of ISAMS measurements (López-Puertas et al., 1998a,b) suggested that a factor between 0.8 and 1.0 times the rate of Inoue and Tsuchiya

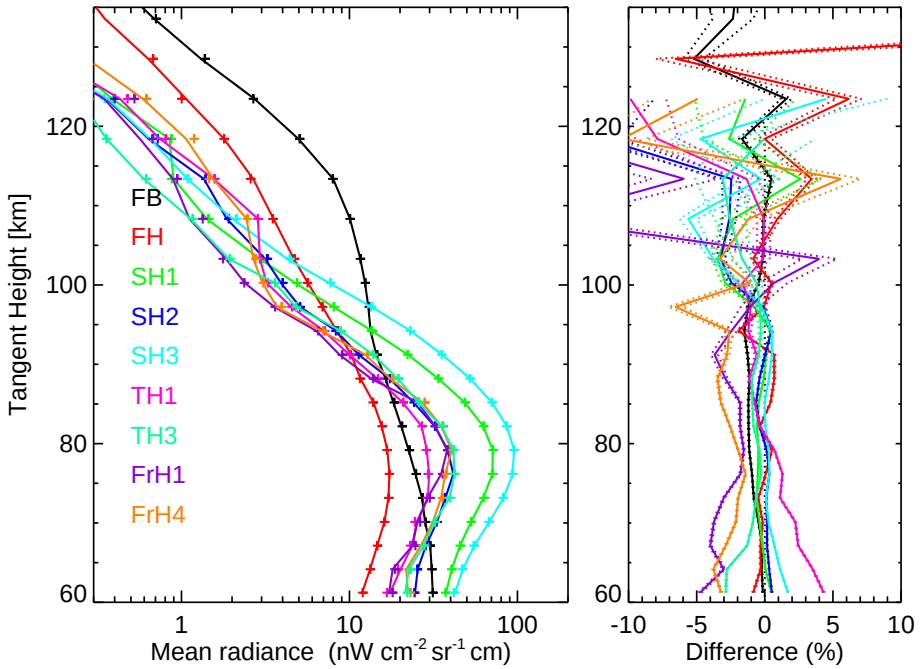

Figure 5.15: Measured (symbols) and simulated (lines) mean radiances in the 2280-2400 cm^{-1} interval) of different CO_2 4.3 μm bands (left panel) (see Table A.1) obtained in the retrievals for the four analysed days (see Fig. 5.14). Right panel shows the differences (simulated-measured) in percentage and their standard deviations (dotted lines).

(1975) was consistent with ISAMS radiances taken at a SZA lower and higher than 60°, respectively. In our analysis we use the fit $k_{vv,0}$=4.64$\cdot 10^{-13}(300/T)^{0.64}$ to the measurements of Inoue and Tsuchiya (1975), which is very similar to the usual form of $k_{vv,0}$=5$\cdot 10^{-13}\sqrt{300/T}$ (see Figure 5.16a).

The rate coefficient $k_{vv,1}$, where the excited state of CO_2 is 01111, has been taken equal to the rate $k_{vv,0}$ of the V-V exchange between CO_2(00011) and N_2 in all the studies mentioned above. Our simulations show that there is little sensitivity to this parameter (see Figure 5.8, 3rd row) and hence has not been retrieved here. We have also assumed the same value as for $k_{vv,0}$.

The rate coefficient $k_{vv,2}$ is crucial for calculating the atmospheric radiation near 4.3 μm at upper mesospheric and lower thermospheric limb paths since the emission from the populations of the 10011 and 10012 levels, generating the second hot bands, are largely controlled by this rate. As for $k_{vv,1}$, this rate has also been taken equal to that of the fundamental band, $k_{vv,0}$, in all previous studies, including the analysis of the SPIRE emission near 2.7 μm (Sharma and Wintersteiner, 1985), except for SAMS and ISAMS. López-Puertas et al. (1998a,b) found, as for $k_{vv,0}$, that a value between 0.8 and 1.0 times that of Inoue and Tsuchiya (1975) fitted better SAMS and ISAMS measurements. Note that López-Puertas and Taylor (1989) derived a rate twice that value but a subsequent analysis showed a factor of 0.8–1 (López-Puertas et al., 1998a,b). The value derived here is significantly larger at temperatures smaller than 300 K, ranging from a factor of 1 to 1.5 from 300 K to 130 K, which

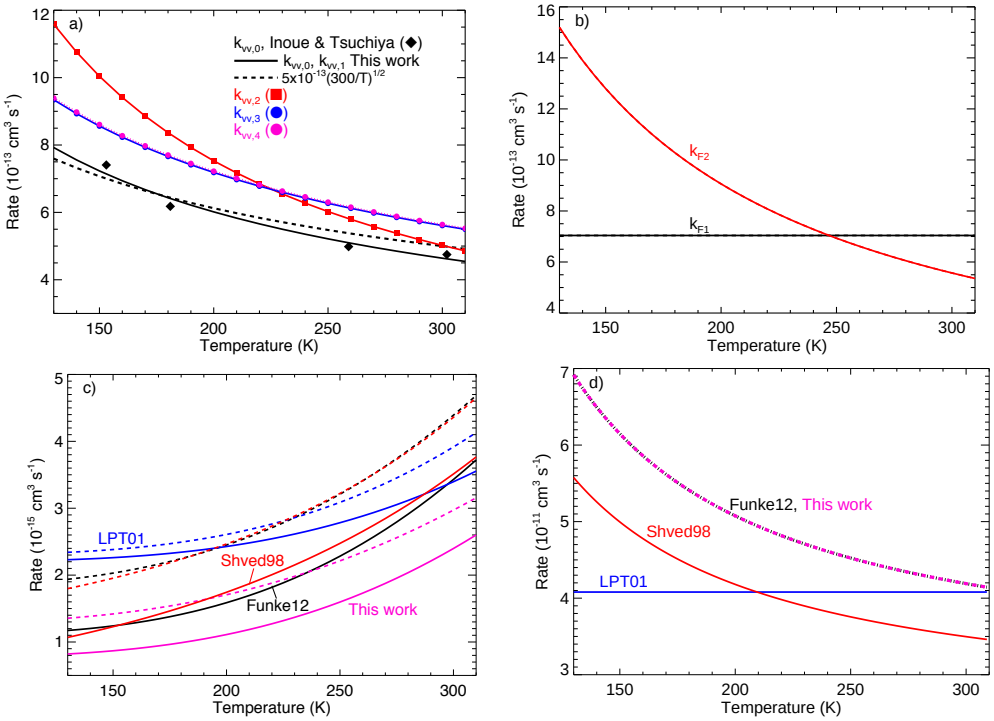

Figure 5.16: Temperature dependence of the collisional rates studied in this work. Panel a): $k_{vv,0}$-$k_{vv,4}$. Panel b) k_{F1} and k_{F2}. Panel c) k_{vt}; the solid lines represents collisions with N_2 and dashed lines collisions with O_2. Panel d) excitation of $N_2(1)$ from $O(^1D)$. Labels indicate references as follows "Shved 98": Shved et al. (1998); "LPT01": López-Puertas and Taylor (2001); and "Funke12": Funke et al. (2012) (see text for more details).

is caused by the stronger temperature dependence retrieved here (compare red and black-dashed lines in Fig. 5.16a). This dependence could not be accounted for by the likely variability of, or change in, any other atmospheric or collisional parameter. This is a major result that significantly affects the 4.3 μm atmospheric limb radiances at tangent heights below around 85-95 km, particularly at polar summer conditions.

The rates for the V-V collisional energy exchange between N_2 and the high-energy levels $CO_2(v_d, v_3{=}1)$ with $v_d{=}2v_1{+}v_2{=}3$ and 4, $k_{vv,3}$ and $k_{vv,4}$, have also been considered equal to $k_{vv,0}$ in most of previous analysis. Only Funke et al. (2012) considered these rates to be different from $k_{vv,0}$, but they have not been used in the analysis of previous measurements. Here we have retrieved a temperature dependence slightly stronger than $1/\sqrt{T}$, $\alpha{=}0.6$, and the values at mesospheric temperatures are also larger than previous rates in about 20%. We have not found any significant difference between $k_{vv,3}$ and $k_{vv,4}$.

The rates k_{F1} and k_{F2} retrieved here are shown in Fig. 5.16b. These rates were very uncertain and a large range of values has been used in previous studies. Sharma and Wintersteiner (1985) derived values of $3{\cdot}10^{-11}$ and $1.5{\cdot}10^{-13}$ cm^{3}s^{-1} for k_{F1} and k_{F2}, respectively, from their analysis of the spectrally resolved SPIRE measurements

near 2.7 μm. They distinguished between the rate for process $CO_2(02211) + M \rightleftharpoons CO_2(10011)$ (k_{F2}) and $CO_2(10012)+M \rightleftharpoons CO_2(02211)$ ($k_{F2'}$), the latter being a factor 2 larger than the former. They made a thorough analysis of the spectra and concluded that those figures could be considered as lower limits. SAMS and ISAMS measurements near 4.3 μm are less sensitive to these rates. López-Puertas and Taylor (1989) and López-Puertas et al. (1998a,b) analysed those observations including values of $2{\cdot}10^{-11}$ and $2.4{\cdot}10^{-12}$ cm^3s^{-1}. These values were based on the measurements of Jacobs et al. (1975) of $2{\cdot}10^{-11}$ cm^3s^{-1} for the re-distribution between the 10001 and 10002 levels, and on the results of Finzi and Moore (1975) who found that the redistribution of the v_1 and v_2 quanta is independent of the vibrational excitation of the v_3 mode. The k_{F1} and k_{F2} rates used in the model of Shved et al. (1998), which was used in the retrieval of CO_2 from CRISTA (Kaufmann et al., 2002) and from SABER measurements (Rezac et al., 2015), are $1.5{\cdot}10^{-13}$ cm^3s^{-1} for k_{F1} and k_{F2}, and $3.0{\cdot}10^{-13}$ cm^3s^{-1} for $k_{F2'}$. Note that these rates differ significantly from those used in the other studies. We have retrieved a value of $7.04{\times}10^{-13}$ $cm^3s^{-1}$for k_{F1}, constant with temperature; and larger values for k_{F2}, $5.57{\times}10^{-13}$ $(300/T)^{1.2}$ cm^3s^{-1}, with a significant temperature dependence. The value for k_{F1} is about 43 times smaller than the rate derived by Sharma and Wintersteiner (1985), and about 4.7 times larger than that used by Shved et al. (1998). For k_{F2}, our rate is about a factor of 9 to 5 (4.5 to 2.5 for $k_{F2'}$) larger than those used by Sharma and Wintersteiner (1985) and Shved et al. (1998) for temperatures of 150 and 250 K, respectively. However, it is a factor of 2 to 3.5 (4 to 7 for $k_{F2'}$) smaller for the same temperature interval when compared to those used in the SAMS and ISAMS analysis (López-Puertas and Taylor, 1989; López-Puertas et al., 1998b). Hence, we should expect significant changes in the simulation of atmospheric radiation of the three 4.3 μm second hot bands when using the new retrieved rates.

The k_{vt} collisional rates used in previous works and those retrieved here are shown in Fig. 5.16c. The values reviewed by López-Puertas and Taylor (2001) (label 'LPT01') were used in the analysis of the SPIRE, SAMS, CLAES and ISAMS measurements (Nebel et al., 1994; López-Puertas and Taylor, 1989; Edwards et al., 1996; López-Puertas et al., 1998a,b). Shved et al. (1998) used significantly smaller values, particularly at mid- and low temperatures. Funke et al. (2012) revised the rates compiled in the review of López-Puertas and Taylor (2001) to lower values, which are very similar to those of Shved et al. (1998). In this work we have retrieved values which are a factor of 0.7 smaller than those used by Funke et al. (2012).

The $k_{O(^1D)}$ collisional rates and efficiencies used in previous works and those retrieved here are shown in Fig. 5.16d. In the analysis of SPIRE (Nebel et al., 1994), CLAES (Edwards et al., 1996), and ISAMS data (López-Puertas et al., 1998a,b), the rate measured by Amimoto et al. (1979) of $2.4{\cdot}10^{-11}$ cm^3s^{-1} was used with an efficiency in the transfer of electronic to vibrational energy of 25% ('LPT01' in Fig. 5.16d). Shved et al. (1998) used in their model a similar rate, which is larger at temperatures below ~210 K and smaller at larger temperatures (Fig. 5.16d). More recently, Funke et al. (2012) has adopted the rate revised by Ravishankara et al. (2002) of $2.1{\cdot}10^{-11}\exp(115/T)$ cm^3s^{-1} and assumed an efficiency of 20%. Here we have derived a value equals to that used by Funke et al. (2012) with an error of

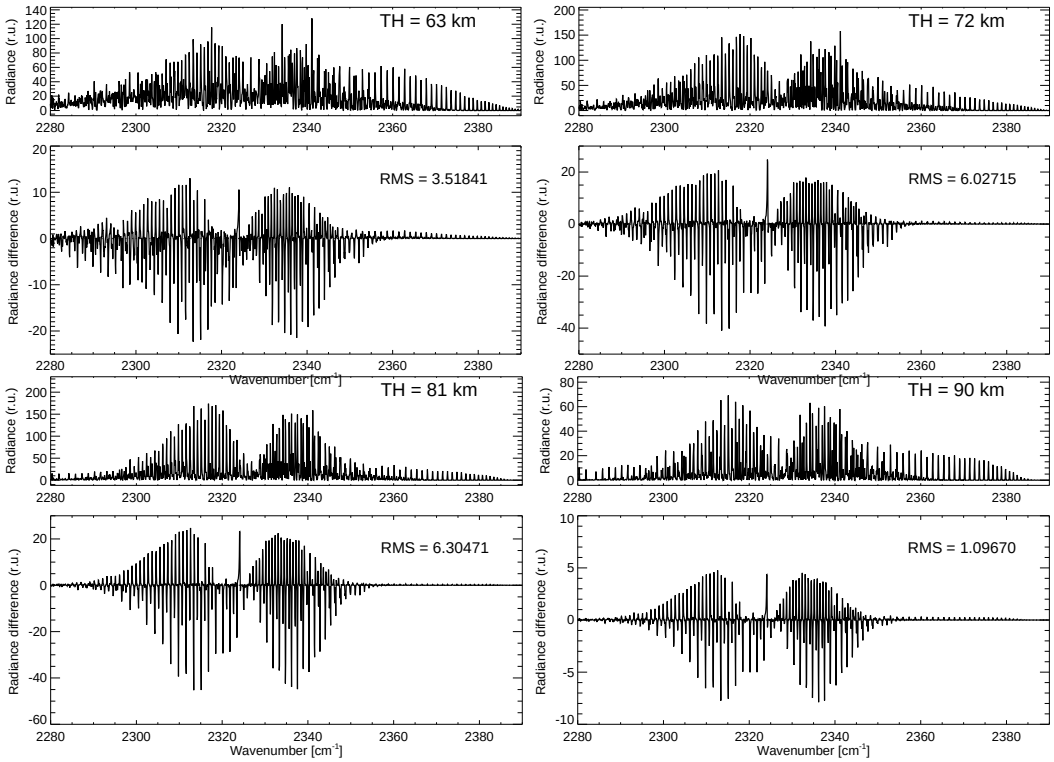

Figure 5.17: Simulation of MIPAS spectra for the retrieved rates and those mainly used in previous studies. Simulated spectra with the retrieved rates (upper panels) and differences (rates of this work−rates of previous works) (lower panels) at tangent heights of 63, 72, 81 and 90 km. Radiance units (r.u.) are in $\mathrm{nW/(cm^2\,sr\,cm^{-1})}$.

∼15%.

To show the impact of the retrieved rates on the atmospheric limb spectral radiance near 4.3 μm we have performed simulations, for the April 45°N daytime (SZA=44.5°) and the polar summer January 75°S (SZA=58.7°) reference atmospheres, by utilizing a set of rate coefficients used in previous works and those retrieved here. As representative of previous works we have taken the rates of Shved et al. (1998). Compared to other previous studies, these authors use similar values for $k_{vv,0}$, $k_{vv,1}$, $k_{vv,2}$, $k_{vv,3}$ and $k_{vv,4}$, and intermediate values for k_{F1} and k_{F2}. Further, they use a k_{vt} rate very similar to the more recent rate used by Funke et al. (2012), and an intermediate rate for $k_{O(^1D)}$. All atmospheric parameters were considered the same in these simulations. Fig. 5.17 shows the differences in the spectra at different tangent heights. Practically all bands are affected at these tangent heights showing very large differences in the spectral shape. Compare, for example, the RMS (root mean square) values obtained for these two simulations with those obtained in the retrieval. They are factors of 8, 13 and 4 larger for tangent heights of 72, 81 and 90 km, respectively.

The radiance in the emission of the second hot bands SH1 and SH3 is about 20-30% smaller for the retrieved rates for tangent heights below around 90 km. This is a consequence of the larger retrieved $k_{vv,2}$ rate, leading to a significantly larger

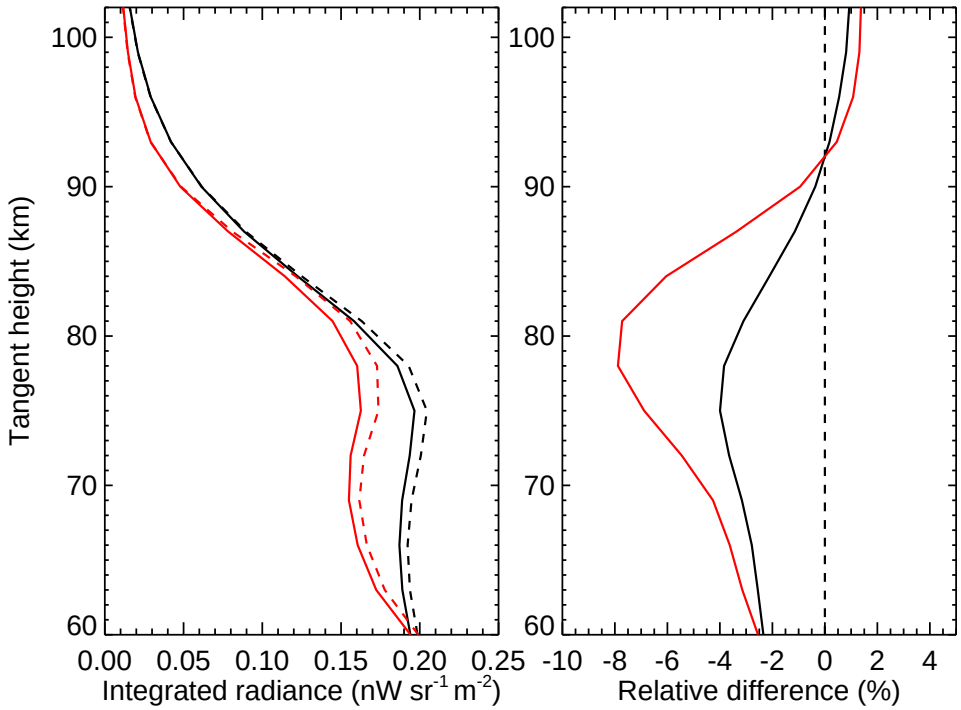

Figure 5.18: Effects of the new retrieved rates on atmospheric integrated radiance profiles. Left: Integrated limb radiance in the 2280-2400 cm^{-1} spectral range calculated for the April 45°N (SZA=44.5°) (in black) and for the polar summer January 75°S (SZA=58.7°) (in red) reference atmospheres (Funke et al., 2012) for a case of collisional rates used in previous works (see text) (dashed) and those retrieved here (solid). The right panel shows the retrieved−previous work relative differences.

relaxation of the 2.7 μm levels. The emission of the SH2 band is, however, larger because of the larger retrieved k_{F2} rate, leading to a larger energy transfer from the states directly pumped by solar radiation (10011 and 10012) to 02211. As for the stronger SH1 and SH3 second hot bands, the emissions originating from the third and fourth hot bands are also smaller for the retrieved rates. This is also a consequence of the larger $k_{vv,3}$ and $k_{vv,4}$ rates retrieved here (compare $k_{vv,3}$ and $k_{vv,4}$ with the dashed line in Fig. 5.16a).

The population of the 00011 level, responsible for the 4.3 μm emission of the fundamental band as well as the 10 μm band laser emissions, is very important for the atmospheric studies. In the lower-middle mesosphere its population is controlled, besides the solar pumping in the 4.3 μm band, by the V-V excitation through $N_2(1)$ from the 2.7 μm levels ($k_{vv,2}$ followed by $k_{vv,0}$), by the excitation of $N_2(1)$ from $O(^1D)$ ($k_{O(^1D)}$), and by the V-T quenching with air molecules (k_{vt}). The $k_{vv,2}$ rate derived here is significantly larger that those used in previous works, the excitation from $O(^1D)$ is similar, and the V-T thermal relaxation is moderately smaller. Overall, these processes lead to a larger excitation of 00011. In consequence the 4.3 μm fundamental band emission is larger for the new rates, in particular it is about 5% below around 90 km for mid-latitude conditions.

The overall effect for the integrated radiance in the 2280-2400 cm^{-1} spectral range is shown in Fig. 5.18. The reduction in the second hot band dominates over the increase in the fundamental, resulting in a reduction in the radiance of 2-4% below about 85 km for mid-latitude conditions and as much as 8% in the polar summer. At the uppermost tangent heights, where the emission from the fundamental band dominates, there is a small increase in about 1%.

Chapter 6

CO_2 Retrieval from MIPAS Data

Abstract

In this chapter, we present the major objective of this work: the inversion of CO_2 from MIPAS limb emission spectra. The retrieval setup is similar to that described in the previous chapter. The differences reside in the micro-windows used (selected from the 4.3 μm solely), the temperature profiles above 95 km (taken from Bermejo-Pantaleón et al. (2011)), and the concentrations of $O(^1D)$, slightly changed to incorporate the solar cycle dependency. The values of the most important collisional rates affecting the populations of the CO_2 energy levels emitting in the 4.3 μm spectral region are those derived in Chapter 5 (see also Jurado-Navarro et al., 2015c). The characterization of the retrieved CO_2 concentrations shows that the precision depends on altitude, varying from ∼1% below 90 km, to 5% around 120 km, and is larger than 10% above 130 km. The vertical resolution of the retrieved CO_2 is about 5–7 km below 120 km, with an increase of up to 12 km at ∼100 km, and between 10 and 20 km at 120-140 km. The analysis of the retrieved CO_2 from MIPAS is performed using the zonal monthly means (2010-2011), the annual mean (2010), and the inter-annual variability from 2010 to 2011. The retrieved MIPAS CO_2 has been compared to previous measurements taken by ACE and SABER, and with 3D global simulations of WACCM[1].

6.1. Introduction

In this chapter we describe the inversion of CO_2 from MIPAS limb emission measurements in the 4.3 μm spectral region. As mentioned in Chapter 2, MIPAS took measurements of the middle and upper atmospheres in three different measurements modes: MA, UA and NLC. Those of the UA mode, ranging from 42 to 172 km, were specifically devised for measuring the thermospheric temperature and NO abundance, and the abundance of CO_2. In the other modes, MA and NLC, MIPAS took spectra up to 102 km but the emission of CO_2 above this tangent height is still very large and many CO_2 lines are still optically thick at those altitudes. Hence, because of this potential problem but also because we are able to retrieve CO_2 in a more extended altitude range we first focus on the retrieval of CO_2 from the UA mode. The problem turned out to be more complex that originally thought and henceforth this work is

[1] A paper describing the results presented in this Chapter is currently in preparation.

focused on this atmospheric mode only, leaving for a future work the development of a retrieval baseline for the MA and UA modes.

MIPAS took measurements of the middle and upper atmosphere in those three modes from 2005 until April 2012. As explained below and in Chapter 5, the retrieval of CO_2 from MIPAS requires first the inversion of other parameters as the temperature (derived from the CO_2 15 μm emission) and O_3 below ~100 km, and the thermospheric temperature (above ~100 km) from the NO 5.3 μm emission. At present, the thermospheric temperature (which is being retrieved simultaneously with the nitric oxide (NO) concentration, which, in turn, requires first the retrievals of other species in the inversion chain, e.g., NO in the mesosphere, NO_2, CO and H_2O) is only available for the measurements taken in 2010 and 2011. Therefore, at this time, we are limited to retrieving CO_2 from MIPAS spectra taken in the UA mode during 2010 and 2011. Nevertheless, since the measurements cover all seasons and latitudes this is not a significant limitation. Only the inter-annual variation in the 2005-2012 period could not been fully studied, although even some investigations could be performed (see Sec. 6.8).

6.2. Retrieval Setup

The retrieval of CO_2 is performed from MIPAS limb emission measurements of the 4.3 μm spectral region. Besides the CO_2 vmr profile, another two parameters are fitted jointly in the retrieval: the line of sight (LOS), to correct pointing errors above 60 km, and the radiance offset to compensate offset calibration errors (Jurado-Navarro et al., 2015a,b). The scheme of the setup is similar to that described in detail in Jurado-Navarro et al. (2015c)[2]. The major differences regarding the CO_2 retrieval are: the altitude range, that embraces from 60 km to 142 km, and the selected micro-windows which are solely located in the 4.3 μm spectral region, in MIPAS channel D (1820-2410 cm^{-1}).

The *a priori* information of CO_2 is taken from the SD-WACCM (P_r=2) CO_2 climatology provided by Garcia et al. (2014) (see Chapter 5, Section 5.2). The CO_2 profile is regularized by means of a Tikhonov-type (Tikhonov, 1963) smoothing constraint. A strong diagonal constraint is added below 60 km in order to force the retrieved CO_2 to be close to the well-known mixing ratio in the lower mesosphere. Above 60 km, the constrain is optimized to obtain stable calculations with a high enough precision to allow for meaningful physical interpretation for he retrieved CO_2 abundance.

The temperature profiles used for the retrieval come from two sources: i) below 95 km, from the retrieval of temperature and LOS by García-Comas et al. (2014) (hereafter TLOS); and ii) above 95 km, from the joint retrieval of temperature and NO (nitric oxide) abundances by Bermejo-Pantaleón et al. (2011) (hereafter 'NOT'). The pressure profiles are implicitly derived from hydrostatic equilibrium. It is important to highlight that, in polar summer conditions, the temperature from NOT shows lower

[2]See also Chapter 5, Section 5.2

values than MSIS in the lower thermosphere of up to 10 K. Thus, the use of NOT temperatures instead of MSIS increases the retrieved CO_2 by up to 15% under these particular conditions.

Regarding the $O(^1D)$ profile, it has been improved compared to that used in the collisional rate retrieval in several aspects. First, the photoabsorption cross sections for O_2 have been updated including the experimental values of Ogawa and Ogawa (1975) and Lu et al. (2010). Secondly, the efficiency of $O(^1D)$ production from O_2 photo-absorption has been modified taking into account that below about 100 nm the O_2 ionization is the dominant channel. Thirdly, the effect of an overhead column proportional to the scale height of O_2 above the top layer of the model has been included. Furthermore, a variable solar spectral irradiance (SSI) input has been included in order to account for solar UV variations along the MIPAS observation period. SSI data has been taken from the NRLSSI model (Lean et al., 2005). This $O(^1D)$ photo-production has been compared with that calculated for similar conditions by an independent 1D model UV radiative transfer model (González-Galindo et al., 2005; Garcia et al., 2014) finding differences smaller than than 2% at all altitudes.

The used atomic oxygen, $O(^3P)$, profiles have been taken as for the retrieval of the collisional rates (see Chapter 5).

The CO_2 non-LTE model is based on that described in Funke et al. (2012) with the values of the main vibrational-vibrational and vibrational-translational processes retrieved from MIPAS spectra as described in Chapter 5 and summarized in Table 5.1 (see also Jurado-Navarro et al., 2015c).

6.3. Selection of the CO_2 Spectral Regions

The selection of the spectral regions sensitive to the CO_2 abundance is performed using the 4.3 μm Jacobians (see Figs. 5.1 and 5.2) and the selection method described in Chapter 5, Section 5.3. In this way, and thanks to the excellent MIPAS spectral resolution, we are able to select the spectral points sensitive to the CO_2 vmr while excluding lines with non-local responses due to spectral saturation. We have selected 18 principal microwindows within the 2300–2380 cm^{-1} range, containing height-dependent sub-microwindows at 23 tangent heights from 60 km up to 142 km. In this altitude region, which embraces the lower mesosphere up to the lower thermosphere, we are able to obtain spectral points where the CO_2 non-LTE emission comes mainly from altitudes very close to the selected tangent heights and yet with a good signal-to-noise ratio.

An illustration of the selection based on the sensitivity of the spectral lines is shown in Figure 6.1. At 60 km, the fundamental band line (black) shows a local response and hence it is selected in the sub-micro-windows mask. On the contrary, the second hot lines (red and orange) do not give a local response (the maxima of the Jacobians are located at altitudes well above the tangent height) and hence are not selected. They are, however, included in the sub-microwindow mask for higher tangent heights, i.e. from 85 km up to 102 km, where they have quite enough local

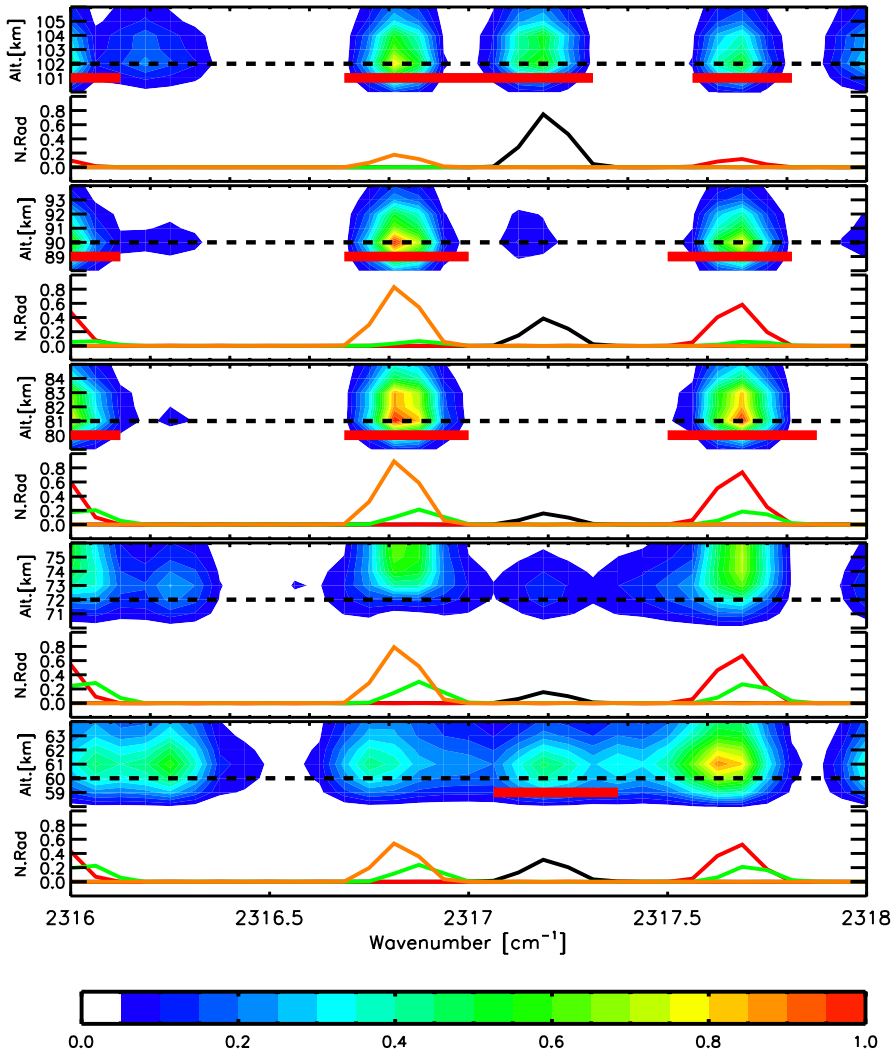

Figure 6.1: Jacobians and radiance for several lines in the 2316-2318 cm^{-1} region for five different tangent altitudes (from bottom to top: 60, 72, 81, 90 and 102 km). Two panels are shown for each tangent altitude. Upper panel: normalized Jacobians at the corresponding tangent height; dashed black line stands for the tangent altitude and thick red line for the sub-microwindow mask. Lower panel: normalized radiance contributions for different lines of CO_2 bands; a line of the fundamental band in black, of the second hot $10^01 \rightarrow 10^00$ band in red, of the $02^21 \rightarrow 02^20$ band in green, and of $02^01 \rightarrow 02^00$ in orange.

sensitivity. In this example the fundamental band line is not selected from 72 to 90 km, although it gives again valuable information at 102 km. Precisely, the 102 km altitude marks the transition height where the information from second hot band ends and that of the fundamental band starts.

In addition to the exclusion of spectral points with non-local response, we restricted the occupation matrix to the strongest lines at each altitude (mainly fundamental and second hot bands lines) for reasons of computational efficiency. Additionally, interferences from the 636, 628, 627, 638 and 637 CO_2 isotopologues have been

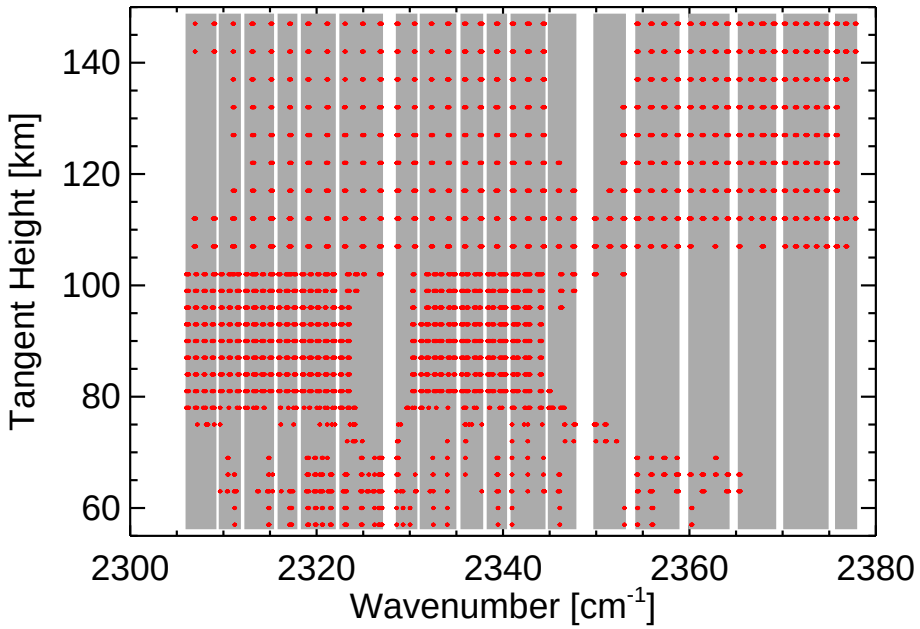

Figure 6.2: Occupation matrix used in the CO_2 retrieval in the 4.3 μm spectral region. Shaded regions represent the microwindows selected and red dots the sub-microwindow mask at each tangent height.

suppressed in order to avoid systematic errors caused by the less accurate non-LTE modeling of these minor species.

An inspection of the resulting occupation matrix, shown in Fig.6.2, reveals that the selected spectral points belong mainly to the lines of the fundamental band in the 60-72 km and 102-142 km regions, and of the second hot bands in the 75-102 km region. More detailed information on the spectral lines contained in the sub-microwindows used in the retrieval of CO_2 is given in Table B.1.

6.4. Characterization of the Retrieved CO_2 vmr

6.4.1. Precision and Vertical Resolution

The vertical resolution and the precision are two important diagnostic parameters for characterizing the quality of any retrieval. Since the MIPAS measurements in the UA mode for 2010 and 2011 cover the four seasons twice, the zonal mean of these parameters are calculated for each season using 3 months: December-January-February, March-April-May, June-July-August and September-October-November (Figure 6.3).

In general, the precision varies with altitude ranging from ∼1% below 90 km, 5% around 120 km and larger than 10% above 130 km. The larger values at higher altitudes are due to the lower signal-to-noise ratio. There are very little latitudinal and seasonal variations, which are driven by the solar illumination conditions.

The vertical resolution is typically around 5–7 km below 120 km. Above that

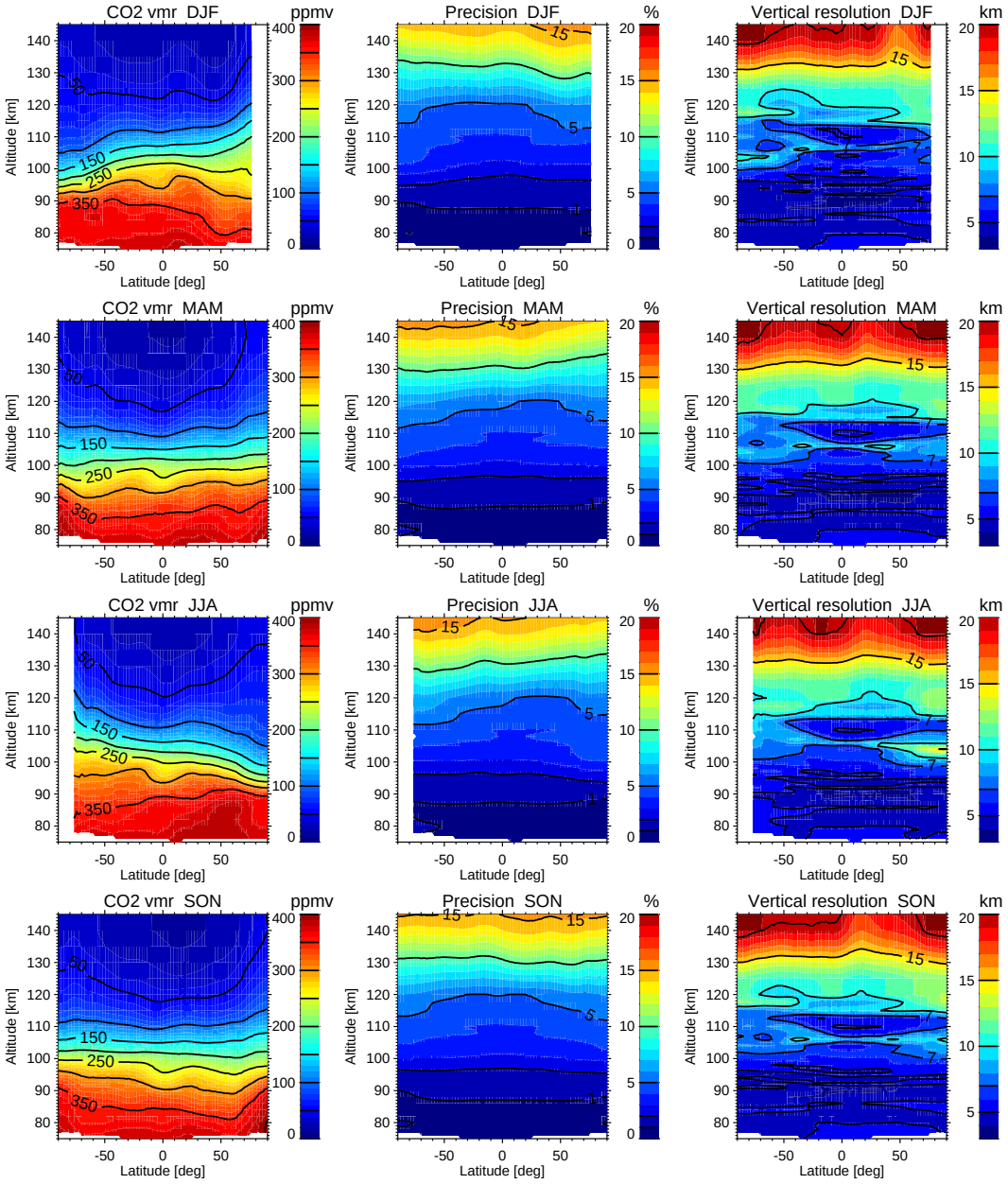

Figure 6.3: Latitude-altitude cross sections of CO_2 (left column), precision (centre column) and vertical resolution (right column). The rows, from top to bottom, correspond to the boreal winter (DJF: December-January-February), the vernal equinox (MAM: March-April-May), the austral winter (JJA: June-July-August) and the autumnal equinox (SON: September-October-November). The MIPAS data include the measurements taken in 2010 and 2011 in the UA mode.

altitude, it is poorer with values higher than 10 km mainly caused by the larger vertical sampling (5 km instead of 3 km).

Around ∼105 km, a slight degradation of the vertical resolution is observed. This

altitude corresponds to the tangent height region where the sub-microwindows include lines from the second hot bands only while the fundamental band lines are used above. The latter, as discussed above in Sec. 6.3, are still rather optically thick at these tangent heights and hence have been rejected.

6.4.2. Retrievals from Synthetic Spectra

In order to test the performance of the retrieval setup, and following the same strategy than for the retrieval of the collisional rates (Chapter 5) Jurado-Navarro et al. (see also 2015c), we have applied the retrieval setup of CO_2 to synthetic spectra calculated with KOPRA for a "known" atmosphere. This approach represents of course an idealized case in the sense that systematic retrieval errors are absent. Systematic errors are discussed in detail in the next section. We have performed synthetic retrievals for two different atmospheric conditions, one corresponding to mid-latitude equinox and the other to polar summer conditions. The major question to answer here is whether the retrieval yields reasonable results even in cases where the CO_2 and LOS *a priori* used is poorly representative for the actual atmospheric and instrumental conditions. Deviations of the retrieved profile from the "true" in these cases are often called smoothing errors. However, while it is important to assess the sensitivity of the retrieval to the *a priori* profile shape, we do not include smoothing errors in the overall error budget. First, because the concept of "smoothing errors" itself is questionable (von Clarmann, 2014), and secondly, because these deviations can be implicitly accounted for in comparisons to model simulations or independent observations by applying the MIPAS averaging kernels to the latter.

We investigate the sensitivity of the retrieval of CO_2 vmr to the CO_2 and LOS *a priori* profiles separately.

The CO_2 *a priori* profile was perturbed by exchanging the corresponding SD-WACCM profiles of the two atmospheric conditions, i.e. the mid-latitude SD-WACCM profile was implemented in the polar summer input and vice versa. Under mid-latitude conditions, the retrieved CO_2 profile differs from the true value by less than 2-3% in the whole altitude region (Figure 6.4 panels a and b). Compared to the difference with the a priori profile (up to 35%), the agreement of the retrieved profile and the "true" is excellent. Regarding polar summer conditions, the differences between the retrieved and the true profiles are generally smaller than 2% except at 95 to 110 km where it ranges at 2–4% (Figure 6.4 panels c and d). We have also tested the effect of the a priori when retrieving only the CO_2 vmr and keeping fixed the LOS (i.e., as a single-parameter retrieval). The result is shown by the green line in Fig. 6.4. We see that, for both atmospheric conditions, the differences between the retrieved CO_2 with and without the joint fit of LOS are only marginal. Also, the inspection of the retrieved LOS in the joint fit case (Fig. 6.5) shows that the mapping of the CO_2 a priori uncertainties on the LOS is very small (less than 20 m).

We also tested the impact of a perturbation of the LOS *a priori* information on the retrieved CO_2. We applied a sine function perturbation to the LOS with a value of 0 m at 60 km and 142 km and a maximum of 200 m at 90 km. Above

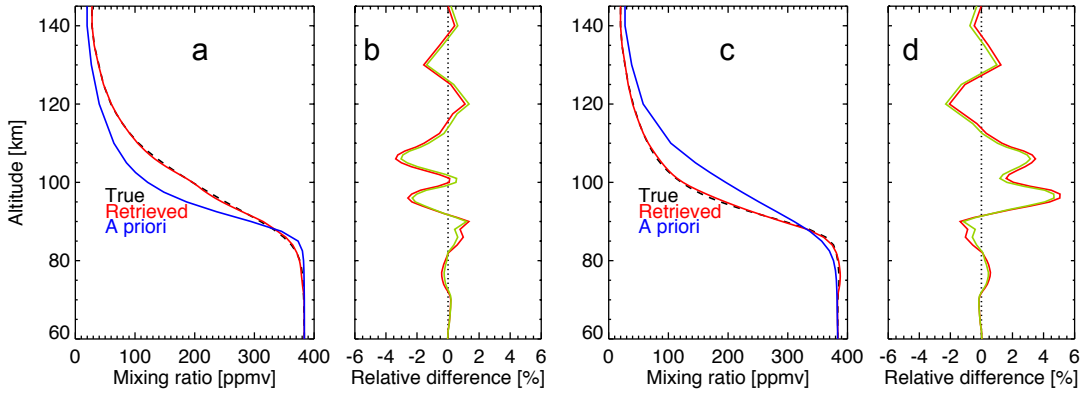

Figure 6.4: Sensitivity of the retrieved CO_2 profile to the a priori for mid-latitudes (panels a and b), and for polar summer conditions (panels c and d). The relatives differences (panels b and d) are referred to the CO_2 and LOS joint retrieval (red solid line) and to the single-parameter CO_2 retrieval (green line).

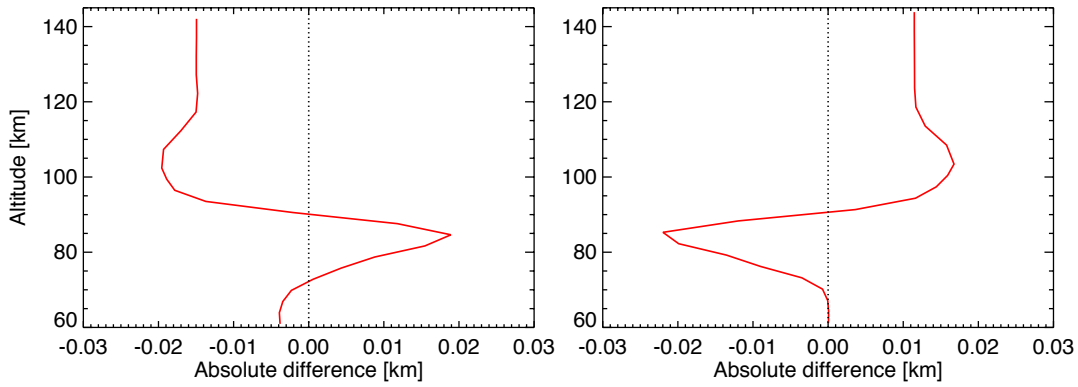

Figure 6.5: Sensitivity of the retrieved LOS to the CO_2 a priori uncertainties for mid-latitude (left) and polar summer (right) conditions. The lines show the retrieved–true LOS differences.

90 km, the use of the perturbed *a priori* LOS profile in the CO_2-LOS joint retrieval introduces deviations of the retrieved CO_2 from the true profile of less than 1–2%, while differences are negligible below (see Figure 6.6, red line). On the other hand, the application of the perturbed LOS in the single-parameter CO_2 retrieval introduces a significant systematic error of up to 3–4% for mid-latitudes and even larger (up to 5%) for polar summer in the whole altitude range above 70 km (see Figs. 6.6b and 6.6d, green lines).

Therefore, these results give us confidence on the retrieval scheme and we can conclude that the impact of *a priori* profile uncertainties on the retrieved CO_2 is very small, $\lesssim$1-2%. Furthermore, the inclusion of the LOS joint fit introduces no degradation on the retrieved CO_2 while it avoids important systematic errors due to LOS uncertainties.

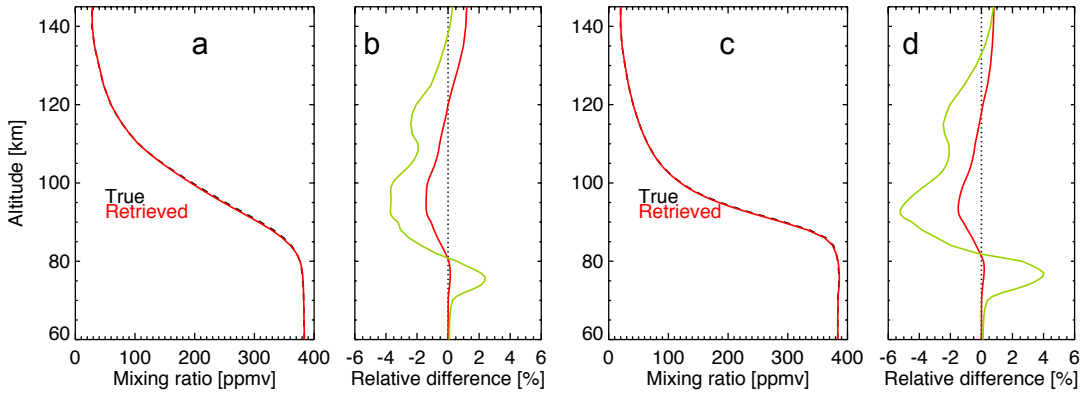

Figure 6.6: Sensitivity of the retrieved CO_2 to LOS a priori uncertainties for mid-latitude (panels a and b), and for polar summer conditions (panels c and d). The relative differences (retrieved–true) (panels b and d) are referred to the joint CO_2-LOS retrieval (red solid line) and to the single-parameter CO_2 retrieval (green line).

6.4.3. Systematic Errors

The systematic errors were estimated from the retrieval response to perturbations of the following parameters: pressure/temperature, O(^1D) and O(^3P) abundances, MIPAS gain calibration and solar flux. The magnitudes of these perturbations are the same as those used in the retrieval of the collisional rates in Chapter 5 (see also Jurado-Navarro et al., 2015c), except for temperature that was assumed with an error of 5 K up to 100 km, 10 K between 100 and 110 km, and 15 K between 110 and 142 km. In addition, systematic CO_2 retrieval errors due to uncertainties in the collisional rates used in the non-LTE modeling need to be taken into account. However, since the CO_2 collisional parameters have been retrieved from MIPAS measurement in the same spectral region (see Chapter 5), using the same model parameters as used here in the CO_2 retrieval, the CO_2 retrieval errors due to systematic errors of the retrieved rates are expected to be correlated with the errors caused by model parameter uncertainties. Therefore, adding the systematic errors due to collisional rate uncertainties quadratically to the other errors would overestimate the total error. For instance, it might occur that an overestimation of the solar flux introduces a low bias of a certain collisional rate, but that the use of the hence underestimated rate in the CO_2 retrieval compensates the "direct" CO_2 error caused by assuming a too low solar flux. Therefore, we explicitly consider the propagation of errors due to pressure/temperature, O(^1D), O(^3P), gain calibration, and solar flux uncertainties of the collisional rate retrieval into the CO_2 retrieval by correcting the retrieval response $\Delta CO_2^{i'}$ to perturbations of each model parameter i in the following way:

$$\Delta CO_2^{i'} = \Delta CO_2^{i} + \frac{\Delta K_{vv2,i}}{\Delta K_{vv2}}\Delta CO2^{K_{vv2}} + \frac{\Delta K_{vv3,i}}{\Delta K_{vv3}}\Delta CO2^{K_{vv3}} + \frac{\Delta K_{vv4,i}}{\Delta K_{vv4}}\Delta CO2^{K_{vv4}} + \frac{\Delta K_{F1,i}}{\Delta K_{F1}}\Delta CO2^{K_{F1}} + \frac{\Delta K_{F2,i}}{\Delta K_{F2}}\Delta CO2^{K_{F2}} + \frac{\Delta f_{vt,i}}{\Delta f_{vt}}\Delta CO2^{f_{vt}}, \quad (6.1)$$

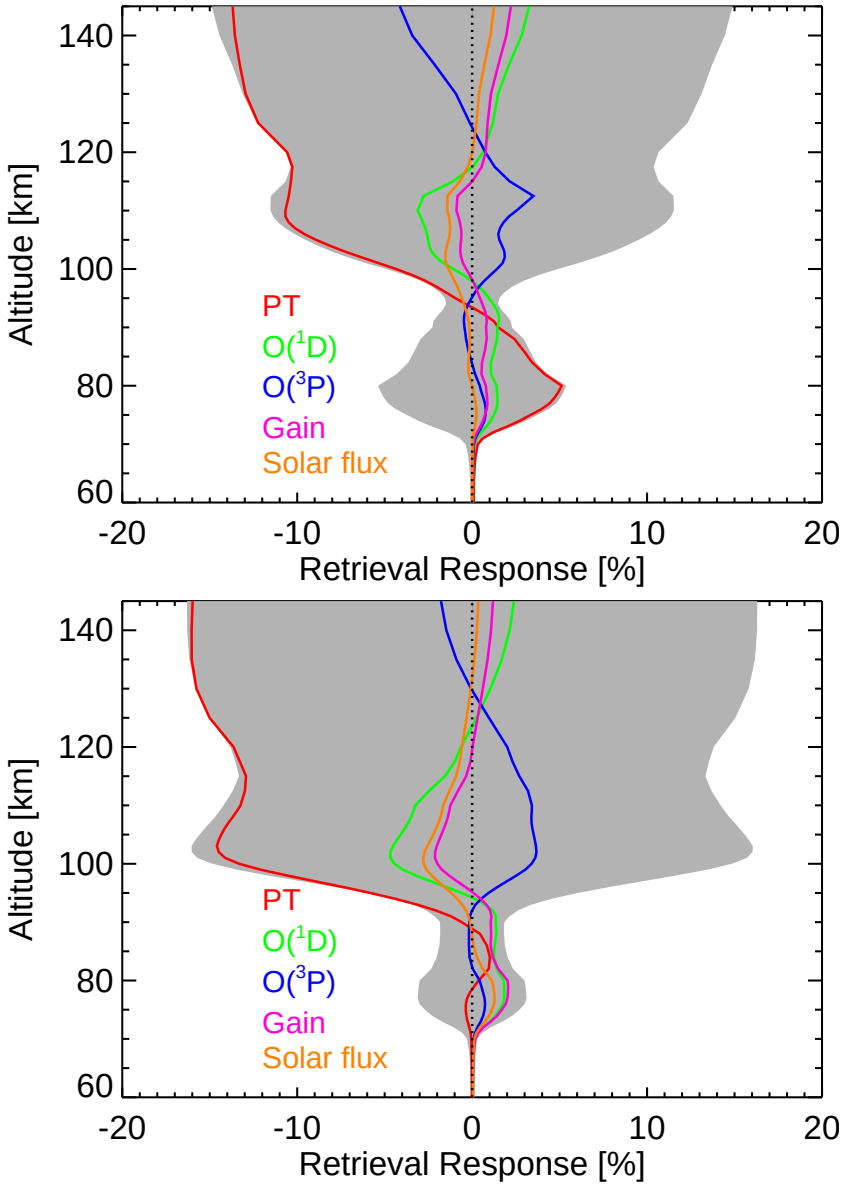

Figure 6.7: Systematic errors of the CO_2 vmr introduced by different error sources for mid-latitude (top) and polar summer (bottom) conditions. CO_2 retrieval responses to individual model parameter perturbations (reflecting their estimated uncertainties) are shown by the colored lines. The shaded area represents the total systematic error.

where ΔCO_2^i is the "direct" response of the CO_2 retrieval to the model parameter perturbation. $\Delta K_{vv2,i}$, $\Delta K_{vv3,i}$, $\Delta K_{vv4,i}$, $\Delta K_{F1,i}$, $\Delta K_{F2,i}$ and $\Delta f_{vt,i}$ are the responses of the collisional parameter retrieval to the model parameter perturbation. These values have been taken the collisional rate error estimation described in Chapter 5 (Table 5.2). $\Delta CO_2^{K_{vv2}}$, $\Delta CO_2^{K_{vv3}}$, $\Delta CO_2^{K_{vv4}}$, $\Delta CO_2^{K_{F1}}$, $\Delta CO_2^{K_{F2}}$ and $\Delta CO_2^{K_{F2}}$ are the responses of the CO_2 retrieval to a perturbation of the respective collisional rate. The resulting corrected retrieval responses to the model parameter perturbations are shown in Fig. 6.7. The total systematic error is then calculated by quadratic summation:

$$\Delta CO_2^{TOTAL} = \sqrt{\sum_{i'} (\Delta CO_2^{i'})^2}. \tag{6.2}$$

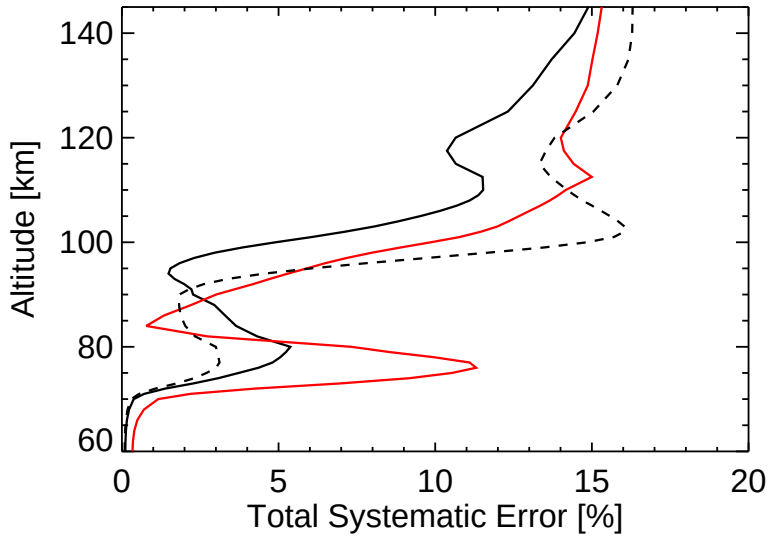

Figure 6.8: Total systematic errors of the main atmospheric parameters from the joint CO_2-LOS (black solid line) and CO_2-only (red line) retrievals for mid-latitude conditions. The dash black line shows the total systematic error of the joint CO_2-LOS retrieval for polar summer. The total errors are calculated from the quadratic sum of the retrieval responses to individual model parameter perturbations shown in Fig. 6.8.

The calculations indicate that the largest error contribution above 100 km comes from the pressure/temperature uncertainties for both considered atmospheric conditions (Fig. 6.7), reaching values up to ∼12% in mid-latitude and ∼16% in polar summer conditions. Below, the pressure/temperature error maximizes again around 80 km, with maximum values at midlatitude conditions up to ∼4%. The MIPAS gain calibration and solar flux uncertainties introduce errors of 2-3% from 85 up to 110 km in both conditions. The total error below 90 km in polar summer conditions is indeed dominated by these uncertainties. The $O(^1D)$ and $O(^3P)$ uncertainties have a non-negligible contribution above 95 km with largest values up to 4% at 105 km in polar summer conditions.

Regarding the total systematic error, it is notably larger for the CO_2-only retrieval

than for the joint CO_2-LOS retrieval (see Fig. 6.8). This indicates that a large fraction of the spectral residuals due to systematic parameter errors is compensated by the LOS in the joint retrieval while in the single parameter CO_2 retrieval all errors map onto the CO_2 profile. In this sense, the joint CO_2-LOS retrieval is also useful to dampen systematic errors of the retrieved CO_2.

6.5. MIPAS CO_2 Climatology for 2010-2011

Figure 6.9 shows the monthly zonal mean CO_2 vmr measured by MIPAS in its UA mode. The figure shows the major features expected for the CO_2 distribution and predicted by models. Namely, the abrupt decline of the CO_2 vmr above around 80-90 km. The other major feature is the seasonal change of the latitudinal distribution, leading to higher CO_2 vmr from 70 up to $\sim$95 km in the polar summer, induced by the ascending branch of the meridional circulation, and lower CO_2 abundances, with respect to the tropics and polar summer, at the same altitudes in the polar winter region. It is noticeable that the distribution reverses above $\sim$95 km, CO_2 being more abundant in the polar winter region than at mid-altitudes and polar summer; also as a consequence of the reversal of the meridional circulation (see, e.g. Smith et al., 2011). The solstice seasonal distribution, with a significant pole-to-pole CO_2 gradient lasts about 2.5 months in each hemisphere (November through February, and May through August), while the seasonal transition occurs quickly, mainly in April and October.

These figures show also another interesting feature. It appears that there is a region of low CO_2 near 80 km in polar summer (months of December and January near the South pole, and May-June-July near the North pole). This could be due to a remnant of CO_2-poor air from the previous season, e.g., as it happens for CO, CH_4 and NO_X but at low altitudes (Funke et al., 2014). However, we cannot discard the possibility that it could be due to a retrieval artifact caused by the complex and difficult situation of the very cold yet illuminated polar sumer region.

Another observed feature is the rapid increase of CO_2 vmr from mid-high latitudes towards the polar regions in the lower thermosphere during equinoxes (more evident in April and October). We cannot find any physical reason for it and we do not discard that this could be a retrieval artifact caused by the inversion of CO_2 in conditions of very high ($>80°$) solar zenith angles.

6.6. Comparison of MIPAS CO_2 with ACE, SABER, and model data

Figures 6.10-6.13 show a comparison of MIPAS CO_2 abundances with those measured by the ACE and SABER instruments and SD-WACCM (P_r=2) simulations for equinox conditions (March and September) and solstice conditions (June and December). Additional comparisons, for each month of the year, are shown in Appendix C), and will be referred to occasionally in the discussion that fol-

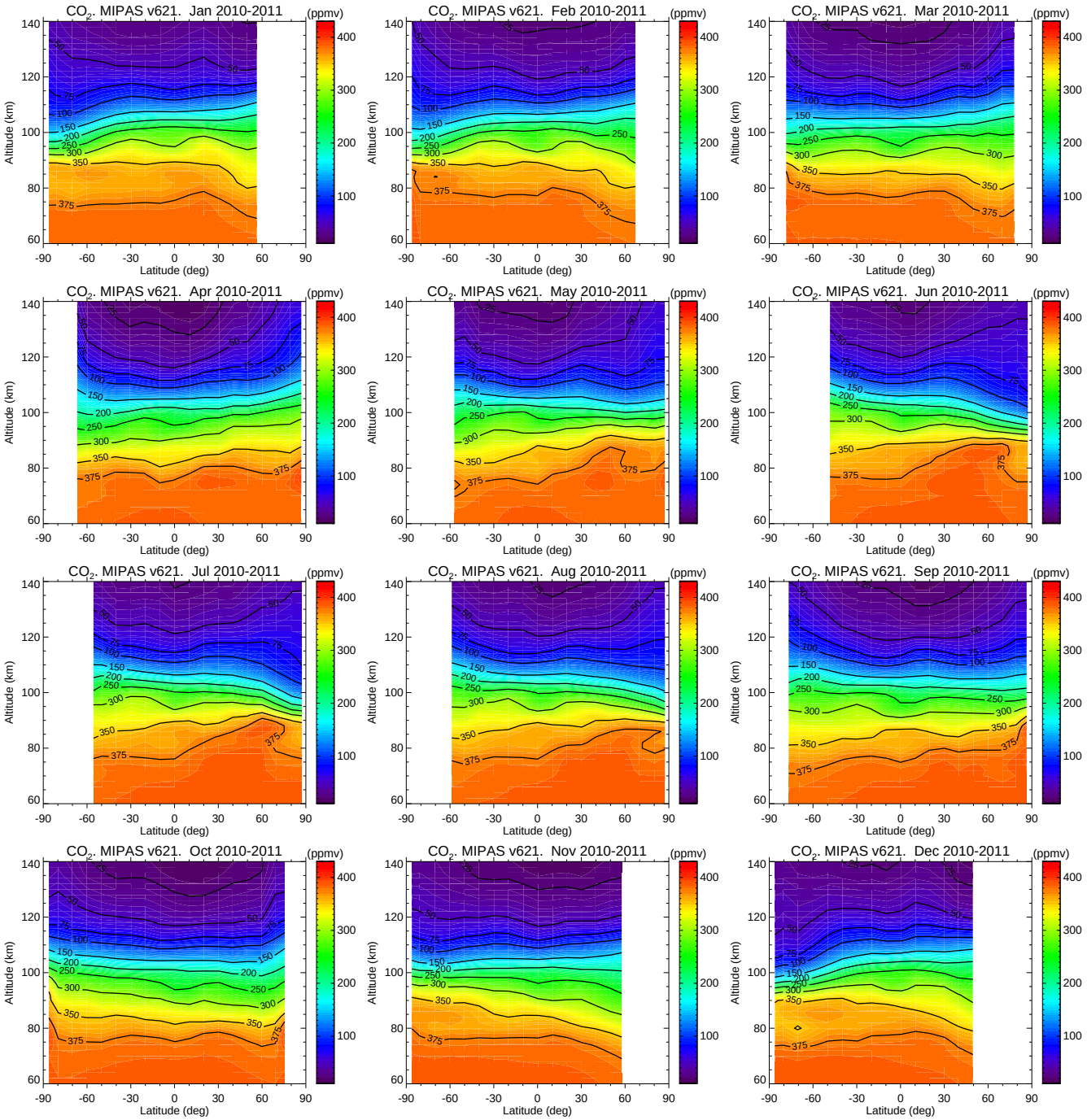

Figure 6.9: Monthly zonal mean CO_2 vmr measured by MIPAS during the 2010–2011 period for the UA mode.

lows. Each figure show the zonal mean distribution for each instrument and WACCM, the zonal mean differences of MIPAS with respect to ACE, SABER and WACCM, and two panels with CO_2 profiles for two latitudinal bands which correspond roughly to the ACE measurements during the given month. We use here version 3.5 of ACE http://www.ace.uwa-terloo.ca/data.html (Beagley et al., 2010; Emmert et al., 2012), which has been filtered by removing very physically unrealistic ('weird') profiles. For SABER we use the only version so far retrieved (ftp://saber.gats-inc.com/Version2_0/Level2C/) (Rezac et al., 2015). As for WACCM, we use the model output for P_r=2 as described by Garcia et al. (2014), which includes the most recent updates on the chemistry of CO and CO_2 in the middle and upper atmosphere. Also, the model version used here is the "Specified troposphere/stratosphere Dynamics" (SD) where WACCM is free running above 1 hPa and has been nudged to MERRA reanalysis below that pressure level. The horizontal bars in the panels that show vertical profiles corresponds to the total errors of the measurements, as reported in previous references for ACE and SABER and in Sec. 6.4.3 for MIPAS. In these figures they are dominated by the systematic errors.

We start the comparison for equinox conditions (Figs. 6.10 and 6.11). Starting with ACE, we observe an overall very good agreement. MIPAS CO_2 is slightly larger ($\sim$5%) between 80 and 100 km. At higher altitudes the differences vary with latitude, being comprised always within $\pm$20%. Excellent agreement is seen for March at 55°N-75°N. However, MIPAS CO_2 is significantly higher at 90–110 km in September at 75°S-55°S.

The agreement with SABER is even better, being within 5% below 100 km. Between 100 and 120 km, MIPAS tends to be larger (20–30%) in the polar regions, and smaller ($\sim$10-20%) near the Equator. It is noticeable that WACCM generally overestimates the CO_2 compared to the three instruments above $\sim$90 km (except for September at 75°S-55°S) suggesting that a value for the Prandtl number of P_r=4, which would effectively reduce eddy diffusion by about a factor of two, would fit better the measurements (see also Sec. 6.7). This is also clearly shown in the bottom left panel of these figures. Another distinctive feature shown in WACCM results but not present in the measurements of any of the three instruments is the weaker decline of CO_2 above 95 km at mid-latitudes in the Southern and Northern Hemispheres (more prominent in March than in September). This might be due to a poor representation of the secondary meridional circulation associated with the semi-annual oscillation (SAO) in WACCM.

In solstice conditions (Figs. 6.12 and 6.13) the agreement among MIPAS, ACE and SABER measurements is also very good, despite of the stronger latitudinal gradient in CO_2 and the fact that the retrieval of CO_2 under stronger gradients of temperature and illumination conditions along the LOS is more challenging. The three instruments show the expected solstice zonal mean distribution –larger CO_2 in the polar summer and smaller in the polar winter–; its seasonal change, and the general patterns agree well with WACCM predictions.

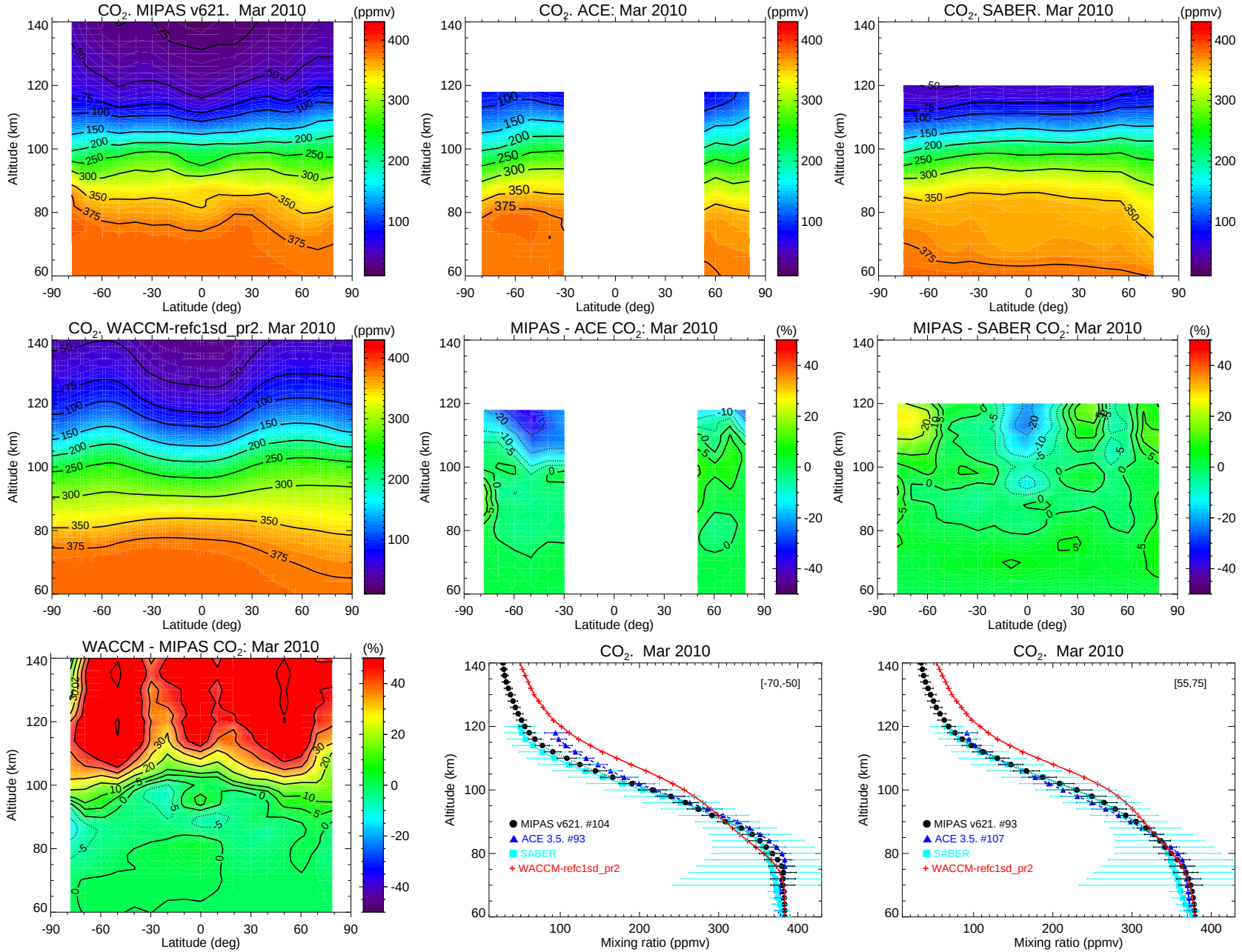

Figure 6.10: CO_2 vmr abundances for March 2010. Top row: zonal mean distribution of MIPAS, ACE and SABER, respectively. Middle row: SD-WACCM (P_r=2) CO_2 distribution, and MIPAS-ACE and MIPAS-SABER CO_2 relative differences in %. Bottom row: WACCM-MIPAS CO_2 differences, and CO_2 vmr profiles for two latitude bands (as labelled) corresponding roughly to the ACE measurements. Horizontal bars in the measurements are the total errors, dominated by the systematic errors.

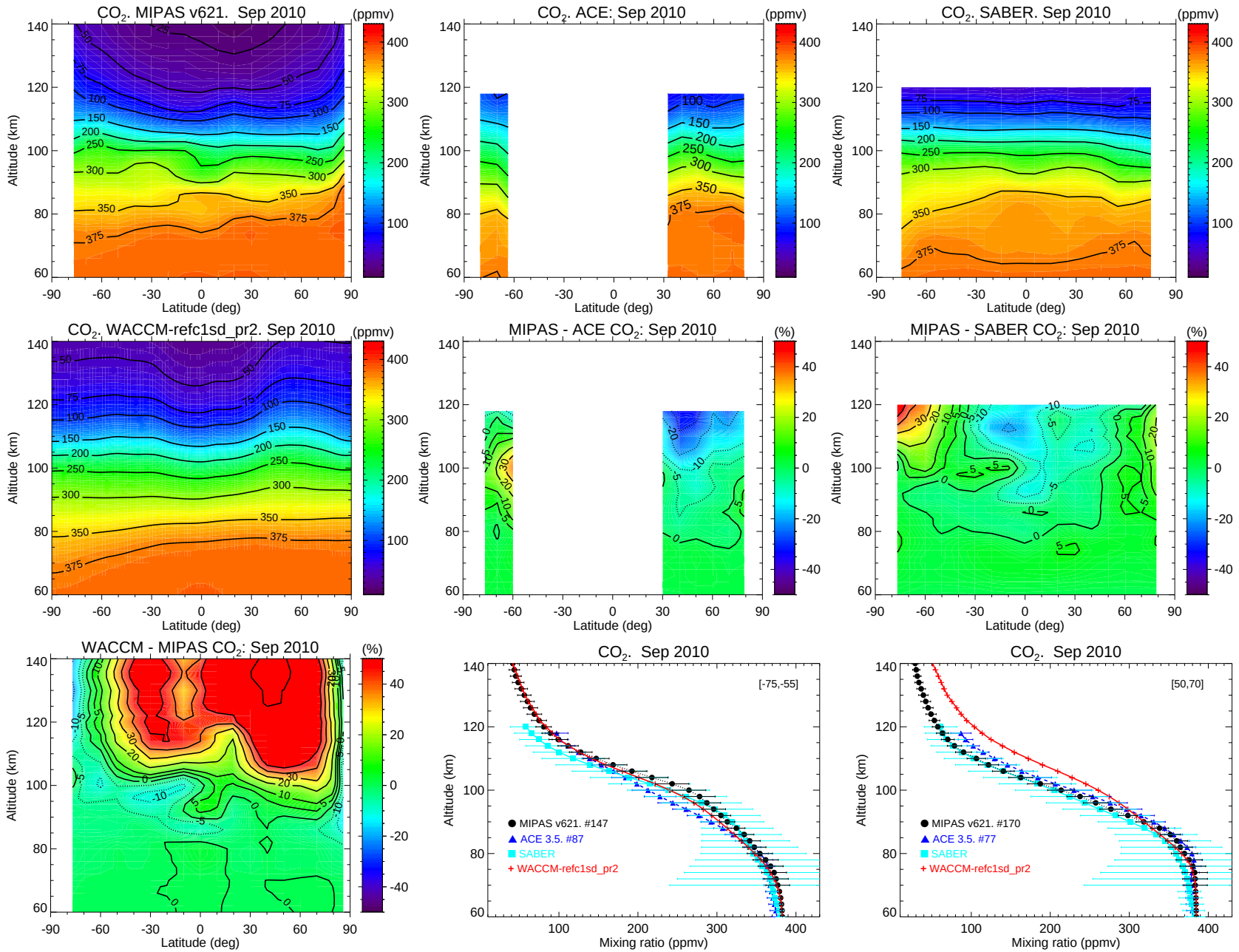

Figure 6.11: As Fig. 6.10 but for September 2010. Note that the latitude bands in the profiles panels are different.

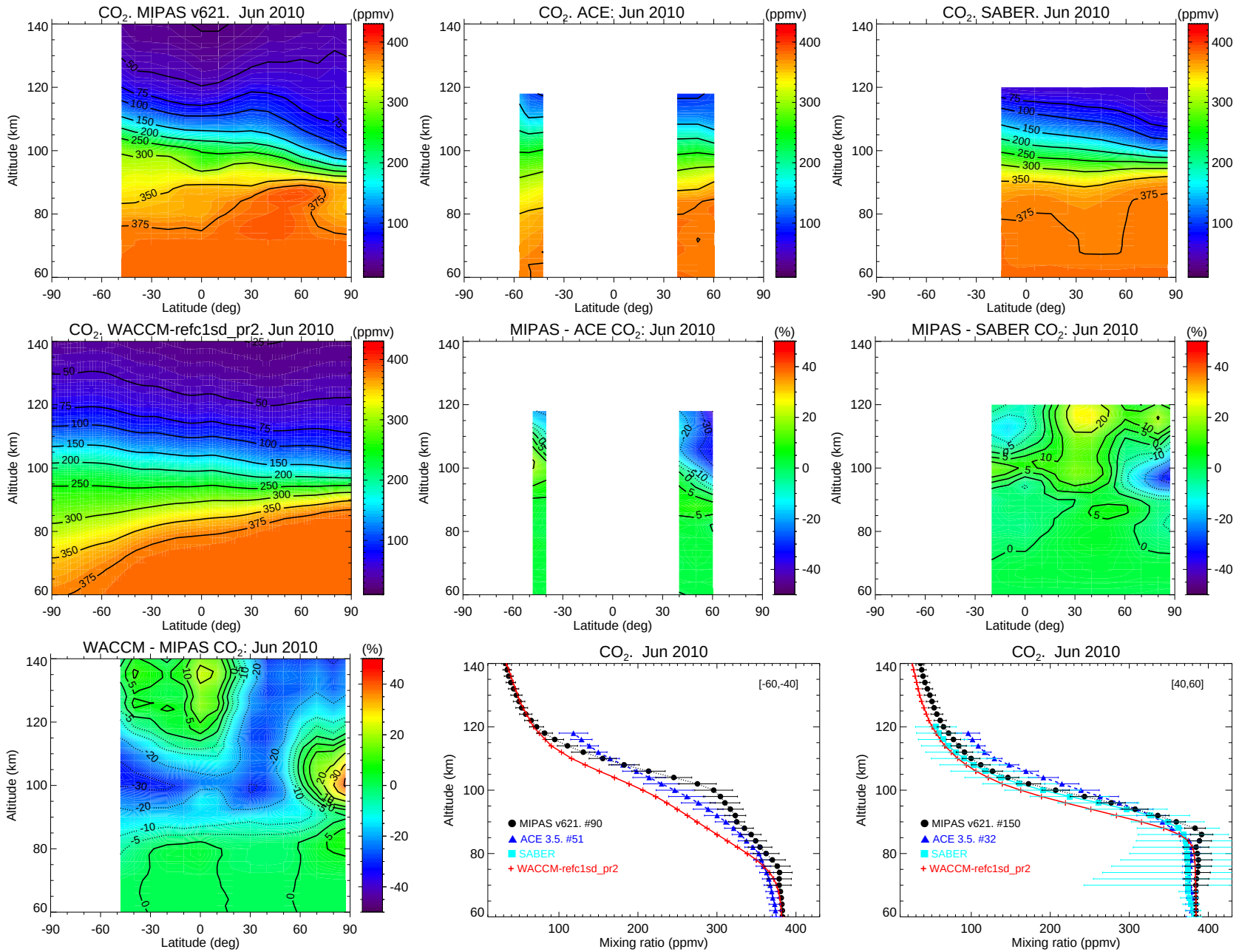

Figure 6.12: As Fig. 6.10 but for June 2010. Note that the latitude bands in the profiles panels are different.

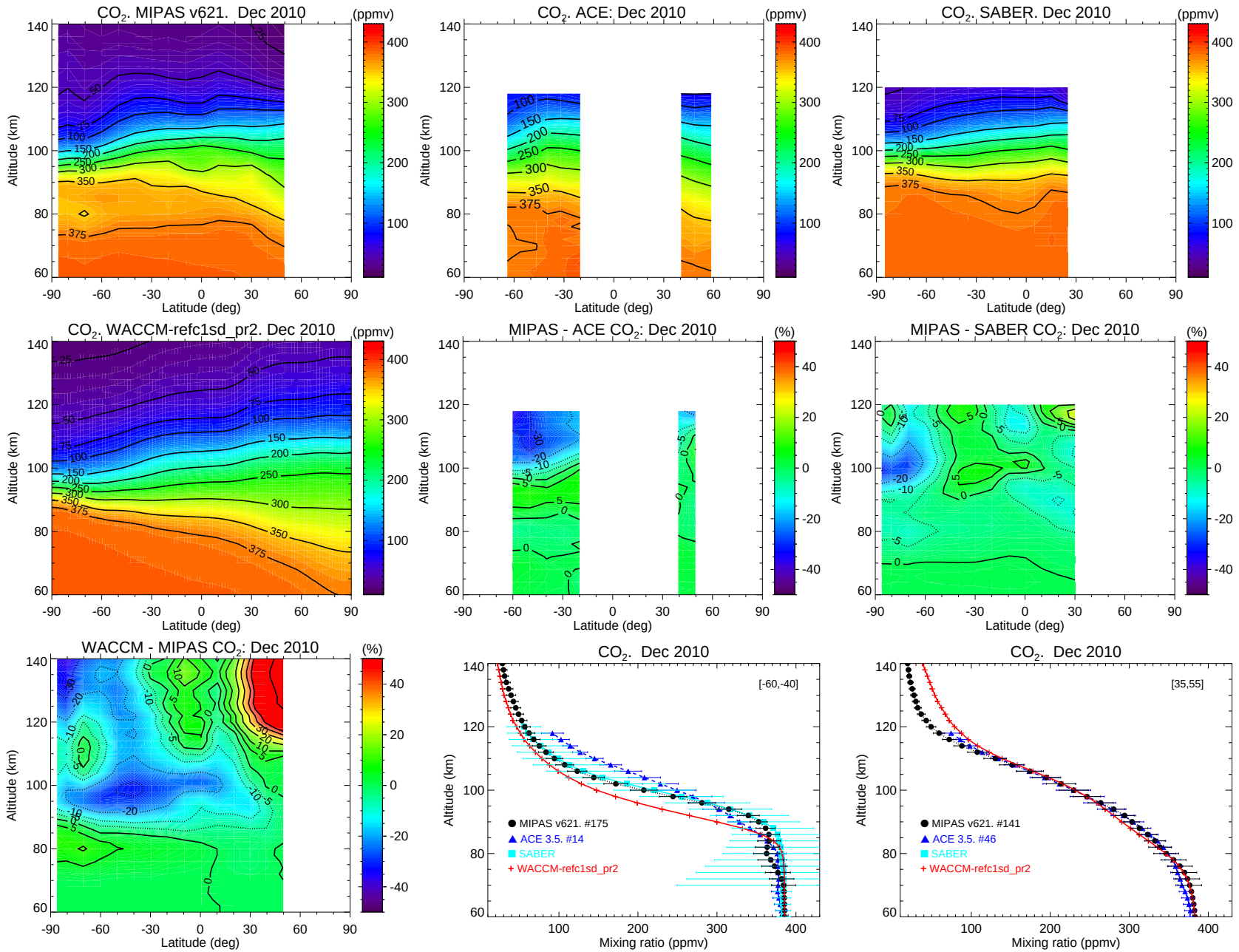

Figure 6.13: As Fig. 6.10 but for December 2010. Note that the latitude bands in the profiles panels are different.

The agreement of MIPAS with ACE is similar as for equinox conditions, but there is a clear difference in the polar summer (see Fig. 6.13, middle panel of bottom row; also seen in January, see Fig. C.1 in Appendix C), where the decay of the CO_2 vmr with altitude above ∼100 km is steeper in MIPAS than in ACE. Actually this behavior is also present in SABER (in excellent agreement with MIPAS) and also predicted by WACCM. The model predicts, however, a CO_2 vmr which is too low at 60°S-40°S (middle panel, bottom row) (more clearly seen in January, see Fig. C.1). The agreement of MIPAS with SABER is in general very good. See, for example, the vertical profiles panels in Figs. 6.12 and 6.13, where, with the exception of June at 60°S-40°S, the profiles are practically identical above ∼90 km. MIPAS CO_2 is, however, low compared to SABER and also ACE (∼4-5%) around 80 km in the polar summer (see Fig. 6.13 and also in Fig. C.1 in Appendix C). On the other hand, for mid-high latitudes in the summer hemisphere, MIPAS is sometimes rather large (∼5%) at 80–90 km (see Fig. 6.12, bottom right panel, although the CO_2 vmr in this case is the largest we have obtained for any month in the 2010-2011 period, see Appendix C).

The agreement between MIPAS and SABER CO_2 in the 60-90 km region is sometimes not so good in the polar summer. This is more evident for January at high latitudes (Figs. C.1 and C.13, bottom right panels), although this seems to be due to an unrealistically low CO_2 abundance of SABER since this is much lower than MIPAS, ACE and WACCM there. In February, however, SABER shows an unrealistically high CO_2 vmr at these altitudes and latitudes (see, e.g., Fig. C.2).

In order to draw more general conclusions about the consistency among the three instruments and WACCM we have compared zonal mean cross-section and latitudinal band profiles for the annual mean of 2010 (see Figs. 6.14 and 6.15). When comparing MIPAS with ACE (bottom left panel of Fig. 6.14), it is evident that MIPAS CO_2 is generally higher by ∼5% between 80 and 100 km but 20-30% lower between 100 and 120 km. MIPAS and SABER, however, agree very well up to 100 km. At 100-120 km, they also agree very well when averaging over all latitudes, but MIPAS CO_2 is generally higher than SABER except near the equator where MIPAS is lower. That is, in the 100-120 km region, globally, ACE shows the highest CO_2, SABER the lowest and MIPAS is in between. Comparing MIPAS with WACCM (see also below), we see a general underestimation by WACCM (P_r=2) of 5-10% at 80-100 km. The same is true for SABER. Part of this could be due to a positive bias in both MIPAS and SABER (both are larger than ACE) caused by and the retrieval of CO_2 in limb emission (MIPAS and SABER) sometimes gives unrealistically large CO_2, see above and also the top panels in Fig. 6.15). However, even though WACCM seems to be a bit low (see lower panel of Fig. 6.15 for the 60°S-60°N latitudinal band). We should mention that increasing the Prandtl number to P_r=4 would worsen the agreement, hence suggesting that P_r=2 seems to be more appropriate at these altitudes.

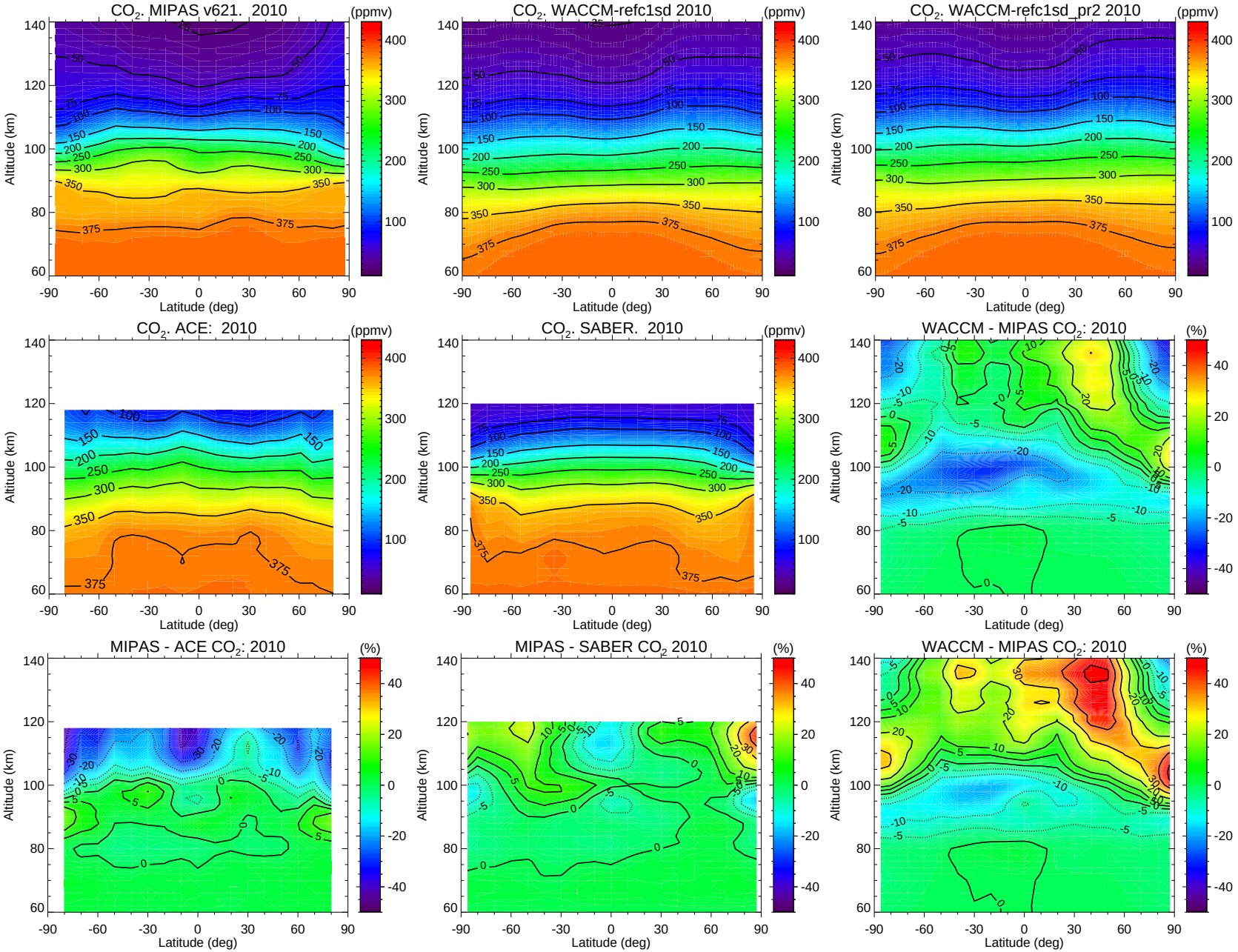

Figure 6.14: Annual mean CO_2 vmr abundances for 2010. Top row: zonal mean distribution of MIPAS, and WACCM (P_r=4) and WACCM (P_r=2), respectively. Middle row: zonal mean distribution of CO_2 for ACE and SABER; and WACCM(P_r=4)–MIPAS differences, respectively. Bottom row: Differences of MIPAS–ACE, MIPAS–SABER, and WACCM(P_r=2)–MIPAS, respectively.

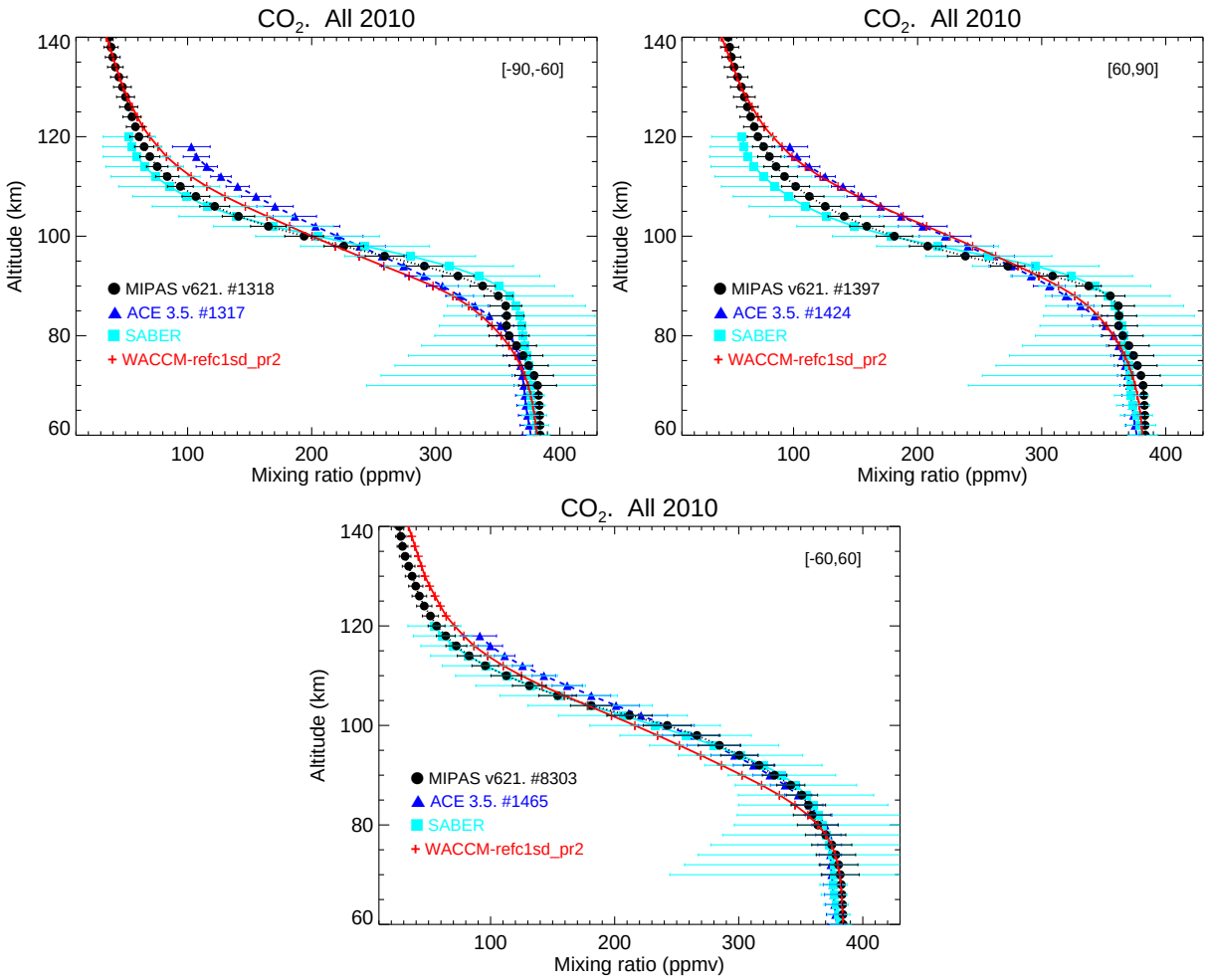

Figure 6.15: Annual mean CO_2 vmr abundances for 2010. Profiles for the Southern polar region (90°S-60°S) (top, left); Northern polar region (60°N-90°N) (top, right); and mid-latitudes and tropics (60°S-60°N) (bottom).

Between 100 and 120 km MIPAS CO_2 is slightly smaller than WACCM(P_r=2), and significantly smaller than ACE. Hence the CO_2 mixing ratio simulated by WACCM lies between that observed by MIPAS and ACE and slightly closer to the former. Inspecting in detail the ACE CO_2 retrieval we observe that above around 110 km the CO_2 vmr unrealistically increases with altitude in quite a few of the scans. This might introduce a positive bias which might be responsible for the ACE larger values in this region. SABER measurements in this altitude region are globally smaller than MIPAS, ACE and WACCM. WACCM simulations with P_r=4 somehow mitigates the WACCM P_r=2 overestimations and give an overall better agreement with MIPAS in the 100-120 km region and above (see Fig. 6.14, middle-right panel). In the uppermost region, 120-140 km, the WACCM-MIPAS differences show a rather strong latitudinal variation, with WACCM underestimating the CO_2 in the polar regions and overestimating it in the tropics and mid-latitudes. That also occurs even when decreasing the eddy diffusion coefficient (P_r=4) (see Fig. 6.14, middle column, right panel).

6.7. Comparison with WACCM Simulations

The Whole Atmosphere Community Climate model (WACCM) has been recently updated with the chemistry of CO and CO_2, as well as the eddy diffusion term, and has been recently compared to ACE CO and CO_2 measurements and MIPAS CO abundances (Garcia et al., 2014). Since this is one of the most complete models of the middle and upper atmosphere we compared the MIPAS CO_2 with the WACCM predictions for several input parameters in order to learn about the dynamics and chemistry of the upper atmosphere. A brief comparison has been done in the previous section. Here we show a more detailed comparison with two WACCM simulations for the standard Prandtl number of $P_r = 4$ and a smaller value of $P_r = 2$, which is equivalent to increasing the eddy diffusion coefficient k_{zz} by a factor of 2. The zonal mean CO_2 WACCM–MIPAS differences for all months of 2010 are shown in Figs. 6.16 and 6.17 for WACCM($P_r = 4$) and WACCM($P_r = 2$), respectively; and Fig. 6.18 shows CO_2 profiles and differences for three latitude bands for March, September, June and December of 2010. Similar figures have been produced by representing the CO_2 fields versus pressure (not shown) but they exhibit essentially the same general features.

In general, MIPAS is more consistent with a value of P_r=2 (larger eddy diffusion) in WACCM predictions in the 80-100 km region. These model simulations give an overall better agreement at practically all latitudes and seasonal conditions (see Fig. 6.18).

Above 100 km, examination of Figs. 6.16 and 6.17 shows that WACCM overestimates the MIPAS CO_2 at equinox at practically all latitudes. However, at mid- and high-latitudes in the summer hemisphere WACCM in general under-predicts the CO_2 distribution. Since the overall effect of decreasing the Prandtl number (increasing the eddy diffusion) is to increase the CO_2 concentration above around 80-90 km, we then have a better agreement between MIPAS and WACCM for solstice conditions (suggesting a larger eddy diffusion, P_r=2), particularly at mid- and high-latitudes in the summer hemisphere. On the contrary, at equinox conditions at almost all latitudes, and for solstice conditions at mid- to high latitudes in the winter hemisphere a smaller eddy diffusion seems to give a better agreement.

Of course there could be other reasons that explain those differences. For example, a weaker residual circulation in the lower thermosphere would lead to less efficient downwards transport of the CO_2-poor air from high altitudes into the polar summer lowermost thermosphere and hence produce a larger CO_2 concentration there. About the larger WACCM concentration at equinox for most latitudes another possible reason could be an underestimation of the photochemical losses of CO_2 in the model.

Overall, WACCM reproduces the major CO_2 vertical distribution patterns and the seasonal and latitudinal variations observed in MIPAS data. Below about 100 km the agreement is very good, with differences generally smaller than $\pm$10% (for $P_r = 2$) except for solstice conditions when they can be as large as 20% being WACCM smaller. In the polar summer MIPAS is generally smaller at these altitudes by up to 5%, which might point to a problem in the retrieval. At 100-140 km

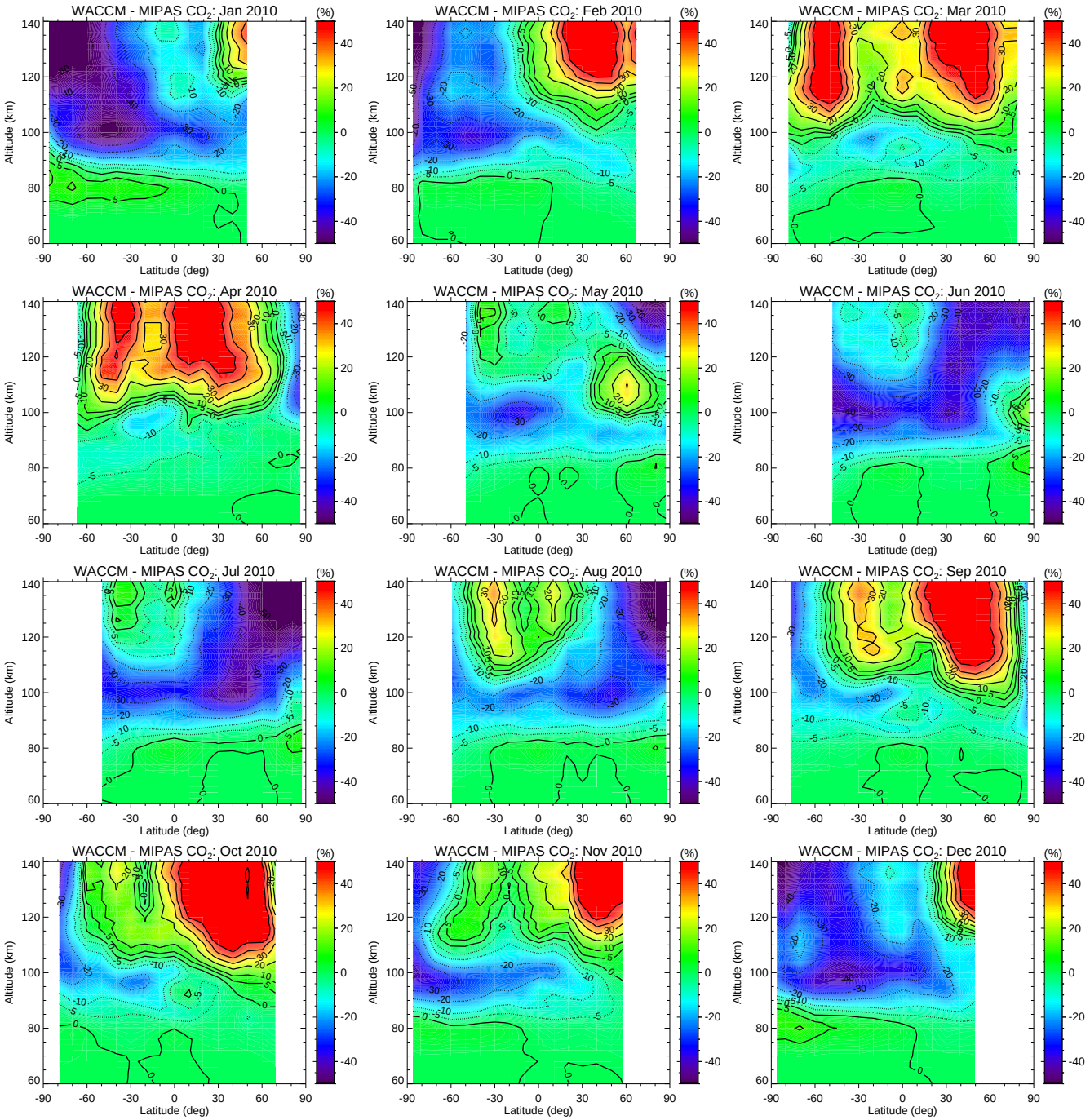

Figure 6.16: Monthly zonal mean CO_2 vmr WACCM(P_r=4)–MIPAS differences for 2010.

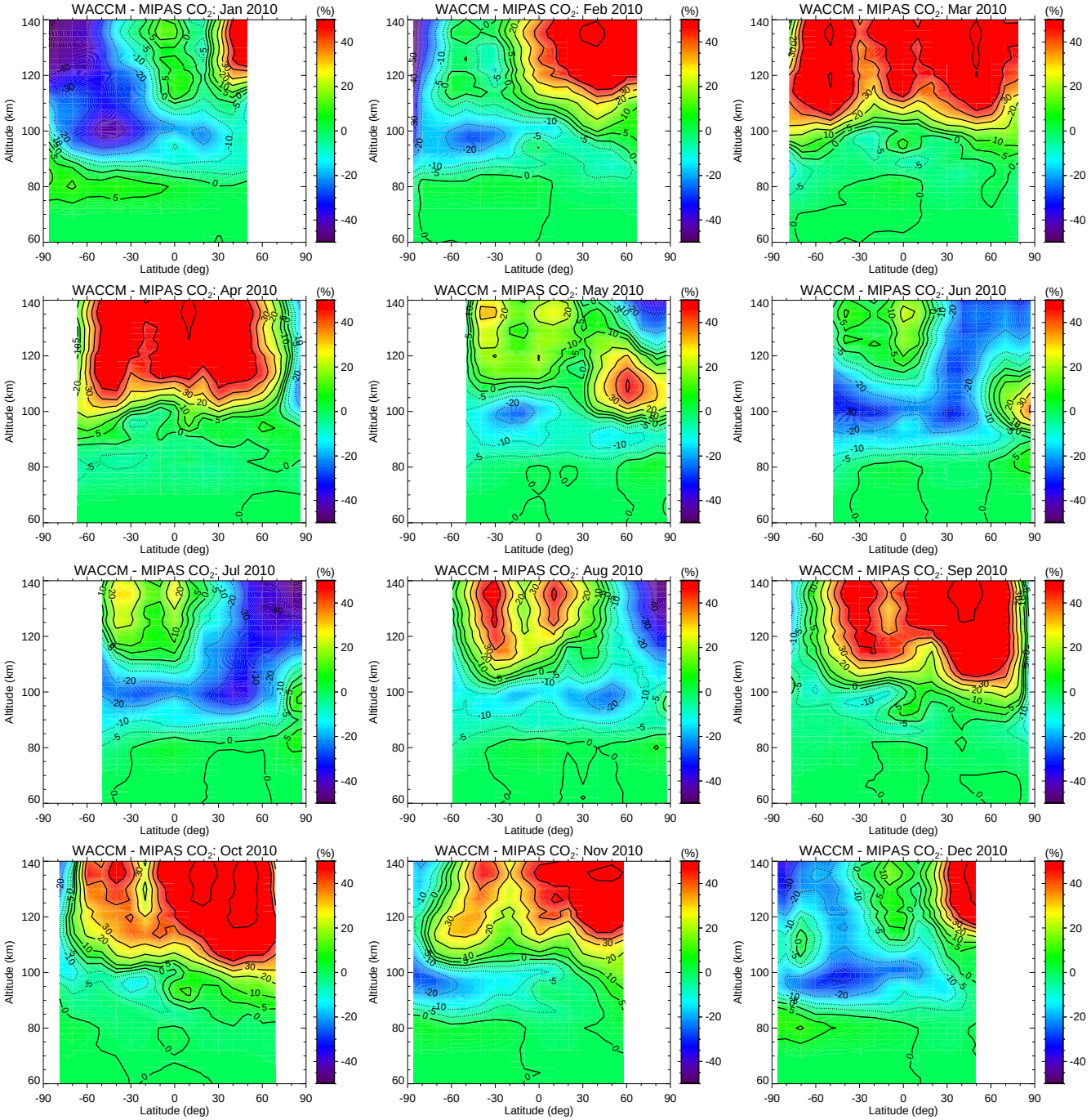

Figure 6.17: Monthly zonal mean CO_2 vmr WACCM(P_r=2)–MIPAS differences for 2010.

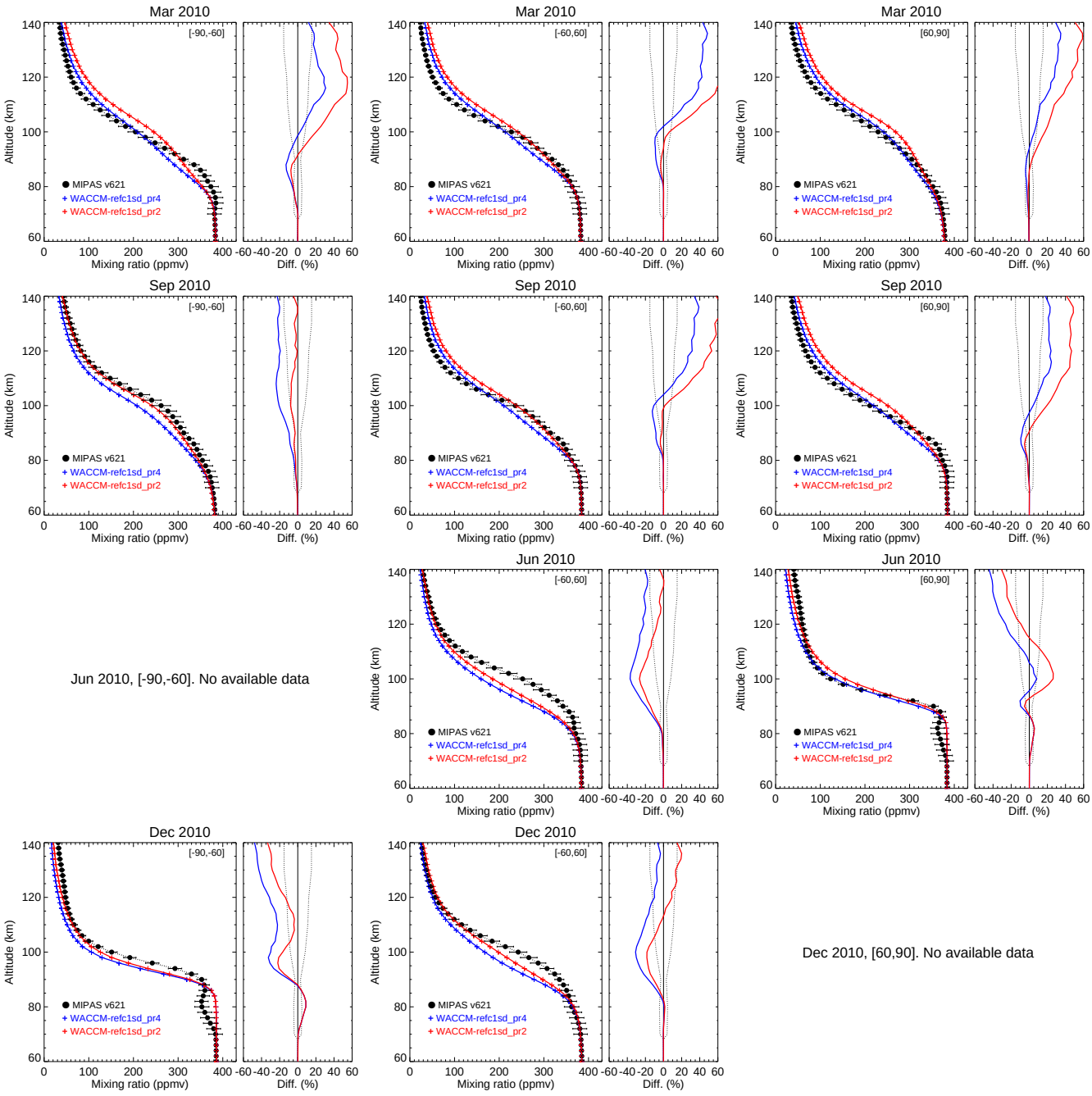

Figure 6.18: Comparison of MIPAS CO_2 with SD-WACCM simulations for P_r=4 (standard) and P_r=2 for March, September, June and December (rows 1-4) of 2010 for the Southern Hemisphere (90°S-60°S) (left column), mid-latitudes and tropics (60°N-60°S) (middle column) and Northern Hemisphere (60°N-90°N) (right column). Empty panels means no available MIPAS data. The right-hand panels show the WACCM–MIPAS differences, and the dotted lines represent the MIPAS total (mainly systematic) errors.

altitudes, WACCM CO_2 is generally larger than MIPAS at equinox at almost all latitudes with differences of 20-100%. In the summer hemispheres, however, WACCM CO_2 is generally lower in 20-70%. In the winter hemispheres WACCM CO_2 is also generally larger than MIPAS although not as large as in equinox. In general, MIPAS favors more a value of $P_r = 2$ (larger eddy diffusion), principally below around 100 km. This WACCM/MIPAS comparison give rise to new questions (it should be bear in mind that no global measurement of CO_2 in the lower thermosphere were taken before MIPAS). For example, if the different CO_2 seasonal/latitudinal distributions could be explained by a seasonal/latitudinal dependence of the eddy diffusion, k_{zz}; or if the lower thermosphere meridional circulation in WACCM is too strong. Also a possible reason for the discrepancies could be due to an underestimation of the photochemical losses of CO_2 in WACCM.

6.8. Inter-Annual Variability

MIPAS took measurements of the middle and upper atmosphere from January 2005 until April 2012. Hence it provides some information about the inter-annual variability of CO_2 in this region. The data from the Middle Atmosphere (MA) mode have not been processed yet. The inversion of CO_2 for this mode is more difficult and would be less accurate because we are missing the information of the CO_2 column above 100 km. Also, only 2 years of Upper Atmosphere (UA) mode data have been processed, because the most recent version of the thermospheric temperature, retrieved from the NO 5.3 μm emission with the same setup as that used here, is currently not available. However, even having only 2 consecutive years of CO_2 data we have looked at the change between these two years. The results are shown in Fig. 6.19 for the bulk of the atmosphere comprised between 60°S to 60°N. The figure shows that MIPAS CO_2 decreases from 2010 to 2011 above around 100 km, as expected for the larger solar activity (larger EUV flux) for 2011 than for 2010. Note that the MIPAS result is consistent with the WACCM prediction and with the SABER measurements. ACE also shows an incipient decrease between 95 and 110 km, that turns into an increase above 110 km. This anomalous increase might be due to the general overestimation of CO_2 by ACE with respect to MIPAS and SABER above 110 km, which, as discussed above might not be realistic but due to a retrieval artifact and might change from year to year.

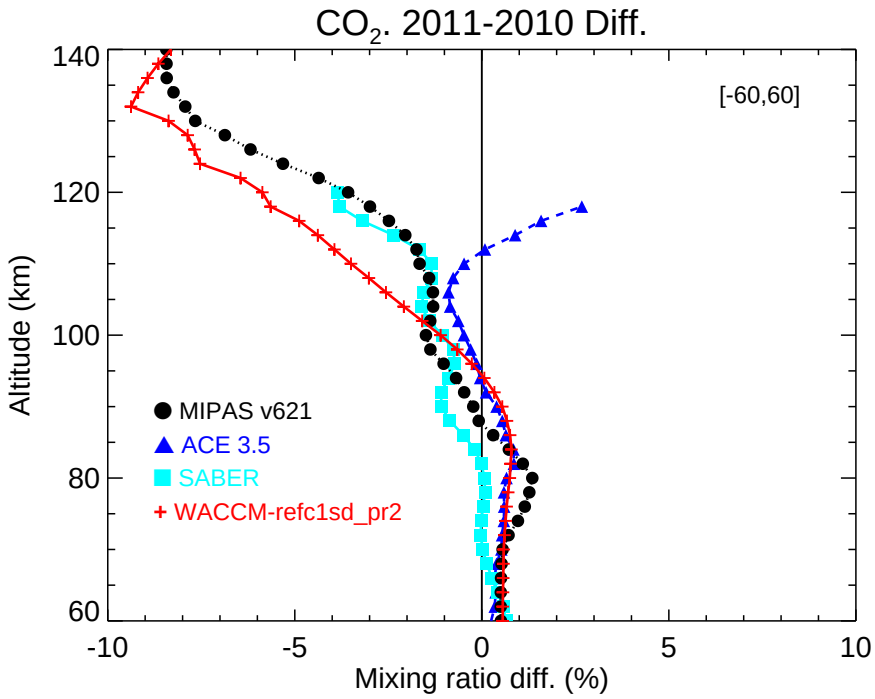

Figure 6.19: Inter-annual variation (2011–2010 differences) of CO_2 vmr from 2010 to 2011 for tropics and mid-latitudes.

Chapter 7

Conclusions and Future Work

Abstract

In this chapter we present the general conclusions from the results of this work. We have analyzed here MIPAS UA measurements from the mesosphere up to the middle thermosphere. First, we make the most of the MIPAS high spectral resolution and wide altitude range to derive new values for the most important vibration-vibration and vibration-thermal collisional rates affecting to the populations of the CO_2 levels emitting in the mid- and near-IR. These have an unprecedented accuracy and have a large impact on atmospheric spectral radiances in the 10, 4.3 and 2.7 μm spectral regions, and, therefore, on the CO_2 retrieval from measurements of these emissions. Secondly, by using these results, we have retrieved global distributions of the CO_2 vmr (volume mixing ratio) in the mesosphere and middle thermosphere (up to 142 km) for 2010 and 2011. This is the first time that the relative CO_2 concentration (vmr) has been retrieved in the middle thermosphere (120-140 km). Furthermore, the retrieved CO_2 has an unprecedented accuracy because of the new rate coefficients derived and the simultaneous measurements of other key atmospheric parameters (temperature in the mesosphere and in the thermosphere, as well as O_3) offered by the MIPAS spectra. A brief description of potential future work is also presented.

7.1. Non-LTE Collisional Rates

In this section we summarize the results on the retrieved collisional rates from MIPAS 10 and 4.3 μm spectra. MIPAS has a high spectral resolution (0.0625 cm^{-1}) and a wide spectral coverage (from 685 to 2410 cm^{-1}) that allow measuring and discriminating among the many bands contributing to the atmospheric limb radiance near 4.3 μm. Further, MIPAS has a high sensitivity that allows measuring this atmospheric emission in a wide altitude range, from 20 to ~170 km. Hence, MIPAS spectra provide unique information on the non-LTE populations of the many CO_2 levels emitting in the 4.3 μm region and on the processes that control them.

A sensitivity study was performed and showed that MIPAS spectra contain significant information on the following collisional rates:

a) $k_{vv,2}$, $k_{vv,3}$ and $k_{vv,4}$: $CO_2(v_d, v_3)+N_2 \rightleftharpoons CO_2(v_d, v_3–1)+N_2(1)$ with $v_d = 2v_1 +$

v_2= 2, v_d=3, and v_d=4, respectively;

b) k_{F1} and k_{F2}: $CO_2(v_1, v_2, l, 1, r)$+M $\rightleftharpoons$ $CO_2(v_1', v_2', l', 1, r')$+M with Δv_d=0 and Δl=0 (k_{F1}), and with Δv_d=0, $\Delta l \neq 0$ (k_{F2});

c) k_{vt}, the thermal relaxation of $CO_2(v_3)$ to the v_1 and v_2 modes, e.g., $CO_2(v_d, v_3)$ + M $\rightleftharpoons$ $CO_2(v_d', v_3$–1) + M with Δv_d=2-4 and Δv_3=–1; and

d) The efficiency of the excitation of $N_2(1)$ by $O(^1D)$.

A non-LTE retrieval scheme, used in previous analysis of the MIPAS non-LTE emission, has been applied to the MIPAS 10 and 4.3 μm spectra. The collisional rates listed above, together with the CO_2 vmr, have been retrieved from four days of MIPAS measurements (17 January, 30 March, 8 June and 26 September of 2010) taken in its 'Upper Atmosphere' mode, covering solstice and equinox conditions and pole-to-pole latitudes. The wide altitude and latitude ranges have allowed to retrieve also the temperature dependence of the collisional rates in the range of 130 to 250 K. The values obtained together with their temperature dependence and errors are shown in Table 5.1. All of them were retrieved with a much better accuracy that known before. The most salient results are:

- The $k_{vv,2}$ derived here has a stronger temperature dependence than that used before. Also, it is significantly larger than previous values at temperatures below 300 K, ranging from a factor of 1 to 1.5 from 300 K to 130 K. This is a result of major importance since this rate controls the populations of the $CO_2(10011)$ and (10012) levels, and therefore the atmospheric radiation near 4.3 μm and 2.7 μm at upper mesospheric and lower thermospheric limb paths.

- The collisional rates for the V-V transfer from high energy levels, $k_{vv,3}$ and $k_{vv,4}$, have been retrieved here for the first time. We have retrieved a temperature dependence of $1/T^{0.6}$, slightly stronger than $1/\sqrt{T}$, with values larger than previous rates by about 20% at mesospheric temperatures. We have not found any significant difference between $k_{vv,3}$ and $k_{vv,4}$.

- We have retrieved values for the k_{F1} and k_{F2} rates very different from those previously used. k_{F1} is about 43 times smaller than the rate derived by Sharma and Wintersteiner (1985) and about 4.7 times larger than that used by Shved et al. (1998). k_{F2} is about a factor of 9 to 5 (4.5 to 2.5 for $k_{F2'}$) larger than those used by Sharma and Wintersteiner (1985) and Shved et al. (1998) for temperatures of 150 and 250 K, respectively; and a factor of 2 to 3.5 (4 to 7 for $k_{F2'}$) smaller for the same temperature interval than those included in López-Puertas and Taylor (1989) and López-Puertas et al. (1998b). This leads to significant changes in the modeled atmospheric radiation of the two stronger 4.3 μm second hot bands, decreasing them by 20-30% for mid-latitude conditions.

- The derived k_{vt} collisional rate is smaller (factor of 0.7) than the values used recently by Funke et al. (2012). It is also smaller by factors of 0.38 and 0.57

at 150 and 250 K than those used in the analysis of SPIRE, SAMS and ISAMS measurements; and by factors of 0.71 and 0.65 than those used by Shved et al. (1998) and incorporated in the analysis of CRISTA and SABER measurements. The $k_{O(^1D)}$ collisional rate derived here jointly with k_{vt}, is very similar to that used by Funke et al. (2012). This means that it is factors of 1.5 and 1.1 (at 150 and 250 K, respectively) larger than those used in the analysis of SPIRE, SAMS and ISAMS measurements; and a factor of 1.21 larger than those used by Shved et al. (1998) and incorporated in the analysis of CRISTA and SABER measurements.

The new rates have very important effects on the atmospheric limb spectral radiances in the 10, 4.3 and 2.7 μm spectral regions when compared to typical collisional rates used in previous works. They also lead to a reduction of the integrated radiance in the 2280-2400 cm^{-1} range of 2-4% at tangent heights below ~85 km for mid-altitudes conditions, and as large as 8% for polar summer. This reduction is expected to be even larger in the 2.7 μm region. Also, a significant increase is expected in the 10 μm laser bands. Thus, these new rates allows a more accurate inversion of the CO_2 vmr in the mesosphere and lower thermosphere from measurements taken in the 10, 4.3 and 2.7 μm regions.

7.2. CO_2 Global Distributions in the Mesosphere and Thermosphere

In this section we summarize the major results of the CO_2 vmr distribution. Using the collisional rates describe above, we have retrieved global distributions of the CO_2 vmr in the mesosphere and thermosphere (up to ~140 km) for 2010 and 2011. This is the first time that the relative CO_2 concentration (vmr) have been retrieved in the middle thermosphere (120-140 km). Furthermore, the retrieved CO_2 has an unprecedented accuracy because of the new rate coefficients derived and the simultaneous measurements of other key atmospheric parameters (temperature in the mesosphere and in the thermosphere, as well as O_3) offered by the MIPAS spectra.

The CO_2 vmrs have been retrieved using MIPAS daytime limb emission spectra from the 4.3 μm region in its upper atmosphere (UA) mode (data version CO2_-620.0). The retrieved CO_2 covers from 70 km up to about 140 km. The inversion has been performed by using a non-LTE retrieval scheme developed at IAA/IMK. It takes the advantage of other (simultaneous) MIPAS measurements of atmospheric parameters, as the kinetic temperature (up to ~100 km) from the CO_2 15 μm region, the thermospheric temperature from the NO 5.3 μm, the O_3 measurements (up to ~100 km), which allows a strong constrain of the $O(^1D)$ concentration below ~100 km, and an accurate calculation of $O(^1D)$ above ~100 km. The non-LTE model incorporates the accurate vibrational-vibrational and vibrational-translational collisional rates derived from the MIPAS spectra.

The precision of the retrieved CO_2 vmr profiles varies with altitude ranging from

$\sim$1% below 90 km, to 5% around 120 km and larger than 10% above 130 km. The larger values at higher altitudes are due to the lower signal-to-noise ratio. There are very little latitudinal and seasonal variations, which are driven by the solar illumination conditions.

The retrieved CO_2 profiles have a vertical resolution of about 5–7 km below 120 km and between 10 and 20 km at 120-140 km.

Retrieval simulations performed with synthetic spectra have demonstrated that the developed retrieval scheme allows to reproduce the CO_2 profile in the 70–140 km range with very high accuracy. Even when using strongly perturbed a priori information, deviations from the "true' profile" are less than 4% for mid-latitude and 6% for polar summer conditions. The major systematic error source is the uncertainty (bias) of the pressure/temperature profiles which are retrieved in a preceding step. They can induce a systematic error up to 15-16% above 100 km and, at mid-latitude conditions, of 5% around 80 km. The systematic errors due to uncertainties of the $O(^1D)$ and $O(^3P)$ profiles are within 3-4% in the 100-120 km region. Finally, the errors due to uncertainties of the gain calibration and the solar flux at 4.3 and 2.7 μm are within $\sim$2% at all altitudes.

The most important features observed on the retrieved CO_2 can be summarized in:

- The retrieved CO_2 shows the major general features expected and predicted by models: the abrupt decline of the CO_2 vmr above 80-90 km, caused by the predominance of the molecular diffusion, and the seasonal change of the latitudinal distribution. The latter is reflected by higher CO_2 abundances in polar summer from 70 km up to $\sim$95 km, and lower CO_2 vmr in the polar winter, both induced by the ascending and descending branches of the meridional circulation, respectively. Above $\sim$95 km, CO_2 is more abundant in the polar winter than at mid-latitudes and polar summer regions, caused by the reversal of the meridional circulation in that altitude region.

- The solstice seasonal distribution, with a significant pole-to-pole CO_2 gradient lasts about 2.5 months in each hemisphere (November through February, and May through August), while the seasonal transition occurs quickly, mainly in April and October.

- We have found a small decrease in MIPAS CO_2 vmr at $\sim$80 km at polar summer latitudes. We are not sure if this is real, e.g., remnant CO_2 air from previous season, or a retrieval artifact caused by a combination of high solar zenith angles and low temperatures.

With the aim of validating the retrieved MIPAS CO_2 vmr, a detailed comparison has been performed with the most recent satellite measurements taken by ACE and SABER. The major results can be summarized in:

- In equinox, MIPAS shows an overall good agreement with ACE. MIPAS CO_2 measurements are slightly larger than those of ACE at 80-100 km. At higher

altitudes, the differences varies with latitude, being comprised always within ±20%.

- Also in equinox, the agreement of MIPAS with SABER is even better than with ACE, being within 5% below 100 km. In the 100-120 km region, MIPAS tends to be a ∼20% larger in polar regions and a ∼10-20% smaller near the tropics.
- During solstice there is, in general, a very good agreement between the CO_2 measurements of the three instruments. The agreement of MIPAS with ACE is similar as for equinox conditions, but there is a clear distinction in the polar summer, where the decay of the CO_2 vmr with altitude above ∼100 km is steeper in MIPAS than in ACE. This behavior is also present in SABER data (in excellent agreement with MIPAS) and is it is even more prominent (probably too steep) in WACCM simulations (see below).
- The agreement of MIPAS with SABER is in general very good. MIPAS CO_2 is, however, smaller (∼5%, and probably too low) around 80 km in the polar summer. SABER, on the other hand, seems to be too low at 60–80 km in the polar winter in January, and too high at 65-95 km in the polar winter in February.
- WACCM generally overestimates the CO_2 of the three instruments above ∼90 km at mid- and tropical latitudes during equinox. However, the opposite occurs during solstice at mid and high latitudes of the summer hemisphere, when WACCM CO_2 decreases more pronouncedly than the CO_2 of the three instruments at those altitudes.

In order to draw more general conclusions we have also compared zonal mean cross-section and latitudinal band profiles for the annual mean of 2010. The results showed that:

- MIPAS measurements are generally larger (∼5%) than ACE ones at 80-100 km and 20-30% smaller at 100-120 km.
- MIPAS and SABER agree very well up to 100 km. At 100-120 km, they also agree very well when averaging over all latitudes, but MIPAS is generally larger than SABER except near the equator where MIPAS is lower. That is, in the 100-120 km region, globally, ACE is the largest, SABER the smallest and MIPAS is in between.
- SABER CO_2 measurements between 100 and 120 km are globally smaller than MIPAS, ACE and WACCM.

From the detailed comparison of WACCM simulations with MIPAS observations we draw the following conclusions:

- Overall, WACCM reproduces the major CO_2 vertical distribution patterns and the seasonal and latitudinal variations observed in MIPAS data.

- Below about 100 km the agreement is very good, with differences smaller than $\pm$10% (for $P_r = 2$) except for solstice conditions near 90-100 km where they can be as large as 20%, being WACCM smaller. In the polar summer, near 80 km, MIPAS is smaller by up to 5%, which might point to a problem in the MIPAS CO_2 retrieval.
- At 100-140 km altitudes, WACCM CO_2 is generally larger than MIPAS at equinox at almost all latitudes with differences of 20-100%. In the summer hemispheres, however, WACCM CO_2 is generally lower in 20-70%. In the winter hemispheres WACCM CO_2 is also generally larger than MIPAS although not as large as in equinox.
- In general, MIPAS favors more a value of $P_r = 2$ (larger eddy diffusion), principally below around 100 km. In the 100-120 km region and above, however, WACCM simulations with P_r=4 somehow mitigates the WACCM P_r=2 overestimations and give an overall better agreement with MIPAS.
- The WACCM/MIPAS comparison give rise to new questions. For example, can the different MIPAS/WACCM CO_2 seasonal/latitudinal distributions be explained by a seasonal/latitudinal dependence of the eddy diffusion?; or is the lower thermosphere residual circulation in WACCM too strong?; or are they caused by an underestimation of the photochemical losses of CO_2 in WACCM?

Finally, the MIPAS global (60°S–60°N) CO_2 vmr above $\sim$100 km showed a decrease in 2011 with respect to 2010, which is consistent with the larger solar activity of 2011. This result is also consistent with SABER measurements and WACCM predictions. ACE measurements show also a decrease from 95 km up to 110 km but not between 110 and 120 km.

7.3. Future Work

In a near future, the most urgent work will be to complete the CO_2 retrieval from the whole MIPAS optimized resolution upper atmosphere (UA) mode data set, from 2005 to the end of the Envisat mission in 2012. This will be done after the retrieval of the thermospheric temperature is available for those years. This CO_2 database will then cover nearly a complete solar cycle and, therefore, could be used to perform an inter-annual variability study. Of particular importance is to check if it shows also a trend of CO_2 in the middle and upper atmosphere larger than that expected from the CO_2 anthropogenic increase in the lower thermosphere, as has been recently reported from the ACE (Emmert et al., 2012) and SABER (Yue et al., 2015) measurements. MIPAS CO_2 measurements, although limited in time with respect to ACE and SABER, have the advantages of providing simultaneously and globally the CO abundance, and covering higher altitudes, up to 140 km. These would allow to study in detail the CO_x chemistry and the dynamics of the middle thermosphere, practically an unexplored region.

Other potential work to be carried out in the future is the study of the upper atmosphere infrared cooling. SABER has measured (still measuring) the CO_2 and NO coolings, but could not derive the temperature and CO_2 and NO volume mixing ratios. MIPAS, however, is able to provide those measurements. Hence, comparison of the CO_2 and NO cooling rates calculated with the MIPAS products and those measured by SABER would be very valuable. Also, comparison with WACCM simulations would be very useful, since MIPAS offers important constraints as the temperature, and the CO, CO_2 and NO relative concentrations.

On the algorithm development side, it would be very useful to develop the "setups" for the retrievals of CO_2 from the middle atmosphere (MA) and Noctilucent Cloud (NLC) MIPAS observations modes. We do not expect to gain much information about the CO_2 distribution, since they cover essentially the same periods and latitudes, but would shed some light on the effect of the CO_2 column above 100 km, hence being of potential use for future retrievals whit limited altitude coverage of the measurements.

Appendix A

Table of CO_2 Bands

Table A.1: Principal CO_2 bands emitting near 4.3 μm included in this work.

Iso[◇]	Band	Upper level[†]	Lower level[†]	$\tilde{\nu}_0$[*] (cm^{-1})	A[‡] (s^{-1})
1	FB	(9) 00011 (00^01)	(1) 00001 (00^00)	2349.14	423.8
1	FH	(16) 01111 (01^11)	(2) 01101 (01^10)	2336.63	413.2
1	SH	(23) 10012 (02^01)	(3) 10002 (02^00)	2327.43	403.3
1	SH	(24) 02211 (02^21)	(4) 02201 (02^20)	2324.14	400.6
1	SH	(25) 10011 (10^01)	(5) 10001 (10^00)	2326.60	401.0
1	TH	(36) 11112 (03^11)	(6) 11102 (03^10)	2315.23	393.7
1	TH	(37) 03311 (03^31)	(7) 03301 (03^30)	2311.67	386.2
1	TH	(38) 11111 (11^11)	(8) 11101 (11^10)	2313.77	390.7
1	FHv_3	(39) 00021 (00^02)	(9) 00011 (00^01)	2324.18	413.6
1	FrH	(43) 20013 (04^01)	(10) 20003 (04^00)	2305.26	385.0
1	FrH	(44) 12212 (04^21)	(11) 12202 (04^20)	2302.97	380.4
1	FrH	(47) 04411 (04^41)	(13) 04401 (04^40)	2299.21	370.2
1	FrH	(48) 20012 (12^01)	(12) 20002 (12^00)	2306.70	379.5
1	FrH	(49) 12211 (12^21)	(14) 12201 (12^20)	2301.06	378.4
1	FrH	(50) 20011 (20^01)	(15) 20001 (20^00)	2302.52	380.0
1	FHv_3,FH	(51) 01121 (01^12)	(16) 01111 (01^11)	2311.70	806.5
1	5thH	(54) 21113 (05^11)	(17) 21103 (05^10)	2293.61	364.5
1	5thH	(56) 13312 (05^31)	(18) 13302 (05^30)	2290.68	368.4
1	5thH	(57) 05511 (05^51)	(20) 05501 (05^50)	2286.80	352.8
1	5thH	(58) 21112 (13^11)	(19) 21102 (13^10)	2293.41	370.7
1	5thH	(59) 13311 (13^31)	(21) 13301 (13^30)	2288.39	364.5
1	5thH	(60) 21111 (21^11)	(22) 21101 (21^10)	2289.90	369.5
1	FHv_3,SH	(61) 10022 (02^02)	(23) 10012 (02^01)	2302.37	787.4
1	FHv_3,SH	(62) 02221 (02^22)	(24) 02211 (02^21)	2299.24	781.8
1	FHv_3,SH	(63) 10021 (10^02)	(25) 10011 (10^01)	2301.91	782.2
1	6thH	(64) 30014 (06^01)	(26) 30004 (06^00)	2283.30	367.9

Continued on next page

Table A.1 continued

Iso[◇]	Band	Upper level[†]	Lower level[†]	$\tilde{\nu}_0$[*] (cm^{-1})	A[‡] (s^{-1})
1	6thH	(65) 22213 (06^21)	(27) 22203 (06^20)	2281.67	364.5
1	6thH	(66) 14412 (06^41)	(28) 14402 (06^40)	2278.39	353.2
1	6thH	(68) 30013 (14^01)	(29) 30003 (14^00)	2285.37	360.5
1	6thH	(69) 06611 (06^61)	(31) 06601 (06^60)	2274.42	333.4
1	6thH	(70) 22212 (14^21)	(30) 22202 (14^20)	2280.62	359.7
1	6thH	(71) 30012 (22^01)	(32) 30002 (22^00)	2283.58	358.7
1	6thH	(73) 14411 (14^41)	(33) 14401 (14^40)	2275.84	349.1
1	6thH	(74) 22211 (22^21)	(34) 22201 (22^20)	2277.17	357.4
1	6thH	(75) 30011 (30^01)	(35) 30001 (30^00)	2277.98	359.8
1	FHv_3,TH	(76) 11122 (03^12)	(36) 11112 (03^11)	2290.25	768.4
1	FHv_3,TH	(77) 03321 (03^32)	(37) 03311 (03^31)	2286.80	753.6
1	FHv_3,TH	(78) 11121 (11^12)	(38) 11111 (11^11)	2289.08	762.0
1	SHv_3	(79) 00031 (00^03)	(39) 00021 (00^02)	2299.26	1211.0
1	SHv_3,FH	(93) 01131 (01^13)	(51) 01121 (01^12)	2286.80	1177.0
2	FB	(9) 00011 (00^01)	(1) 00001 (00^00)	2283.49	376.6
2	FH	(16) 01111 (01^11)	(2) 01101 (01^10)	2271.76	367.4
2	SH	(23) 10012 (02^01)	(3) 10002 (02^00)	2261.91	359.6
2	SH	(24) 02211 (02^21)	(4) 02201 (02^20)	2260.05	356.4
2	SH	(25) 10011 (10^01)	(5) 10001 (10^00)	2262.85	355.5
2	TH	(36) 11112 (03^11)	(6) 11102 (03^10)	2250.69	330.2
2	TH	(37) 03311 (03^31)	(7) 03301 (03^30)	2248.36	343.8
2	TH	(38) 11111 (11^11)	(8) 11101 (11^10)	2250.60	346.7
2	FHv_3	(39) 00021 (00^02)	(9) 00011 (00^01)	2260.06	735.7
2	FrH	(43) 20013 (04^01)	(10) 20003 (04^00)	2240.54	344.1
2	FrH	(44) 12212 (04^21)	(11) 12202 (04^20)	2239.30	340.5
2	FrH	(47) 04411 (04^41)	(13) 04401 (04^40)	2236.68	329.8
2	FrH	(48) 20012 (12^01)	(12) 20002 (12^00)	2242.32	337.6
2	FrH	(49) 12211 (12^21)	(14) 12201 (12^20)	2238.57	336.1
2	FrH	(50) 20011 (20^01)	(15) 20001 (20^00)	2240.76	336.0
3	FB	(9) 00011 (00^01)	(1) 00001 (00^00)	2332.11	418.7
3	FH	(16) 01111 (01^11)	(2) 01101 (01^10)	2319.74	408.8
3	SH	(23) 10012 (02^01)	(3) 10002 (02^00)	2311.71	398.0
3	SH	(24) 02211 (02^21)	(4) 02201 (02^20)	2307.38	795.2
3	SH	(25) 10011 (10^01)	(5) 10001 (10^00)	2309.29	397.6
4	FB	(9) 00011 (00^01)	(1) 00001 (00^00)	2340.01	409.1
4	FH	(16) 01111 (01^11)	(2) 01101 (01^10)	2327.58	399.0
4	SH	(23) 10012 (02^01)	(3) 10002 (02^00)	2318.96	388.8
4	SH	(25) 10011 (10^01)	(5) 10001 (10^00)	2317.32	387.5
5	FB	(9) 00011 (00^01)	(1) 00001 (00^00)	2265.97	369.4
6	FB	(9) 00011 (00^01)	(1) 00001 (00^00)	2274.09	380.6

Continued on next page

Table A.1 continued

Iso$^{\diamond}$	Band	Upper level†	Lower level†	$\tilde{\nu}_0{}^{*}$ (cm^{-1})	$A^{\ddagger}$ (s^{-1})

$^{\diamond}$The isotopologue numbers refer to those in the HITRAN compilation. †Energy levels are given with the HITRAN identifier number (in parenthesis) and the HITRAN and Herzberg (in parenthesis) notations. *Band center. ‡Einstein coefficient at 250 K calculated from the HITRAN 2008 edition (Rothman et al., 2009). FB stands for fundamental band, FH for first hot (v_d=1), SH for second hot (v_d=2), TH for third hot (v_d=3), FrH for fourth hot (v_d=4), 5thH for fifth hot (v_d=5), 6thH for sixth hot (v_d=6), FHv_3 for v_3-first hot (v_3=2), FHv_3,FH for v_3-first hot v_d-first hot (v_3=2,v_d=1), FHv_3,SH for v_3-first hot v_d-second hot (v_3=2,v_d=2), FHv_3,TH for v_3-first hot v_d-third hot (v_3=2,v_d=3), SHv_3 for v_3-second hot ($v_3 = 3$), and SHv_3,FH for v_3-second hot v_d-first hot (v_3=3,v_d=1).

Appendix B

Table of CO_2 Sub-Microwindows

Table B.1: Sub-microwindows used in the joint retrieval of CO_2 and LOS.

Tangent Height (km)	Sub-microwindows (cm^{-1})
60	2311.188-2311.250, 2314.812-2314.938, 2317.062-2317.375, 2319.000-2319.188, 2319.812-2320.000, 2320.562-2320.688, 2321.438-2321.625, 2323.000-2323.250, 2324.750-2324.938, 2326.188-2326.250, 2326.625-2326.812, 2326.938-2327.062, 2328.562-2328.625, 2329.250-2329.312, 2330.000-2330.062, 2332.500-2332.562, 2334.000-2334.062, 2339.438-2339.500, 2340.938-2341.000, 2346.062-2346.125, 2353.000-2353.062, 2354.375-2354.500, 2355.938-2356.125, 2360.188-2360.312
63	2309.625-2309.688, 2310.375-2310.500, 2311.125-2311.438, 2313.625-2313.812, 2314.688-2314.938, 2315.250-2315.312, 2316.188-2316.250, 2317.062-2317.312, 2317.438-2317.500, 2318.875-2319.188, 2319.688-2320.000, 2320.312-2320.688, 2321.188-2321.688, 2322.812-2323.250, 2324.688-2324.938, 2325.375-2325.625, 2326.000-2326.250, 2326.625-2327.062, 2328.562-2328.625, 2329.000-2329.062, 2329.250-2329.312, 2330.562-2330.750, 2332.125-2332.250, 2332.500-2332.562, 2334.000-2334.062, 2337.688-2337.750, 2339.312-2339.562, 2340.875-2341.000, 2342.625-2342.688, 2344.312-2344.500, 2345.875-2346.125, 2354.375-2354.562, 2355.750-2356.062, 2358.562-2358.875, 2361.312-2361.625, 2363.938-2364.250, 2365.250-2365.500
66	2310.438-2310.562, 2311.125-2311.250, 2314.812-2314.938, 2315.250-2315.312, 2318.938-2319.188, 2319.750-2320.000, 2320.312-2320.375, 2320.562-2320.688, 2321.438-2321.688, 2323.000-2323.312, 2324.750-2324.938, 2325.562-2325.625, 2326.188-2326.250, 2326.625-2327.062, 2328.562-2328.625, 2328.750-2328.812, 2330.562-2330.625, 2332.438-2332.562, 2334.000-2334.062, 2335.938-2336.000, 2339.312-2339.500, 2340.938-2341.000, 2342.625-2342.688, 2344.312-2344.375, 2345.938-2346.125, 2354.312-2354.500, 2355.812-2356.062, 2357.188-2357.438, 2358.562-2358.875, 2360.000-2360.250, 2361.312-2361.562, 2362.750-2362.938, 2364.000-2364.250, 2365.250-2365.500

Continued on next page

Table B.1 continued

Tangent Height (km)	Sub-microwindows (cm^{-1})
69	2310.438-2310.562, 2314.812-2314.938, 2318.938-2319.188, 2319.750-2319.938, 2320.562-2320.688, 2321.125-2321.188, 2324.750-2324.938, 2326.188-2326.250, 2326.688-2327.062, 2328.562-2328.812, 2332.438-2332.500, 2334.000-2334.062, 2335.938-2336.000, 2339.312-2339.500, 2340.938-2341.000, 2342.625-2342.688, 2344.312-2344.375, 2354.312-2354.500, 2355.875-2356.000, 2357.188-2357.438, 2358.625-2358.750, 2362.750-2362.938
72	2323.250-2323.312, 2323.875-2324.188, 2324.875-2324.938, 2328.625-2328.812, 2334.000-2334.062, 2335.938-2336.062, 2340.938-2341.000, 2342.625-2342.688, 2346.625-2346.688, 2347.562-2347.625, 2349.938-2350.000, 2350.938-2351.125, 2352.125-2352.250
75	2307.188-2307.250, 2308.125-2308.188, 2308.312-2308.375, 2309.000-2309.062, 2309.625-2309.688, 2316.125-2316.188, 2317.500-2317.562, 2320.312-2320.375, 2321.125-2321.188, 2321.625-2321.688, 2321.938-2322.000, 2323.562-2323.625, 2323.875-2324.188, 2328.750-2328.812, 2329.000-2329.062, 2335.875-2336.062, 2336.312-2336.438, 2336.625-2336.688, 2337.688-2337.750, 2340.938-2341.000, 2342.250-2342.312, 2342.625-2342.688, 2344.188-2344.250, 2346.562-2346.688, 2347.562-2347.812, 2349.750-2350.062, 2350.875-2351.125
78	2306.000-2306.312, 2306.938-2307.188, 2307.812-2307.875, 2308.000-2308.125, 2308.750-2309.062, 2309.625-2309.688, 2310.562-2310.625, 2311.438-2311.500, 2311.688-2311.750, 2312.312-2312.375, 2312.562-2312.625, 2313.188-2313.250, 2313.438-2313.625, 2314.312-2314.438, 2316.062-2316.188, 2316.938-2317.000, 2317.500-2317.562, 2317.750-2317.875, 2318.625-2318.688, 2319.188-2319.312, 2320.000-2320.062, 2320.312-2320.375, 2320.875-2320.938, 2321.125-2321.188, 2321.688-2321.750, 2321.938-2322.000, 2322.500-2322.812, 2323.312-2323.562, 2323.938-2324.188, 2329.625-2329.875, 2330.250-2330.312, 2330.500-2330.562, 2331.125-2331.375, 2332.000-2332.062, 2332.812-2332.875, 2334.062-2334.125, 2335.750-2336.062, 2336.875-2336.938, 2337.125-2337.188, 2338.500-2338.625, 2339.625-2339.688, 2339.875-2339.938, 2340.938-2341.250, 2342.312-2342.438, 2342.688-2342.938, 2343.938-2344.188, 2344.875-2345.438, 2346.125-2346.625
81	2306.000-2306.312, 2306.938-2307.188, 2307.875-2308.125, 2308.750-2309.000, 2309.625-2309.938, 2310.562-2310.812, 2311.438-2311.750, 2312.312-2312.625, 2313.188-2313.562, 2314.062-2314.438, 2314.938-2315.250, 2315.875-2316.125, 2316.688-2317.000, 2317.500-2317.875, 2318.375-2318.688, 2319.188-2319.500, 2320.000-2320.375, 2320.875-2321.188, 2321.688-2322.000, 2322.500-2322.812, 2323.312-2323.562, 2330.250-2330.562, 2331.125-2331.375, 2331.750-2332.062, 2332.562-2332.875, 2333.188-2333.500, 2334.062-2334.375, 2334.625-2334.938, 2335.500-2335.812, 2336.000-2336.312, 2336.875-2337.188, 2337.438-2337.688, 2338.312-2338.625, 2338.812-2339.062, 2339.625-2339.938, 2340.062-2340.375, 2341.000-2341.250, 2341.438-2341.688, 2342.312-2342.562, 2342.688-2342.938, 2343.938-2344.188, 2344.875-2345.125

Continued on next page

Table B.1 continued

Tangent Height (km)	Sub-microwindows (cm^{-1})			
84	2306.062-2306.312, 2309.625-2309.938, 2313.188-2313.562, 2316.688-2317.000, 2320.000-2320.312, 2323.312-2323.562, 2332.562-2332.812, 2335.500-2335.688, 2338.312-2338.625, 2341.000-2341.250, 2343.938-2344.188	2306.938-2307.188, 2310.562-2310.812, 2314.062-2314.438, 2317.562-2317.812, 2320.875-2321.188, 2330.250-2330.562, 2333.188-2333.500, 2336.000-2336.312, 2338.812-2339.000, 2341.438-2341.688,	2307.875-2308.062, 2311.500-2311.750, 2314.938-2315.250, 2318.438-2318.688, 2321.688-2321.938, 2331.125-2331.312, 2334.062-2334.250, 2336.938-2337.188, 2339.625-2339.938, 2342.312-2342.562,	2308.750-2309.000, 2312.312-2312.625, 2315.875-2316.125, 2319.188-2319.500, 2322.500-2322.750, 2331.750-2332.000, 2334.688-2334.875, 2337.438-2337.688, 2340.062-2340.375, 2342.688-2342.938,
87	2306.000-2306.312, 2309.688-2309.938, 2313.188-2313.562, 2316.688-2317.000, 2320.000-2320.312, 2323.312-2323.562, 2332.562-2332.875, 2335.500-2335.812, 2338.312-2338.625, 2341.000-2341.250, 2343.938-2344.188	2306.938-2307.188, 2310.562-2310.812, 2314.062-2314.375, 2317.500-2317.812, 2320.875-2321.188, 2330.250-2330.562, 2333.188-2333.500, 2336.000-2336.312, 2338.812-2339.062, 2341.438-2341.688,	2307.875-2308.125, 2311.438-2311.750, 2314.938-2315.250, 2318.375-2318.688, 2321.688-2322.000, 2331.125-2331.375, 2334.062-2334.375, 2336.875-2337.188, 2339.625-2339.938, 2342.312-2342.562,	2308.750-2309.000, 2312.312-2312.625, 2315.875-2316.125, 2319.188-2319.500, 2322.500-2322.812, 2331.750-2332.062, 2334.625-2334.938, 2337.438-2337.688, 2340.062-2340.375, 2342.688-2342.938,
90	2306.000-2306.312, 2309.688-2309.938, 2313.188-2313.562, 2316.688-2317.000, 2320.000-2320.312, 2323.312-2323.562, 2332.562-2332.875, 2335.500-2335.812, 2338.312-2338.625, 2341.000-2341.250, 2343.938-2344.188	2306.938-2307.188, 2310.562-2310.812, 2314.062-2314.375, 2317.500-2317.812, 2320.875-2321.188, 2330.250-2330.562, 2333.188-2333.500, 2336.000-2336.312, 2338.812-2339.062, 2341.438-2341.688,	2307.875-2308.125, 2311.438-2311.750, 2314.938-2315.250, 2318.375-2318.688, 2321.688-2322.000, 2331.125-2331.375, 2334.062-2334.375, 2336.875-2337.188, 2339.625-2339.938, 2342.312-2342.562,	2308.750-2309.000, 2312.312-2312.625, 2315.875-2316.125, 2319.188-2319.500, 2322.500-2322.812, 2331.750-2332.062, 2334.625-2334.938, 2337.438-2337.688, 2340.062-2340.375, 2342.688-2342.938,
93	2306.000-2306.312, 2309.688-2309.938, 2313.188-2313.562, 2316.688-2317.000, 2320.000-2320.312, 2323.312-2323.562, 2332.562-2332.875, 2335.500-2335.812, 2338.312-2338.562, 2341.062-2341.312, 2343.938-2344.188	2306.938-2307.188, 2310.562-2310.812, 2314.125-2314.375, 2317.500-2317.812, 2320.875-2321.125, 2330.250-2330.500, 2333.188-2333.500, 2336.062-2336.312, 2338.812-2339.062, 2341.438-2341.688,	2307.875-2308.125, 2311.438-2311.750, 2314.938-2315.250, 2318.375-2318.688, 2321.688-2322.000, 2331.125-2331.375, 2334.125-2334.375, 2336.875-2337.188, 2339.625-2339.938, 2342.312-2342.562,	2308.750-2309.000, 2312.312-2312.625, 2315.875-2316.125, 2319.250-2319.500, 2322.500-2322.812, 2331.750-2332.062, 2334.625-2334.938, 2337.438-2337.625, 2340.062-2340.375, 2342.688-2342.938,

Continued on next page

Table B.1 continued

Tangent Height (km)	Sub-microwindows (cm^{-1})			
96	2306.000-2306.312,	2306.938-2307.188,	2307.875-2308.125,	2308.750-2309.000,
	2309.688-2309.938,	2310.562-2310.812,	2311.438-2311.750,	2312.312-2312.625,
	2313.188-2313.562,	2314.125-2314.375,	2314.938-2315.312,	2315.875-2316.125,
	2316.688-2317.000,	2317.500-2317.812,	2318.375-2318.688,	2319.250-2319.500,
	2320.000-2320.312,	2320.875-2321.062,	2321.688-2322.000,	2322.562-2322.812,
	2323.312-2323.562,	2330.250-2330.500,	2331.750-2332.062,	2332.562-2332.875,
	2333.188-2333.500,	2334.125-2334.375,	2334.625-2334.938,	2335.500-2335.812,
	2336.062-2336.312,	2336.875-2337.188,	2337.438-2337.625,	2338.312-2338.562,
	2338.812-2339.062,	2339.625-2339.938,	2340.062-2340.375,	2341.062-2341.312,
	2341.438-2341.688,	2342.312-2342.562,	2342.688-2342.938,	2343.938-2344.188,
	2346.125-2346.375			
99	2306.000-2306.312,	2306.938-2307.188,	2307.875-2308.125,	2308.750-2309.000,
	2309.688-2309.938,	2310.562-2310.812,	2311.438-2311.750,	2312.312-2312.625,
	2313.188-2313.562,	2314.125-2314.375,	2314.938-2315.312,	2315.875-2316.125,
	2316.688-2317.000,	2317.500-2317.812,	2318.375-2318.688,	2319.250-2319.500,
	2320.000-2320.312,	2320.875-2321.062,	2321.688-2322.000,	2323.250-2323.562,
	2324.125-2324.375,	2330.250-2330.438,	2331.750-2332.062,	2332.562-2332.875,
	2333.250-2333.500,	2334.125-2334.375,	2334.625-2334.938,	2335.500-2335.812,
	2336.062-2336.312,	2336.875-2337.188,	2337.438-2337.625,	2338.312-2338.562,
	2338.812-2339.062,	2339.625-2339.938,	2340.062-2340.375,	2341.062-2341.312,
	2341.438-2341.688,	2342.312-2342.938,	2343.938-2344.250,	2346.125-2346.375,
	2347.500-2347.750			
102	2306.000-2306.312,	2307.000-2307.188,	2307.875-2308.125,	2308.875-2309.188,
	2309.688-2309.938,	2310.562-2310.812,	2310.938-2311.188,	2311.500-2311.750,
	2312.375-2312.625,	2313.062-2313.562,	2314.125-2314.375,	2315.000-2315.375,
	2315.875-2316.125,	2316.688-2317.312,	2317.562-2317.812,	2318.375-2318.688,
	2319.250-2319.500,	2320.062-2320.312,	2320.875-2321.250,	2321.688-2321.938,
	2323.250-2323.562,	2324.125-2324.438,	2325.000-2325.188,	2326.688-2327.000,
	2330.312-2330.500,	2331.750-2332.062,	2332.562-2332.875,	2333.250-2333.500,
	2334.125-2334.375,	2334.625-2334.938,	2335.500-2335.750,	2336.062-2336.312,
	2336.938-2337.188,	2337.438-2337.625,	2338.312-2338.562,	2338.812-2339.062,
	2339.625-2339.938,	2340.062-2340.375,	2341.062-2341.312,	2341.438-2341.688,
	2342.312-2342.938,	2343.625-2344.250,	2346.125-2346.375,	2347.438-2347.750,
	2349.750-2350.062,	2352.812-2353.062		

Continued on next page

Table B.1 continued

Tangent Height (km)	Sub-microwindows (cm^{-1})			
107	2306.812-2307.062,	2308.875-2309.188,	2310.938-2311.250,	2313.062-2313.312,
	2315.000-2315.375,	2317.000-2317.312,	2319.000-2319.312,	2321.000-2321.312,
	2322.938-2323.188,	2324.812-2325.125,	2326.688-2327.000,	2328.562-2328.875,
	2330.438-2330.688,	2332.250-2332.500,	2334.000-2334.312,	2335.812-2336.062,
	2337.500-2337.812,	2339.250-2339.500,	2340.938-2341.250,	2342.562-2342.875,
	2344.250-2344.500,	2345.875-2346.125,	2347.438-2347.750,	2349.750-2350.062,
	2351.312-2351.625,	2352.812-2353.125,	2354.312-2354.562,	2355.750-2356.000,
	2357.188-2357.438,	2358.625-2358.875,	2360.000-2360.250,	2362.688-2362.875,
	2365.250-2365.500,	2367.750-2368.000,	2370.188-2370.375,	2371.312-2371.562,
	2372.438-2372.688,	2373.562-2373.750,	2374.625-2374.875,	2375.688-2375.938,
	2376.750-2376.938			
112	2306.812-2307.062,	2308.875-2309.188,	2310.938-2311.250,	2313.062-2313.312,
	2315.000-2315.375,	2317.000-2317.312,	2319.000-2319.312,	2321.000-2321.312,
	2322.938-2323.188,	2324.812-2325.125,	2326.750-2327.000,	2328.562-2328.875,
	2330.375-2330.688,	2332.250-2332.500,	2334.062-2334.312,	2335.750-2336.062,
	2337.500-2337.812,	2339.250-2339.500,	2340.938-2341.250,	2342.562-2342.875,
	2344.188-2344.500,	2345.875-2346.125,	2347.438-2347.750,	2349.750-2350.062,
	2351.312-2351.625,	2352.812-2353.125,	2354.250-2354.625,	2355.750-2356.062,
	2357.188-2357.438,	2358.625-2358.875,	2359.938-2360.250,	2361.312-2361.625,
	2362.688-2362.938,	2364.000-2364.250,	2365.250-2365.500,	2366.562-2366.750,
	2367.750-2368.000,	2368.938-2369.188,	2370.125-2370.375,	2371.312-2371.562,
	2372.438-2372.688,	2373.562-2373.812,	2374.625-2374.875,	2375.688-2375.938,
	2376.688-2376.938,	2377.750-2377.938		
117	2311.000-2311.250,	2313.062-2313.312,	2315.062-2315.312,	2317.062-2317.312,
	2319.000-2319.312,	2321.000-2321.312,	2322.938-2323.188,	2324.875-2325.125,
	2326.750-2327.000,	2328.562-2328.875,	2330.375-2330.688,	2332.250-2332.562,
	2334.062-2334.312,	2335.750-2336.062,	2337.500-2337.812,	2339.188-2339.500,
	2340.938-2341.250,	2342.562-2342.875,	2344.188-2344.500,	2345.875-2346.125,
	2347.438-2347.750,	2351.312-2351.625,	2352.812-2353.125,	2354.250-2354.625,
	2355.750-2356.062,	2357.188-2357.438,	2358.625-2358.875,	2360.000-2360.250,
	2361.312-2361.562,	2362.688-2362.938,	2363.938-2364.250,	2365.250-2365.500,
	2366.500-2366.750,	2367.750-2368.062,	2368.938-2369.188,	2370.125-2370.375,
	2371.312-2371.562,	2372.438-2372.688,	2373.562-2373.812,	2374.625-2374.875,
	2375.688-2375.938			
122	2313.062-2313.312,	2315.062-2315.312,	2317.062-2317.312,	2319.000-2319.312,
	2321.000-2321.250,	2322.938-2323.188,	2324.875-2325.125,	2326.750-2327.000,
	2328.562-2328.875,	2330.375-2330.688,	2332.250-2332.500,	2334.062-2334.312,
	2335.812-2336.062,	2337.500-2337.750,	2339.250-2339.500,	2340.938-2341.250,
	2342.562-2342.875,	2344.250-2344.500,	2345.875-2346.125,	2352.812-2353.125,
	2354.312-2354.562,	2355.750-2356.062,	2357.188-2357.438,	2358.625-2358.875,
	2360.000-2360.250,	2361.312-2361.562,	2362.688-2362.938,	2363.938-2364.250,
	2365.250-2365.500,	2366.500-2366.750,	2367.750-2368.062,	2368.938-2369.250,
	2370.125-2370.375,	2371.312-2371.562,	2372.438-2372.688,	2373.562-2373.812,
	2374.625-2374.875,	2375.688-2375.938		

Continued on next page

Table B.1 continued

Tangent Height (km)	Sub-microwindows (cm^{-1})
127	2311.000-2311.188, 2313.062-2313.312, 2315.062-2315.312, 2317.062-2317.312, 2319.000-2319.312, 2321.062-2321.250, 2322.938-2323.188, 2324.875-2325.125, 2326.750-2327.000, 2328.562-2328.812, 2330.375-2330.688, 2332.250-2332.500, 2334.062-2334.312, 2335.812-2336.062, 2337.500-2337.750, 2339.250-2339.500, 2340.938-2341.250, 2342.562-2342.875, 2344.250-2344.500, 2352.812-2353.062, 2354.312-2354.562, 2355.750-2356.062, 2357.188-2357.438, 2358.625-2358.875, 2360.000-2360.250, 2361.312-2361.562, 2362.688-2362.938, 2363.938-2364.250, 2365.250-2365.500, 2366.500-2366.750, 2367.750-2368.062, 2368.938-2369.250, 2370.125-2370.375, 2371.312-2371.562, 2372.438-2372.688, 2373.562-2373.812, 2374.625-2374.875, 2375.688-2375.938
132	2311.000-2311.188, 2313.062-2313.312, 2315.062-2315.250, 2317.062-2317.250, 2319.000-2319.250, 2321.062-2321.312, 2322.938-2323.125, 2324.875-2325.062, 2326.688-2327.000, 2328.562-2328.812, 2330.438-2330.625, 2332.250-2332.438, 2334.000-2334.250, 2335.812-2336.062, 2337.500-2337.750, 2339.188-2339.500, 2340.938-2341.188, 2342.562-2342.875, 2344.250-2344.500, 2352.812-2353.062, 2354.312-2354.562, 2355.750-2356.062, 2357.188-2357.438, 2358.625-2358.875, 2360.000-2360.250, 2361.312-2361.562, 2362.688-2362.938, 2363.938-2364.250, 2365.250-2365.500, 2366.500-2366.750, 2367.750-2368.062, 2368.938-2369.250, 2370.125-2370.375, 2371.312-2371.562, 2372.438-2372.688, 2373.562-2373.812, 2374.625-2374.875, 2375.688-2375.938
137	2311.000-2311.125, 2313.000-2313.250, 2315.062-2315.250, 2317.062-2317.250, 2319.000-2319.250, 2321.062-2321.250, 2323.000-2323.125, 2324.875-2325.062, 2326.750-2327.000, 2328.562-2328.812, 2330.438-2330.625, 2332.250-2332.438, 2334.000-2334.250, 2335.812-2336.062, 2337.500-2337.812, 2339.250-2339.500, 2340.938-2341.188, 2342.562-2342.875, 2344.250-2344.500, 2354.312-2354.562, 2355.750-2356.062, 2357.188-2357.438, 2358.625-2358.875, 2360.000-2360.250, 2361.312-2361.562, 2362.688-2362.938, 2363.938-2364.250, 2365.250-2365.500, 2366.500-2366.750, 2367.688-2368.062, 2368.938-2369.250, 2370.125-2370.375, 2371.312-2371.562, 2372.438-2372.688, 2373.562-2373.812, 2374.625-2374.875, 2375.688-2375.938, 2376.688-2376.938
142	2306.938-2307.000, 2308.938-2309.125, 2311.000-2311.125, 2313.000-2313.250, 2315.062-2315.250, 2317.062-2317.250, 2319.000-2319.250, 2321.062-2321.250, 2323.000-2323.125, 2324.875-2325.062, 2326.750-2327.000, 2328.562-2328.812, 2330.438-2330.625, 2332.250-2332.438, 2334.000-2334.250, 2335.812-2336.062, 2337.500-2337.812, 2339.250-2339.500, 2340.938-2341.188, 2342.562-2342.875, 2344.250-2344.500, 2354.312-2354.562, 2355.812-2356.062, 2357.188-2357.438, 2358.625-2358.875, 2360.000-2360.250, 2361.312-2361.562, 2362.688-2362.938, 2363.938-2364.250, 2365.250-2365.500, 2366.500-2366.750, 2367.688-2368.062, 2368.938-2369.250, 2370.125-2370.375, 2371.312-2371.562, 2372.438-2372.688, 2373.562-2373.812, 2374.625-2374.875, 2375.688-2375.938, 2376.688-2376.938, 2377.750-2377.938

Continued on next page

Table B.1 continued

Tangent Height (km)	Sub-microwindows (cm^{-1})			
147	2306.938-2307.000, 2315.062-2315.250, 2323.000-2323.125, 2330.438-2330.625, 2337.500-2337.812, 2344.250-2344.500, 2358.625-2358.875, 2363.938-2364.250, 2368.938-2369.250, 2373.562-2373.812, 2377.750-2377.938	2308.938-2309.125, 2317.062-2317.250, 2324.875-2325.062, 2332.250-2332.438, 2339.250-2339.500, 2354.312-2354.562, 2360.000-2360.250, 2365.250-2365.500, 2370.125-2370.375, 2374.625-2374.875,	2311.000-2311.125, 2319.000-2319.250, 2326.750-2327.000, 2334.000-2334.250, 2340.938-2341.188, 2355.812-2356.062, 2361.312-2361.562, 2366.500-2366.750, 2371.312-2371.562, 2375.688-2375.938,	2313.000-2313.250, 2321.062-2321.250, 2328.562-2328.812, 2335.812-2336.062, 2342.562-2342.875, 2357.188-2357.438, 2362.688-2362.938, 2367.688-2368.062, 2372.438-2372.688, 2376.688-2376.938,
152	2306.938-2307.000, 2315.062-2315.250, 2323.000-2323.125, 2330.438-2330.625, 2337.500-2337.812, 2344.250-2344.500, 2358.625-2358.875, 2363.938-2364.250, 2368.938-2369.250, 2373.562-2373.812, 2377.750-2377.938	2308.938-2309.125, 2317.062-2317.250, 2324.875-2325.062, 2332.250-2332.438, 2339.250-2339.500, 2354.312-2354.562, 2360.000-2360.250, 2365.250-2365.500, 2370.125-2370.375, 2374.625-2374.875,	2311.000-2311.125, 2319.000-2319.250, 2326.750-2327.000, 2334.000-2334.250, 2340.938-2341.188, 2355.812-2356.062, 2361.312-2361.562, 2366.500-2366.750, 2371.312-2371.562, 2375.688-2375.938,	2313.000-2313.250, 2321.062-2321.250, 2328.562-2328.812, 2335.812-2336.062, 2342.562-2342.875, 2357.188-2357.438, 2362.688-2362.938, 2367.688-2368.062, 2372.438-2372.688, 2376.688-2376.938,
157	2306.938-2307.000, 2315.062-2315.250, 2323.000-2323.125, 2330.438-2330.625, 2337.500-2337.812, 2344.250-2344.500, 2358.625-2358.875, 2363.938-2364.250, 2368.938-2369.250, 2373.562-2373.812, 2377.750-2377.938	2308.938-2309.125, 2317.062-2317.250, 2324.875-2325.062, 2332.250-2332.438, 2339.250-2339.500, 2354.312-2354.562, 2360.000-2360.250, 2365.250-2365.500, 2370.125-2370.375, 2374.625-2374.875,	2311.000-2311.125, 2319.000-2319.250, 2326.750-2327.000, 2334.000-2334.250, 2340.938-2341.188, 2355.812-2356.062, 2361.312-2361.562, 2366.500-2366.750, 2371.312-2371.562, 2375.688-2375.938,	2313.000-2313.250, 2321.062-2321.250, 2328.562-2328.812, 2335.812-2336.062, 2342.562-2342.875, 2357.188-2357.438, 2362.688-2362.938, 2367.688-2368.062, 2372.438-2372.688, 2376.688-2376.938,
162	2306.938-2307.000, 2315.062-2315.250, 2323.000-2323.125, 2330.438-2330.625, 2337.500-2337.812, 2344.250-2344.500, 2358.625-2358.875, 2363.938-2364.250, 2368.938-2369.250, 2373.562-2373.812, 2377.750-2377.938	2308.938-2309.125, 2317.062-2317.250, 2324.875-2325.062, 2332.250-2332.438, 2339.250-2339.500, 2354.312-2354.562, 2360.000-2360.250, 2365.250-2365.500, 2370.125-2370.375, 2374.625-2374.875,	2311.000-2311.125, 2319.000-2319.250, 2326.750-2327.000, 2334.000-2334.250, 2340.938-2341.188, 2355.812-2356.062, 2361.312-2361.562, 2366.500-2366.750, 2371.312-2371.562, 2375.688-2375.938,	2313.000-2313.250, 2321.062-2321.250, 2328.562-2328.812, 2335.812-2336.062, 2342.562-2342.875, 2357.188-2357.438, 2362.688-2362.938, 2367.688-2368.062, 2372.438-2372.688, 2376.688-2376.938,

Continued on next page

Table B.1 continued

Tangent Height (km)	Sub-microwindows (cm^{-1})			
167	2306.938-2307.000, 2315.062-2315.250, 2323.000-2323.125, 2330.438-2330.625, 2337.500-2337.812, 2344.250-2344.500, 2358.625-2358.875, 2363.938-2364.250, 2368.938-2369.250, 2373.562-2373.812, 2377.750-2377.938	2308.938-2309.125, 2317.062-2317.250, 2324.875-2325.062, 2332.250-2332.438, 2339.250-2339.500, 2354.312-2354.562, 2360.000-2360.250, 2365.250-2365.500, 2370.125-2370.375, 2374.625-2374.875,	2311.000-2311.125, 2319.000-2319.250, 2326.750-2327.000, 2334.000-2334.250, 2340.938-2341.188, 2355.812-2356.062, 2361.312-2361.562, 2366.500-2366.750, 2371.312-2371.562, 2375.688-2375.938,	2313.000-2313.250, 2321.062-2321.250, 2328.562-2328.812, 2335.812-2336.062, 2342.562-2342.875, 2357.188-2357.438, 2362.688-2362.938, 2367.688-2368.062, 2372.438-2372.688, 2376.688-2376.938,
172	2306.938-2307.000, 2315.062-2315.250, 2323.000-2323.125, 2330.438-2330.625, 2337.500-2337.812, 2344.250-2344.500, 2358.625-2358.875, 2363.938-2364.250, 2368.938-2369.250, 2373.562-2373.812, 2377.750-2377.938	2308.938-2309.125, 2317.062-2317.250, 2324.875-2325.062, 2332.250-2332.438, 2339.250-2339.500, 2354.312-2354.562, 2360.000-2360.250, 2365.250-2365.500, 2370.125-2370.375, 2374.625-2374.875,	2311.000-2311.125, 2319.000-2319.250, 2326.750-2327.000, 2334.000-2334.250, 2340.938-2341.188, 2355.812-2356.062, 2361.312-2361.562, 2366.500-2366.750, 2371.312-2371.562, 2375.688-2375.938,	2313.000-2313.250, 2321.062-2321.250, 2328.562-2328.812, 2335.812-2336.062, 2342.562-2342.875, 2357.188-2357.438, 2362.688-2362.938, 2367.688-2368.062, 2372.438-2372.688, 2376.688-2376.938,

Appendix C

Figures of the Comparison of MIPAS CO_2 with ACE, SABER, and WACCM

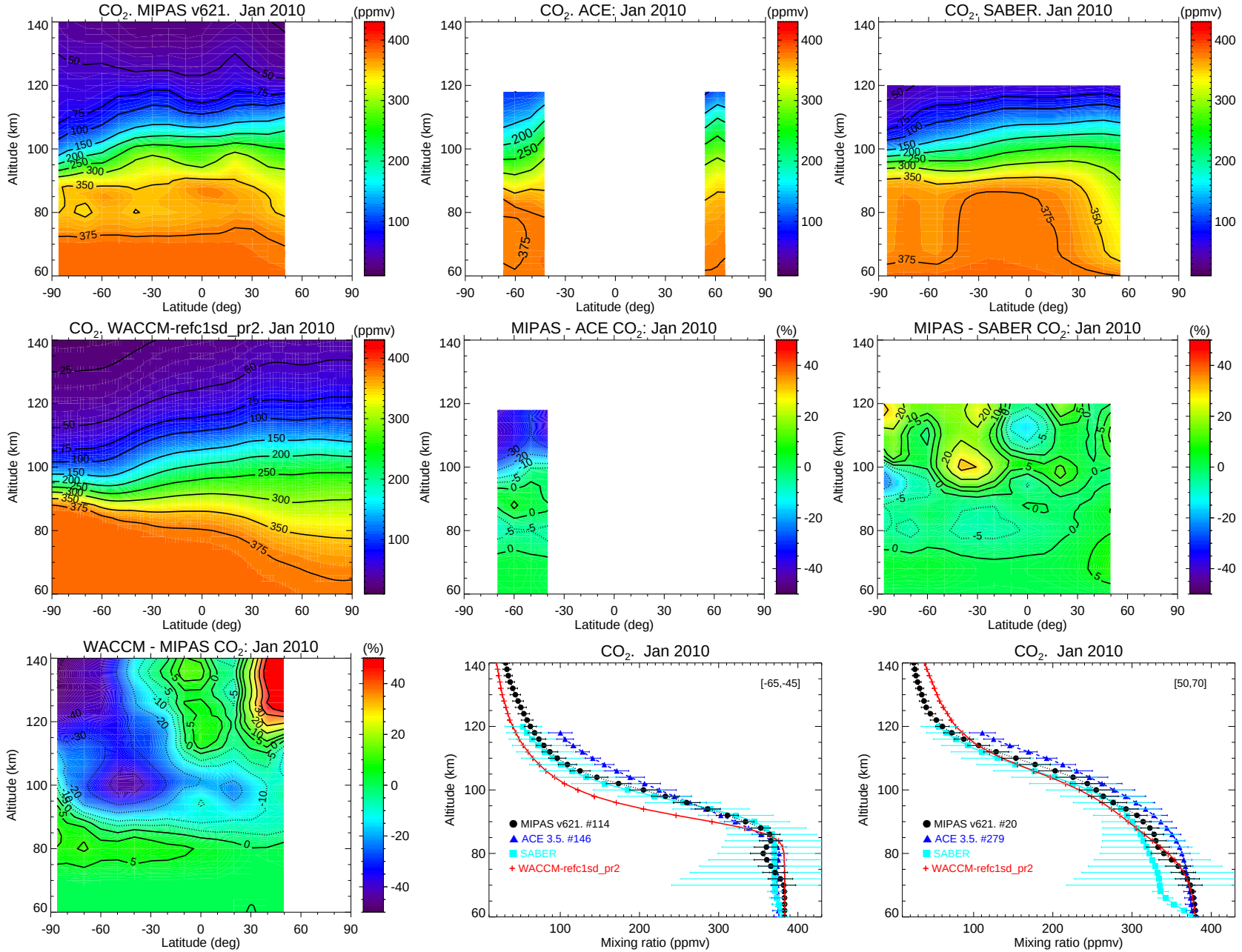

Figure C.1: CO_2 vmr abundances for January 2010. Top row: zonal mean distribution of MIPAS, ACE and SABER, respectively. Middle row: SD-WACCM (P_r=2) CO_2 distribution, and MIPAS-ACE and MIPAS-SABER CO_2 relative differences in %. Bottom row: WACCM-MIPAS CO_2 differences, and CO_2 vmr profiles for two latitude bands (as labelled) corresponding roughly to the ACE measurements. Horizontal bars in the measurements are the total errors, dominated by the systematic errors.

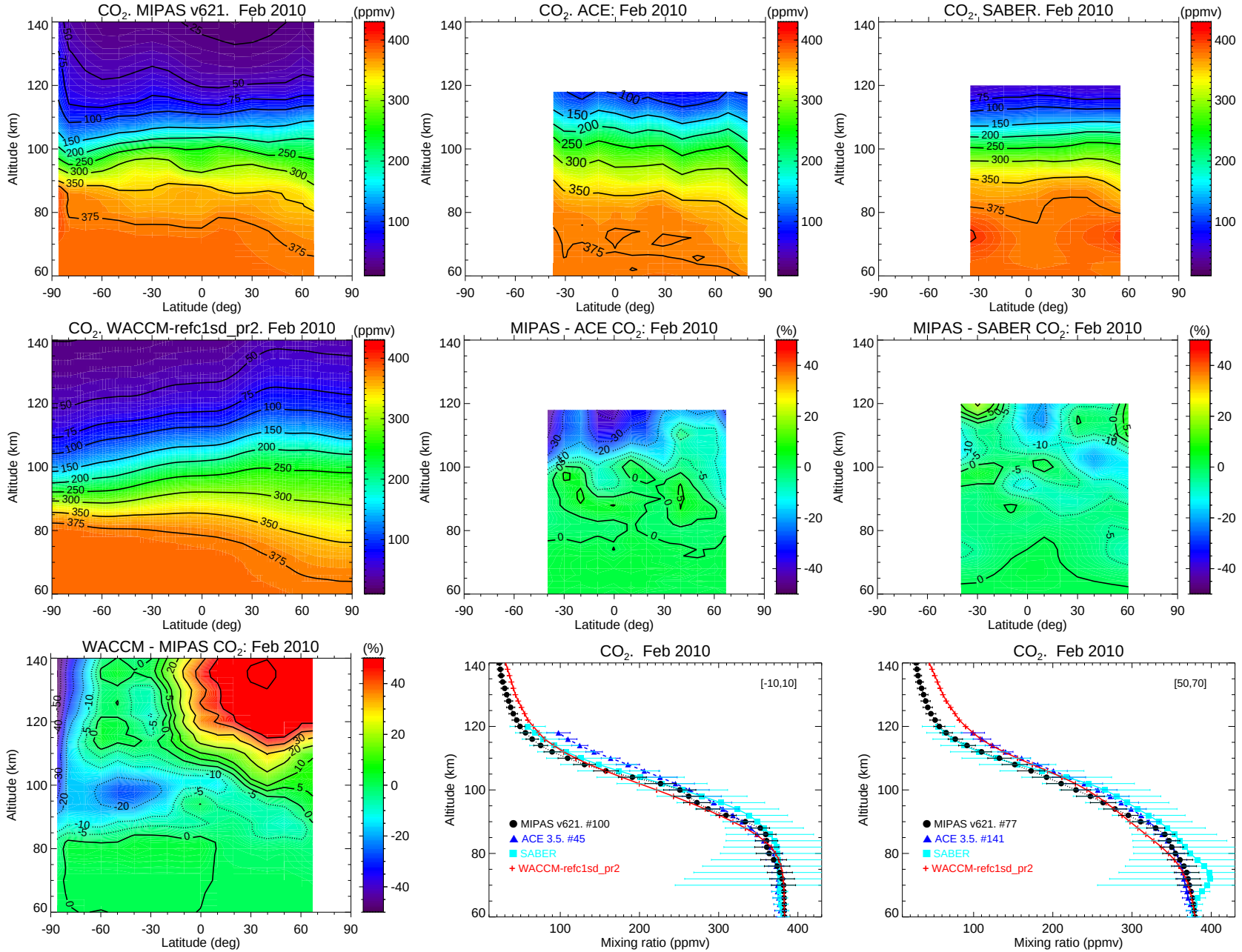

Figure C.2: As Fig. C.1 but for February 2010. Note that the latitude bands in the profiles panels can be different.

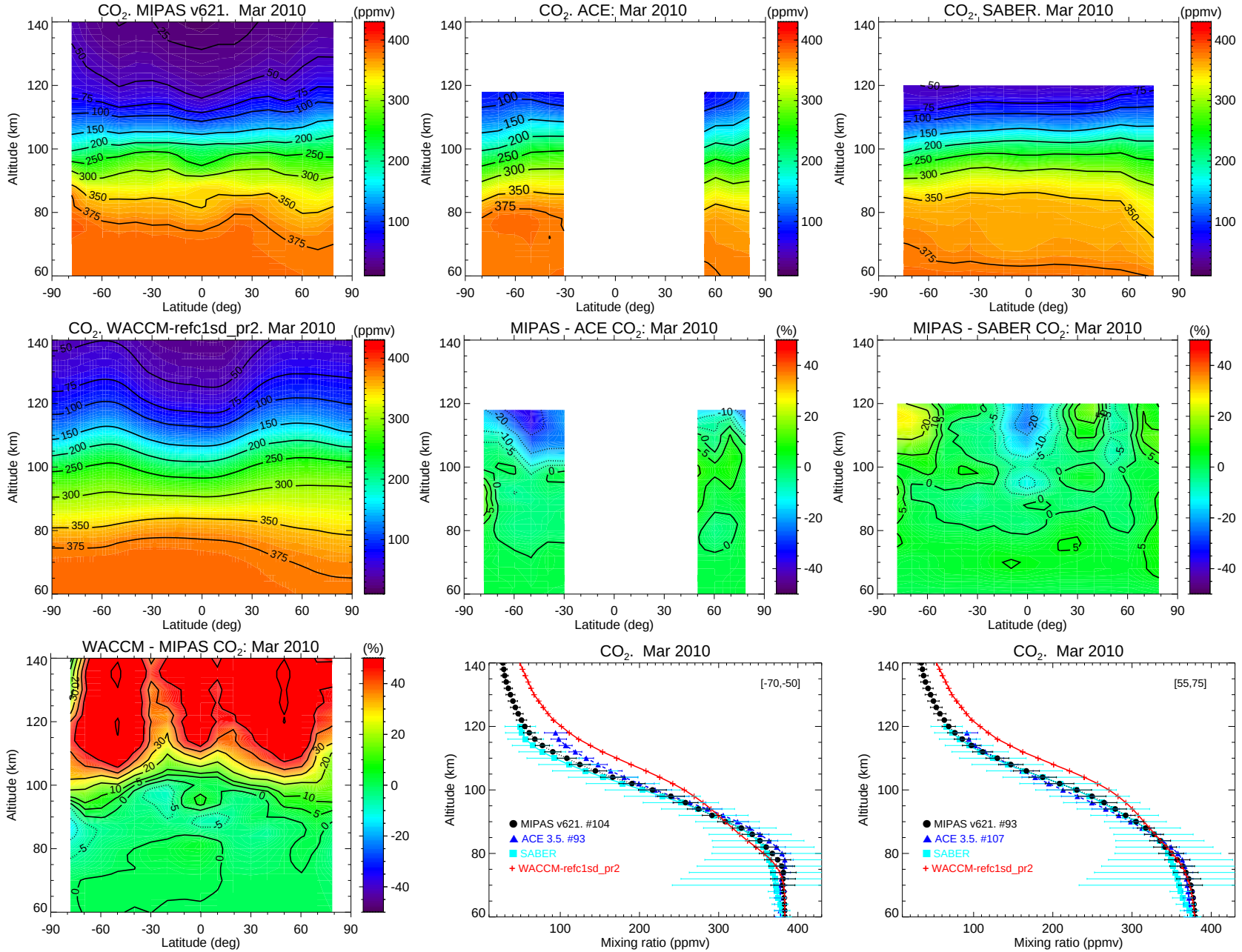

Figure C.3: As Fig. C.1 but for March 2010. Note that the latitude bands in the profiles panels can be different.

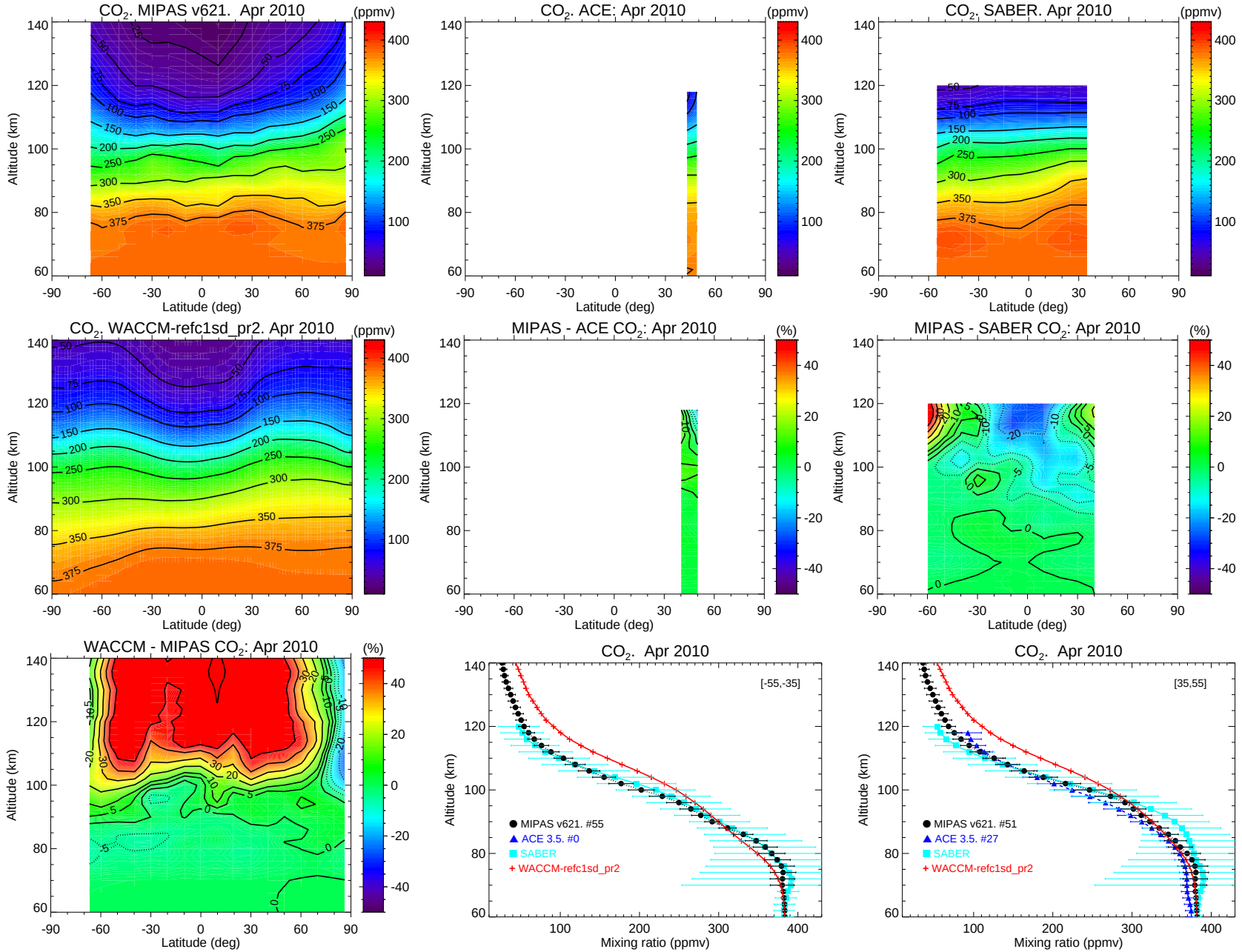

Figure C.4: As Fig. C.1 but for April 2010. Note that the latitude bands in the profiles panels can be different.

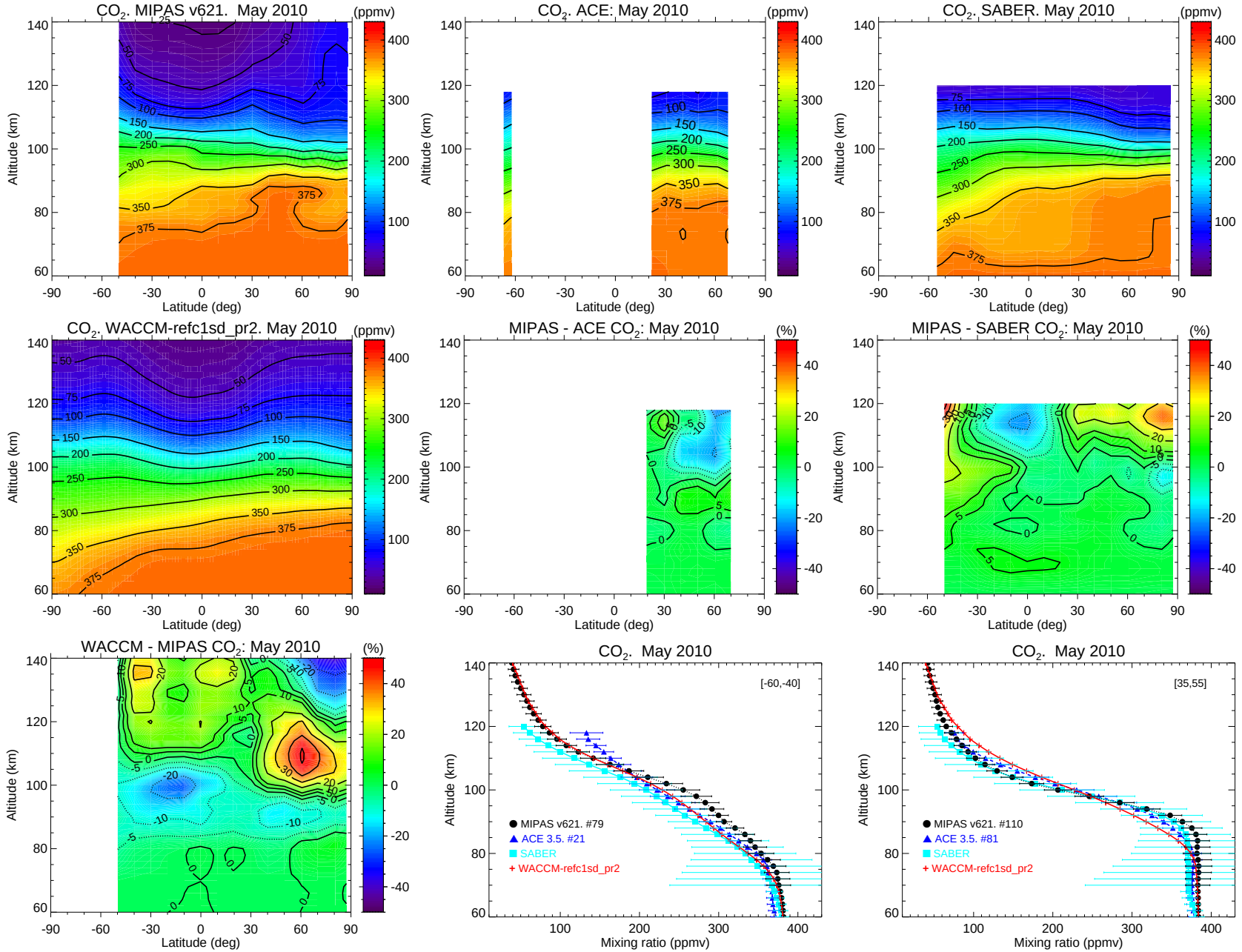

Figure C.5: As Fig. C.1 but for May 2010. Note that the latitude bands in the profiles panels can be different.

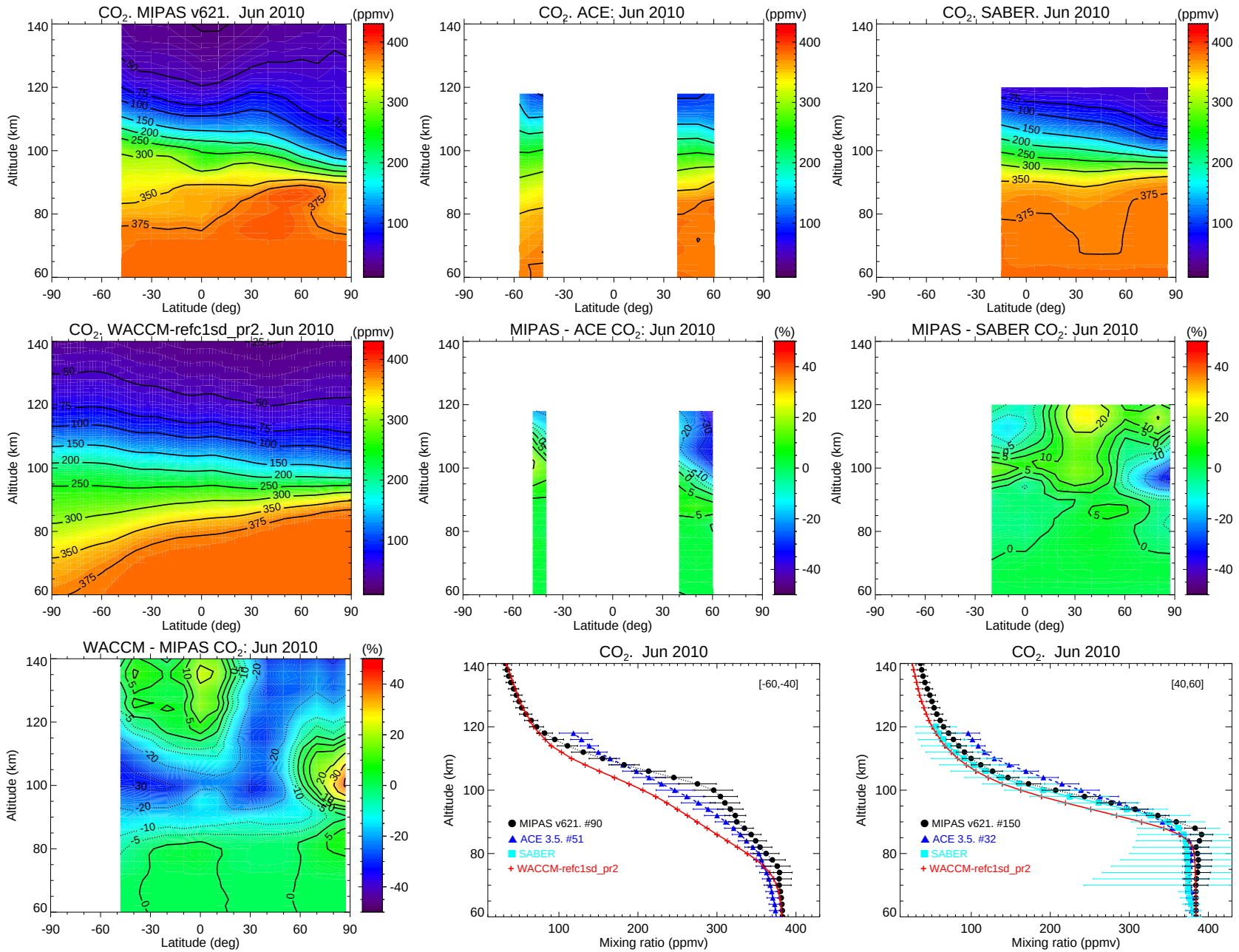

Figure C.6: As Fig. C.1 but for June 2010. Note that the latitude bands in the profiles panels can be different.

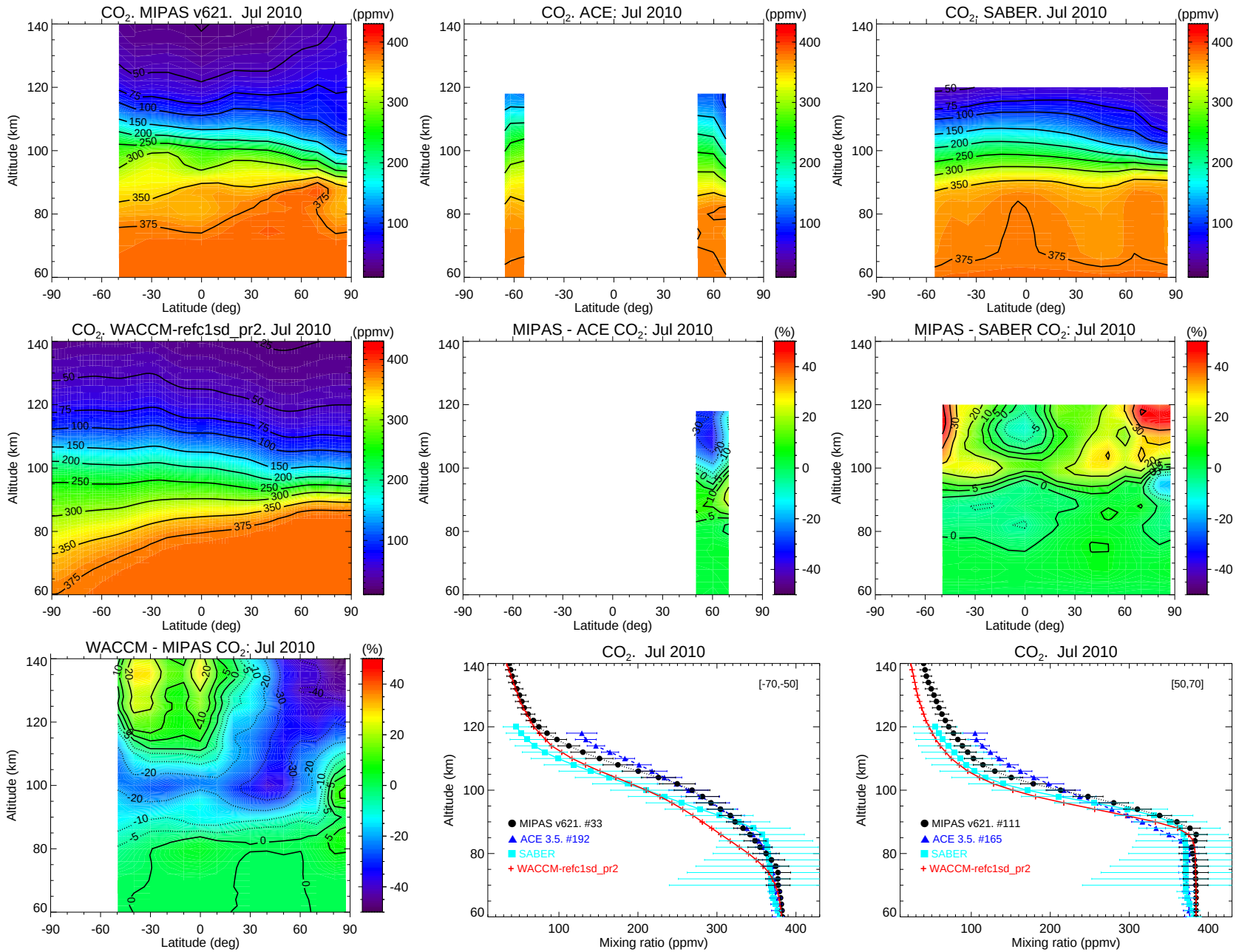

Figure C.7: As Fig. C.1 but for July 2010. Note that the latitude bands in the profiles panels can be different.

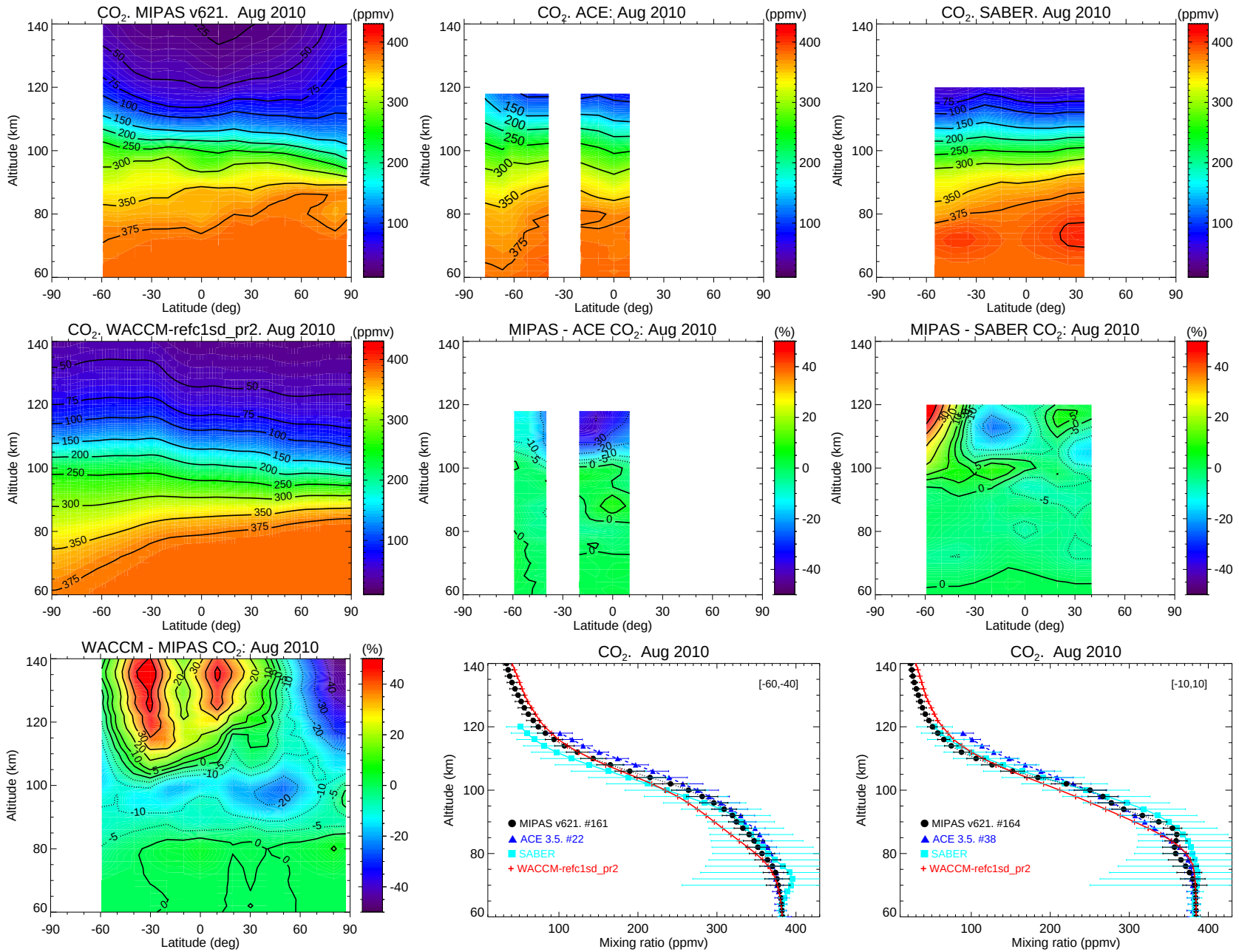

Figure C.8: As Fig. C.1 but for August 2010. Note that the latitude bands in the profiles panels can be different.

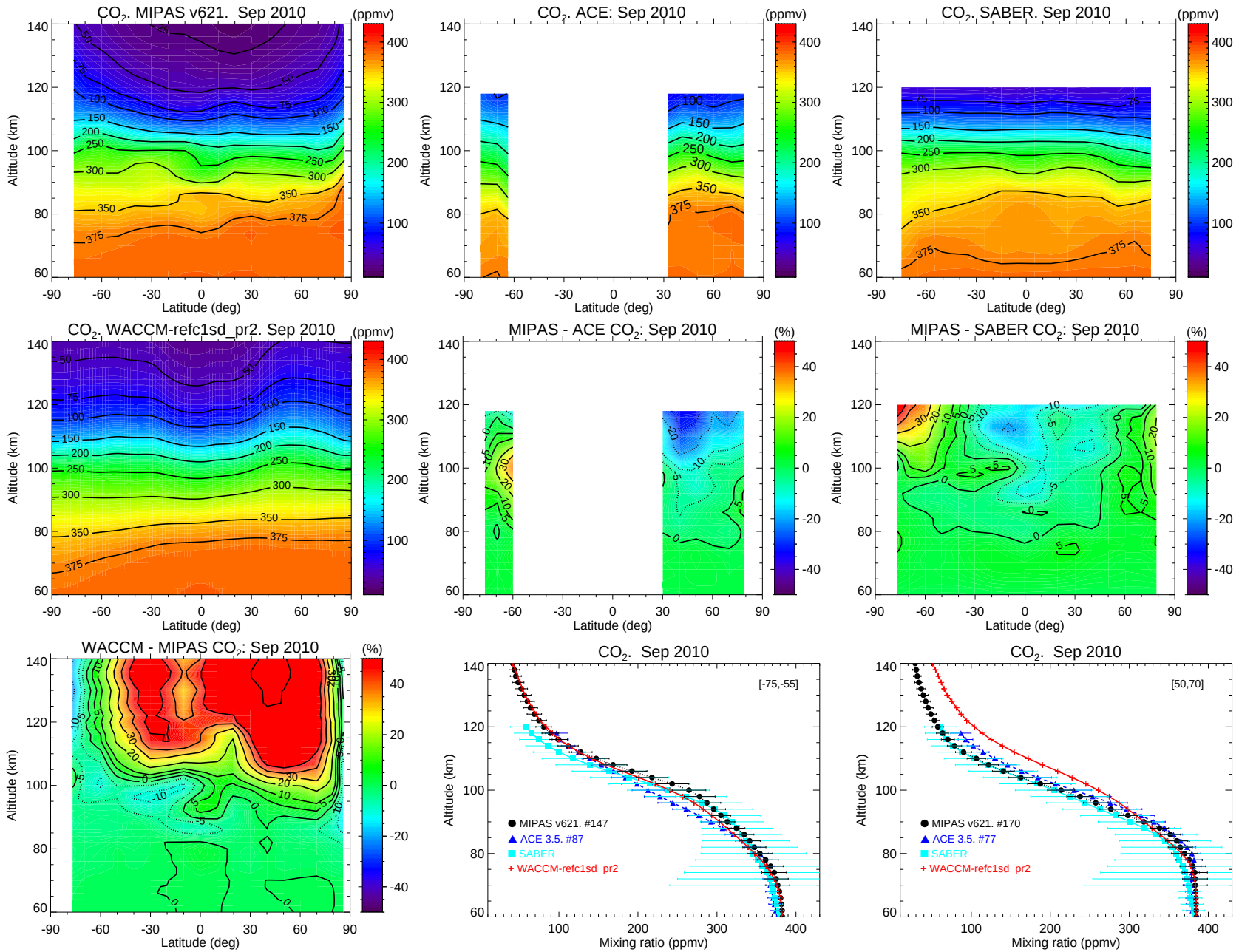

Figure C.9: As Fig. C.1 but for September 2010. Note that the latitude bands in the profiles panels can be different.

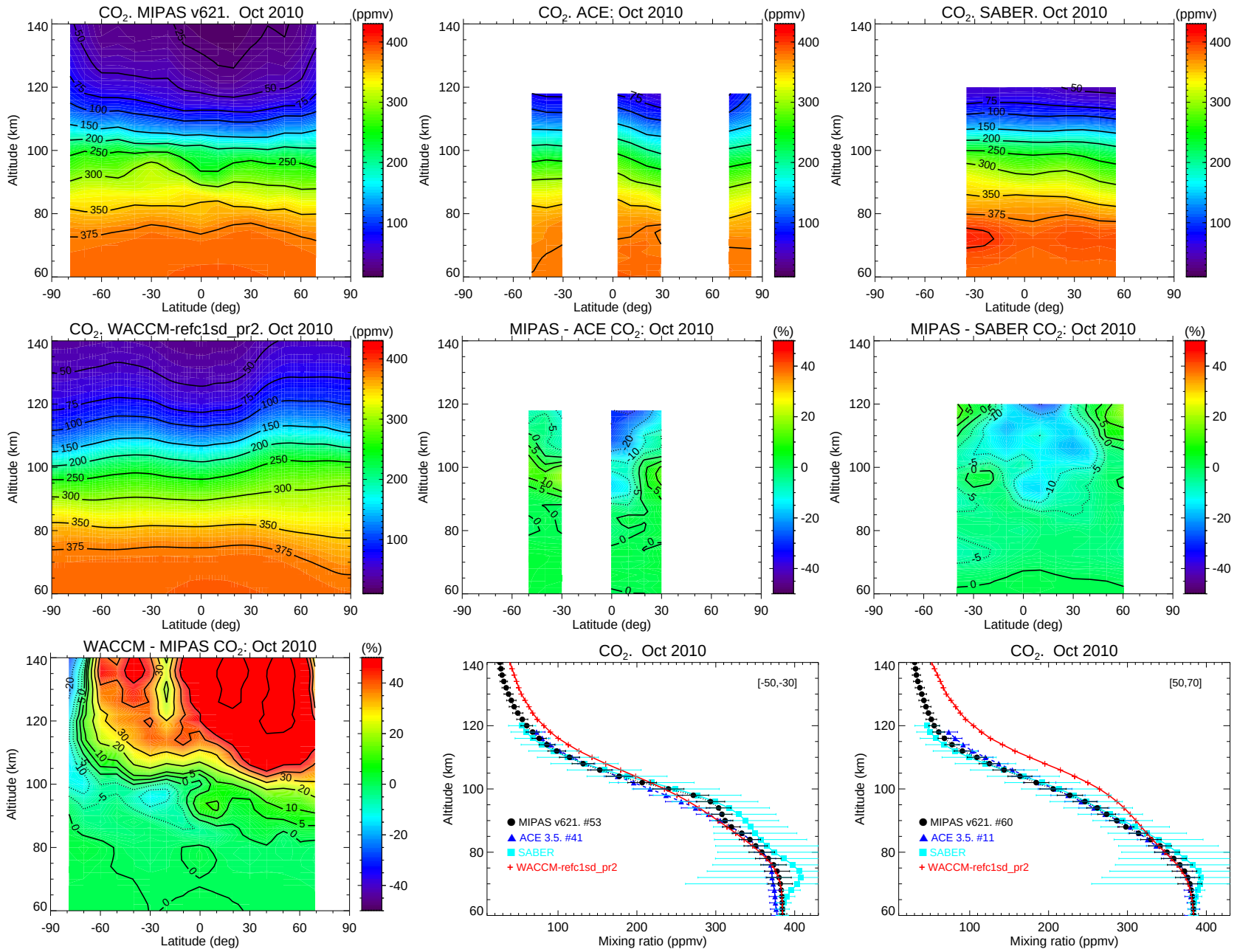

Figure C.10: As Fig. C.1 but for October 2010. Note that the latitude bands in the profiles panels can be different.

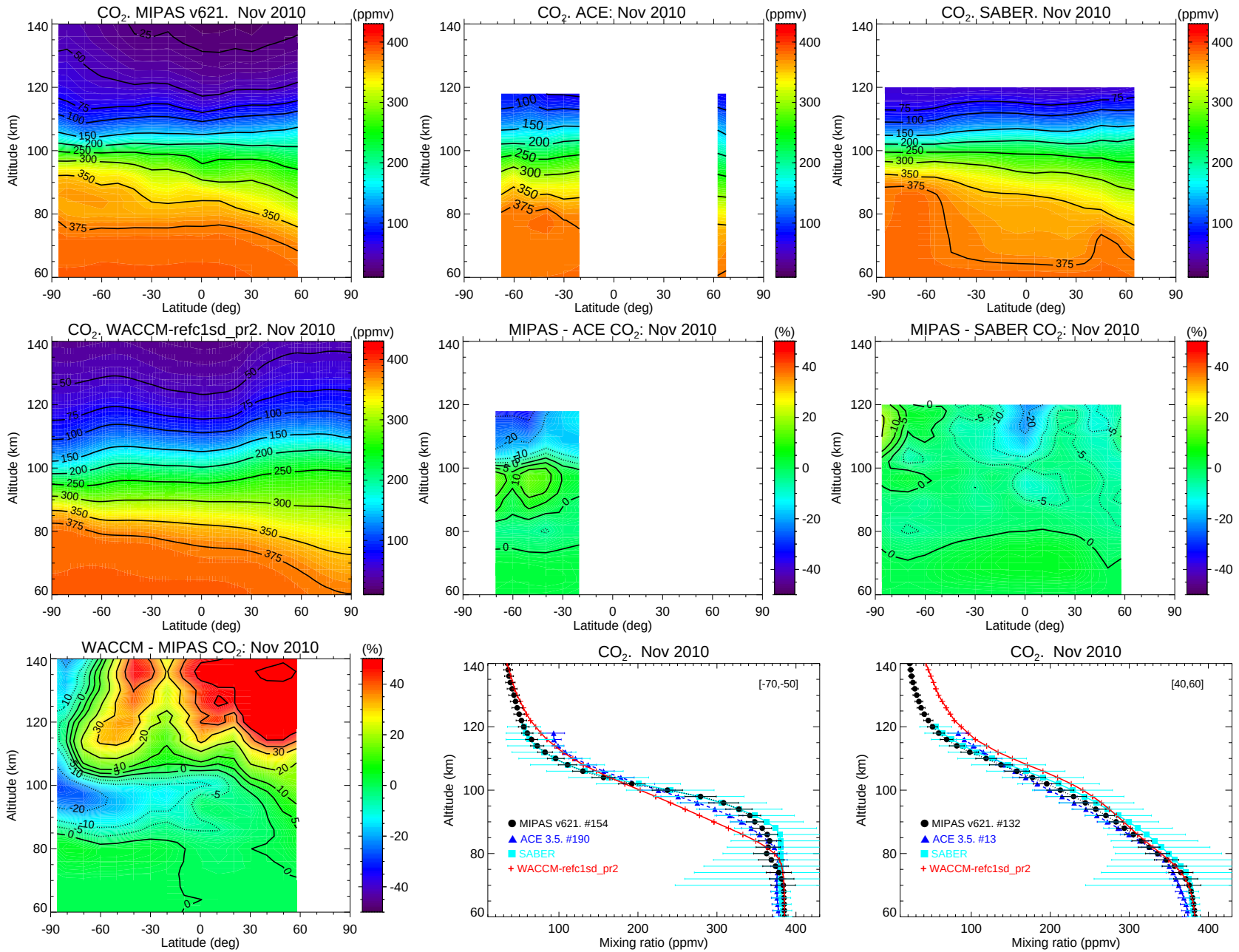

Figure C.11: As Fig. C.1 but for November 2010. Note that the latitude bands in the profiles panels can be different.

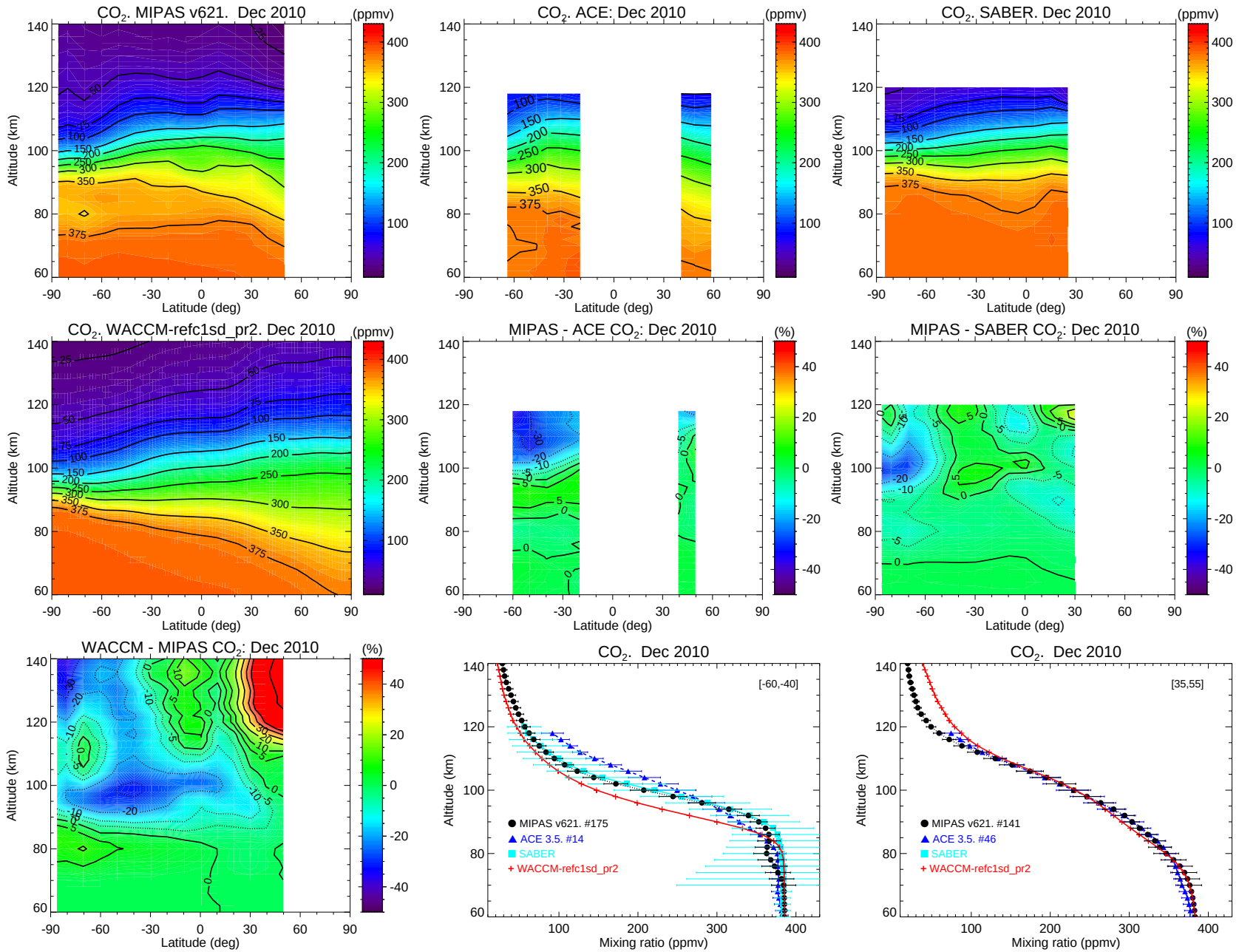

Figure C.12: As Fig. C.1 but for December 2010. Note that the latitude bands in the profiles panels can be different.

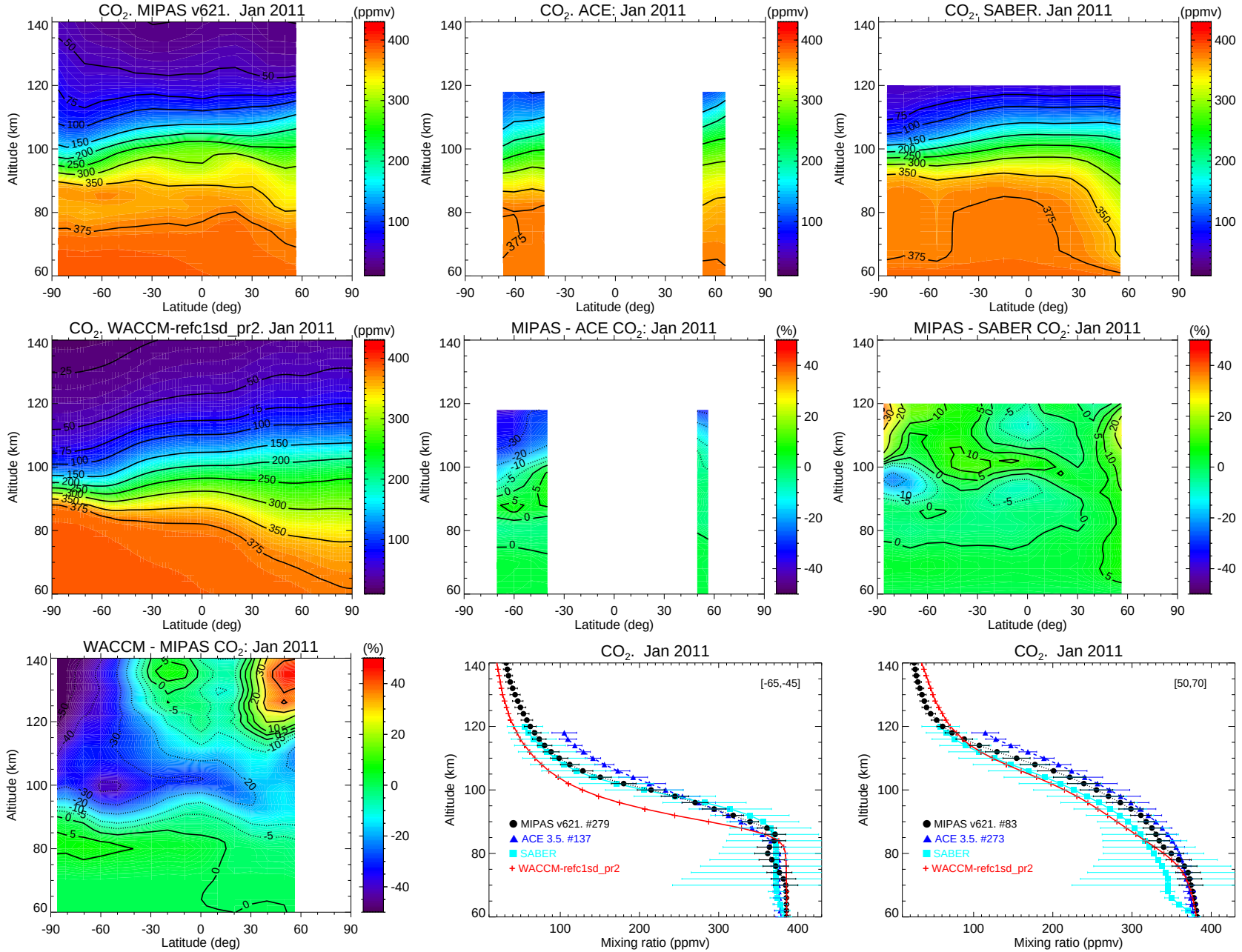

Figure C.13: CO_2 vmr abundances for January 2011. Top row: zonal mean distribution of MIPAS, ACE and SABER, respectively. Middle row: SD-WACCM (P_r=2) CO_2 distribution, and MIPAS-ACE and MIPAS-SABER CO_2 relative differences in %. Bottom row: WACCM-MIPAS CO_2 differences, and CO_2 vmr profiles for two latitude bands (as labelled) corresponding roughly to the ACE measurements. Horizontal bars in the measurements are the total errors, dominated by the systematic errors.

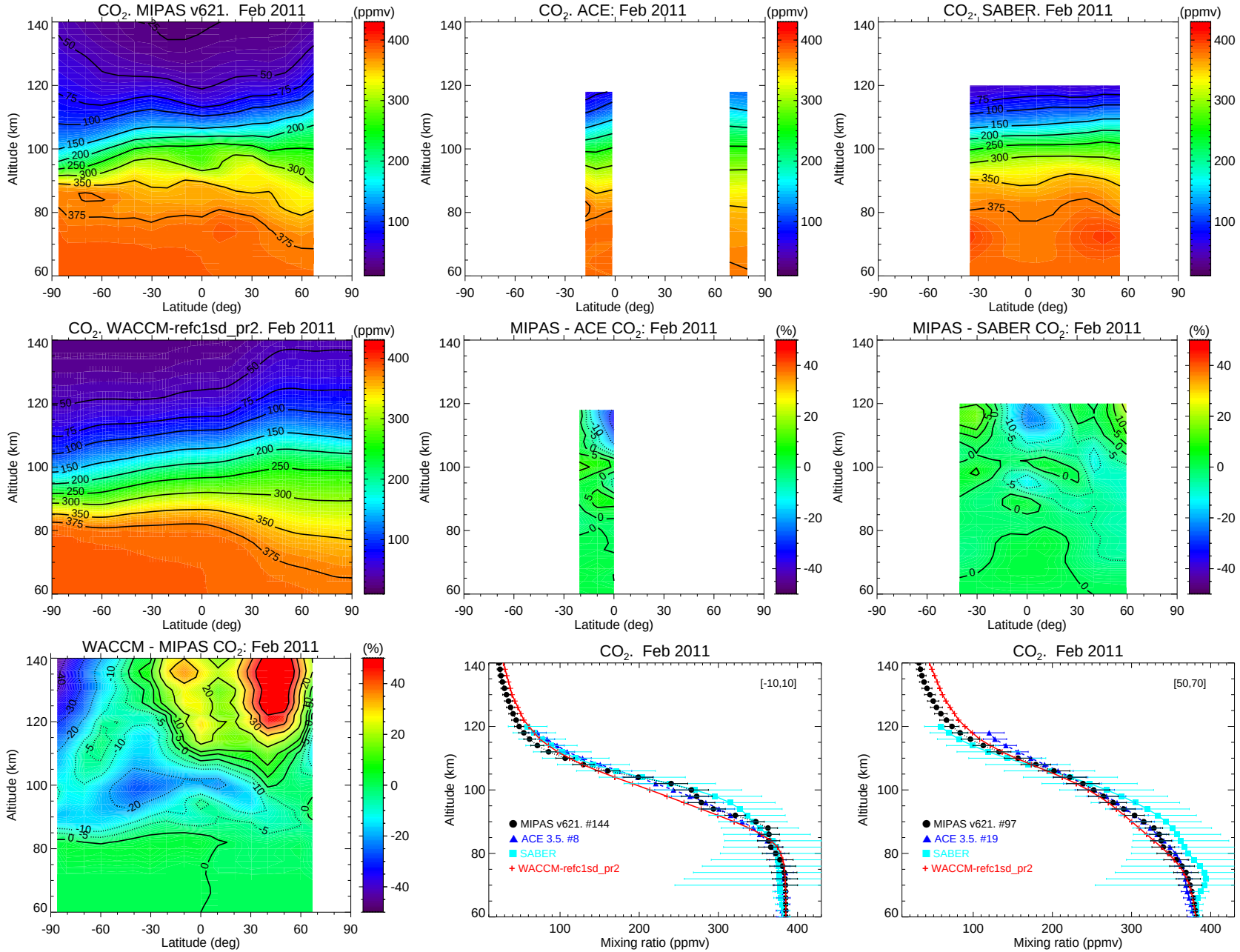

Figure C.14: As Fig. C.1 but for February 2011. Note that the latitude bands in the profiles panels can be different.

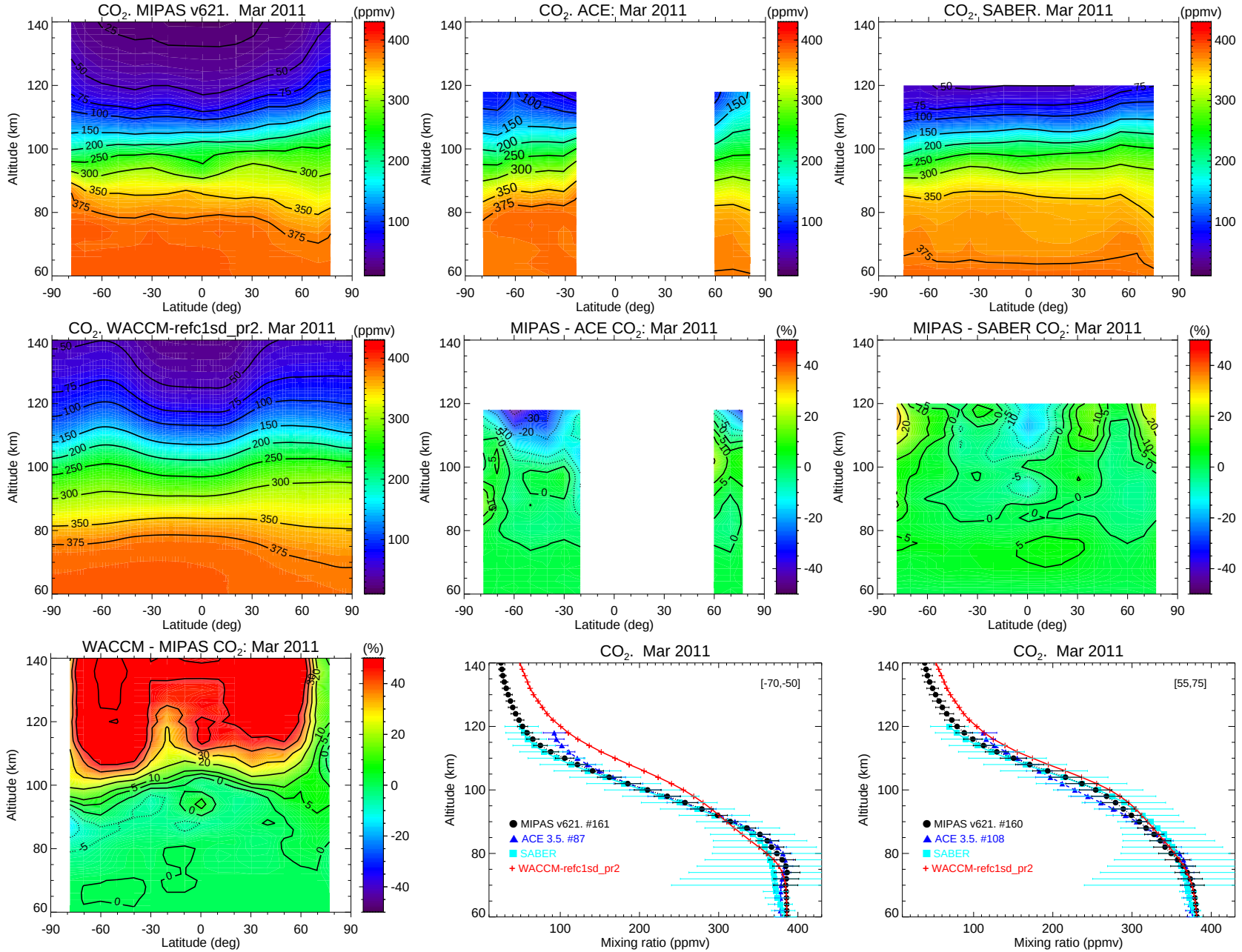

Figure C.15: As Fig. C.1 but for March 2011. Note that the latitude bands in the profiles panels can be different.

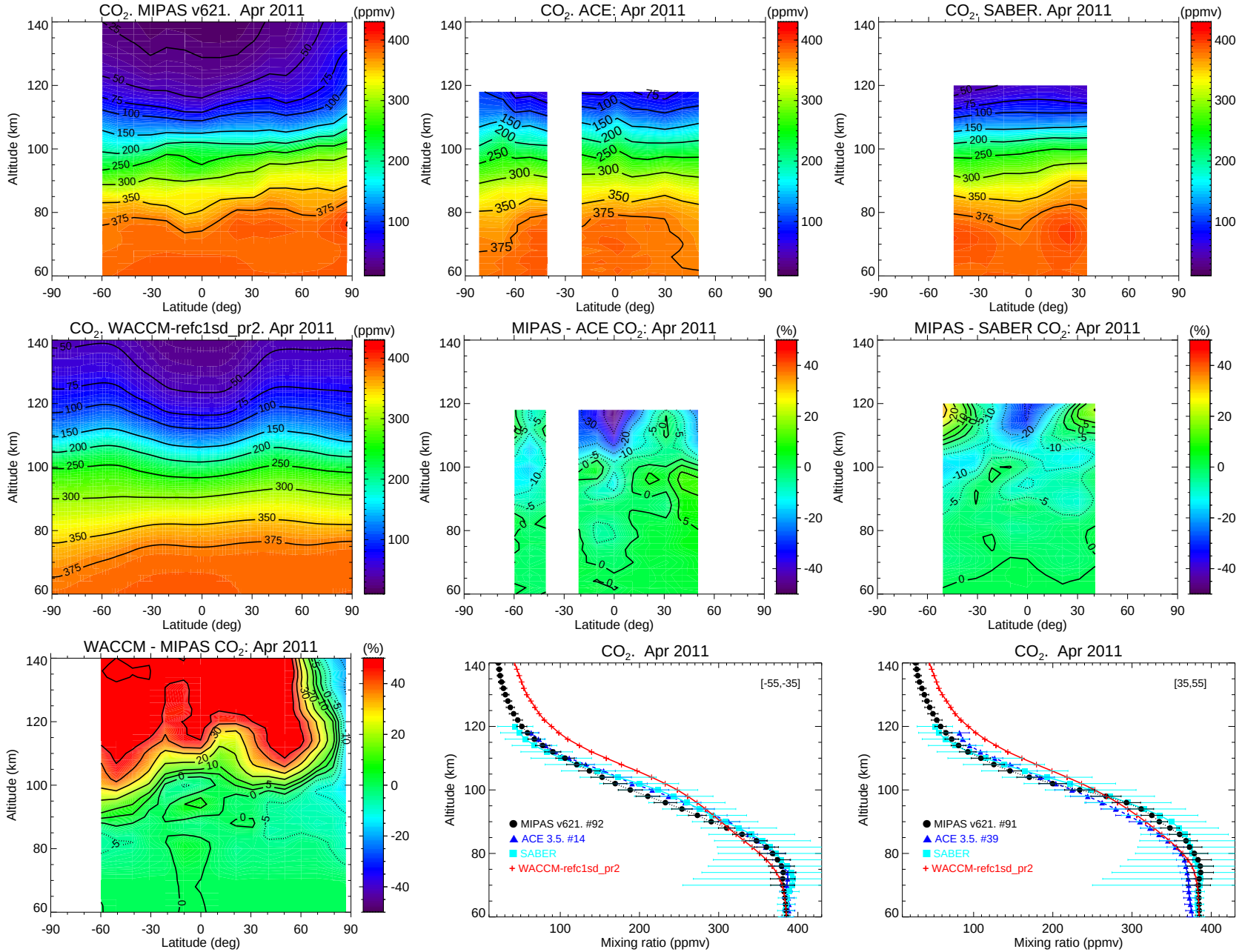

Figure C.16: As Fig. C.1 but for April 2011. Note that the latitude bands in the profiles panels can be different.

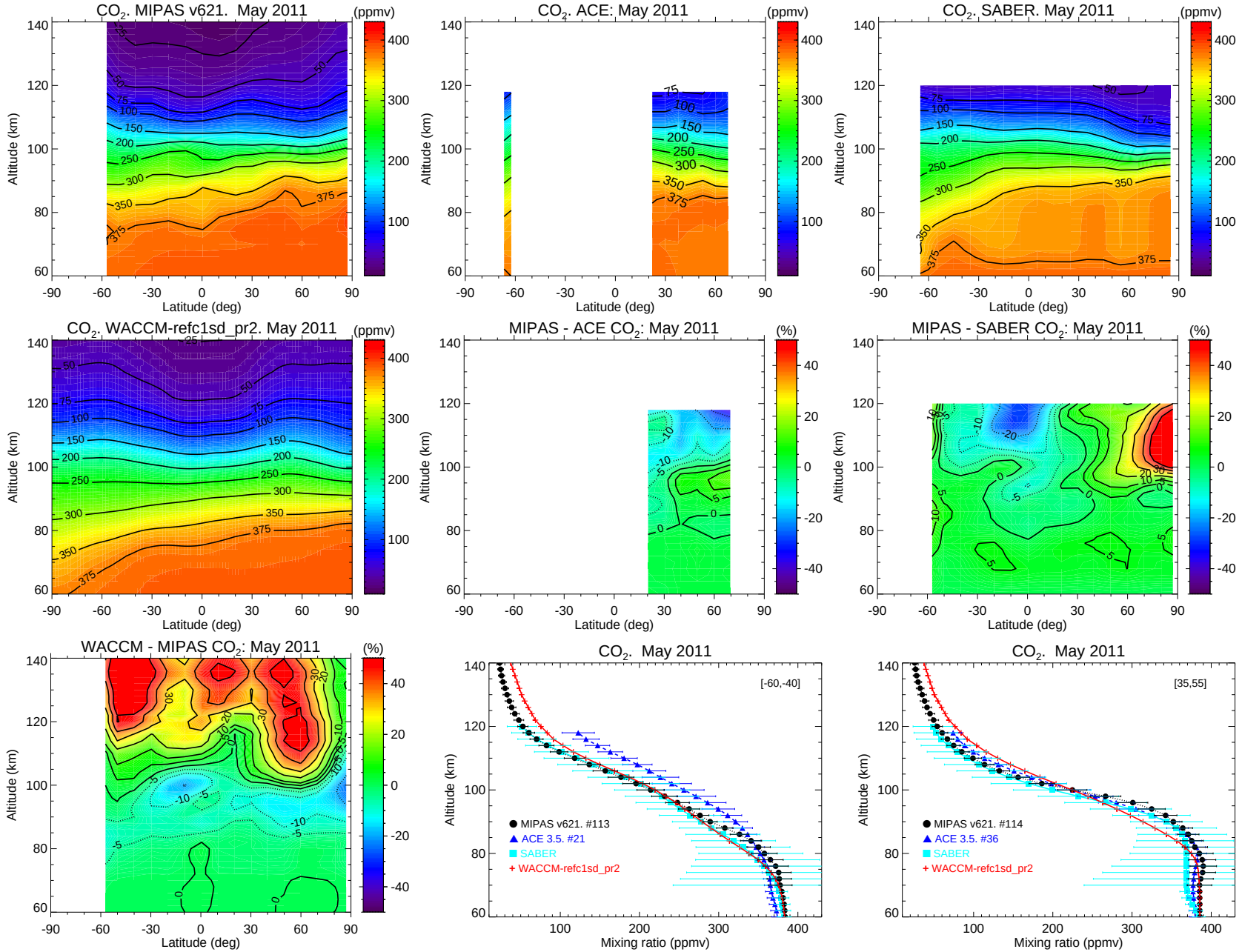

Figure C.17: As Fig. C.1 but for May 2011. Note that the latitude bands in the profiles panels can be different.

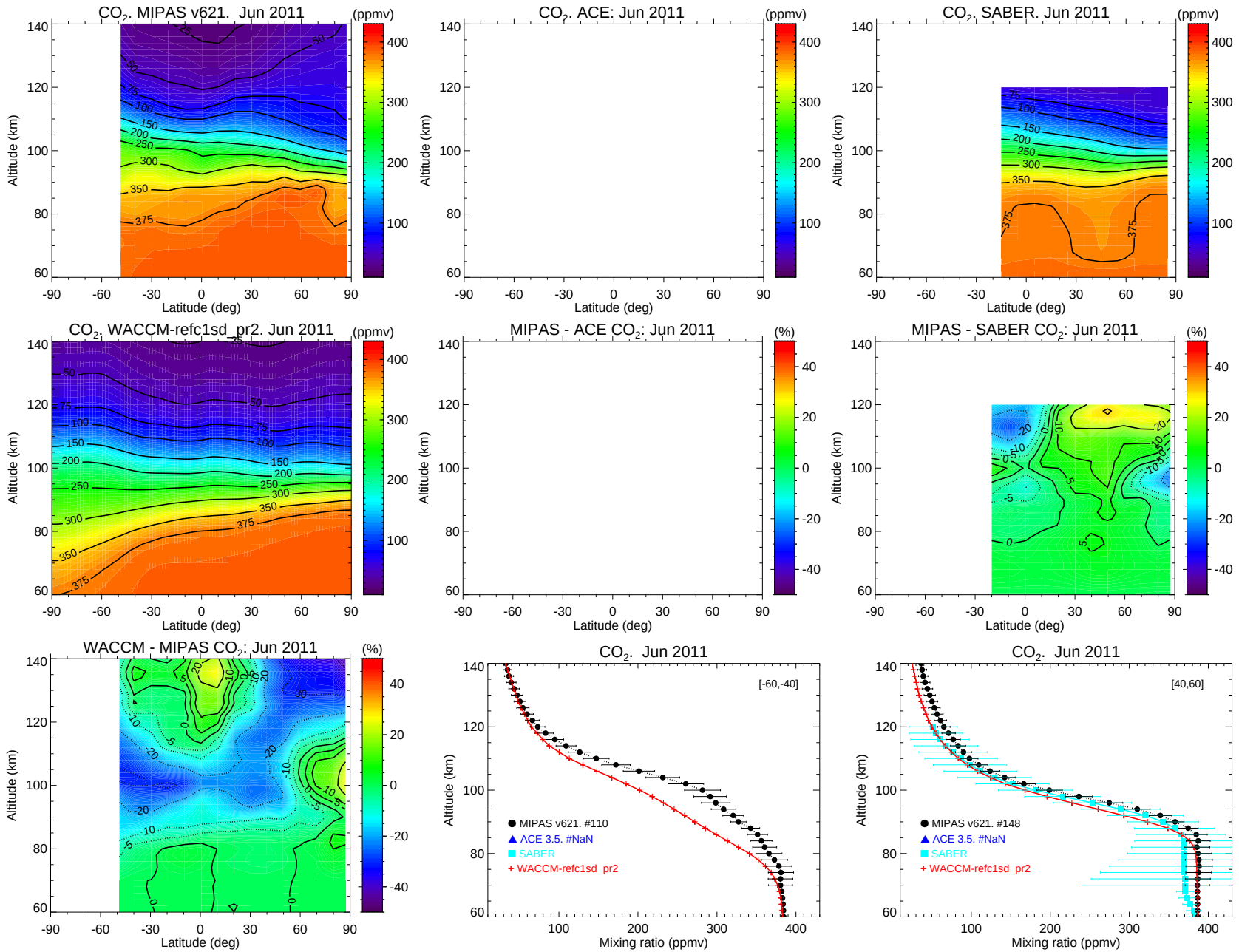

Figure C.18: As Fig. C.1 but for June 2011. Note that the latitude bands in the profiles panels can be different.

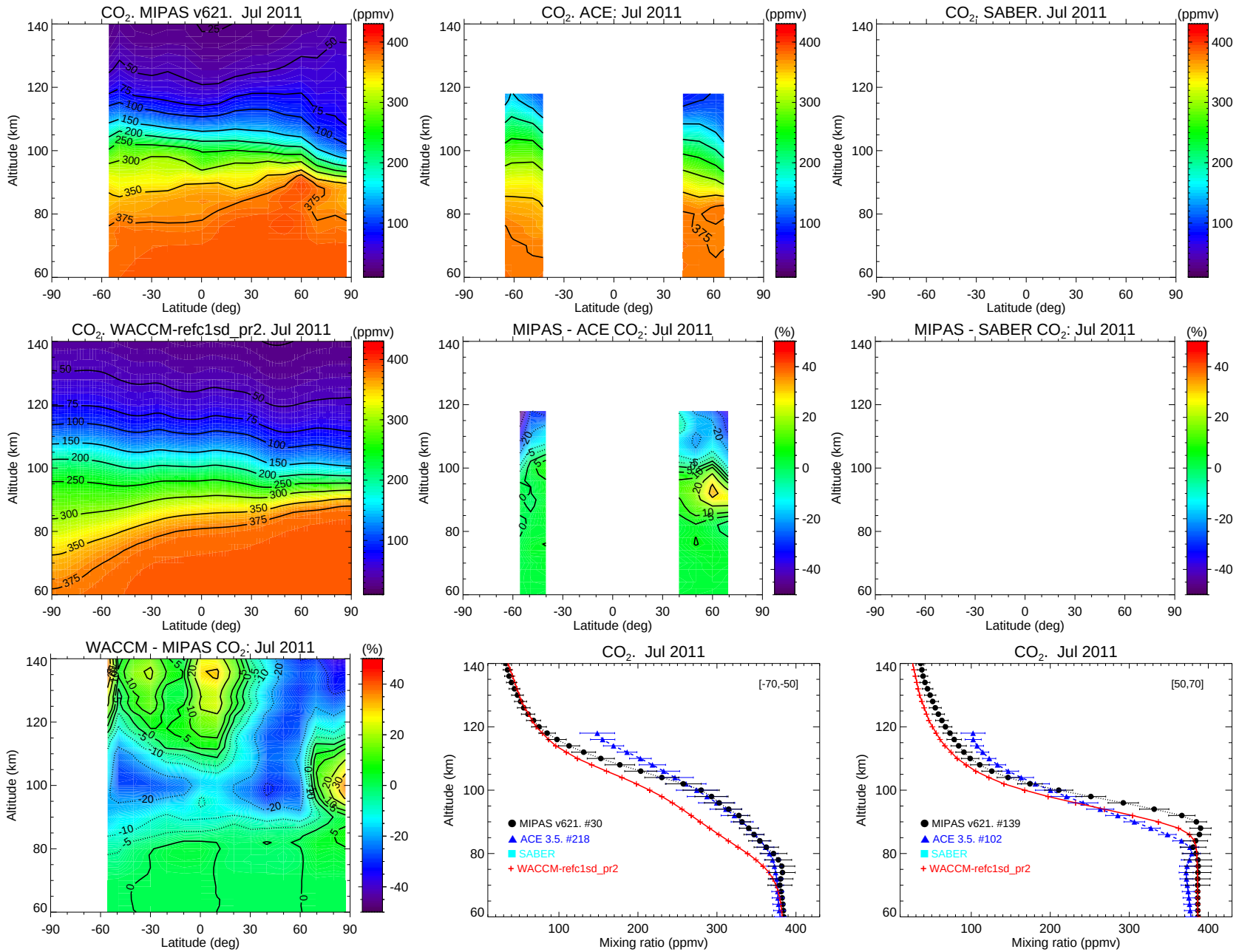

Figure C.19: As Fig. C.1 but for July 2011. Note that the latitude bands in the profiles panels can be different.

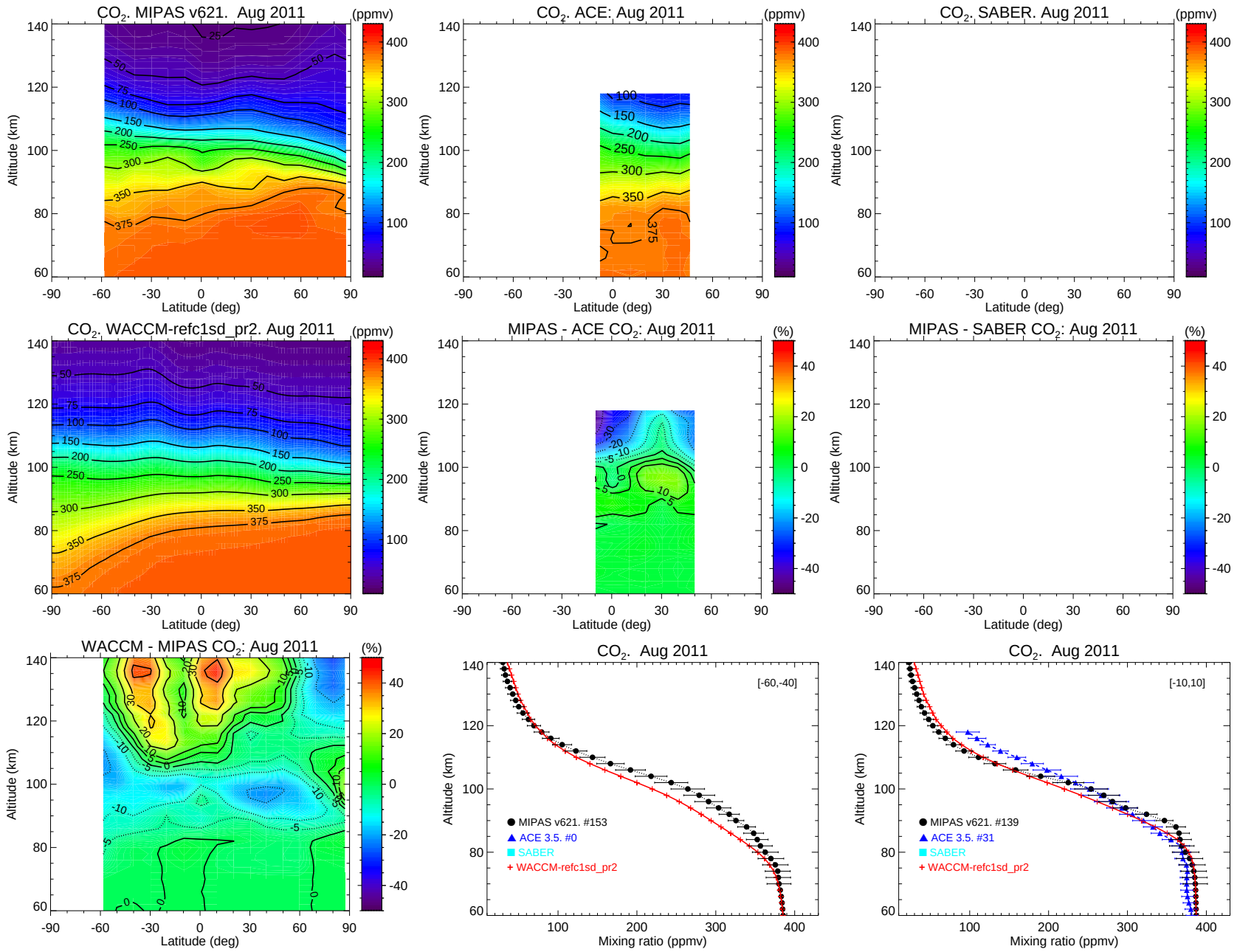

Figure C.20: As Fig. C.1 but for August 2011. Note that the latitude bands in the profiles panels can be different.

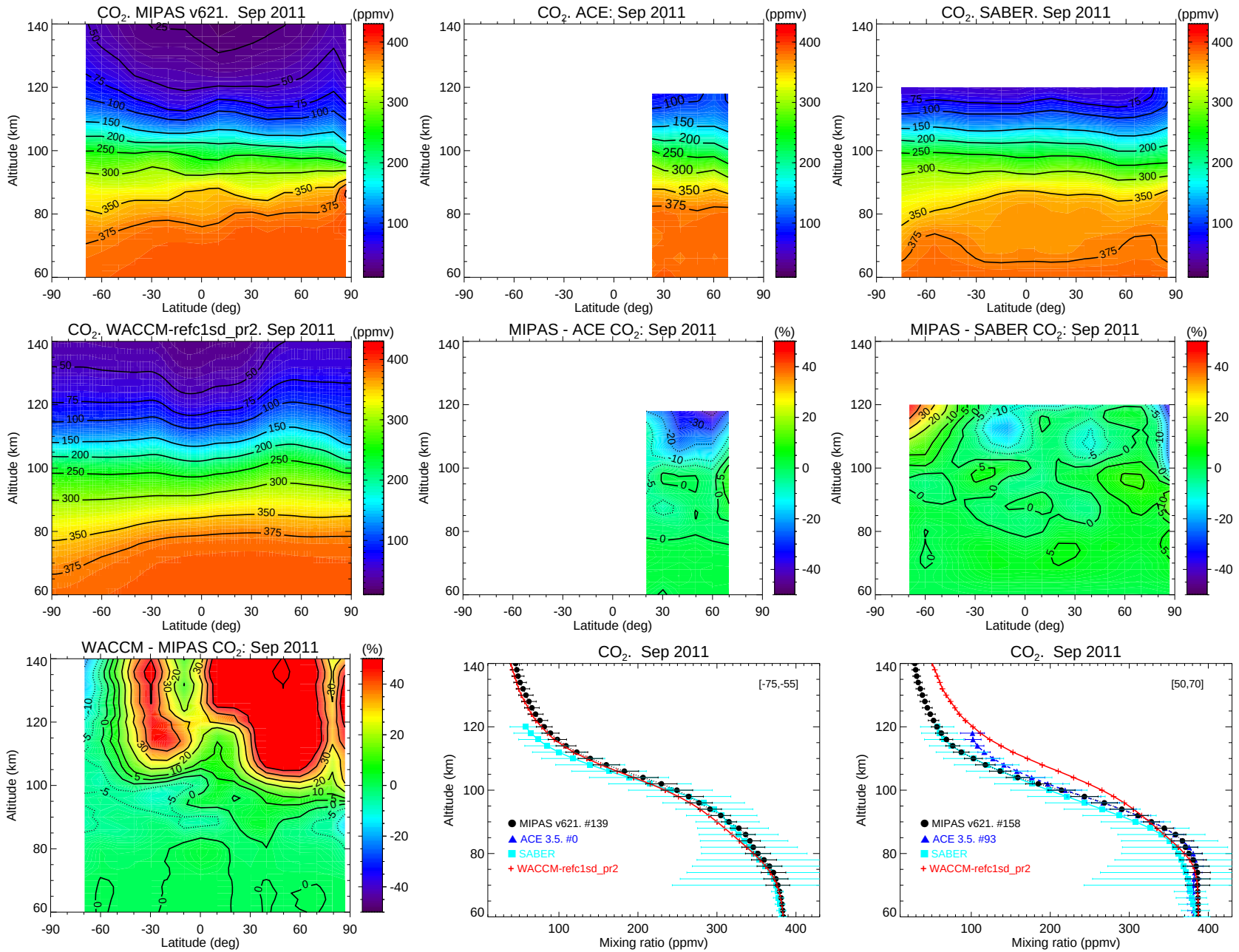

Figure C.21: As Fig. C.1 but for September 2011. Note that the latitude bands in the profiles panels can be different.

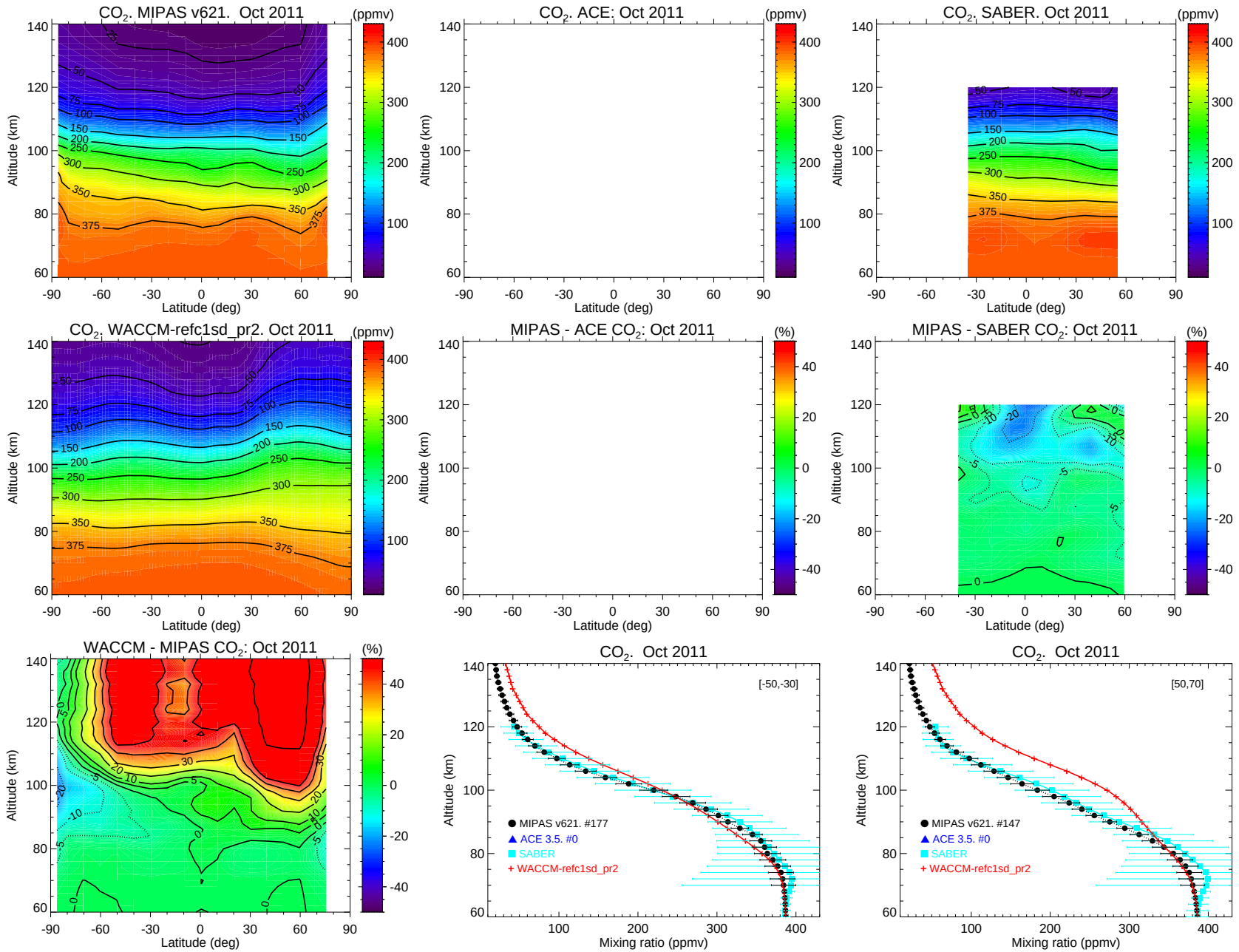

Figure C.22: As Fig. C.1 but for October 2011. Note that the latitude bands in the profiles panels can be different.

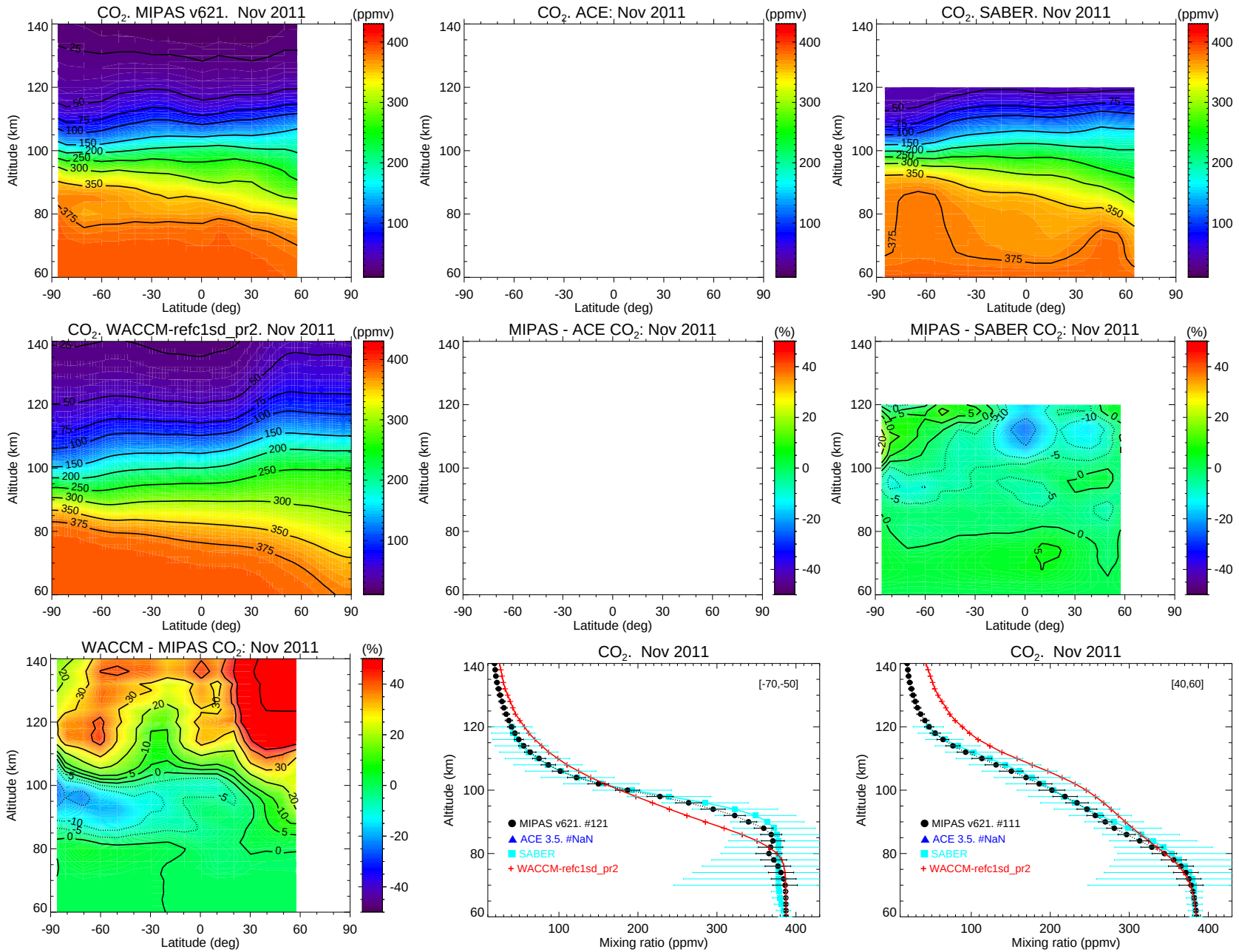

Figure C.23: As Fig. C.1 but for November 2011. Note that the latitude bands in the profiles panels can be different.

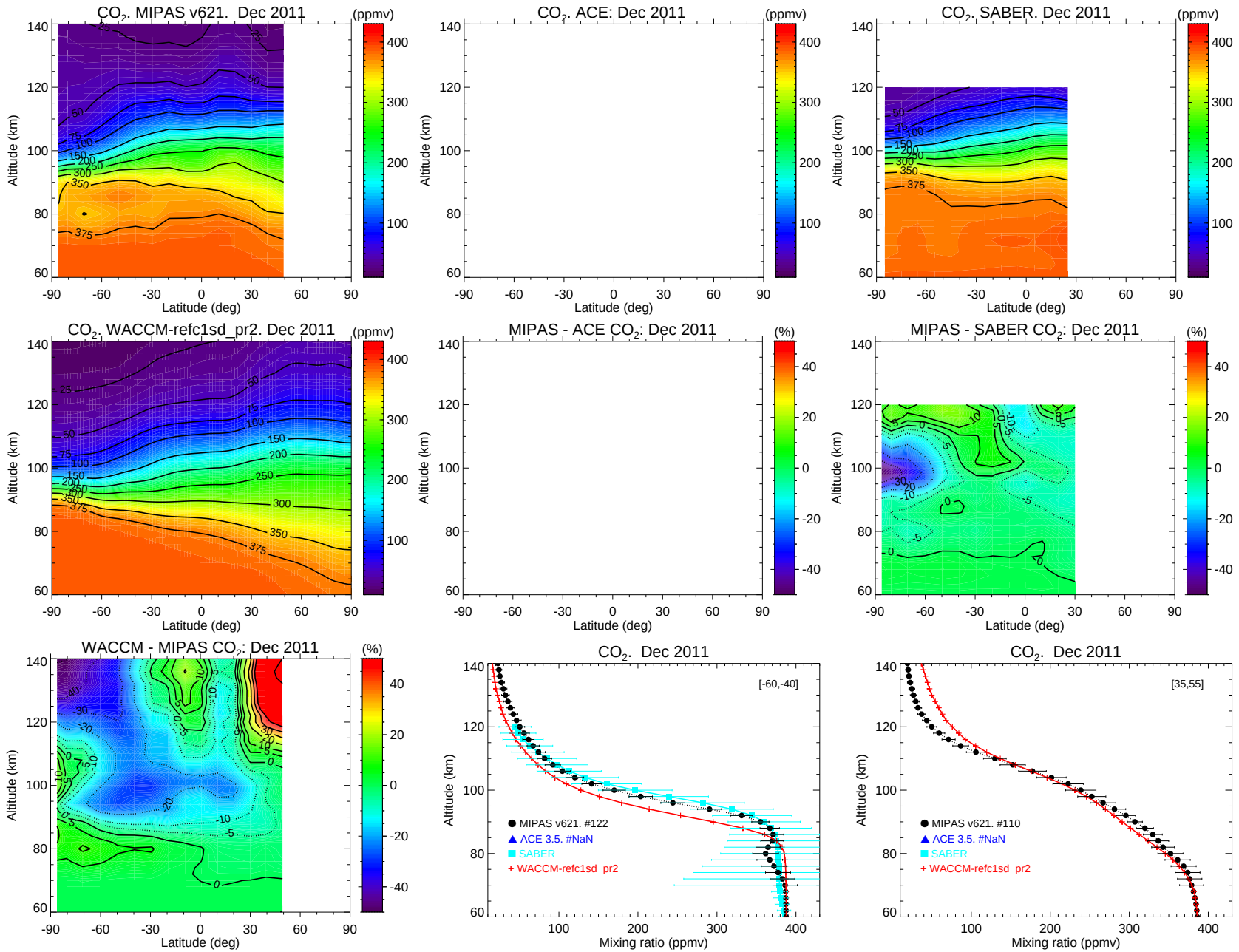

Figure C.24: As Fig. C.1 but for December 2011. Note that the latitude bands in the profiles panels can be different.

Bibliography

Adler-Golden, S.: Kinetic parameters for OH nightglow modeling consistent with recent laboratory measurements, Journal of Geophysical Research: Space Physics, 102, 19 969–19 976, doi:10.1029/97JA01622, 1997.

Akmaev, R.: Modeling the cooling due to CO_2 increases in the mesosphere and lower thermosphere, Physics and Chemistry of the Earth, 27, 521–528, doi:10.1016/S1474-7065(02)00033-5, 2002.

Alexander, J. A. F., Houghton, J. T., and McKnight, W. B.: Collisional relaxation from the v_3 vibration of CO_2, Journal of Physics B: Atomic and Molecular Physics, 1, 1225, 1968.

Amimoto, S. T., Force, A. P., Gulotty, R. G., and Wiesenfeld, J. R.: Collisional deactivation of $O(1^1D_2)$ by the atmospheric gases, The Journal of Chemical Physics, 71, 3640–3647, doi:http://dx.doi.org/10.1063/1.438807, 1979.

Barth, C. A., Lu, G., and Roble, R.: Joule heating and nitric oxide in the thermosphere, J. Geophys. Res., 114, 05 301, doi:doi:10.1029/2008JA013765, 2009.

Beagley, S. R., Boone, C. D., Fomichev, V. I., Jin, J. J., Semeniuk, K., McConnell, J. C., and Bernath, P. F.: First multi-year occultation observations of CO_2 in the MLT by ACE satellite: observations and analysis using the extended CMAM, Atmospheric Chemistry and Physics, 10, 1133–1153, doi:10.5194/acp-10-1133-2010, 2010.

Beig, G., Keckhut, P., Lowe, R. P., Roble, R. G., Mlynczak, M. G., Scheer, J., Fomichev, V. I., Offermann, D., French, W. J. R., Shepherd, M. G., Semenov, A. I., Remsberg, E. E., She, C. Y., Lübken, F. J., Bremer, J., Clemesha, B. R., Stegman, J., Sigernes, F., and Fadnavis, S.: Review of mesospheric temperature trends, Reviews of Geophysics, 41, 1015, doi:10.1029/2002RG000121, 2003.

Bermejo-Pantaleón, D., Funke, B., Lopez-Puertas, M., García-Comas, M., Stiller, G. P., von Clarmann, T., Linden, A., Grabowski, U., Höpfner, M., Kiefer, M., Glatthor, N., Kellmann, S., and Lu, G.: Global Observations of Thermospheric Temperature and Nitric Oxide from MIPAS spectra at 5.3 μm, J. Geophys. Res., 116, A10 313, 2011.

Bovensmann, H., Burrows, J. P., Buchwitz, M., Frerick, J., Nöel, S., Rozanov, V. V., Chance, K. V., and Goede, A. P. H.: SCIAMACHY: mission objectives and measurement modes, J. Atmos. Sci, 56, 127–150, 1999.

Brasseur, G. and Solomon, S.: Aeronomy of the Middle Atmosphere–Chemistry and Physics of the Stratosphere and Mesosphere, Atmospheric and Oceanographic Sciences Library 32, Springer, P. O. Box 17, 3300 AA Dordrecht, The Netherlands, third edn., 2005.

Brown, S. B., Jensen, M., Jensen, S., Hansen, G., Zollinger, L., Esplin, R., and Miller, J. B.: Sounding of the atmosphere using broadband emission radiometry (SABER): sensor design, performance, and lessons learned, Proc. SPIE, 6297, 62 970U–62 970U–12, doi:10.1117/12.684137, 2006.

Chapman, S.: On ozone and atomic oxygen in the upper atmosphere, Philosophical Magazine, 10, 369–383, 1930.

Chen, Y., Han, Y., van Delst, P., and Weng, F.: Assessment of Shortwave Infrared Sea Surface Reflection and Nonlocal Thermodynamic Equilibrium Effects in the Community Radiative Transfer Model Using IASI Data, Journal of Atmospheric and Oceanic Technology, 30, 2152–2160, doi:10.1175/JTECH-D-12-00267.1, 2013.

Curtis, A. R.: The computation of radiative heating rates in the atmosphere, Proc. R. Soc. London, Ser. A, 236, 156–159, 1956.

Dang, C., Reld, J., and Garside, B.: Dynamics of the CO_2 lower laser levels as measured with a tunable diode laser, Applied Physics B: Lasers and Optics, 31, 163–172, doi:10.1007/BF00688838, 1983.

DeSouza-Machado, S. G., Strow, L. L., Hannon, S. E., Motteler, H. E., Lopez-Puertas, M., Funke, B., and Edwards, D. P.: Fast forward radiative transfer modeling of 4.3 μm nonlocal thermodynamic equilibrium effects for infrared temperature sounders, Geophysical Research Letters, 34, n/a–n/a, doi:10.1029/2006GL026684, l01802, 2007.

Eddy, J.: The Sun, The Earth, and Near Earth Space: A Guide to the Sun-Earth System, US National Aeronautics and Space Admin, 2009.

Edwards, D. P., Kumer, J. B., López-Puertas, M., Mlynczak, M. G., Gopalan, A., Gille, J. C., and Roche, A.: Non-local thermodynamic equilibrium limb radiance near 10 μm as measured by UARS CLAES, Journal of Geophysical Research: Atmospheres, 101, 26 577–26 588, doi:10.1029/96JD02133, 1996.

Emmert, J. T., Lean, J. L., and Picone, J. M.: Record-low thermospheric density during the 2008 solar minimum, Geophys. Res. Lett., 37, L12 102, doi:10.1029/2010GL043671, 2010.

Emmert, J. T., Stevens, M. H., Bernath, P. F., Drob, D. P., and Boone, C. D.: Observations of increasing carbon dioxide concentration in Earth/'s thermosphere, Nature Geosci, 5, 868–871, 2012.

Ermolli, I., Matthes, K., Dudok de Wit, T., Krivova, N. A., Tourpali, K., Weber, M., Unruh, Y. C., Gray, L., Langematz, U., Pilewskie, P., Rozanov, E., Schmutz, W., Shapiro, A., Solanki, S. K., and Woods, T. N.: Recent variability of the solar spectral irradiance and its impact on climate modelling, Atmospheric Chemistry & Physics, 13, 3945–3977, doi:10.5194/acp-13-3945-2013, 2013.

Finzi, J. and Moore, C. B.: Relaxation of $CO_2(1001)$, $CO_2(0201)$, and $N_2O(1001)$ vibrational levels by near-resonant V-V energy transfer, The Journal of Chemical Physics, 63, 2285–2288, doi:http://dx.doi.org/10.1063/1.431678, 1975.

Fischer, H., Birk, M., Blom, C., Carli, B., Carlotti, M., von Clarmann, T., Delbouille, L., Dudhia, A., Ehhalt, D., Endemann, M., Flaud, J. M., Gessner, R., Kleinert, A., Koopmann, R., Langen, J., López-Puertas, M., Mosner, P., Nett, H., Oelhaf, H., Perron, G., Remedios, J., Ridolfi, M., Stiller, G., and Zander, R.: MIPAS: an instrument for atmospheric and climate research, Atmos. Chem. Phys., 8, 2151–2188, 2008.

Fomichev, V. I., Ogibalov, V. P., and Beagley, S. R.: Solar heating by the near-IR CO_2 bands in the mesosphere, Geophysical Research Letters, 31, n/a–n/a, doi:10.1029/2004GL020324, 2004.

Foucher, P. Y., Chédin, A., Armante, R., Boone, C., Crevoisier, C., and Bernath, P.: Carbon dioxide atmospheric vertical profiles retrieved from space observation using ACE-FTS solar occultation instrument, Atmospheric Chemistry and Physics, 11, 2455–2470, doi:10.5194/acp-11-2455-2011, 2011.

Fuller-Rowell, T. J.: The Dynamics of the Lower Thermosphere, in: The upper Mesosphere and Lower Thermosphere: A Review of Experiment and Theory, Geophysical Monograph 87, edited by Johnson, R. M. & Killeen, T. L., pp. 23–+, AGU, 1995.

Funke, B., López-Puertas, M., García-Comas, M., Kaufmann, M., Höpfner, M., and Stiller, G.: GRANADA: A Generic RAdiative traNsfer AnD non-LTE population algorithm, Journal of Quantitative Spectroscopy and Radiative Transfer, 113, 1771–1817, 2012.

Funke, B., López-Puertas, M., Stiller, G. P., and von Clarmann, T.: Mesospheric and stratospheric NOy produced by energetic particle precipitation during 2002–2012, Journal of Geophysical Research, 119, 4429–4446, 2014.

Garcia, R. R., López-Puertas, M., Funke, B., Marsh, D. R., Kinnison, D. E., Smith, A. K., and González-Galindo, F.: On the distribution of CO_2 and CO in the mesosphere and lower thermosphere, Journal of Geophysical Research: Atmospheres, 119, 5700–5718, doi:10.1002/2013JD021208, 2014.

García-Comas, M., López-Puertas, M., Marshall, B., Wintersteiner, P. P., Funke, B., Bermejo-Pantaleón, D., Mertens, C. J., Remsberg, E. E., Gordley, L. L., Mlynczak, M., and Russell, J.: Errors in SABER kinetic temperature caused by non-LTE model parameters, J. Geophys. Res., 113, D24106, doi:10.1029/2008JD010105, 2008.

García-Comas, M., Funke, B., López-Puertas, M., Bermejo-Pantaleón, D., Glatthor, N., Clarmann, T. v., Stiller, G. P., Grabowski, U., Boone, C. D., French, W. J., Leblanc, T., López-González, M. J., and Schwartz, M.: On the Quality of MIPAS Kinetic Temperature in the Middle Atmosphere, Atmos. Chem. Phys. Discuss., 11, 24 233–24 312, doi:10.5194/acpd-11-24233-2011, 2011.

García-Comas, M., Funke, B., López-Puertas, M., Bermejo-Pataleón, D., Glatthor, N., von Clarmann, T., Stiller, G., Grabowski, U., Boone, C. D., French, W. J. R., Leblanc, T., López-González, M. J., and Schwartz, M. J.: On the quality of MIPAS kinetic temperature in the middle atmosphere, Atmos. Chem. Phys., 12, 6009–6039, 2012.

García-Comas, M., Funke, B., Gardini, A., López-Puertas, M., Jurado-Navarro, A., von Clarmann, T., Stiller, G., Kiefer, M., Boone, C. D., Leblanc, T., Marshall, B. T., Schwartz, M. J., and Sheese, P. E.: MIPAS temperature from the stratosphere to the lower thermosphere: Comparison of vM21 with ACE-FTS, MLS, OSIRIS, SABER, SOFIE and lidar measurements, Atmospheric Measurement Techniques, 7, 3633–3651, doi:10.5194/amt-7-3633-2014, 2014.

Gil-López, S., López-Puertas, M., Kaufmann, M., Funke, B., García-Comas, M., Koukouli, M. E., Glatthor, N., Grabowski, U., Höpfner, Stiller, G. P., and von Clarmann, T.: Retrieval of stratospheric and mesospheric O_3 from high resolution MIPAS spectra at 15 and 10 μm, Adv. Space Res., 36, 943–951, doi:10.1016/j.asr.2005.05.123, 2005.

Girard, A., Besson, J., Brard, D., Laurent, J., Lemaitre, M., Lippens, C., Muller, C., Vercheval, J., and Ackerman, M.: Global results of grille spectrometer experiment on board Spacelab 1, Planetary and Space Science, 36, 291–300, doi:http://dx.doi.org/10.1016/0032-0633(88)90136-5, 1988.

González-Galindo, F., López-Valverde, M. A., Angelats i Coll, M., and Forget, F.: Extension of a Martian general circulation model to thermospheric altitudes: UV heating and photochemical models, Journal of Geophysical Research, 110, 09 008, 2005.

Gregory, E. A., Maricq, M. M., Siddles, R. M., Wickham Jones, C. T., and Simpson, C. J. S. M.: Vibrational relaxation of gaseous CO($v = 1$) and N_2($v = 1$) from 300 K to liquid temperatures: A comparison with liquid state relaxation, The Journal of Chemical Physics, 78, 3881–3892, doi:http://dx.doi.org/10.1063/1.445166, 1983.

Gurk, C., Fischer, H., Hoor, P., Lawrence, M., Lelieveld, J., and Wernli, H.: Airborne in-situ measurements of vertical, seasonal and latitudinal distributions of carbon dioxide over Europe, Atmospheric Chemistry and Physics Discussions, 8, 7315–7337, 2008.

Hase, F., Demoulin, P., Sauval, A. J., Toon, G. C., Bernath, P. F., Goldman, A., Hannigan, J. W., and Rinsland, C. P.: An empirical line–by–line model for the infrared solar transmittance spectrum from 700 to 5000 cm^{-1}, J. Quant. Spectrosc. Radiat. Transfer, 102, 450–463, doi:10.1016/j.jqsrt.2006.02.026, 2006.

Houghton, J. T.: The Physics of Atmospheres, Cambridge University Press, Cambridge, second edn., 1986.

Inoue, G. and Tsuchiya, S.: Vibration-to-Vibration Energy Transfer of CO_2(0001) with N_2 and CO at Low Temperatures, Journal of the Physical Society of Japan, 39, 479–486, doi:10.1143/JPSJ.39.479, 1975.

IPCC report: Climate Change 2014: Synthesis Report. Contribution of Working Groups I, II and III to the Fifth Assessment Report of the Intergovernmental Panel on Climate Change, The Core Writing Team, R. K. Pachauri and L.A. Meyeres (eds.), IPCC, Geneva, Switzerland, 2014.

Jacobs, R. R., Pettipiece, K. J., and Thomas, S. J.: Rate constants for the CO_2 02^00-10^00 relaxation, Phys. Rev. A, 11, 54–59, doi:10.1103/PhysRevA.11.54, 1975.

Jurado-Navarro, A., López-Puertas, M., Funke, B., García-Comas, M., Gardini, A., Stiller, G., von Clarmann, T., Grabowski, U., and Glatthor, N.: Analysis of MIPAS Spectra in the CO_2 10 and 4.3 μm Regions in the Mesosphere and Lower Thermosphere, eSA ATMOS 2012, ESA Special Publication SP-708 (CD-ROM), Bruges, Belgium, 18-22 June 2012, 2012.

Jurado-Navarro, A., López-Puertas, M., Funke, B., García-Comas, M., Gardini, A., Stiller, G., von Clarmann, T., Grabowski, U., and Glatthor, N.: Analysis of MIPAS Spectra in the CO_2 10 and 4.3 μm regions in the Mesosphere and Lower Thermosphere, eSA-ESRIN Atmospheric Composition Validation And Evolution, Frascati, Italy, 13–15 March 2015, 2013.

Jurado-Navarro, A., López-Puertas, M., Funke, B., García-Comas, M., Gardini, A., Stiller, G., von Clarmann, T., Grabowski, U., and Glatthor, N.: Non-LTE Retrievals Of CO_2 Collisional Rates and VMRs Using Limb Emission High Resolution Spectra From MIPAS/ENVISAT, eSA ATMOS 2015 conference proceedings (ESA SP-735), Heraklion, Greece, 8-12 June 2015, 2015, 2015a.

Jurado-Navarro, A., López-Puertas, M., Funke, B., García-Comas, M., Gardini, A., Stiller, G., von Clarmann, T., Grabowski, U., and Glatthor, N.: Non-LTE Retrievals Of CO_2 Collisional Rates and VMRs Using Limb Emission High Resolution Spectra From MIPAS/ENVISAT, sPARC Regional Workshop, Granada, Spain, 12–13 January 2015, 2015b.

Jurado-Navarro, A. A., López-Puertas, M., Funke, B., García-Comas, M., Gardini, A., Stiller, G. P., and von Clarmann, T.: Vibration-vibration and vibration-thermal energy transfers of CO_2 with N_2 from MIPAS high resolution limb spectra, Journal of Geophysical Research, p. 2015JD023429, 2015c.

Kaufmann, M., Gusev, O. A., Grossmann, K. U., Roble, R. G., Hagan, M. E., Hartsough, C., and Kutepov, A. A.: The vertical and horizontal distribution of CO_2 densities in the upper mesosphere and lower thermosphere as measured by CRISTA, Journal of Geophysical Research: Atmospheres, 107, CRI 10–1–CRI 10–19, doi:10.1029/2001JD000704, 2002.

Kaufmann, M., Gil-López, S., López-Puertas, M., Funke, B., García-Comas, M., Glatthor, N., Grabowski, U., Höpfner, M., Stiller, G. P., von Clarmann, T., Koukouli, M. E., Hoffmann, L., and Riese, M.: Vibrationally excited ozone in the middle atmosphere, J. Atmos. Solar-Terr. Phys., 68, 202–212, doi:10.1016/j.jastp.2005.10.006, 2006.

Kaufmann, M., Zhu, Y., Ern, M., and Riese, M.: Global distribution of atomic oxygen in the mesopause region as derived from SCIAMACHY O(1S) green line measurements, Geophysical Research Letters, 41, 6274–6280, doi:10.1002/2014GL060574, 2014.

Kiefer, M., von Clarmann, T., Grabowski, U., De Laurentis, M., Mantovani, R., Milz, M., and Ridolfi, M.: Characterization of MIPAS elevation pointing, Atmos. Chem. Phys., 7, 1615–1628, 2007.

Kockarts, G.: Nitric oxide cooling in the terrestrial thermosphere, Geophys. Res. Lett., 7, 137–140, 1980.

Kurucz, R. L.: The Kurucz Smithsonian Atomic and Molecular Database, in: Astrophysical Applications of Powerful New Databases, edited by Adelman, S. J. and Wiese, W. L., vol. 78 of *Astronomical Society of the Pacific Conference Series*, p. 205, 1995.

Kutepov, A. A., Kunze, D., Hummer, D. G., and Rybicki, G. B.: The solution of radiative transfer problems in molecular bands without the LTE assumption by accelerated lambda iteration methods, J. Quant. Spectrosc. Radiat. Transfer, 46, 347–366, 1991.

Kyrölä, E., Tamminen, J., Leppelmeier, G., Sofieva, V., Hassinen, S., Bertaux, J., Hauchecorne, A., Dalaudier, F., Cot, C., Korablev, O., dÂndon, O. F., Barrot, G., Mangin, A., Théodore, B., Guirlet, M., Etanchaud, F., Snoeij, P., Koopman, R., Saavedra, L., Fraisse, R., Fussen, D., and Vanhellemont, F.: GOMOS on Envisat: an overview, Advances in Space Research, 33, 1020–1028, doi:http://dx.doi.org/10.1016/S0273-1177(03)00590-8, climate Change Processes in the Stratosphere, Earth-Atmosphere-Ocean Systems, and Oceanographic Processes from Satellite Data, 2004.

Laurentis, M. D.: Planning of MIPAS new special modes January 2005 campaign, Tech. rep., ESA Technical Note, ENVI-SPPA-EOPG-TN-05-0002, 1253–1254, 2005.

Lean, J., Rottman, G., Harder, J., and Kopp, G.: SORCE Contributions to New Understanding of Global Change and Solar Variability, Solar Physics, 230, 27–53, 2005.

Lepoutre, F., Louis, G., and Manceau, H.: Collisional relaxation in CO_2 between 180 K and 400 K measured by the spectrophone method, Chemical Physics Letters, 48, 509–514, doi:http://dx.doi.org/10.1016/0009-2614(77)85082-3, 1977.

Levenberg, K.: A method for the solution of certain non–linear problems in least squares, Quart. Appl. Math., 2, 164–168, 1944.

López-Puertas, M. and Funke, B.: Non-Local Thermodynamic Equilibrium, in: Encyclopedia of Atmospheric Sciences, 2nd edition, edited by North, G. R., Pyle, J., and Zhang, F., pp. 16–26, Elsevier, 2015.

López-Puertas, M. and Taylor, F. W.: Carbon dioxide 4.3 μm emission in the Earth's atmosphere: A comparison between Nimbus 7 SAMS measurements and non-local thermodynamic equilibrium radiative transfer calculations, Journal of Geophysical Research: Atmospheres, 94, 13 045–13 068, doi:10.1029/JD094iD10p13045, 1989.

López-Puertas, M. and Taylor, F. W.: Non-LTE radiative transfer in the Atmosphere, World Scientific Pub., Singapore, 2001.

López-Puertas, M., Rodrigo, R., López-Moreno, J. J., and Taylor, F. W.: A non–LTE radiative transfer model for infrared bands in the middle atmosphere. II. CO_2 (2.7 and 4.3 μm) and water vapour (6.3 μm) bands and $N_2(1)$ and $O_2(1)$ vibrational levels, J. Atmos. Terr. Phys., 48, 749–764, 1986a.

López-Puertas, M., Rodrigo, R., Molina, A., and Taylor, F. W.: A non–LTE radiative transfer model for infrared bands in the middle atmosphere. I. Theoretical basis and application to CO_2 15 μm bands, J. Atmos. Terr. Phys., 48, 729–748, 1986b.

López-Puertas, M., López-Valverde, M. A., Rinsland, C. P., and Gunson, M. R.: Analysis of the upper atmosphere $CO_2(v_2)$ vibrational temperatures retrieved from ATMOS/Spacelab 3 observations, Journal of Geophysical Research: Atmospheres, 97, 20 469–20 478, doi:10.1029/92JD02026, 1992.

López-Puertas, M., Zaragoza, G., López-Valverde, M. Á., and Taylor, F. W.: Non local thermodynamic equilibrium (LTE) atmospheric limb emission at 4.6 μm 1. An update of the CO_2 non–LTE radiative transfer model, J. Geophys. Res., 103, 8499–8513, 1998a.

López-Puertas, M., Zaragoza, G., López-Valverde, M. Á., and Taylor, F. W.: Non local thermodynamic equilibrium (LTE) atmospheric limb emission at 4.6 μm 2. An analysis of the daytime wideband radiances as measured by UARS improved stratospheric and mesospheric sounder, J. Geophys. Res., 103, 8515–8530, 1998b.

López-Puertas, M., López-Valverde, M. Á., García, R. R., and Roble, R. G.: A review of CO_2 and CO abundances in the middle atmosphere, in: Atmospheric Science Across the Stratopause, edited by Siskind, D. E., Eckermann, S. D., and Summers, M. E., vol. 123 of *Geophysical Monograph Series*, p. 83, American Geophysical Union, 2000.

López-Puertas, M., García-Comas, M., Funke, B., Picard, R. H., Winick, J. R., Wintersteiner, P. P., Mlynczak, M. G., Mertens, C. J., Russell III, J. M., and Gordley, L. L.: Evidence for an OH(υ) excitation mechanism of CO_2 4.3 μm nighttime emission from SABER/TIMED measurements, J. Geophys. Res., 109, D09307, doi:10.1029/2003JD004383, 2004.

López-Puertas, M., Funke, B., Gil-López, S., López-Valverde, M. A., von Clarmann, T., Fischer, H., Oelhaf, H., Stiller, G. P., Kaufmann, M., Koukouli, M. E., and Flaud, J.-M.: Atmospheric non-local thermodynamic equilibrium emissions as observed by the Michelson Interferometer for Passive Atmospheric Sounding (MIPAS), Comptes Rendus Physique, 6, 848–863, doi:10.1016/j.crhy.2005.07.012, 2005.

López-Puertas, M., Funke, B., García-Comas, Bermejo-Pantaleón, D., Kaufmann, M., and Dudhia, A.: Extension of the Reference atmospheres and Vibrational Temperatures (WP9220). Support to MIPAS Level 2 product validation (MIPAS L2), Report ESA ESRIN contract no 21719/08/i-ol, European Space Agency, 2009.

Lu, H. C., Chen, H. K., Chen, H. F., Cheng, B. M., and Ogilvie, J. F.: Absorption cross section of molecular oxygen in the transition $E^3\Sigma_u^-$ $v=$ 0–$X^3\Sigma_g^-$ v= 0 at 38 K, Astronomy and Astrophysics, 520, A19, 2010.

Maricq, M., Gregory, E., and Simpson, C.: Non-resonant V–V energy transfer between diatomic molecules at low temperatures, Chemical Physics, 95, 43–56, 1985.

Marquardt, D. W.: An algorithm for least–squares estimation of nonlinear parameters, J. Soc. Indust. Appl. Math., 11, 431–441, 1963.

Mengtao, Y. and Xiaolei, Z.: Non Local Thermal Equilibrium Effect on Bias Characteristics of CrIS Shortwave Temperature Sounding Channels (Submitted), J. Geophys. Res., 110, 2015.

Mertens, C. J., III, J. M. R., Mlynczak, M. G., She, C.-Y., Schmidlin, F. J., Goldberg, R. A., López-Puertas, M., Wintersteiner, P. P., Picard, R. H., Winick, J. R., and Xu, X.: Kinetic temperature and carbon dioxide from broadband infrared limb emission measurements taken from the TIMED/SABER instrument, Advances in Space Research, 43, 15–27, doi:http://dx.doi.org/10.1016/j.asr.2008.04.017, 2009.

Milne, E. A.: Thermodynamics of stars, in: Handbuch of Astrophysik, p. 65, Handbuch of Astrophysik, 1930.

Milz, M., von Clarmann, T., Fischer, H., Glatthor, N., Grabowski, U., Höpfner, M., Kellmann, S., Kiefer, M., Linden, A., Mengistu Tsidu, G., Steck, T., Stiller, G. P., Funke, B., López-Puertas, M., and Koukouli, M. E.: Water Vapour Distributions Measured with the Michelson Interferometer for Passive Atmospheric Sounding on board Envisat (MIPAS/Envisat), J. Geophys. Res., 110, D24307, doi:10.1029/2005JD005973, 2005.

Mlynczak, M. G. and Marshall, B. T.: A reexamination of the role of solar heating in the O2 atmospheric and infrared atmospheric bands, Geophysical Research Letters, 23, 657–660, 1996.

Mlynczak, M. G. and Solomon, S.: A Detailed Evaluation Of The Heating Efficiency In The Middle Atmosphere, Journal of Geophysical Research, 98, 10 517–10 541, 1993.

Mlynczak, M. G., Hunt, L. A., Marshall, B. T., Martin-Torres, F. J., Mertens, C. J., Russell, III, J. M., Remsberg, E. E., López-Puertas, M., Picard, R. H., Winick, J. R., Wintersteiner, P. P., Thompson, R. E., and Gordley, L. L.: Observations of infrared radiative cooling in the thermosphere on daily to multiyear timescales from the TIMED/SABER instrument, Journal of Geophysical Research, 115, A03 309, 2010.

Mlynczak, M. G., Hunt, L. A., Mertens, C. J., Thomas Marshall, B., Russell, J., Woods, T. N., Earl Thompson, R., and Gordley, L. L.: Influence of solar variability on the infrared radiative cooling of the thermosphere from 2002 to 2014, Geophysical Research Letters, 41, 2014GL059 556, 2014.

Nebel, H., Wintersteiner, P. P., Picard, R. H., Winick, J. R., and Sharma, R. D.: CO_2 non-local thermodynamic equilibrium radiative excitation and infrared dayglow at 4.3 μm: Application to Spectral Infrared Rocket Experiment data, Journal of Geophysical Research: Atmospheres, 99, 10 409–10 419, doi:10.1029/94JD00315, 1994.

NOAA report: State of the Climate: Global Analysis for December 2014, NOAA National Climatic Data Center, 2015.

Oelhaf, H.: MIPAS Mission Plan, ESA Technical Note ENVI-SPPA-EOPG-TN-07-0073, 2008.

Offermann, D. and Grossmann, K. U.: Thermospheric density and composition as determined by a mass spectrometer with cryo ion source, Journal of Geophysical Research, 78, 8296–8304, doi:10.1029/JA078i034p08296, 1973.

Offermann, D., Friedrich, V., Ross, P., and Zahn, U. V.: Neutral gas composition measurements between 80 and 120 km, Planetary and Space Science, 29, 747–764, doi:http://dx.doi.org/10.1016/0032-0633(81)90046-5, 1981.

Ogawa, S. and Ogawa, M.: Absorption Cross Sections of $O_2(a^1\Delta_g)$ and $O_2(X^3\Sigma_g^-)$ in the Region from 1087 to 1700 Å, Canadian Journal of Physics, 53, 1845–1852, 1975.

Perron, G., Aubertin, G., Desbiens, R., et al.: MIPAS level 1b algorithm evolutions, ESA Living Planet Symposium 2010 (Bergen, Norway), SP-686, 2010.

Picone, J., Hedin, A., Drob, D., and Aikin, A.: NRLMSISE-00 empirical model of the atmosphere: Statistical comparisons and scientific issues, J. Geophys. Res., 107, 1468, doi:10.1029/2002JA009 430, 2002.

Platnick, S. and Fontenla, J.: Model Calculations of Solar Spectral Irradiance in the 3.7-αm Band for Earth Remote Sensing Applications, J. Appl. Meteor. Climatol., 47, 124–134, doi:10.1175/2007JAMC1571.1, 2008.

Raspollini, P., Carli, B., Ceccherini, S., Bianco, S. D., Sgheri, L., Ridolfi, M., Carlotti, M., Dinelli, B., Castelli, E., Remedios, J., Sembhi, H., Moore, D., Dudhia, A., López-Puertas, M., Funke, B., Flaud, J.-M., von Clarmann, T., Hoepfner, M., Oelhaf, H., Kiefer, M., Chippefield, M., Perron, G., Aubertin, G., Levebre, M., Leroux, J.-F., Dub, S., Moreau, L., Kleinert, A., Birk, M., Wagner, G., Gessner, R., Mosner, P., Schmitt, M., Fehr, T., Niro, F., and DÁlba, L.: Level 2 near–real–time analysis of MIPAS measurements on ENVISAT, ESA Living Planet Symposium 2010 (Bergen, Norway), SP-686, pp. 11–d2, 2010.

Ravishankara, A. R., Dunlea, E. J., Blitz, M. A., Dillon, T. J., Heard, D. E., Pilling, M. J., Strekowski, R. S., Nicovich, J. M., and Wine, P. H.: Redetermination of the rate coefficient for the reaction of O(^{1}D) with N_2, Geophysical Research Letters, 29, 35–1–35–4, doi:10.1029/2001GL014850, 2002.

Rees, M. H.: Physics and Chemistry of the Upper Atmosphere, Cambridge University Press, 1989.

Rezac, L., Kutepov, A., III, J. R., Feofilov, A., Yue, J., and Goldberg, R.: Simultaneous retrieval of T(p) and CO_2 VMR from two-channel non-LTE limb radiances and application to daytime SABER/TIMED measurements, Journal of Atmospheric and Solar-Terrestrial Physics, 130-131, 23–42, doi:http://dx.doi.org/10.1016/j.jastp.2015.05.004, 2015.

Ridolfi, M., Carli, B., Carlotti, M., von Clarmann, T., Dinelli, B., Dudhia, A., Flaud, J.-M., Höpfner, M., Morris, P. E., Raspollini, P., Stiller, G., and Wells, R. J.: Optimized Forward and Retrieval Scheme for MIPAS Near-Real-Time Data Processing, Appl. Opt., 39, 1323–1340, 2000.

Rienecker, M., Suarez, M., Gelaro, R., et al.: MERRA: NASA´s Modern-Era Retrospective Analysis for Research and Applications, Journal of Climate, 24, 3624–3648, doi:doi:10.1175/JCLI-D-11-00015.1, 2011.

Rinsland, C. P., Gunson, M. R., Zander, R., and López-Puertas, M.: Middle and upper atmosphere pressure-temperature profiles and the abundances of CO_2 and CO in the upper atmosphere from ATMOS/Spacelab 3 observations, Journal of Geophysical Research: Atmospheres, 97, 20 479–20 495, doi:10.1029/92JD01622, 1992.

Rishbeth, H.: A greenhouse effect in the ionosphere?, Planetary and Space Science, 38, 945–948, doi:10.1016/0032-0633(90)90061-T, 1990.

Rishbeth, H. and Roble, R. G.: Cooling of the upper atmosphere by enhanced greenhouse gases - Modelling of thermospheric and ionospheric effects, Planetary and Space Science, 40, 1011–1026, doi:10.1016/0032-0633(92)90141-A, 1992.

Roble, R. G.: Energetics of the Mesosphere and Thermosphere, Geophys. Monograph, 87, 1–21, 1995.

Rodgers, C. D.: Inverse Methods for Atmospheric Sounding: Theory and Practice, vol. 2 of *Series on Atmospheric, Oceanic and Planetary Physics, F. W. Taylor, ed.*, World Scientific, 2000.

Rosser, W. A. and Gerry, E. T.: De-excitation of Vibrationally Excited CO_2* (ν^3) by Collisions with He, O_2, and H_2O, The Journal of Chemical Physics, 51, 2286–2287, doi:http://dx.doi.org/10.1063/1.1672337, 1969.

Rosser, W. A., Wood, A. D., and Gerry, E. T.: Deactivation of Vibrationally Excited Carbon Dioxide (ν^3) by Collisions with Carbon Dioxide or with Nitrogen, The Journal of Chemical Physics, 50, 4996–5008, doi:http://dx.doi.org/10.1063/1.1670996, 1969.

Rothman, L., Gordon, I., Barbe, A., Benner, D., Bernath, P., Birk, M., Boudon, V., Brown, L., Campargue, A., Champion, J.-P., Chance, K., Coudert, L., Dana, V., Devi, V., Fally, S., Flaud, J.-M., Gamache, R., Goldman, A., Jacquemart, D., Kleiner, I., Lacome, N., Lafferty, W., Mandin, J.-Y., Massie, S., Mikhailenko, S., Miller, C., Moazzen-Ahmadi, N., Naumenko, O., Nikitin, A., Orphal, J., Perevalov, V., Perrin, A., Predoi-Cross, A., Rinsland, C., Rotger, M., Simecková, M., Smith, M., Sung, K., Tashkun, S., Tennyson, J., Toth, R., Vandaele, A., and Auwera, J. V.: The HITRAN 2008 molecular spectroscopic database, Journal of Quantitative Spectroscopy and Radiative Transfer, 110, 533–572, doi:http://dx.doi.org/10.1016/j.jqsrt.2009.02.013, HITRAN, 2009.

Rothman, L., Gordon, I., Babikov, Y., Barbe, A., Benner, D. C., Bernath, P., Birk, M., Bizzocchi, L., Boudon, V., Brown, L., Campargue, A., Chance, K., Cohen, E., Coudert, L., Devi, V., Drouin, B., Fayt, A., Flaud, J.-M., Gamache, R., Harrison, J., Hartmann, J.-M., Hill, C., Hodges, J., Jacquemart, D., Jolly, A., Lamouroux, J., Roy, R. L., Li, G., Long, D., Lyulin, O., Mackie, C., Massie, S., Mikhailenko, S., Müller, H., Naumenko, O., Nikitin, A., Orphal, J., Perevalov, V., Perrin, A., Polovtseva, E., Richard, C., Smith, M., Starikova, E., Sung, K., Tashkun, S., Tennyson, J., Toon, G., Tyuterev, V., and Wagner, G.: The HITRAN 2012 molecular spectroscopic database, Journal of Quantitative Spectroscopy and Radiative Transfer, 130, 4–50, doi:http://dx.doi.org/10.1016/j.jqsrt.2013.07.002, {HITRAN2012} special issue, 2013.

Rothman, L. S. and Young, L. D. G.: Infrared energy levels and intensities of carbon dioxide - II., J. Quant. Spectrosc. Radiat. Transfer, 25, 505–524, doi:10.1016/0022-4073(81)90026-1, 1981.

Rothman, L. S., Jacquemart, D., Barbe, A., Chris Benner, D., Birk, M., Brown, L. R., Carleer, M. R., Chackerian, C., Chance, K., Coudert, L. H., Dana, V., Devi, V. M., Flaud, J.-M., Gamache, R. R., Goldman, A., Hartmann, J.-M., Jucks, K. W., Maki, A. G., Mandin, J.-Y., Massie, S. T., Orphal, J., Perrin, A., Rinsland, C. P., Smith, M. A. H., Tennyson, J., Tolchenov, R. N., Toth, R. A., Vander Auwera, J., Varanasi, P., and Wagner, G.: The HITRAN 2004 molecular spectroscopic database, J. Quant. Spectrosc. Radiat. Transfer, 96, 139–204, 2005.

Rybicki, G. B. and Hummer, D. G.: An accelerated lambda iteration method for multilevel radiative transfer. I - Non-overlapping lines with background continuum, Astron. Astrophys, 245, 171–181, 1991.

Sawa, Y., Machida, T., and Matsueda, H.: Seasonal variations of CO2 near the tropopause observed by commercial aircraft, Journal of Geophysical Research: Atmospheres, 113, n/a–n/a, doi:10.1029/2008JD010568, 2008.

Schuck, T. J., Brenninkmeijer, C. A. M., Slemr, F., Xueref-Remy, I., and Zahn, A.: Greenhouse gas analysis of air samples collected onboard the CARIBIC passenger aircraft, Atmospheric Measurement Techniques, 2, 449–464, doi:10.5194/amt-2-449-2009, 2009.

Sharma, R. D. and Wintersteiner, P. P.: CO2 component of daytime Earth limb emission at 2.7 micrometers, Journal of Geophysical Research: Space Physics, 90, 9789–9803, doi:10.1029/JA090iA10p09789, 1985.

Sharma, R. D. and Wintersteiner, P. P.: Role of carbon dioxide in cooling planetary thermospheres, Geophys. Res. Lett., 17, 2201–2204, 1990.

Shved, G., Kutepov, A., and Ogibalov, V.: Non-local thermodynamic equilibrium in {CO2} in the middle atmosphere. I. Input data and populations of the v_3 mode manifold states, Journal of Atmospheric and Solar-Terrestrial Physics, 60, 289–314, doi:http://dx.doi.org/10.1016/S1364-6826(97)00076-X, 1998.

Siddles, R., Wilson, G., and Simpson, C.: The vibrational deactivation of the bending modes of {CD4} and {CH4} measured down to 90 K, Chemical Physics, 188, 99–105, doi:http://dx.doi.org/10.1016/0301-0104(94)00248-7, 1994.

Siskind, D. E., Eckermann, S. D., and Summers, M. E., eds.: Atmospheric Science Across the Stratopause, vol. 123 of *AGU Geophysical Monograph Series*, AGU, Washington, 2000.

Smith, A. K., Garcia, R. R., Marsh, D. R., and Richter, J. H.: WACCM simulations of the mean circulation and trace species transport in the winter mesosphere, Journal of Geophysical Research, 116, D20 115, 2011.

Smith, A. K., López-Puertas, M., Xu, J., and Mlynczak, M. G.: Updated Calculation of the Heating Efficiency of the Exothermic Reaction H+O3 in the Mesosphere, J. Geophys. Res., accepted, 2015.

Stair, A. T., Sharma, R. D., Nadile, R. M., Baker, D. J., and Grieder, W. F.: Observations of limb radiance with Cryogenic Spectral Infrared Rocket Experiment, Journal of Geophysical Research: Space Physics, 90, 9763–9775, doi:10.1029/JA090iA10p09763, 1985.

Steffen, W., Richardson, K., Rockström, J., Cornell, S. E., Fetzer, I., Bennett, E. M., Biggs, R., Carpenter, S. R., de Vries, W., de Wit, C. A., Folke, C., Gerten, D., Heinke, J., Mace, G. M., Persson, L. M., Ramanathan, V., Reyers, B., and Sörlin, S.: Planetary boundaries: Guiding human development on a changing planet, Science, 347, doi:10.1126/science.1259855, 2015.

Stephens, G. L., Li, J., Wild, M., Clayson, C. A., Loeb, N., Kato, S., L'Ecuyer, T., Stackhouse, P. W., Lebsock, M., and Andrews, T.: An update on Earth's energy balance in light of the latest global observations, Nature Geoscience, 5, 691–696, doi:10.1038/ngeo1580, 2012.

Stiller, G. P., von Clarmann, T., Funke, B., Glatthor, N., Hase, F., Höpfner, M., and Linden, A.: Sensitivity of trace gas abundances retrievals from infrared limb emission spectra to simplifying approximations in radiative transfer modelling, Journal of Quantitative Spectroscopy and Radiative Transfer, 72, 249–280, doi: http://dx.doi.org/10.1016/S0022-4073(01)00123-6, 2002.

Taine, J. and Lepoutre, F.: Determination of energy transferred to rotation-translation in deactivation of CO_2(0001) by N_2 and O_2 and of CO(1) by CO_2, Chemical Physics Letters, 75, 448–451, doi: http://dx.doi.org/10.1016/0009-2614(80)80552-5, 1980.

Tikhonov, A.: On the solution of incorrectly stated problems and method of regularization, Dokl. Akad. Nauk. USSR, 151, 501–504, 1963.

Trinks, H. and Fricke, K. H.: Carbon dioxide concentrations in the lower thermosphere, Journal of Geophysical Research: Space Physics, 83, 3883–3886, doi:10.1029/JA083iA08p03883, 1978.

Trinks, H., Offermann, D., von Zahn, U., and Steinhauer, C.: Neutral composition measurements between 90 and 220 km altitude by rocket-borne mass spectrometer, Journal of Geophysical Research: Space Physics, 83, 2169–2176, doi:10.1029/JA083iA05p02169, 1978.

Vercheval, J., Lippens, C., Muller, C., Ackerman, M., and Lemaitre, M.: CO_2 and CO vertical distribution in the middle atmosphere and lower thermosphere deduced from infrared spectra, Annales Geophysicae, 56, 161–164, 1994.

Vollmann, K. and Grossmann, K.: Excitation of 4.3μm CO_2 emissions by O(^{1}D) during twilight, Advances in Space Research, 20, 1185–1189, doi:http://dx.doi.org/10.1016/S0273-1177(97)00770-9, coupling and Energetics in the Stratosphere-Mesosphere-Thermosphere- Ionosphere System, 1997.

von Clarmann, T.: Smoothing error pitfalls, Atmospheric Measurement Techniques, 7, 3023–3034, doi:10.5194/amt-7-3023-2014, 2014.

von Clarmann, T. and Echle, G.: Selection of optimized microwindows for atmospheric spectroscopy, Appl. Opt., 37, 7661–7669, 1998.

von Clarmann, T., Dudhia, A., Edwards, D. P., Funke, B., Höpfner, M., Kerridge, B., Kostsov, V., Linden, A., López-Puertas, M., and Timofeyev, Y. M.: Intercomparison of radiative transfer codes under non-local thermodynamic equilibrium conditions, J. Geophys. Res., 107, 4631, doi:10.1029/2001JD001551, 2002.

von Clarmann, T., Glatthor, N., Grabowski, U., Höpfner, M., Kellmann, S., Kiefer, M., Linden, A., Mengistu Tsidu, G., Milz, M., Steck, T., Stiller, G. P., Wang, D. Y., Fischer, H., Funke, B., Gil-López, S., and López-Puertas, M.: Retrieval of temperature and tangent altitude pointing from limb emission spectra recorded from space by the Michelson Interferometer for Passive Atmospheric Sounding (MIPAS), J. Geophys. Res., 108, 4736, doi:10.1029/2003JD003602, 2003.

Whitson, M. E. and McNeal, R. J.: Temperature dependence of the quenching of vibrationally excited N_2 by NO and H_2O, The Journal of Chemical Physics, 66, 2696–2700, doi:http://dx.doi.org/10.1063/1.434217, 1977.

Wintersteiner, P. P., Picard, R. H., Sharma, R. D., Winick, J. R., and Joseph, R. A.: Line–by–line Radiative Excitation Model for the Non–Equilibrium Atmosphere: Application to CO_2 15–μm Emission, J. Geophys. Res., 97, 18,083–18,117, 1992.

Yue, J., Russell, III, J. M., Jian, Y., Rezac, L., Garcia, R. R., López-Puertas, M., and Mlynczak, M. G.: Increasing carbon dioxide concentration in the upper atmosphere observed by SABER, Geophysical Research Letters, 42, 1–6, 2015.

Zaragoza, G., López-Puertas, M., López-Valverde, M., and Taylor, F. W.: Global distribution of CO_2 in the upper mesosphere as derived from UARS/ISAMS measurements, Journal of Geophysical Research: Atmospheres, 105, 19 829–19 839, doi:10.1029/2000JD900243, 2000.